Semiconductors, Vol. 38, No. 11, 2004, pp. 1241–1244. Translated from Fizika i Tekhnika Poluprovodnikov, Vol. 38, No. 11, 2004, pp. 1281–1284.

ATOMIC STRUCTURE AND NONELECTRONIC PROPERTIES OF SEMICONDUCTORS

Effects of Pressure and Hydrogen on the Formation of Vacancies and Divacancies in Crystalline Silicon

V. G. Zavodinsky*^, A. A. Gnidenko*, A. Misiuk, and J. Bak-Misiuk*****

**Institute of Materials Science, Far East Division, Russian Academy of Sciences, Khabarovsk, 680042 Russia*

^e-mail: vzavod@mail.ru

***Institute of Electron Technology, Warsaw, 02-668 Poland*

****Institute of Physics, Polish Academy of Sciences, Warsaw, 02-668 Poland*

Submitted October 30, 2003; accepted for publication April 1, 2004

Abstract—The electron-density functional and pseudopotential methods are used to study the effects of hydrogen and pressure on the formation of vacancies and divacancies in silicon. It is shown that the formation energy of vacancies can be reduced by 1.8–3.5 eV and that of divacancies by 2.0–5.4 eV in the presence of hydrogen. As a result, the spontaneous generation of vacancies and vacancy-containing complexes becomes possible at high concentrations of hydrogen. At the same time, the presence of hydrogen makes silicon less sensitive to pressure and, at high hydrogen concentrations, can completely suppress the tendency toward additional formation of vacancies in the sample exposed to pressure. *© 2004 MAIK "Nauka/Interperiodica".*

1. INTRODUCTION

The presence of hydrogen in a silicon crystal lattice affects various properties of silicon. As it has high diffusivity, hydrogen (whose sources are many of the reactants used in semiconductor technology and water vapor) can easily penetrate silicon crystals even at room temperature and, thus, can interact with various defects of the crystal lattice. Hydrogen has a high chemical activity and reacts with impurities and crystal-lattice defects. Intrinsic point defects and their complexes with impurity atoms are formed in silicon crystals during technological treatment. Studying the interaction of these defects with hydrogen therefore has both scientific and practical significance.

Calculations from first principles show that hydrogen can be present in both atomic [1] and molecular [2, 3] states in silicon that is free of defects and other impurities. The molecular state is more favorable and yields an energy gain per hydrogen atom of 1.0 eV [4]. At the same time, the presence of hydrogen in silicon is conducive to the formation of vacancies [5, 6]. The difference between the energy of the Si–H bond and that of isolated interstitial hydrogen (2.2 eV) is sufficiently large to initiate the spontaneous formation of vacancies if four dangling silicon bonds are saturated simultaneously with hydrogen [7]. Even the formation of microvoids in silicon is possible if the hydrogen concentration is high [8]. In addition, it is well known that pressure also stimulates the appearance of vacancies in silicon by reducing their formation energy [9]. However, the combined effect of hydrogen and pressure on the formation of vacancies and vacancy-containing complexes has so far not been studied.

The objective of this study was to gain insight into the effect of pressure on the processes of formation of isolated vacancies and divacancies in crystalline silicon that contains hydrogen. We will not discuss issues related to the kinetics of these processes; i.e., we will not consider the diffusion of hydrogen molecules and atoms and that of silicon self-interstitials that appear as a result of the formation of vacancies. In other words, we will not consider the activation energies of the processes; we will only compare the energies of the initial and final states. Such an approach is justified in the case of high temperatures when we are interested only in the final result rather than in the process rate. Since we will compare our calculations with high-temperature (~1000°C) experiments [8], the approach above is completely justified. The effect of pressure on the diffusion-related processes will be considered in a separate publication.

2. METHOD AND PARAMETERS OF CALCULATION

The theoretical studies reported in this paper are based on the theory of the electron-density functional [10] in the local-density approximation [11, 12], which is combined with the pseudopotential method in the Troullier–Martins approximation [13].

For the calculations, we used the FHI96md software package [14], which made it possible to optimize the atomic configuration of the system and determine its total energy. Plane waves were chosen as the basis; the cutoff energy was varied from 8 to 20 Ry. In order to take into account the relaxation of the silicon crystal lattice around defects, we performed all the calcula-

tions for a silicon supercell composed of 64 silicon atoms. We used the Γ point of the Brillouin zone as the *k* point.

The equilibrium value of the silicon lattice constant was equal to 5.35 Å according to our calculations. In order to simulate the compression, we reduced the silicon lattice constant by 1–5%, which corresponded to a pressure of 1–5 GPa. These values are consistent with the pressures that actually exist in silicon and arise in semiconductor devices when they are used in conditions of dynamic loads and under the effect of thermoelastic stresses at the interfaces between silicon and other materials.

3. RESULTS AND DISCUSSION

3.1. Vacancies and Divacancies in High-Purity Silicon under Atmospheric Pressure

The vacancy-formation energy was determined from the following formula:

$$E_f(\text{vac}) = E_{\text{Si}_{64}} - (E_{\text{Si}_{63}} + E_{\text{Si}}).$$

Here, $E_{\text{Si}_{64}}$ is the energy of a silicon supercell, $E_{\text{Si}_{63}}$ is the energy of a silicon supercell with a vacancy, and E_{Si} is the silicon chemical potential whose value was determined from separate calculations. Accordingly, we have the following expression for a divacancy:

$$E_f(\text{divac}) = E_{\text{Si}_{64}} - (E_{\text{Si}_{62}} + 2E_{\text{Si}}).$$

Here, $E_{\text{Si}_{62}}$ is the energy of a silicon supercell with a divacancy. It is implied that the "excess" silicon atoms released as a result of the formation of vacancies and divacancies reach the surface and become incorporated into it; thus, one of the "surface" atoms is transformed into a "volume" atom, so that the number of volume atoms is conserved.

Different values of formation energy for vacancies and divacancies in silicon are reported in various publications [15–17]. The energy for a vacancy ranges from 3 to 4 eV; for a divacancy, 4–5 eV. Our calculations (with a cutoff energy of 8 Ry) yielded values of 3.0 and 4.2 eV, respectively, which are in good agreement with published data.

3.2. Hydrogen in Silicon under Atmospheric Pressure

Since the molecular state of hydrogen in silicon that does not contain other impurities and intrinsic defects is more favorable than the atomic state, we will compare the energy of hydrogen in various defect structures with that of molecular hydrogen. In the absence of lattice defects, the tetragonal interstitial site is the most favorable site for molecular hydrogen in silicon [18, 19]. The formation energies for a vacancy and a divacancy in the presence of a hydrogen molecule decreases because a spontaneous dissociation of the H_2 molecule and saturation of dangling silicon bonds with hydrogen occur when hydrogen transfers from an interstitial site to a vacancy (divacancy). In this case, the formation energies are defined by the following formulas:

$$E_f(\text{vac}) = E_{\text{Si}_{64}+\text{H}_2} - (E_{\text{Si}_{63}+2\text{H}} + E_{\text{Si}}),$$

$$E_f(\text{divac}) = E_{\text{Si}_{64}+\text{H}_2} - (E_{\text{Si}_{62}+2\text{H}} + 2E_{\text{Si}}).$$

Here, $E_{\text{Si}_{64}+\text{H}_2}$ is the energy of a system that consists of silicon and a hydrogen molecule at a tetragonal site, $E_{\text{Si}_{63}+2\text{H}}$ is the energy of a system that consists of silicon and two hydrogen atoms in a vacancy, and $E_{\text{Si}_{62}+2\text{H}}$ is the energy of a system consisting of silicon and two hydrogen atoms that reside in a divacancy.

Our calculations yielded 1.2 eV for the formation energy for a vacancy in the presence of a hydrogen molecule and 2.3 eV for the case of a divacancy. Thus, the presence of a small amount of hydrogen in silicon reduces the formation energy for both vacancy and divacancy by about 2 eV. Only partial passivation of the internal dangling bonds of silicon occurs in this situation. Hydrogen can passivate all the dangling bonds if its concentration is higher. In that case, a vacancy attracts two hydrogen molecules, while a divacancy attracts three. A gain in the energy becomes so large that the formation energies become negative: –0.5 eV for a vacancy and –1.3 eV for a divacancy. Consequently, at high hydrogen concentrations, vacancies and divacancies can be formed spontaneously without any additional energy (for example, thermal) expenses, and they are immediately filled with hydrogen, which is consistent with experimental data [8].

The available published theoretical data are also consistent with our results. For example, Van der Walle *et al.* [4] showed that the energy of a silicon crystal is reduced by ~2.2 eV owing to the passivation of a single dangling bond when an isolated hydrogen atom is transferred from an interstitial site to a vacancy; two hydrogen atoms reduce the crystal energy by 4.4 eV if these atoms passivate two dangling bonds. Since we are considering molecular hydrogen (rather than atomic hydrogen) as the initial state, we should subtract the dissociation energy of a hydrogen molecule (equal to 2 eV [4]) from 4.4 eV in order to compare the data of [4] with our results. Thus, according to [4], the formation energy for a vacancy in the presence of a hydrogen molecule is reduced by 2.4 eV, which is not very different from our value of 2 eV.

3.3. The Combined Effect of Pressure and Hydrogen

We studied the effect of pressure on the formation of vacancies and divacancies in silicon that contains and does not contain hydrogen. In this case, the formation energy for a vacancy was determined from the expression

$$E_f^P = (E_{\text{Si}_{63}}^P + E_{\text{Si}}^P) - E_{\text{Si}_{64}}^P,$$

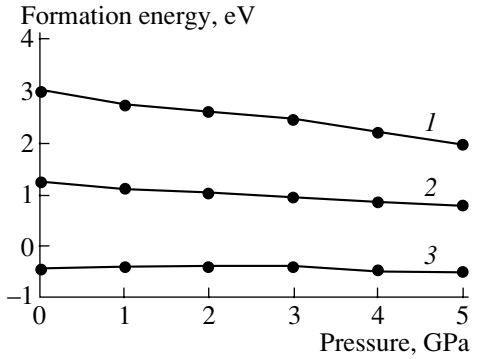

Fig. 1. Dependences of the vacancy-formation energy on pressure in silicon (*1*) without hydrogen, (*2*) in the presence of a hydrogen molecule, and (*3*) in the presence of three hydrogen molecules.

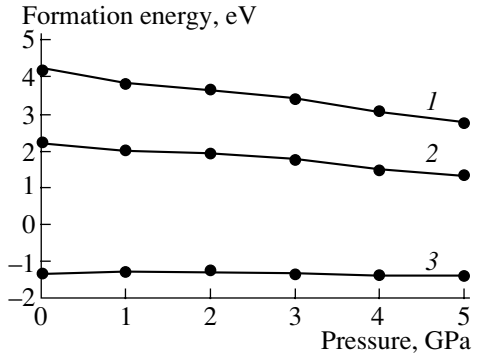

Fig. 2. Dependences of the divacancy-formation energy on pressure in silicon (*1*) without hydrogen, (*2*) in the presence of a hydrogen molecule, and (*3*) in the presence of three hydrogen molecules.

where the superscript P indicates the dependence of corresponding parameters on pressure.

The formation energy for a vacancy in silicon that contains hydrogen and is subjected to pressure was determined from the formula

$$E_f^P = (E^P_{\mathrm{Si}_{63}+2N\mathrm{H}} + E^P_{\mathrm{Si}}) - E^P_{\mathrm{Si}_{64}+N\mathrm{H}_2},$$

where $N = 1, 2$ is the number of hydrogen molecules.

In Fig. 1 we show the calculated dependences of the formation energies for a vacancy E_f on pressure in silicon that contains and does not contain hydrogen. The value of E_f decreases linearly with increasing pressure in silicon without hydrogen: as the pressure increases to 5 GPa, the value of E_f decreases by 1 eV. This result is qualitatively consistent with the data reported previously [9] but differs from these data quantitatively: according to [9], the vacancy-formation energy decreases by only 0.2 eV as the pressure increases to 5 GPa. In our opinion, this discrepancy is caused by the fact that a cell with 32 silicon atoms was used in [9] to simulate the behavior of a vacancy, whereas we used a cell composed of 64 atoms. As shown previously [20], it is necessary to use a cell with no less than 70 atoms in order to describe realistically the relaxation properties of a vacancy in silicon (these properties are important in studying the effect of pressure). As the number of atoms decreases, the error increases drastically. This behavior is understandable since the boundary atoms in the cell are fixed during simulation and cannot contribute to the relaxation. At the same time, there are a relatively large number of boundary atoms in cells with a small number of atoms. Specifically, 26 atoms are involved in relaxation around a vacancy in a cell composed of 64 atoms, whereas only 4 atoms are involved in this relaxation in a cell composed of 32 atoms. The result we obtained indicates that pressure has a relatively strong effect on vacancy formation and is implicitly consistent with the results reported in [21], where the effect of pressure on the activation energy of As diffusion (with a vacancy-related origin) in silicon was studied and a decrease in E_f by 0.7 eV was observed under a pressure of 6 GPa.

A decrease in the vacancy-formation energy as a result of exposure to pressure is attributed to the fact that pressure reduces the distances between atoms, specifically, between the atoms that have dangling bonds and surround the vacant site in the crystal lattice. As a result, we have an increased overlap of the wave functions that correspond to dangling bonds and an increase in the exchange (covalent) interaction. Simultaneously, a partial (proportional to the pressure) saturation of dangling bonds occurs, the vacancy energy decreases, and the vacancy-formation energy decreases.

Hydrogen reduces the vacancy-formation energy by saturating (passivating) the dangling bonds. Therefore, one would not expect the pressure to have a significant effect on the formation energy for vacancies with completely passivated dangling bonds. The effect of pressure is expected to be less in the case of incomplete passivation than in the case of the absence of hydrogen. Indeed, as can be seen from Fig. 1, the curve representing the dependence of E_f on pressure in the presence of a single H_2 molecule has slope that is smaller by a factor of two in the absence of hydrogen. Two hydrogen molecules completely neutralize the effect of pressure (within the accuracy of the calculation and simulation methods used). Similar results were also obtained for a divacancy (Fig. 2). A pressure of 5 GPa applied to silicon devoid of hydrogen reduces the divacancy-formation energy by 1.4 eV. In the presence of a single hydrogen molecule, the formation energy decreases by 2 eV, continues to decrease with increasing pressure, and attains a value of 1.3 eV at 5 GPa. At higher hydrogen concentrations (three hydrogen molecules per divacancy), in which case all the dangling bonds are saturated, the divacancy-formation energy at the zero pressure is equal to –1.3 eV. The divacancy-formation energy remains nearly constant as pressure increases further (Fig. 2, curve *3*).

The values of the vacancy- and divacancy-formation energies (in eV) in relation to the cutoff energy E_{cut}

Energy	E_{cut} = 8 Ry	E_{cut} = 16 Ry	E_{cut} = 20 Ry
E_f (vac)	3.0	2.9	3
E_f (vac, H_2)	1.2	1.1	1.1
E_f (divac)	4.2	4.0	4.0

In order to estimate the reliability of the results reported here, we performed test calculations at higher cutoff energies (16 and 20 Ry). The results obtained are listed in the table.

The difference in the vacancy-formation energies calculated at various values of the cutoff energy is within the error of the calculation method (0.1 eV). For a divacancy, the difference in energies represents an error within 0.2 eV, which is within the range of the spread in the available published data.

4. CONCLUSION

Calculations from first principles show that pressure stimulates significantly the appearance of vacancies and divacancies in silicon by decreasing the energy of their formation owing to the fact that atoms with dangling bonds are forced closer to each other and that exchange interaction between these atoms increases. As hydrogen is introduced into silicon, the effect of pressure is reduced, as hydrogen atoms passivate the dangling bonds. If the amount of hydrogen is insufficient to passivate all the dangling bonds, the pressure has almost no additional effect on the formation of vacancies and divacancies.

ACKNOWLEDGMENTS

This study was supported in part by the Presidium of the Far East Division, Russian Academy of Sciences, project no. 03-3-B-02-1-003.

REFERENCES

1. C. G. Van de Walle, P. J. H. Denteneer, Y. Bar-Yam, and S. T. Pantelides, Phys. Rev. B **39**, 10791 (1989).
2. J. W. Corbett, S. N. Sahu, T. S. Shi, and L. C. Snyder, Phys. Lett. A **93A**, 303 (1983).
3. A. Mainwood and A. M. Stoneham, Physica B & C (Amsterdam) **116**, 101 (1983); J. Phys. C **17**, 2513 (1984).
4. C. G. Van de Walle, Y. Bar-Yam, and S. T. Pantelides, Phys. Rev. Lett. **60**, 2761 (1988).
5. S. K. Estreicher, J. L. Hastings, and P. A. Fedders, Phys. Rev. B **57**, R12663 (1998).
6. M. A. Roberson and S. K. Estreicher, Phys. Rev. B **49**, 17040 (1994).
7. C. G. Van de Walle, Phys. Rev. B **49**, 4579 (1994).
8. A. Misiuk, H. B. Surma, I. V. Antonova, *et al.*, Solid State Phenom. **69–70**, 345 (1999).
9. A. Antonelli and J. Bernholc, Phys. Rev. B **40**, 10643 (1989).
10. P. Hohenberg and W. Kohn, Phys. Rev. **136**, 864 (1964).
11. D. M. Ceperley and B. J. Alder, Phys. Rev. Lett. **45**, 567 (1980).
12. J. P. Perdew and A. Zunger, Phys. Rev. B **23**, 5048 (1981).
13. N. Troullier and J. L. Martins, Phys. Rev. B **43**, 1993 (1991).
14. M. Bockstedte, A. Kley, J. Neugebauer, and M. Scheffler, Comput. Phys. Commun. **107**, 187 (1997).
15. T. J. Lenosky, J. D. Kress, I. Kwon, *et al.*, Phys. Rev. B **55**, 1528 (1997).
16. M. Tang, L. Colombo, J. Zhu, and T. D. de la Rubia, Phys. Rev. B **55**, 14 279 (1997).
17. N. Bernstein, M. J. Mehl, D. Papaconstantopoulos, *et al.*, Phys. Rev. B **62**, 4477 (2000).
18. K. G. Nakamura, K. Ishioka, M. Kitajima, and K. Murakami, Solid State Commun. **101**, 735 (1997).
19. H. Takaba, A. Endou, A. Yamada, *et al.*, Jpn. J. Appl. Phys. **39**, 2744 (2000).
20. S. Öğüt, H. Kim, and J. Chelikowsky, Phys. Rev. B **56**, R11353 (1997).
21. O. Sugino and A. Oshiyama, Phys. Rev. Lett. **68**, 1858 (1992).

Translated by A. Spitsyn

Semiconductors, Vol. 38, No. 11, 2004, pp. 1245–1253. Translated from Fizika i Tekhnika Poluprovodnikov, Vol. 38, No. 11, 2004, pp. 1285–1293.

ATOMIC STRUCTURE AND NONELECTRONIC PROPERTIES OF SEMICONDUCTORS

$(IV_2)_{1-x}(III–V)_x$ Solid Solutions Obtained from a Bounded Tin Melt–Solution

B. Sapaev, M. S. Saidov, A. S. Saidov^, and S. Zh. Karazhanov

Physicotechnical Institute, Physics–Sun Scientific Production Union, Academy of Sciences of Uzbekistan, Tashkent, 700084 Uzbekistan

^e-mail: amin@physic.uzsci.net

Submitted July 30, 2003; accepted for publication October 17, 2003

Abstract—The formation of a continuous series of substitutional solid solutions is theoretically considered from the viewpoint of taking into account generalized moments and differences in the valence and the covalent radii of atoms or molecules of initial components. These considerations are used to develop technology for the fabrication of $(Si_2)_{1-x}(GaAs)_x$ $(0 \le x \le 0.96)$ and $(Si_2)_{1-x}(GaP)_x$ $(0 \le x \le 1)$ epitaxial layers on silicon substrates from a tin melt–solution by the forced cooling method. The distribution of components over the thickness of the $(Si_2)_{1-x}(GaAs)_x$ and $(Si_2)_{1-x}(GaP)_x$ layers, the photosensitivity, and the current–voltage characteristics of Si–$(Si_2)_{1-x}(GaAs)_x$ and Si–$(Si_2)_{1-x}(GaP)_x$ heterostructures were studied. The analysis of results of X-ray investigations and photoelectric properties indicate that the grown epitaxial layers of $(IV_2)_{1-x}(III–V)_x$ solid solutions are structurally perfect. © *2004 MAIK "Nauka/Interperiodica".*

1. INTRODUCTION

The study of the liquid-phase epitaxy and properties of grown epitaxial films with the aim of expanding the range and reducing the cost of semiconductor materials, as well as to fabricate structures with new properties suitable for devices of modern microelectronics and optoelectronics, remains a problem of current interest in semiconductor materials science and photoelectronics. Therefore, it is very promising to investigate the feasibility of growing III–V compounds and epitaxial layers of their solid solutions on less expensive substrates, such as single-crystal and polycrystalline Si, using liquid-phase epitaxy. The III–V compounds and their solid solutions are the most suitable materials for producing semiconductor devices, such as high-efficiency solar cells, injection GaAs lasers, and optical-range GaP light-emitting diodes. It is possible to considerably expand the scope of these semiconductors using their $(IV_2)_{1-x}(III–V)_x$ solid solutions due to the possibility of controllably varying the band gap and individual properties while keeping other properties unchanged.

The possibilities for the practical application of solid solutions based on Group-IV elements and III–V compounds and their heterostructures have still not been completely clarified. Therefore, a further search is required to improve the purity of materials and clarify the behavior of impurities, as well as to attain high crystalline quality. In this context, it is very important to perform combined theoretical and experimental studies of conditions for growing the epitaxial layers of wide-gap $(IV_2)_{1-x}(III–V)_x$ solid solutions and to fabricate heterostructures with the specified properties based on them. In this paper, we report the results of experimental and theoretical studies of the properties of Si–$(IV_2)_{1-x}(III–V)_x$ structures.

2. METHODS

2.1. Conditions for the Formation of a Continuous Series of Solid Solutions in Multicomponent Systems

For the solubility of multicomponent systems, Saidov [1] suggested the formula

$$C'_{Ni} = \frac{C''_{Ni}\exp[-(1/kT)(a\Delta Z_i + b\Delta r_i)]}{1 + \sum_{i=1}\{\exp[-(1/kT)(a\Delta Z_i + b\Delta r_i)] - 1\}C''_{Ni}}. \quad (1)$$

For two-component systems ($i = 1$), formula (1) is written as

$$C'_{N1} = \frac{C''_{N1}\exp[-(1/kT)(a\Delta Z_1 + b\Delta r_1)]}{1 + \{\exp[-(1/kT)(a\Delta Z_1 + b\Delta r_1)] - 1\}C''_{N1}}, \quad (2)$$

where

$$\Delta Z_i = Z_i - Z_j, \quad \Delta r_i = r_i - r_j. \quad (3)$$

In expressions (1)–(3), C'_{Ni} and C''_{Ni} are the mole fractions of the (') and (") phases, Z_i is the valence, r_i is the covalent radius of atoms of the ith component, k is the Boltzmann constant, T is the absolute temperature, and

Parameters of components of hypothetical solid solutions

CD	E_g, eV	$R_A + R_B$, Å / $R_C + R_D$, Å	A_2, AB: Si_2	SiGe	SiSn
		E_g, eV	1.08	<1.08	<1.08
			2.34	2.39	2.57
AlP	2.42	2.36	–0.02	0.03	0.21
GaP	2.25	2.36	–0.02	0.03	0.21
InP	1.34	2.54	–0.20	–0.15	0.03
AlAs	2.16	2.44	–0.10	–0.05	0.13
GaAs	1.45	2.44	–0.10	–0.05	0.13
AlSb	1.60	2.62	–	0.23	–0.05
GaSb	0.79	2.62	–	0.23	–0.05
InSb	0.18	2.80	–	–	–0.23
ZnS	3.54	2.35	–0.01	0.04	0.22
ZnSe	2.80	2.45	–0.11	–0.06	0.12
ZnTe	2.30	2.63	–	–	0.06
CdS	2.48	2.52	–0.18	–0.13	0.05
CdSe	1.85	2.62	–	–	–0.05
CdTe	1.47	2.80	–	–	–0.23

Note: Values of Δr are given in Å.

a and *b* are constants determined experimentally; the subscript *j* refers to a solvent.

According to formula (2), the lower $|\Delta Z_1|$ and $|\Delta r_1|$, the higher the solubility of component 1. If the system components are binary compounds of the A_2, AB, and CD type (A and B are the Group-IV elements, and CD denotes III–IV, II–VI, and I–VII compounds), we have

$$\Delta Z_i = (Z_A + Z_B) - (Z_C + Z_D), \quad (4)$$

$$\Delta r_i = (r_A + r_B) - (r_C + r_D). \quad (5)$$

Generalizing the experimental data according to which a continuous series of solid solutions on the basis of elementary metals [2] and binary semiconductor compounds [3] is formed if their components have identical types of crystal lattices and chemical compounds, and the difference in the radii of their atoms or molecules is less than 15%, Saidov [1] used formulas (4) and (5) to suggest the following conditions for the formation of continuous substitutional solid solutions for binary compounds:

$$\Delta Z = 0, \quad (6)$$

$$\Delta r = (r_A + r_B) - (r_C + r_D) < 0.1(r_A + r_B). \quad (7)$$

In the table, we list some III–V and II–VI compounds and silicon-containing IV_2 and IV–IV compounds, their band gaps (E_g), sums of radii of atoms of elements ($R_A + R_B$, $R_C + R_D$), and Δr values that satisfy condition (7). As can be seen, Si_2 and SiGe can form a continuous series of solid solutions with III–V and II–VI compounds in approximately 14 cases.

2.2. Experimental Setup and Method of Growth

Two types of continuous solid solutions, $(Si_2)_{1-x}(GaP)_x$ and $(Si_2)_{1-x}(GaAs)_x$, were prepared, and their properties were studied. The solubility was measured by the weight-loss method applied to a semiconductor crystal after the liquid phase has attained saturation in an atmosphere of hydrogen purified by passing through palladium. In [4], the effect of certain elements on the solubility of silicon in tin was determined. We developed this line of investigation and report in this paper the results of studying the effect of the third component on the solubility of silicon, gallium phosphide, and gallium arsenide in tin and in tin solutions containing GaP, GaAs, GaSb, and Sb at various temperatures. The temperature was measured by a Chromel–Alumel thermocouple. Semiconductor plates (GaP, GaAs, and Si) attached to the special graphite holder were immersed into the melt. The crystal was extracted from the melt after its saturation at a given temperature, and the solubility of the material was calculated from the weight-loss measurement using a VLR-200 balance with an accuracy of 0.05 mg. The holder and crucible were made of spectral-purity graphite. The purity of the materials used was no worse than 99.999%.

Epitaxial layers of $(Si_2)_{1-x}(GaAs)_x$ solid solutions were grown on polycrystalline silicon substrates 20 mm in diameter. Single-crystal silicon substrates 20 and 40 mm in diameter were used to grow the layers of $(Si_2)_{1-x}(GaP)_x$ solid solutions. We used a vertical-type reactor with horizontally arranged substrates (Fig. 1). In this case, the epitaxial films grow from a small volume of melt–solution bounded by two substrates. It corresponds to the requirements of highest efficiency; i.e., the epitaxy is carried out with a minimal quantity of melt–solution. The growth was carried out in an atmosphere of hydrogen purified by passing it through palladium. In this case, the reactor was first evacuated to a residual pressure of 10^{-2} Pa; then, the purified hydrogen was let in. Hydrogen was passed through the reactor for a period of 10–15 min, after which the heating began. When the temperature attained a certain value, the system was switched to automatic mode. Over a period of 30–40 min, the melt–solution became homogenized. Then, the substrates were brought into contact with the melt–solution. At the initial moment of growth, Si was crystallized from the melt–solution according to the diagram of states and the coefficient of distribution because the solution is saturated with Si at the epitaxy temperature. At lower temperatures, the conditions for growing $(Si_2)_{1-x}(GaAs)_x$ and $(Si_2)_{1-x}(GaP)_x$ solid solutions are satisfied; i.e., at these temperatures, the melt–solution becomes supersaturated with silicon, gallium arsenide, or gallium phosphide.

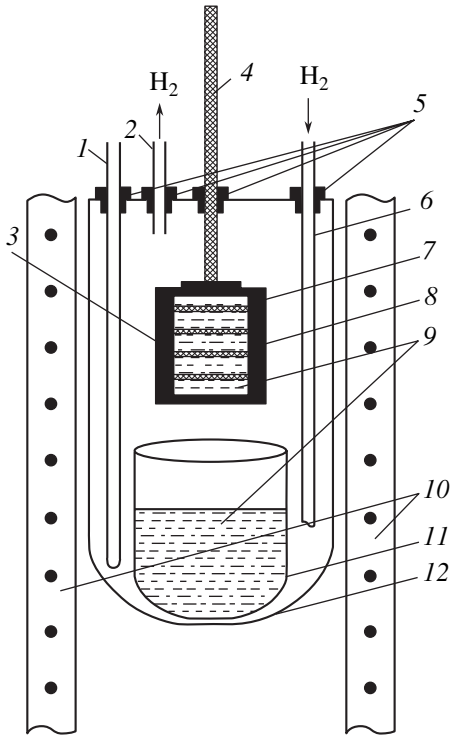

Fig. 1. Schematic representation of setup for growing solid solutions from the bounded melt–solution volume. (*1*) quartz tube for thermocouple, (*2*) H_2 outlet, (*3*) silicon substrates, (*4*) rod with the sample holder, (*5*) bolts for hermetic sealing, (*6*) H_2 inlet, (*7*) graphite cartridge, (*8*) graphite gasket, (*9*) melt–solution, (*10*) electric furnace, (*11*) quartz glass, and (*12*) quartz chamber.

3. RESULTS

3.1. A Study of Conditions for the Formation of a Continuous Series of Solid Solutions

Until now, we experimentally obtained $(Si_2)_{1-x}(GaP)_x$, $(Si_2)_{1-x}(GaAs)_x$, $(Si_2)_{1-x}(ZnS)_x$, $(Si_2)_{1-x}(InSb)_x$, and $(Ge_2)_{1-x}(InP)_x$ solid solutions. The found solubilities for GaP, GaAs, and Si in tin at 600–1000°C are in a good agreement with known data [5, 6]. It follows from the temperature dependence of solubility of silicon in Sn + GaSb (1 mol %) solution that the presence of GaSb in the tin melt at temperatures of 850°C or higher increases the solubility of silicon, which is probably induced by the decomposition of GaSb. Studying the effect of GaP, GaAs, GaSb, and Sb on the solubility of silicon in tin at 800°C shows that GaP, GaAs, and GaSb cause the solubility of Si to increase. This is also true of Ga [4], whereas Sb hardly changes the solubility of Si.

3.2. Growth and Properties of $(Si_2)_{1-x}(GaAs)_x$

To determine the composition of the melt–solution, the diagrams of states of the Si–GaAs–solvent system were preliminarily investigated by the solubility method. In this case, the published data [5, 7] were used. The technological procedure for growing the epitaxial films includes conventional technological operations [8]. The films of $(Si_2)_{1-x}(GaAs)_x$ solid solutions were grown in a hydrogen atmosphere from a bounded tin melt–solution in the temperature range 850–700°C. As substrates, we used wafers 20 mm in diameter and 350–400 μm thick cut from ingots of fine- and coarse-grained polycrystalline silicon of *n* and *p* types with a resistivity $\rho \approx 30$ and 0.1–3.0 Ω cm, respectively.

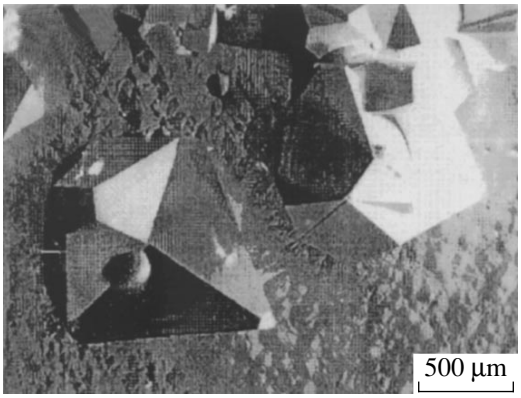

Fig. 2. Polyhedrons grown on a thin film at temperature $T_{cr} = 700$°C.

In order to establish the dependence of the parameters of $(Si_2)_{1-x}(GaAs)_x$ films on the growth conditions, all the film samples under study were grown by varying the temperature of the onset of crystallization and with different gaps δ between the substrates located in a horizontal plane. In some cases, in order to obtain a mirror-smooth surface and improve the melt–solution wettability, we added aluminum with a concentration of ~0.1% [8]. As a result, the epitaxial films grown on *p*-type substrates formed a *p–n* junction at the substrate boundary, whereas the films grown on the *n*-type substrates formed an isotype *n–n* junction.

When crystallization set in at temperatures $T_{cr} \leq 700$°C, the structural elements of the film had the form of dendrite polyhedral pyramids and, sometimes, simply polyhedrons (Fig. 2) located on the substrate and strongly bonded to it. On the substrate, there were areas with a very thin film (as thin as 0.1–0.3 μm) between dendrites. If the crystallization set in at temperatures $T_{cr} > 800$°C, the film structure was also dendritic. In this case, the dendrites grew together with the film, and the thickness of the film between dendrites was ~5–10 μm. As the temperature of the onset of crystallization is increased, the dendrites increase in sizes, reach the upper substrate (Fig. 3), and bond to it. The solid-solution films obtained under optimal conditions (crystallization-onset temperature T_{cr}, final growth temperature T_f, and the gap δ between substrates) had a smooth and lustrous surface with patterns that reproduced the polycrystalline structure of the Si substrate (Fig. 4).

Studies of the thickness and structure of films as functions of the growth rate and initial growth temper-

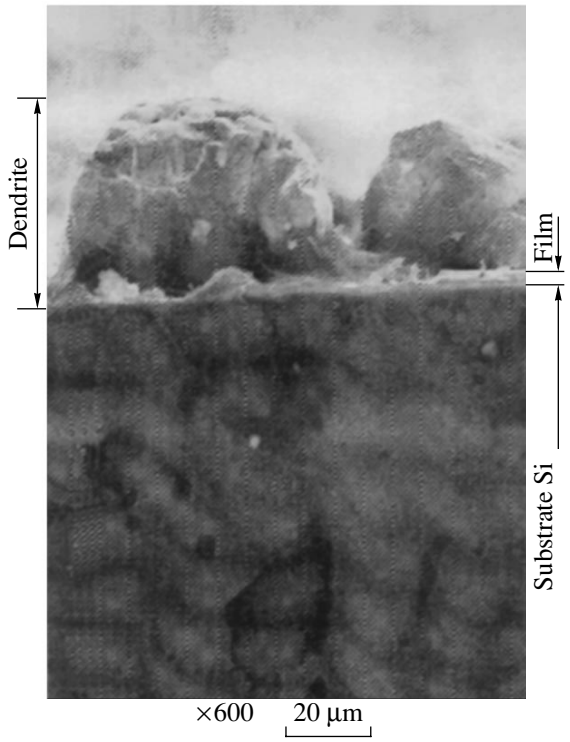

Fig. 3. Dendrites grown at temperature $T_{cr} > 800°C$. Image of a cleaved surface of the Si–$(Si_2)_{1-x}(GaAs)_x$ structure.

ature showed that, at $T_{cr} < 700°C$, the film growth at a cooling rate above 1.5 K/min resulted in an increase in the dendrite sizes. Under these conditions, there is no appreciable improvement in the parameters of films. It should be noted that growth at $T_{cr} > 800°C$ and a cooling rate above 1.0–1.2 K/min was found to be undesirable because volume crystallization began in the melt–solution bulk. This fact is corroborated by the appearance of dendrites, which are not bonded or weakly bonded to a film and can be easily separated from the film, sometimes without damaging its surface. The films grown at a rate lower than 0.5–0.75 K/min are formed almost without dendrites. The film grown in the temperature range $T_{cr} = 700–800°C$ at a cooling rate of 0.75–1.0 K/min are found to be more smooth and mirrorlike.

Using the X-ray radiometric analysis of thin layers [9], we determined the component composition and thickness of the epitaxial films. The characteristic radiation of Ga and As was excited by X-ray photons from a ^{109}Cd source, and the characteristic radiation of Sn was excited by γ-ray photons from a ^{241}Am source (Fig. 5). In order to detect the characteristic radiation of the chemical element under study, we used a Si(Li) detector with an energy resolution of 300 eV and spectrometric equipment with an AI-1024-95-02 pulse-height analyzer. The composition of $(Si_2)_{1-x}(GaAs)_x$ solid solutions was determined by comparing the intensities of characteristic lines of chemical elements in

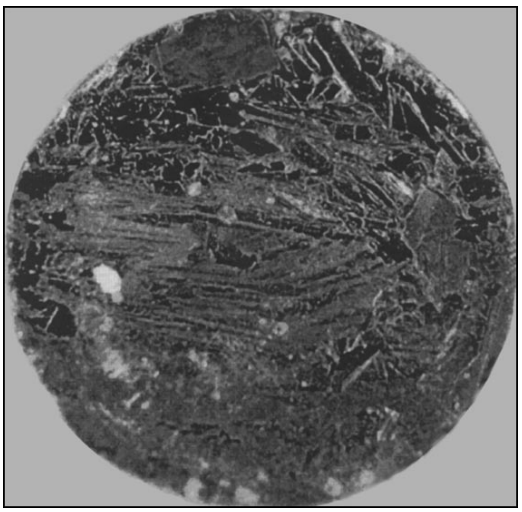

Fig. 4. Surface of the epitaxial layer grown under optimal conditions.

layers with unknown and known contents of components. For X-ray radiometric analysis, we used several wafers of polycrystalline Si with $(Si_2)_{1-x}(GaAs)_x$ epitaxial layers of various composition.

The content of a chemical element in the epitaxial layer was determined using the formula from [9]. For example, we have the following formula for As:

$$C_{As} = \frac{I_{As} C^{st}_{As}}{I^{st}_{As}}. \quad (8)$$

Here, C_{As} and C^{st}_{As} are the contents of As (in grams) in the studied and reference samples; I_{As} and I^{st}_{As} are the

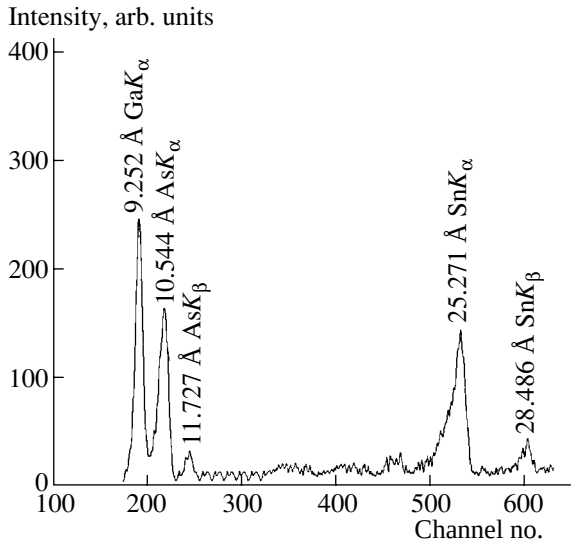

Fig. 5. Characteristic radiation of Ga, As, and Sn elements in $(Si_2)_{1-x}(GaAs)_x$ samples.

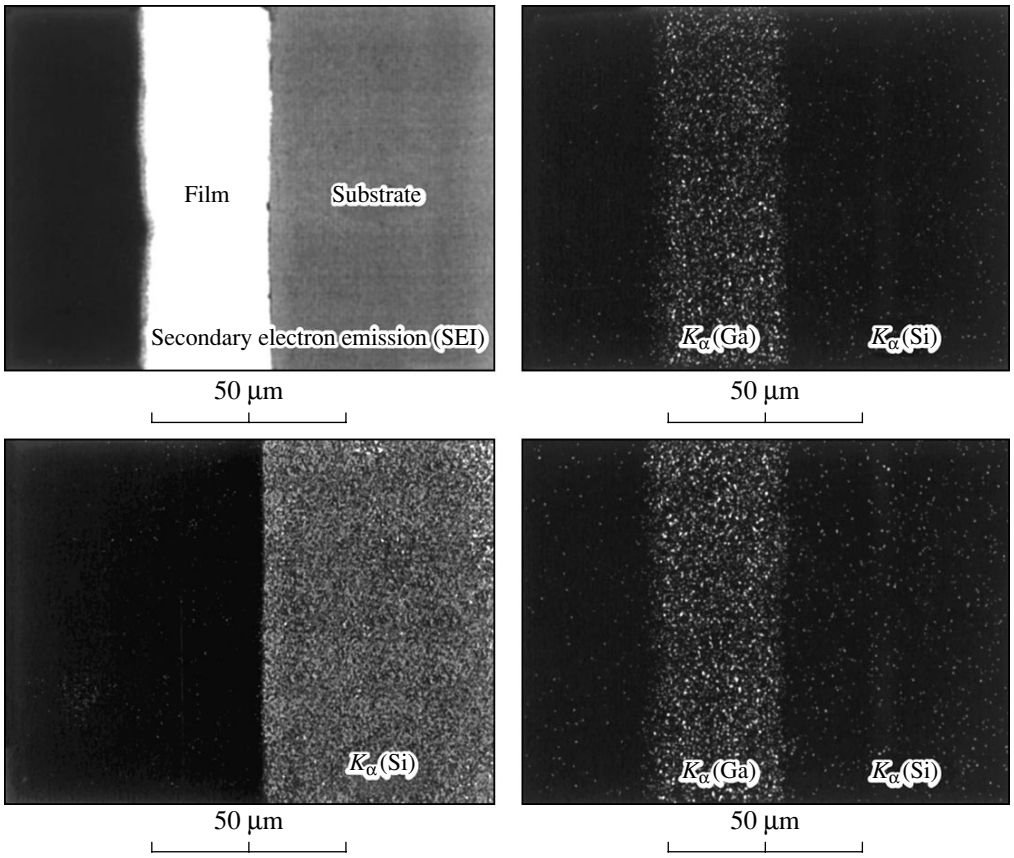

Fig. 6. Scan patterns obtained from cleaved surfaces of Si–$(Si_2)_{1-x}(GaAs)_x$ structures using an X-ray microanalyzer.

intensities of characteristic lines in the studied and reference samples, respectively. The percentage relation describing the composition of films was determined using data on the content of an element (in grams), which was used further for estimating the density and thickness of the film under study. The error in measured values was less than 5%.

A Jeol JSM 5910 LV-Japan X-ray microanalyzer was used for studying the chemical composition of the surface and the cleavage of the grown $(Si_2)_{1-x}(GaAs)_x$ epitaxial layers. The results of studies over a cleaved surface (scan patterns) are shown in Fig. 6. The analysis of the scan patterns of the layer surface showed that there are no macroscopic defects and metal inclusions in the obtained solid-solution epitaxial layers. The distribution of components both over the epitaxial-layer surface and in the solid-solution bulk is uniform.

The degree of structural quality of the grown layers was studied by X-ray diffraction using a DRON-3M diffractometer. The voltage and current on the anode of a radiating element were 30 kV and 20 mA, respectively. We chose specially grown samples of $(Si_2)_{1-x}(GaAs)_x$ solid solutions with thin layers (thickness d = 3–5 μm). The diffraction spectra (Fig. 7) were measured using filtered CuK_α radiation with wavelengths λ = 1.5405 Å (Cu$K_{\alpha1}$) and λ = 1.5443 Å (Cu$K_{\alpha2}$) and the separate recording of reflections from the same plane, which allowed us to increase the accuracy of determining the interplanar spacings d_{hkl} (h, k, l are the Miller indices). When the spectrograph is used at suffi-

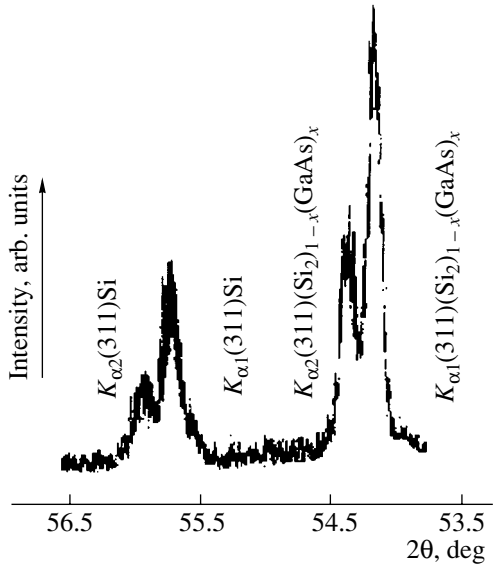

Fig. 7. Diffraction pattern of Si–$(Si_2)_{1-x}(GaAs)_x$ heterostructures.

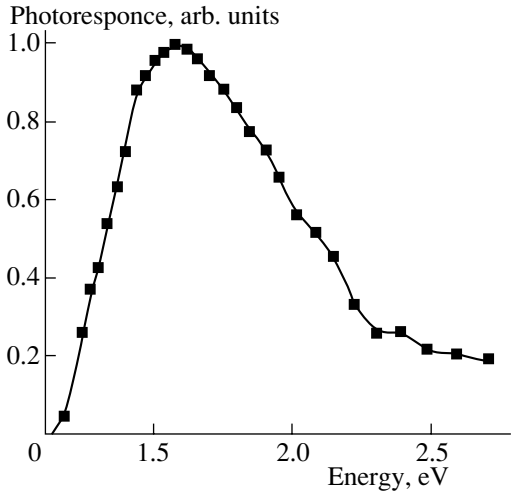

Fig. 8. Spectral characteristic of photosensitivity of a Si–$(Si_2)_{1-x}(GaAs)_x$ structure.

ciently high resolution, the K_α line is detected in the form of a $K_{\alpha1}$ and $K_{\alpha2}$ doublet. Figure 7 distinctly shows the spectral-line splitting into the $K_{\alpha1}$ and $K_{\alpha2}$ doublet.

In order to determine the crystal-lattice parameters, the chosen reflections were detected in the discrete scanning mode with step $\Delta(2\theta) = 0.01°$ and scanning time $\tau = 20$ s at each point. The Wulf–Bragg equation has the form $\lambda = 2d_{hkl}\sin\theta$ (d_{hkl} is the spacing between atomic planes in the system with the indices *hkl*, θ is the angle of reflection of X-ray photons or the Bragg angle, and λ is the wavelength of the used radiation). Then, the lattice parameter is calculated from the expression $a = d_{hkl}\sqrt{h^2 + k^2 + l^2}$ [10]. The calculated error of determining the interplanar spacing d_{hkl} in the angular range $2\theta = 53°–58°$ for the (311) reflection (Fig. 7) amounts to ~0.0001 Å, which introduces an error $\Delta a \approx 0.0004$ Å into the determination of the parameter *a*. For grown films, we obtained the lattice parameter $a = 5.6519$ Å.

The absence of other peaks in the diffraction pattern and the appearance of the $K_{\alpha1}$ and $K_{\alpha2}$ doublet are indicative of the good crystalline quality of the grown epitaxial layers.

Some electrical parameters of the grown $(Si_2)_{1-x}(GaAs)_x$ epitaxial layers were studied. The Hall and four-probe resistivity measurements showed that the $(Si_2)_{1-x}(GaAs)_x$ epitaxial films grown from a tin melt–solution were self-doped with *n*-type conductivity and resistivity $\rho \approx 0.5–1.5\ \Omega$ cm. The electron and hole mobilities were $\mu_n \approx 800–1200$ cm^2/(V s) and $\mu_p \approx 500–800$ cm^2/(V s), respectively. We also investigated the spectral photosensitivity and current–voltage characteristics of the obtained *p*-Si–*n*-$(Si_2)_{1-x}(GaAs)_x$ structures. It should be noted that the rectifying properties of such a structure are retained in the temperature range $T = 77–300$ K, and the current-flow mechanism is complicated.

The prepared Si–$(Si_2)_{1-x}(GaAs)_x$ structures are photosensitive in the wavelength range $\lambda \approx 0.427–1.1$ μm (Fig. 8). The photoresponse in the energy range $E \approx 1.1–1.4$ eV is related to the generation of nonequilibrium charge carriers in the Si substrate and the $(Si_2)_{1-x}(GaAs)_x$ epitaxial film. At $E \approx 1.42–1.6$ eV, an increase in the photocurrent is attributed to the generation of nonequilibrium charge carriers in the *p–n* junction of the structure and in the GaAs layer adjoining it (energy range $E = 1.6–2.8$ eV). A fraction of nonequilibrium charge carriers from the GaAs layer has time to reach the *p–n* junction in the structure and contribute to the photocurrent. Another fraction of these carriers is captured by deep levels that play the role of traps in the GaAs layer, and this leads to a signal-amplitude deficit in the range $\lambda \approx 0.427–0.77$ μm. The open-circuit voltage and short-circuit current density of the structures without blooming are as follows: $V_{oc} \approx 0.80–0.83$ V and $I_{sc} \approx 10–12$ mA/cm^2. The results obtained are consistent with the published data for GaAs structures with *p–n* homojunctions and are comparable to the data for similar structures obtained on single-crystal GaAs substrates.

The studies performed show that the epitaxial films of $(Si_2)_{1-x}(GaAs)_x$ solid solutions grown on polycrystalline Si substrates can be used instead of similar films grown on expensive GaAs substrates.

Thus, the technology developed allows us to synthesize new epitaxial $(Si_2)_{1-x}(GaAs)_x$ solid solutions and expand the material resources for devices of modern electronics.

3.3 Growth and Properties of Si–$(Si_2)_{1-x}(GaP)_x$ Heterostructures

Analysis of the solubility of Si and GaP in liquid metals has shown that the use of tin as a solvent is possible. In a combination with a reasonably low growth temperature (750–900°C), the conditions necessary for the formation of $(Si_2)_{1-x}(GaP)_x$ solid solutions are satisfied. The technological process of growing the Si–$(Si_2)_{1-x}(GaP)_x$ heterostructures from a bounded melt–solution is described in [8].

The $(Si_2)_{1-x}(GaP)_x$ epitaxial layers were of the *n* type, and their thickness varied within 15–30 μm. From the data on the distribution of components over thickness (obtained using the Jeol JSM 5910 LV-Japan microanalyzer), the GaP content in a graded-gap $(Si_2)_{1-x}(GaP)_x$ epitaxial layer increases along the growth axis, and a content of 48 and 52% for Ga and P, respectively, is attained on the layer surface. We measured the intensities of characteristic radiation of components from the surface of epitaxial layers; the spectrum is shown in Fig. 9. According to the scan patterns obtained from the cleaved surfaces of structures (Fig. 10), the layers are structurally perfect, and the dis-

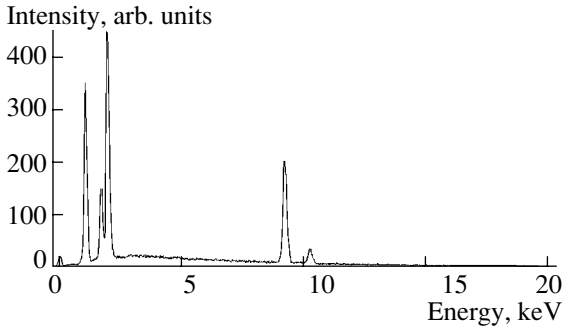

Fig. 9. Spectrum obtained from the surface of an epitaxial layer of a Si–$(Si_2)_{1-x}(GaP)_x$ structure using a microanalyzer.

tribution of components at the interface is reasonably uniform. Detailed analysis showed that the distribution of components over the surface is also uniform. Smooth epitaxial layers are obtained on cooling the melt–solution at a rate of 0.5–1.5 K/min for the gap δ = 0.75–1.0 mm between two horizontal substrates.

Our method for growing epitaxial layers is based on the forced cooling of the melt at a rate of 0.5–5.0 K/min. When a film grows in the forced-cooling mode, the heat removal from the last crystallizing layers proceeds faster than the heat removal from the initial layers. This distinction increases with the cooling rate. As a result, thermoelastic stresses arise, which are compressive at a depth and tensile closer to the surface. In turn, these stresses induce plastic strain, crack formation, and even the fracture of the film.

In [11] the causes of formation of defects are given: these are a mismatch of lattice parameters, thermal stress, a composition gradient through the epilayer thickness, and the inheritance of substrate defects. A mismatch in the lattice parameters of the Si–GaP heterocouple defined as [11]

$$f = \frac{(a_{Si} - a_{GaP})}{(1/2)(a_{Si} + a_{GaP})}100\% \quad (9)$$

is negligible (0.36%); therefore, stress arising at the heterointerface due to a mismatch of lattice parameters between the substrate and the epitaxial layer is excluded. The content of chemical components smoothly varies from zero to unity ($0 \le x \le 1$). The inheritance of substrate defects can also be eliminated by choosing dislocation-free (perfect-structure) substrates. The basic stress source resulting in defect formation in the Si–$(Si_2)_{1-x}(GaP)_x$ structure in our study is the difference in the thermal-expansion coefficients of the solid solution and the substrate (5.8×10^{-6} and 2.44×10^{-6} K^{-1}, respectively). Additional causes can arise during the growth due to an imperfection in the growth technology. This fact is also not excluded. The appearance of cracks depends on the film thickness and the chemical composition of solid solutions. A similar cracking of Ge layers in Ge–Si structures and ZnSe thick layers grown on Ge and GaAs was observed in [12–14]. The stresses arising in a film due to the differ-

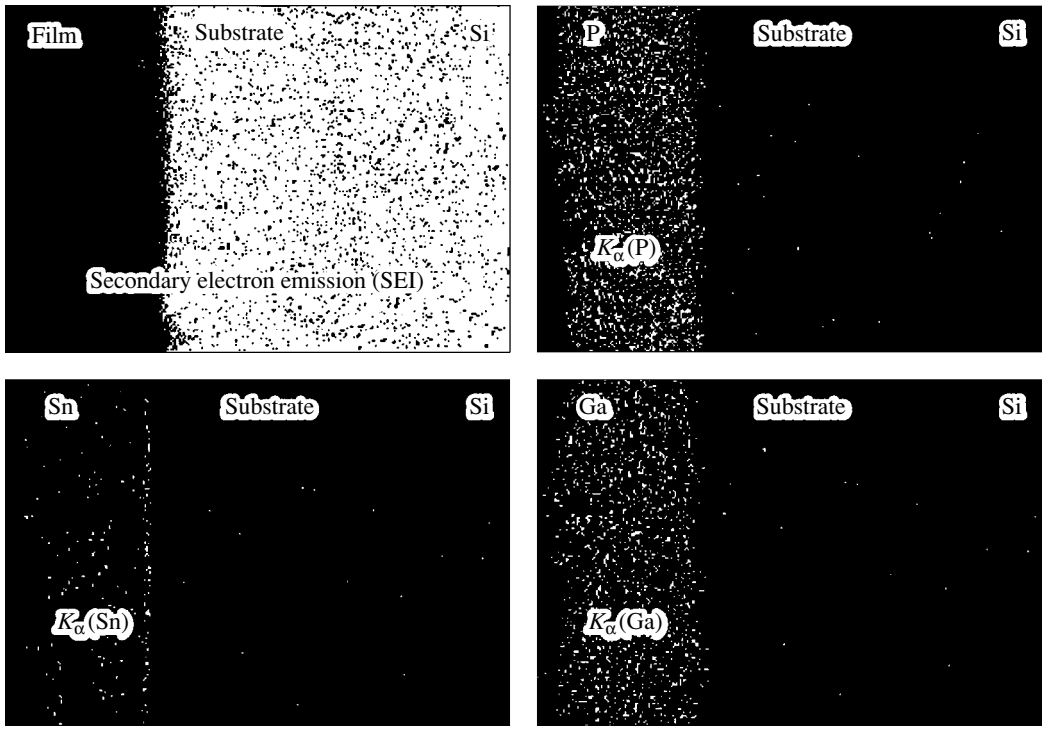

Fig. 10. Scan patterns obtained from a cleaved surface of Si–$(Si_2)_{1-x}(GaP)_x$ structures using a microanalyzer.

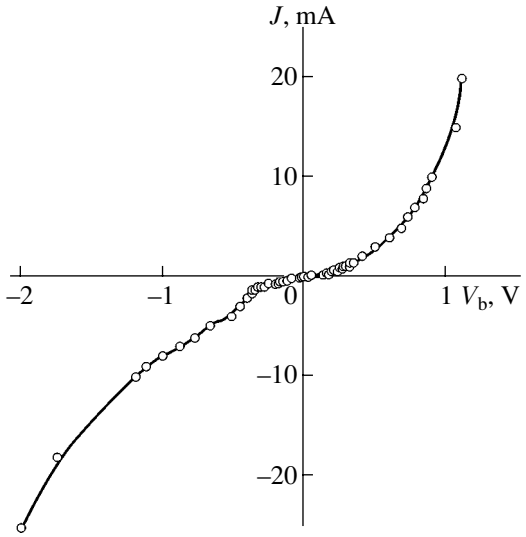

Fig. 11. Dark *I–V* characteristic of a *p*-Si–*n*-$(Si_2)_{1-x}(GaP)_x$ heterostructure.

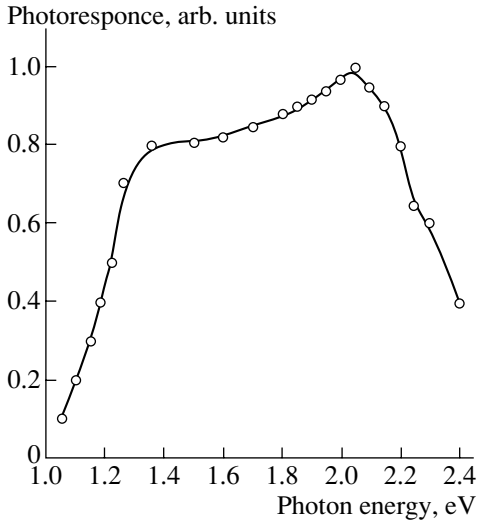

Fig. 12. Spectral dependence of photoresponse for a *p*-Si–*n*-$(Si_2)_{1-x}(GaP)_x$ heterostructures.

ence in thermal-expansion coefficients are estimated from the formula [15]

$$\sigma_{\Delta\alpha} = \frac{E}{1-\gamma}\Delta\alpha\Delta T, \qquad (10)$$

where E is the Young modulus, γ is the Poisson ratio, $\Delta\alpha$ is the difference in thermal-expansion coefficients, and ΔT is the difference between the growth and room temperatures. With decreasing temperature, $\sigma_{\Delta\alpha}$ increases virtually linearly, while the plasticity of crystals varies exponentially; therefore, the relaxation of a thermal stress is hampered, which may result in the destruction of epitaxial layers [14]. With increasing GaP content in $(Si_2)_{1-x}(GaP)_x$ epitaxial layers, the thermal-expansion coefficient of the layer increases and approaches that characteristic of GaP. However, for optimal thicknesses, the role of the thermal-expansion coefficient is reduced because of a gradual passage from Si to GaP in the epitaxial layer. Therefore, no bends and cracks of the film are observed in our case.

We preliminarily investigated electrical properties of the grown solid solutions. Ohmic contacts were fabricated using the Ga–In compound.

3.4. Current–Voltage Characteristic of the p-Si–n-$(Si_2)_{1-x}(GaP)_x$ Heterojunction

The dark current–voltage (*I–V*) characteristics of the *p*-Si–*n*-$(Si_2)_{1-x}(GaP)_x$ heterojunctions were detected in the forward and reverse directions at a room temperature (Fig. 11). There are many theoretical models for the *I–V* characteristics of homojunctions and heterojunctions. It is known that the electrical characteristics of a *p–n* junction at the forward bias depend on the potential-barrier height V_d and the resistivity of semiconductors. Irrespective of the theoretical model chosen for the description of *I–V* characteristics, a forward current J_{forw} increases exponentially according to the law $J_{forw} \propto \exp(qV_b/kT) - 1$ with increasing bias V_b. In our case, the potential barrier V_d determined by extrapolating the linear portion of the *I–V* characteristic amounted to $V_d \approx 0.5$ V. A further increase in the current with V_b is associated with physical processes occurring in the semiconductor bulk.

In the reverse *I–V* characteristic, it is easy to note three typical portions corresponding to voltage ranges V_b = 0–0.3, 0.3–1.25 V, and $V_b > 1.25$ V. In the first of them, corresponding to small voltages, the reverse current increases only slightly with the bias and follows approximately the law $J = BV_b^n$, where B is a constant and $n < 1$. In the second range, a substantial increase in the current is observed. At higher voltages, impact ionization takes place in the *p–n* heterojunction bulk resulting in a soft electric breakdown.

The observed increase in the current J in the second range is most likely associated with the development impact ionization in an area adjoining the *p–n* heterojunction rather than in the bulk.

3.5. Photoelectric Properties of Si–$(Si_2)_{1-x}(GaP)_x$ Heterojunctions

In Fig. 12 we show the spectral dependence of a photoresponse for heterojunctions. The heterojunctions were illuminated perpendicularly to the plane of the *p–n* junction. Studies show that the spectral dependence has the form of a broad peak at T = 290 K in the photon-energy range $1.32 \le h\nu \le 2.1$ eV; i.e., at energies between the Si and GaP band gaps. The analysis shows that the photoresponse is generally induced by the generation of charge carriers from impurity centers located in the depletion region of the *p–n* junction adjoining the Si substrate.

4. CONCLUSION

Graded-gap $(Si_2)_{1-x}(GaAs)_x$ and $(Si_2)_{1-x}(GaP)_x$ epitaxial layers are grown. It is shown that the growth of $(Si_2)_{1-x}(GaAs)_x$ films is possible on polycrystalline Si substrates instead of expensive GaAs substrates. The possibility of subsequently growing $Al_xGa_{1-x}As$ solid solutions on such layers opens up new fields for their use by developing highly efficient cascade solar cells on Si substrates. Varying the composition of $(Si_2)_{1-x}(GaP)_x$ solid solutions, one can vary the band gap, which makes it possible to use these solutions for fabricating optoelectronic devices that cover a wide spectral range.

REFERENCES

1. M. S. Saidov, Geliotekhnika, Nos. 5–6, 57 (1997).
2. Ya. S. Umanskiĭ, V. N. Finnel'shteĭn, M. E. Blanter, S. T. Kishkin, N. S. Fastov, and S. S. Gorelik, *Physical Metallurgy* (Metallurgizdat, Moscow, 1955), p. 122 [in Russian].
3. L. I. Marina, A. Ya. Nashel'skiĭ, and L. I. Kolesnik, *The III–V Semiconductor Phosphides and Solid Solutions Based on These Compounds* (Metallurgiya, Moscow, 1974), p. 45 [in Russian].
4. M. S. Saidov and I. Shukurov, Izv. Akad. Nauk SSSR, Neorg. Mater. **8**, 2077 (1972).
5. V. M. Andreev, L. M. Dolginov, and D. N. Tret'yakov, *Liquid-Phase Epitaxy in the Technology of Semiconductor Devices* (Sovetskoe Radio, Moscow, 1975) [in Russian].
6. C. D. Thurmond, J. Phys. Chem. Solids **28**, 2257 (1967).
7. M. Hansen and K. Anderko, *Constitution of Binary Alloys*, 2nd ed. (McGraw-Hill, New York, 1958; Metallurgizdat, Moscow, 1962).
8. B. Sapaev, A. S. Saidov, and U. T. Davlatov, Vestn. Gullist. Gos. Univ., No. 1, 50 (2001).
9. S. V. Mamikanyan, *Equipment and Methods of Fluorescent X-ray Radiometric Analysis* (Atomizdat, Moscow, 1976) [in Russian].
10. E. F. Vegman, Yu. G. Rufanov, and I. N. Fedorchenko, *Crystallography, Mineralogy, Petrography, and X-ray Diffraction Analysis* (Metallurgiya, Moscow, 1990) [in Russian].
11. M. G. Mil'vidskiĭ and V. B. Osvenskiĭ, *Structural Defects in Epitaxial Layers of Semiconductors* (Metallurgiya, Moscow, 1985) [in Russian].
12. A. K. Riben, B. L. Feucht, and W. G. Oldham, J. Electrochem. Soc. **113** (3), 245 (1966).
13. H. J. Howel and A. G. Milnes, J. Electrochem. Soc. **116**, 843 (1969).
14. A. G. Milnes and D. L. Feucht, *Heterojunctions and Metal–Semiconductor Junctions* (Academic, New York, 1972; Mir, Moscow, 1975).
15. M. G. Mil'vidskiĭ and V. B. Osvenskiĭ, Kristallografiya **22**, 431 (1977) [Sov. Phys. Crystallogr. **22**, 246 (1977)].

Translated by V. Bukhanov

Semiconductors, Vol. 38, No. 11, 2004, pp. 1254–1259. Translated from Fizika i Tekhnika Poluprovodnikov, Vol. 38, No. 11, 2004, pp. 1294–1300.

ATOMIC STRUCTURE AND NONELECTRONIC PROPERTIES OF SEMICONDUCTORS

Atomic-Force-Microscopy Visualization of Si Nanocrystals in SiO_2 Thermal Oxide Using Selective Etching

M. S. Dunaevskiĭ*, J. J. Grob, A. G. Zabrodskiĭ*, R. Laiho***, and A. N. Titkov***

**Ioffe Physicotechnical Institute, Russian Academy of Sciences, St. Petersburg, 194021 Russia*

***Laboratoire PHASE, Université Louis Pasteur, BP20CR, Strasbourg, 67037 France*

****Wihuri Laboratory, Turku University, Turku, 20014 Finland*

Submitted March 22, 2004; accepted for publication April 6, 2004

Abstract—The topography and local hardness of the etched surfaces of layers of SiO_2 thermal oxide that contained Si nanocrystals in its bulk were studied using atomic-force microscopy. The Si nanocrystals were obtained by implanting Si^+ ions into the oxide with subsequent high-temperature annealing. It is shown that the use of selective etching that removes the oxide material makes it possible to reveal Si nanocrystals that appear in the profile of etched surfaces in the form of nanohillocks with a height of up to 2–3 nm. These values are in satisfactory agreement with the average radius of Si nanocrystals in the SiO_2 oxide layer. Independent confirmation of the Si-nanocrystal observation was obtained by comparing the topography of etched surfaces with the local-hardness maps obtained for the same surfaces; in these maps, the hillocks appear as sites at the surface with a reduced hardness. The phase precipitation of implanted Si is also observed in the form of extended flat clusters oriented in the oxide bulk parallel to the oxide surface. The suggested method for revealing the Si nanocrystals and clusters incorporated into the oxide provides a convenient way to study the specific features of nucleation growth and spinodal decomposition in the Si solid solution in the SiO_2 oxide. © *2004 MAIK "Nauka/Interperiodica".*

1. INTRODUCTION

At present, there is notable interest in Si nanocrystals incorporated into thermal SiO_2 oxide and obtained by implanting Si^+ ions into the oxide with subsequent heat treatment. The interest in this system is related to the prospects for using it in devices of semiconductor microelectronics, for example, in light-emitting diodes [1, 2] and memory devices [3–5]. It is important that the formation of Si nanocrystals in the matrix of thermal SiO_2 be compatible with the technology of production of silicon devices.

The formation of Si nanocrystals in a SiO_2 layer using ion implantation with subsequent annealing depends on many factors, such as the implantation dose, the temperature of the sample during implantation, the implantation rate, the temperature and duration of annealing, the thickness of the oxide layer into which the Si^+ ions are implanted, the chemical composition of the oxide, and so on. As a result, the formation of Si nanocrystals is an extremely irregular process and requires continuous control, starting with the confirmation of the very fact that Si nanocrystals are obtained and including the subsequent characterization of their linear dimensions, structure, and spatial distribution. Transmission electron microscopy (TEM) is typically used for this control when the plan view or cross section of the oxide layer is studied. This method has some merits but also certain disadvantages, such as the time-consuming procedure for preparation of the samples, the small size of the analyzed surface areas, and the averaging of the results over the thickness of the region under study.

In this study, we suggest a simpler method for revealing the Si nanocrystals in the SiO_2 layer using selective etching and monitoring the topography of the etched surface by atomic-force microscopy (AFM) under atmospheric conditions. This approach was successfully used recently to reveal the Fe nanoparticles in a SiO_2 layer [6] and the InAs nanoislands in a GaAs layer [7]. The feasibility of applying this approach to a system of Si nanocrystals in a SiO_2 layer was not obvious. First, the results of TEM measurements indicate that Si nanocrystals are very small (no larger than 5 nm in diameter [8, 9]); their sizes are severalfold smaller than those of the nanoparticles observed previously [6, 7]. Such small Si nanocrystals may simply not be observed in the topography of the etched surface. Second, if the Si nanocrystals are found at the surface and are exposed to atmospheric air, they should naturally be oxidized themselves and, as a result, become indistinguishable from the surrounding oxide material. We showed that Si nanocrystals can nevertheless be observed on a selectively etched surface of thermal oxide in the shape of nanohillocks, and they can be identified using the difference in mechanical strength between thermal and natural oxides. To this end, we studied selectively etched surfaces of the SiO_2 oxide with incorporated Si nanocrystals in two AFM modes simultaneously: in the topography mode and in the mode of detection of local

hardness of the surface beneath the probe of an atomic-force microscope.

2. EXPERIMENTAL

We studied 300-nm-thick thermal oxide SiO_2 layers on a *p*-Si substrate. Using sequential implantation of Si^+ ions with five different energy levels (30, 50, 75, 105, and 150 keV) into the oxide layer, we obtained an initially uniform distribution of silicon in the oxide layer. The integrated dose of implantation was 6×10^{16} cm^{-2}. The Si nanocrystals were formed by annealing the samples for 1 h at 1100°C in a nitrogen atmosphere. The formation of Si nanocrystals in the oxide layer was confirmed by the observation of a characteristic photoluminescence line peaked at 740 nm at room temperature [10]. We studied the oxide-layer surfaces before implantation, after implantation and annealing, and after selective etching of the implanted and annealed oxide. For selective etching, we used the Ammonium Fluoride Etchant (Merck AF 87.5-12.5), which affected the SiO_2 oxide but did not affect the Si nanocrystals. In order to reveal nanometer-sized objects in the oxide bulk, an etchant with a fairly low etching rate is required. The etchant we chose provided an acceptable etching rate of 1 nm/s for unimplanted oxide; this rate is even lower when the implanted oxide is etched. The oxide thickness after etching was determined using optical ellipsometry.

We carried out the measurements using a P47-Semi atomic-force microscope (NT-MDT, Zelenograd, Russia) in the contact mode, which made it possible to determine the surface topography and simultaneously plot a map of local surface hardness. A schematic representation of the experiment is shown in Fig. 1. The behavior of the AFM probe, which is a small pyramid installed on a flexible cantilever, is monitored using the reflection of a laser beam from the top surface of the cantilever; this beam is then directed to a four-section photodiode. In the case of determining the topography (see Fig. 1a), the position of the reflected laser beam at the photodiode and, accordingly, the signal from the photodiode were maintained constant. As the probe approaches a hillock during scanning of the surface, an additional flexure of the cantilever is caused, together with a related shift of the reflected laser beam over the sensitive area of the photodiode. In order to return the reflected beam to the initial position, a feedback signal *H* is applied to the scanner that carries the probe; this signal moves the probe away from the surface until the initial flexure of the cantilever is restored. In the course of scanning the surface, the feedback signal *H* fed to the scanner is detected and carries information about the surface topography.

In the mode of detection of the local stiffness of the surface (see Fig. 1b), the device's probe is additionally introduced into a state of forced flexural vibrations, which causes a vibrational motion of the reflected laser beam over the surface of the photodiode. The amplitude *A*

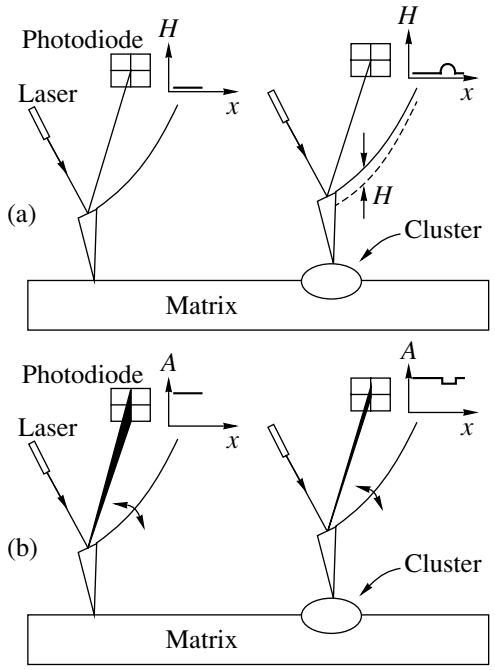

Fig. 1. Diagrams of the AFM experiment with detection of (a) the topography and (b) a map of the local stiffness of surfaces with nanoinclusions.

of vibrations of the probe, one end of which is fixed at the cantilever while the other end is fixed by the contact of the pyramid to the surface under study, depends on the degree of rigidity of this contact and, thus, makes it possible to characterize the local stiffness of the surface. For example, a decrease in the hardness of a surface area leads to the "softening" of the probe contact to this area and causes a decrease in the amplitude of flexural vibrations; as a result, a decrease in hardness is detected from the decrease in the signal at the photodetector.

In our studies, we chose probes with pyramids of silicon nitride Si_3N_4 (Olympus, Japan), which is a stronger material than silicon. The higher strength of the probe material compared to that of silicon was required both to reduce the wear of the probing pyramid in the case of contact scanning of the surface and to decrease the contribution of elastic strains in the pyramid to the detected signal of stiffness. The relatively large curvature radius of the tip of the probing pyramid at a level of 30 nm is one disadvantage of the probes we used.

3. RESULTS AND DISCUSSION

In Fig. 2, we show AFM images of the topography and the characteristic profiles of the surfaces of the thermal oxide (SiO_2) layers (Fig. 2a) before implantation, (Fig. 2b) after implantation and annealing, and (Fig. 2c) after subsequent selective etching to a depth of 50 nm. The surfaces under study exhibit a fairly high degree of planarity that is not affected by all the processes carried out: the maximal spread in height was no

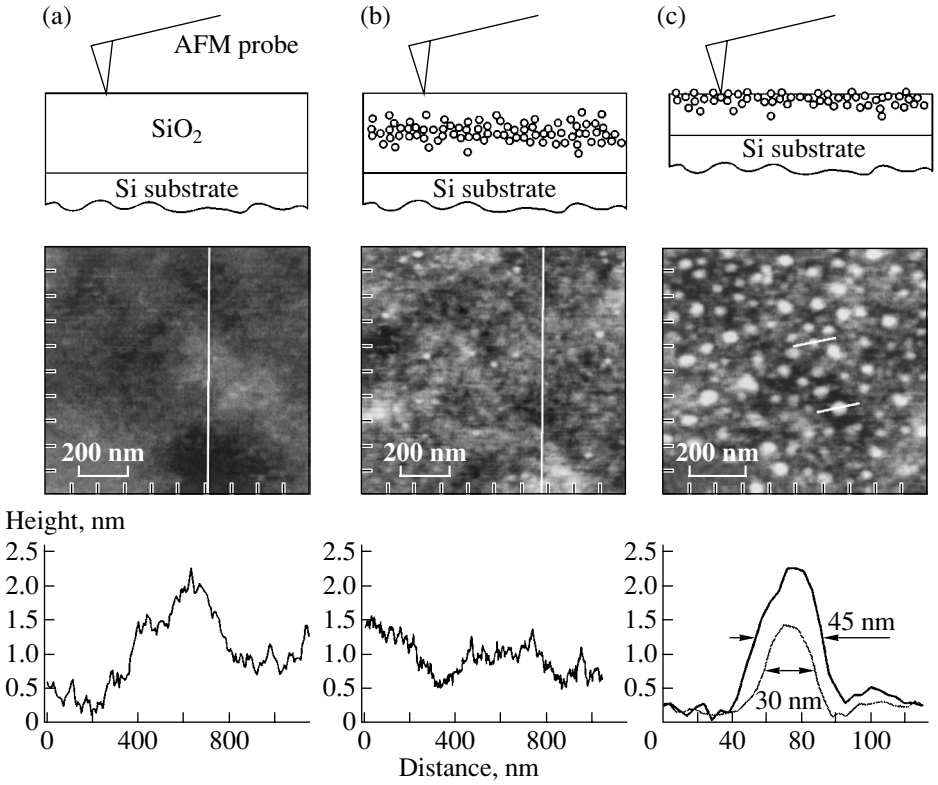

Fig. 2. AFM image and the characteristic surface profiles of the SiO_2 layer (a) before implantation and (b) after implantation, with Si nanocrystals formed in the bulk of the oxide layer; (c) the oxide layer with Si nanocrystals after selective etching to a depth of 50 nm. The geometry of measurements is illustrated in the upper part of the figure.

larger than 1–2 nm over an area no smaller than 1 μm^2. This circumstance was an important factor in the success of the suggested method for revealing Si nanocrystals in the bulk of the oxide layer. Note also that implanting Si^+ ions has only a slight effect on the local roughness of the oxide surface; the increase in the roughness as a result of implantation was within the subnanometer range of heights.

The presence of a large number of nanohillocks with heights no larger than 2–3 nm is characteristic of the etched oxide surface whose AFM image is shown in Fig. 2c. Note that etching an unimplanted oxide layer does not affect the surface topography (illustrated in Fig. 2a). Therefore, it is reasonable to assume that the nanohillocks observed in Fig. 2c are the manifestation of Si nanocrystals formed in the bulk of the oxide as a result of implanting Si^+ ions with subsequent high-temperature annealing. According to the available data of TEM measurements, the average diameter of Si nanocrystals formed using this technology is within the range 3–5 nm. The observed heights of nanohillocks fall in this range and are even slightly smaller, which one would expect since Si nanocrystals must be embedded into the oxide in order to hold their position on the oxide surface. The observed widths of the nanohillocks exceed appreciably the expected values of diameters of Si nanocrystals and are as large as 30–40 nm for the hillock with the largest height (2.5 nm). We attribute this discrepancy to a broadening of the AFM topographic images, which is caused by the finite curvature radius of the tip of the probing pyramid. The value of this instrument-related broadening of AFM images of nanohillocks is given by $L_{spread} = 2(2Rh)^{0.5}$ [11], where R is the curvature radius of the pyramid's tip and h is the nanohillock height. Substituting the value $R = 30$ nm, which is characteristic of Si_3N_4 probes, and the nanohillock height $h = 2.5$ nm, we obtain $L_{spread} = 25$ nm, which is close to the experimental values. It is worth noting that the topographic resolution in AFM images of Si nanocrystals can be improved later on by selecting "softer" modes of scanning (discarding the measurements of the surface hardness) and using sharper probe tips in this case.

Figure 3 illustrates the AFM topography of the implanted and annealed surface area of the oxide layer; this area is larger than that shown in Fig. 2. In addition to the previously revealed nanohillocks with a density of $\sim 10^{10}$ cm^{-2}, we also observe a significant number of cluster inclusions at the surface. It is interesting that the elevation of clusters above the surface is almost the same as in the case of nanohillocks (i.e., 1–2 nm).

Figure 4 shows another AFM image that illustrates the surface topography of the etched oxide. Here, we also see nanohillocks with a nanometer height; at the same time, a large number of small pits whose depth

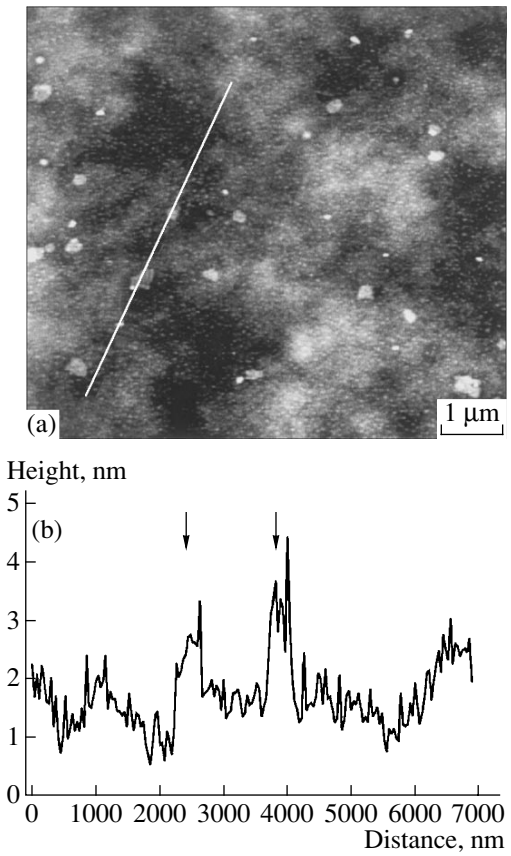

Fig. 3. (a) AFM image of Si nanocrystals and clusters on a selectively etched surface of the SiO_2 layer with an area of 8×8 μm^2 and (b) a profile drawn through two clusters whose positions are indicated by the arrows.

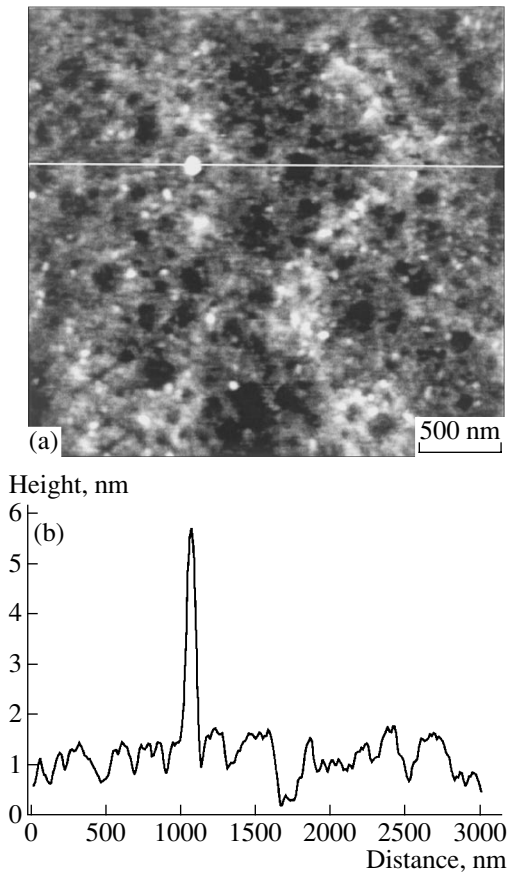

Fig. 4. (a) AFM image of nanopits on a selectively etched surface of the SiO_2 layer with an area of 3×3 μm^2 and (b) the profile drawn through a nanohillock with a large height in the upper part of the topographic image.

does not exceed 1–2 nm can also be seen at the surface. We believe that the observed pits are the sites of initial attachment of Si nanocrystals and the large clusters observed in Fig. 3. The profile in Fig. 4b is drawn through a separate high hillock in the upper part of the AFM image shown in Fig. 4a; the height of this hillock is 4.5 nm. We may assume that here we detected a Si nanocrystal that is almost completely free of the oxide matrix.

In this study, it was important for us to independently confirm that the observed nanohillocks and clusters are in fact inclusions of another phase in the thermal-oxide matrix rather than a result of specific features of the etching of the oxide. This confirmation was obtained by examining the maps of local stiffness of the etched surfaces. In Fig. 5, we compare the AFM topography with the maps of local stiffness for the same area of the etched surface that includes both nanohillocks and large clusters. It can be seen from the data shown in Figs. 5b and 5c that the nanohillocks and clusters in the stiffness map correspond to areas with a stiffness reduced by about 20% (the darker areas correspond to a smaller amplitude of flexural vibrations of the fixed probe). In measuring the local stiffness, it is important to realize that measurements for hillocks can yield smaller values than those for a plane due to the effect of the geometrical shape of the area under examination [12]. In our case, this effect was much less pronounced than the observed decrease in stiffness. Indeed, it can be seen from Fig. 5a that the tops of the clusters are almost flat and the size of these clusters (200–300 nm) far exceeds the diameter of curvature of the tip of the probing pyramid; the decrease in the local stiffness near the clusters (see Fig. 5b) is almost constant over the entire surface of the cluster. These observations show that the detected variations in the stiffness of clusters cannot be caused by changes in the surface shape; rather, these variations should indicate that the cluster material is different. The detection of almost the same decrease in the stiffness for both nanohillocks and clusters indicates that, in this case as well, the material of a hillock differs from that of the surrounding oxide matrix. In order to confirm this inference, we note that a careful examination of the clusters' structure in Fig. 5a shows that several hillocks are included in this structure. There are also voids in the clusters, which can be seen as dark areas against the bright background in the clusters' topography. The nanohillocks and voids contained in the

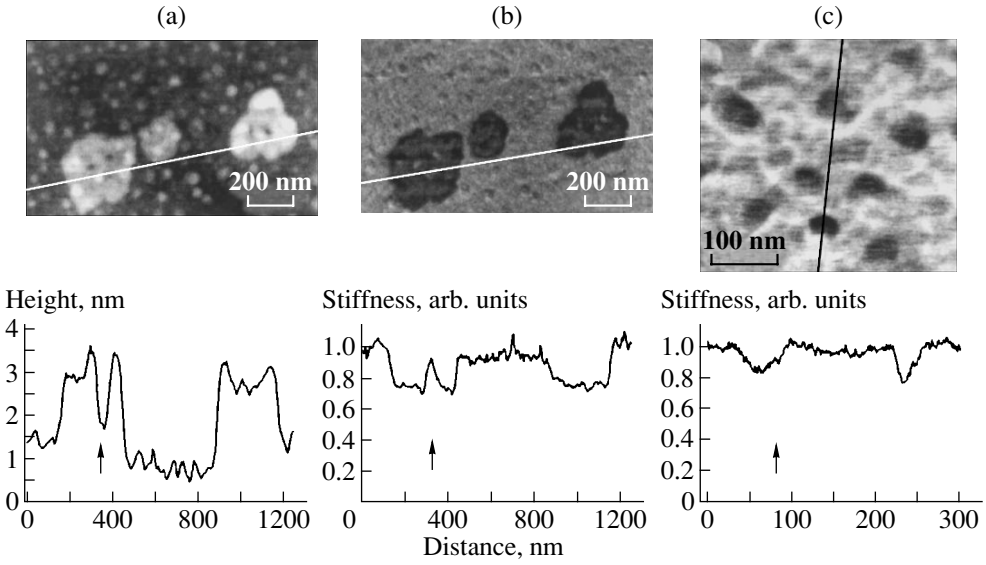

Fig. 5. Comparison of manifestations of Si nanoclusters (a) in AFM topographic images and (b) in maps of local stiffness of the etched surface of SiO_2 oxide; (c) manifestation of Si nanocrystals in a map of local stiffness with a higher magnification. For all the images, the characteristic profiles are shown below.

clusters also manifest themselves in the surface profile. At the same time, a noticeable decrease in stiffness is not observed on the stiffness map in either hillocks or at the edges of voids; this circumstance indicates that the topographic contribution to the stiffness signal is small.

It is reasonable to assume that the material of clusters and hillocks is Si introduced intentionally in considerable amounts into the SiO_2 thermal oxide as a result of implantation. However, an interesting circumstance should be noted here. If the Si nanocrystals and clusters are found at the oxide surface as a result of etching, they should also become oxidized rather rapidly (almost completely), since the natural-oxide thickness at the Si surface is expected to be 4 nm [13], which is close to the average diameter of Si nanocrystals. Therefore, we attribute the difference found in the value to the difference in hardness between the thermal and natural SiO_2 oxides; the latter oxide is known to have a lower strength.

It follows from the known models of formation of Si nanocrystals in SiO_2 layers implanted with Si^+ ions [14, 15] that implanted silicon tends to agglomerate predominantly at the oxide midplane after annealing; it is in this part of the oxide that most of the Si nanocrystals are formed. This inference is also confirmed qualitatively by our observations. Si nanocrystals were not observed on the oxide surface immediately after implantation. We had to etch off the top part of the oxide to a considerable depth in order to detect the nanocrystals.

The observation of agglomeration of separate Si nanocrystals in comparatively large clusters was a new result. We used conventional conditions of implantation and annealing (see [9, 10, 16]) in order to obtain the Si nanocrystals. The Si layers that we implanted and annealed had the photoluminescence characteristic of Si nanocrystals; the AFM studies revealed Si nanocrystals with sizes as expected. Therefore, we may assume that our samples should not be radically different from the samples studied previously. Note that in the studies available the structure of silicon inclusions and their distribution in the bulk of the oxide were not generally analyzed in detail. The data of TEM observations of separate Si nanocrystals were mainly reported as a confirmation of the formation of Si nanocrystals. In contrast, we obtained topographic information about the formation of silicon inclusions in large areas of an oxide layer after implantation and annealing.

We believe that the simultaneous formation of Si nanocrystals and clusters could occur in many cases. It has been shown theoretically [15] that the phase precipitation of silicon implanted into SiO_2 depends on the implantation dose and the temperature and duration of subsequent annealing and can occur in two stages. Nanocrystals grow at the nucleation sites in the initial stage. Spinodal decomposition with the formation of extended clusters can occur if the atomic fraction of the implanted Si exceeds a certain value (about 10%). It is important to note that the regions with a silicon content exceeding the critical value can be formed owing to (i) either a higher dose of implantation or (ii) (at lower doses) subsequent redistribution of silicon over the layer thickness as a result of annealing. Consequently, in the second case, the oxide can contain neighboring layers with a different structural state of silicon in the form of Si nanocrystals and clusters, as well as transition layers that include both types of the Si structural precipitates. We believe that this second situation is what appears in our experiments.

It is interesting to note that the shape of clusters is flat and their thickness is on the nanometer scale. The nanometer-scale values of both the elevation of clusters above the etched surface and the depth of pits on the surface at the sites of the initial position of clusters indicate that the cluster thickness does not exceed 10 nm. The clusters extend parallel to the oxide surface to large distances (200–300 nm), which are comparable with the total thickness of the oxide layer. In fact, clusters grow in the shape of nearly flat and extended platelets with a nanometer-scale thickness in an oxide layer that does not have a crystalline structure and, consequently, specific planes for growth. Evidently, the fact that flat clusters are oriented parallel to the oxide surface is caused by the planarity of the distribution of implanted silicon in the oxide layer; the gradient in the silicon density is perpendicular to the oxide surface.

4. CONCLUSION

We developed a convenient method for revealing the Si nanocrystals and clusters in the bulk of SiO_2 oxide. This method consists in selective etching of the oxide material with a subsequent AFM study of the topography and stiffness of the etched surfaces. We used an Ammonium Fluoride Etchant (Merck AF 87.5-12.5) selective etchant that ensured a fairly low etching rate for the SiO_2 oxide (less than 1 nm/s). It is shown that Si nanocrystals manifest themselves as nanohillocks with a height as large as 2–3 nm on the etched surface.

Our experimental studies of SiO_2 oxide layers implanted with Si^+ ions show that the phase precipitates of Si in the bulk of the SiO_2 oxide may occur in the shape of both Si nanocrystals and extended flat clusters oriented parallel to the oxide surface. Evidently, the formation of clusters is related to the nonuniform distribution of implanted silicon in the oxide layer; this nonuniformity becomes more pronounced after subsequent annealing. As a result, at a certain distance from the oxide surface, the concentration of implanted silicon may exceed the critical value that gives rise to the spinodal decomposition of the Si solid solution in SiO_2.

The experimental data obtained indicate that it is important to study the type of Si phase precipitates and their distribution over the thickness of the implanted oxide layer. The method suggested above makes it possible to carry out these studies using the controlled layer-by-layer etching of oxide layers. To this end, AFM experiments should be performed with the probe and sample installed in a liquid-phase cell that is consecutively filled first with a selective etchant and then with deionized water, and vice versa. The small volume of the liquid-phase cells produced by NT-MDT makes it possible to rapidly replace one liquid with the other and carry out layer-by-layer etching with a step of 10 nm or less.

ACKNOWLEDGMENTS

This study was supported by the Russian Foundation for Basic Research (project no. 03-02-17635) and the Ministry of Industry, Science, and Technology of the Russian Federation (the program “Low-Dimensional Quantum Structures”).

REFERENCES

1. D. Muller, P. Knapek, J. Faure, *et al.*, Nucl. Instrum. Methods Phys. Res. B **148**, 997 (1999).
2. P. Protopoulps and A. G. Nassiopoulou, Appl. Phys. Lett. **77**, 1816 (2000).
3. Yi Shi, K. Ishikuro, and T. Hiramoto, J. Appl. Phys. **84**, 2358 (1998).
4. E. Kapetanakis, P. Normand, D. Tsoukas, *et al.*, Appl. Phys. Lett. **77**, 3450 (2000).
5. G. Ben Assayag, C. Bonafos, M. Carrada, *et al.*, Appl. Phys. Lett. **82**, 200 (2003).
6. A. A. Bukharaev, N. I. Nurgazizov, and A. V. Sugonyako, Mikroélektronika **31**, 121 (2002) [Russ. Microelectronics **31**, 103 (2002)].
7. I. A. Karpovich, N. V. Baidus, B. N. Zvonkov, *et al.*, Phys. Low-Dimens. Semicond. Struct., No. 3/4, 341 (2001).
8. S. Guha, J. Appl. Phys. **84**, 5210 (1998).
9. M. L. Brongersma, A. Polman, K. S. Min, and H. A. Atwater, J. Appl. Phys. **86**, 759 (1999).
10. S. Cheylan and R. G. Elliman, Appl. Phys. Lett. **78**, 1912 (2001).
11. V. J. Garcia, L. Martinez, J. M. Briceno-Valero, and C. H. Schilling, Probe Microsc. **1**, 107 (1997).
12. B. Kracke and B. Damaschke, Appl. Phys. Lett. **77**, 361 (2000).
13. G. D. Wilk, Yi Wei, H. Edwards, and R. M. Wallace, Appl. Phys. Lett. **70**, 2288 (1997).
14. M. Strobel, R.-H. Heinig, and W. Moeller, Phys. Rev. B **64**, 245 422 (2001).
15. T. Mueller, R.-H. Heinig, and W. Moeller, Appl. Phys. Lett. **81**, 3049 (2002).
16. S. P. Withrow, C. W. White, D. M. Hembree, and J. C. Barbour, J. Appl. Phys. **86**, 396 (1999).

Translated by A. Spitsyn

Semiconductors, Vol. 38, No. 11, 2004, pp. 1260–1262. Translated from Fizika i Tekhnika Poluprovodnikov, Vol. 38, No. 11, 2004, pp. 1301–1303.

ATOMIC STRUCTURE AND NONELECTRONIC PROPERTIES OF SEMICONDUCTORS

On the High-Dose Effect in the Case of Ion Implantation of Silicon

D. I. Tetelbaum^ and A. I. Gerasimov

Physicotechnical Research Institute, Nizhni Novgorod State University, pr. Gagarina 23/5, Nizhni Novgorod, 603950 Russia

^e-mail: Tetelbaum@phys.unn.ru

Submitted March 23, 2004; accepted for publication April 14, 2004

Abstract—In order to gain insight into the mechanism of the so-called high-dose effect, several experiments were performed with ion implantation of phosphorus into silicon. On the basis of experimental data, it is concluded that the effect under consideration is caused by the weakening of interatomic bonds in amorphous silicon heavily doped with phosphorus, and this is stimulated both by irradiation and increased temperature. An interruption in irradiation after the dose for amorphization is attained leads to the stabilization of the amorphous state. © *2004 MAIK "Nauka/Interperiodica".*

1. INTRODUCTION

It was reported previously [1, 2] that an unusual dose dependence of the degree of disorder is observed in the case of ion implantation of silicon with boron, phosphorus, and arsenic: the surface layer is amorphized at certain doses, while this layer is found to be crystalline (a mosaic crystal with inclusions of polycrystalline phase) at doses that far exceed the dose for amorphization. This phenomenon was referred to as the high-dose effect (HDE). This effect was attributed [1, 2] to the athermal amorphous-layer crystallization stimulated by the decomposition of chemical compounds synthesized at high implantation doses and by the excitation of the electronic subsystem in silicon. However, the fact that the process is athermal is not obvious since the heating of the sample can be appreciable with the ion-current densities used if a special heat sink is not employed. The mechanism of electronic excitation is also problematic. It is also unclear whether amorphization has time to occur before the time instant when the crystal is heated to a temperature at which the amorphization becomes impossible [3].

In this study, we performed a number of experiments with the aim of gaining insight into the HDE mechanism and determining the conditions at which this effect manifests itself or, on the contrary, is suppressed.

2. EXPERIMENTAL

Silicon with *p*-type conductivity, (111) orientation, and a resistivity of 15 Ω cm was grown by the Czochralski method, was then subjected to the conventional treatment, and was finally irradiated with phosphorus ions in the scanning mode using an ILU-200 ion implanter. The target chamber of the implanter was pumped out so that the residual pressure near the target was ~10^{-3} Pa. The samples were fastened to a copper target holder that was cooled using running water, the temperature of which was controlled with a thermostat. The check measurements using a thermocouple showed that the thermal conditions of implantation were quite reproducible in the case under consideration. The surface-layer structure was studied using reflection electron diffraction with an electron energy equal to 100 keV. We used layer-by-layer chemical etching in order to study the structure of deep-lying layers and determine the thickness of the layer with the changed structure.

3. RESULTS AND DISCUSSION

The experimental results are listed in the table. First of all, we checked whether amorphization actually occurred at some stage of irradiation under conditions when the HDE was observed. To this end, some of the samples (the first group) were irradiated under conditions that were typical of the effect under study (ion energy E = 40 keV, average ion-current density j = 5–30 μA/cm^2, and dose $\Phi = 6 \times 10^{16}$ cm^{-2}). Other samples (the second group) were irradiated under the same conditions, except for the dose ($\Phi = 2 \times 10^{15}$ cm^{-2}). After irradiation, the samples of the first group had the structure of a mosaic single crystal with inclusions of the polycrystalline phase. In contrast, the samples of the second group were found to be amorphized to a typical depth of $h \approx R_p + \Delta R_p$, where R_p is the mean projected range of ions and ΔR_p is its straggling. Consequently, amorphization takes place in the HDE at the first stage of irradiation. The crystalline state observed as the dose increases is caused by crystallization of the initially amorphized layer.

In order to clarify the role of the thermal factor in the HDE, some of the samples were pressed to the target

holder with an intermediate layer of In–Ga paste, which improved the thermal contact. The initial temperature of the holder T_0 was varied by adjusting the temperature of the water that flowed through the holder. We used a thermocouple attached to the sample to measure the sample's temperature. The results showed that this temperature increased by 60°C in the first 5 min of irradiation if the sample was irradiated with $j = 20$ μA/cm^2, and then the temperature remained constant. We found that crystallization did not occur up to the highest radiation dose (3×10^{17} cm^{-2}) used if $T_0 \le 10$°C. In contrast, crystallization is observed if $T_0 \ge 20$°C. Therefore, the HDE is not a purely athermal phenomenon and is a result of the combined effect of ion implantation and some heating of the sample by the ion beam.

The following experiment was aimed at clarifying the role of the high phosphorus concentration accumulated in the amorphized layer (in principle, one can imagine a scenario unrelated to the impurity accumulation). To this end, we experimented with two-stage irradiation with P^+ ions. At the first stage of irradiation, the ion energy was $E = 50$ keV, the dose $\Phi = 6 \times 10^{14}$ cm^{-2}, and the initial temperature $T_0 = 20$°C. The ion energy was then increased to 100 keV, and the samples were irradiated for the second time with a dose of 6×10^{16} cm^{-2} at $j = 16$ μA/cm^2 and $T_0 = 200$°C. The layer remained amorphous after this two-stage irradiation notwithstanding the increased temperature at the second irradiation. This behavior can be attributed to the fact that, due to the difference in the ion energies, the second irradiation did not introduce a significant amount of phosphorus into the layer amorphized as a result of the first irradiation. Thus, the accumulation of a high concentration of the impurity (in the case under consideration, phosphorus) is indeed necessary for the HDE.

A very important factor revealed in the course of our experiments was the effect of interruptions in irradiation on the HDE (aging). The sample was first irradiated with the dose $\Phi = 6 \times 10^{14}$ cm^{-2} ($E = 50$ keV, $T_0 = 20$°C), and the irradiation was then interrupted for 10 min. After that, the irradiation was resumed and was performed under the usual conditions for an HDE (the dose was increased to 2×10^{17} cm^{-2} at $j = 16$ μA/cm^2). In this case, the layer was found to be amorphous; i.e., the HDE did not manifest itself.

Thus, the mechanism of the HDE can be conceived as following. At first, amorphization occurs as the concentration of radiation defects increases. If irradiation continues, a high concentration of the impurity (phosphorus) is accumulated in the amorphous layer and at its boundary. Since the Si–P bond is weaker than the Si–Si bond [4], the energy barrier for the reverse process (radiation-stimulated recrystallization [5]) is reduced, and recrystallization begins to dominate over the process of spontaneous amorphization. An increase in temperature as a result of irradiation (if special precautions were not taken in order to ensure efficient heat removal) is also conducive to the recrystallization process.

The structure of Si layers irradiated with P^+ ions under various conditions (according to the data of reflection electron diffraction)

Energy, keV; dose, cm^{-2}	Ion-current density, μA/cm^2	T_0, °C	Structure
40; 6×10^{16}	5–30	≥20	Mosaic single crystal, polycrystal
40; 2×10^{15}	5–30	≥20	Amorphization
40; 3×10^{17}	20	≤10	Amorphization
40; 6×10^{16}	20	≥20	Mosaic single crystal, polycrystal
1) 50; 6×10^{14}	16	20	
2) 100; 6×10^{16}	16	200	Amorphization
1) 50; 6×10^{14}; interruption for 10 min	16	20	
2) 50; 2×10^{17}	16	20	Amorphization

The experiment with aging indicate that an interruption of irradiation after the onset of amorphization leads to the stabilization of the amorphous phase. As a result, even the subsequent introduction of a high phosphorus concentration becomes insufficient for radiation-stimulated crystallization. It is likely that the stabilization is related to either structural relaxation [6] or the penetration of impurities (O, N, C) from the adsorbed layer; these impurities form stronger bonds with Si atoms compared to the Si–Si bonds [4]. In the latter case, the degree of vacuum and the extent to which vacuum is oil-free are important.

It is important from the application-oriented standpoint that the procedure described above makes it possible to avoid crystallization, i.e., to suppress the HDE if we want to obtain heavily doped Si layers in the amorphous state. As mentioned above, lowering of the sample temperature during irradiation is another method for suppressing the HDE.

4. CONCLUSION

The experiments performed in this study show that the high-dose effect (HDE) is the process stimulated by the radiation and affected by temperature and is caused by the weakening of chemical bonds in amorphous Si as a result of the buildup of a high concentration of the implanted impurity. Our studies were restricted to irradiation with phosphorus ions; however, the inferences drawn are apparently also valid for use in HDEs of other impurities that have a bonding energy to Si lower than that of the Si–Si bond, for example, boron and arsenic. Preliminary results of this study were published previously [8]. It is worth noting that the HDE was also apparently observed in the case of ion-implantation doping of nanocrystals in the SiO_2 matrix [9],

despite the fact that the behavior of nanocrystals can differ from that of a bulk sample.

REFERENCES

1. N. I. Gerasimenko, A. V. Dvurechenskiĭ, S. I. Romanov, and L. S. Smirnov, Fiz. Tekh. Poluprovodn. (Leningrad) **6**, 1978 (1972) [Sov. Phys. Semicond. **6**, 1692 (1972)].
2. N. I. Gerasimenko, A. V. Dvurechenskiĭ, S. I. Romanov, and L. S. Smirnov, Fiz. Tekh. Poluprovodn. (Leningrad) **7**, 2195 (1973) [Sov. Phys. Semicond. **7**, 1461 (1973)].
3. F. F. Morehead and B. L. Crowder, Radiat. Eff. **6** (1–2), 27 (1970).
4. V. I. Vedeneev, L. V. Gurvich, V. N. Kondrat'ev, V. A. Medvedev, and E. L. Frankevich, *Energies for Splitting the Chemical Bonds. Ionization Potentials and Electron Affinity* (Akad. Nauk SSSR, Moscow, 1962) [in Russian].
5. A. I. Titov, V. S. Belyakov, P. Cardwell, and G. Farrel, Radiat. Eff. **139**, 189 (1996).
6. E. P. Donovan, F. Spaepen, J. M. Poate, and D. C. Jacobson, Appl. Phys. Lett. **55**, 1516 (1989).
7. E. P. Kennedy, L. Csepregi, J. W. Mayer, and T. W. Sigmon, J. Appl. Phys. **48**, 4241 (1977).
8. A. I. Gerasimov, D. I. Tetel'baum, and A. F. Khokhlov, in *Interaction of Atomic Particles with Solids* (MRI, Minsk, 1978), Part 2, p. 93 [in Russian].
9. G. A. Kachurin, S. G. Yanovskaya, D. I. Tetel'baum, and A. N. Mikhaĭlov, Fiz. Tekh. Poluprovodn. (St. Petersburg) **37**, 738 (2003) [Semiconductors **37**, 713 (2003)].

Translated by A. Spitsyn

Semiconductors, Vol. 38, No. 11, 2004, pp. 1263–1266. Translated from Fizika i Tekhnika Poluprovodnikov, Vol. 38, No. 11, 2004, pp. 1304–1307.

ATOMIC STRUCTURE AND NONELECTRONIC PROPERTIES OF SEMICONDUCTORS

A Mechanism of Low-Temperature Stimulated Processes in Plasma Anodization of Metals and Semiconductors

A. P. Bibilashvili^ and A. B. Gerasimov

Tbilisi State University, Tbilisi, 0128 Georgia

^e-mail: amiranbib@yahoo.com

Submitted March 30, 2004; accepted for publication May 11, 2004

Abstract—A mechanism of stimulation of low-temperature plasma anodization using a catalyst or ultraviolet radiation in the case of the formation of oxide films of metals and semiconductors is suggested. The stimulating effect of a catalyst or ultraviolet radiation on the process of plasma anodization is attributed to the appearance of an additional concentration of antibonding quasiparticles (electrons and holes) that weaken the chemical bonds in the anodized material. The conditions for implementing the stimulated processes are reported.

1. INTRODUCTION

Progress in microelectronics and nanoelectronics has stimulated the design of fundamentally new methods for producing oxide films, as well as the further development of conventional methods. High-temperature treatment leads to the spread of diffusion regions, the diffusion of unwanted impurities, the generation of defects (dislocations, voids, cracks), the violation of the ratio between the components in binary semiconductor compounds, and so on. All these factors have a detrimental effect on the parameters of integrated circuits and the yield of devices. Taking into account the factors above, we have reason to believe that low-temperature methods are very promising. Despite this circumstance, the low-temperature process of plasma anodization of metals and semiconductors has not found wide use for the formation of insulator layers owing to its low efficiency and the low growth rate of the oxide [1].

The results of low-temperature catalytic plasma anodization of metals and semiconductors using a catalyst based on ZrO_2 were reported previously [2–5]. However, it was stated [2–5] that the problem of removing the ZrO_2 film from the surface of anodized material after the process is completed was not solved. In addition, the mechanism of the catalytic effect of ZrO_2 on the process of plasma anodization was not clarified in [2–5].

In this paper, we report the results of studying the promotion of the plasma anodization of metals and semiconductors and suggest mechanisms for the methods of low-temperature plasma anodization that increase the oxidation efficiency and the growth rate of the oxide. Stimulation is attained using either a catalyst (a rare earth element) deposited on the surface of the material to be anodized [6–9] or ultraviolet (UV) radiation in the course of the plasma anodization [10]. We used the oxides of rare earth elements (REEs) as catalysts on the surface of Al, Si, and SiC.

2. EXPERIMENTAL

n-Si(100) wafers with a resistivity of 4.5 Ω cm, epitaxial *n*-GaAs(100) layers with a majority-carrier concentration of 2×10^{17} cm^{-3}, and single-crystal 6*H*-SiC wafers with concentration $N_d - N_a = 10^{18}$ cm^{-3} and a (0001) surface orientation were used as the substrates. In order to form an Al_2O_3 oxide layer on the Si surface, we deposited Al layers using the resistive evaporation of Al in vacuum at a substrate temperature of 423 K. A thin continuous layer of a catalyst (Y, Sm, or Yb) was deposited using electron-beam sputtering in vacuum at a substrate temperature of 373 K. Prior to the technological processes, the surface of the substrate was treated chemically using conventional methods.

The processes of plasma anodization of structures consisting of an REE and the material to be anodized were carried out in a setup of the three-electrode type with a dc source of oxygen-containing plasma. The plasma anodization was performed under galvanostatic conditions, i.e., at a constant current density of oxide forming.

The catalyst (an REE oxide) was removed chemically without damaging the Al_2O_3 or SiO_2 surfaces after completion of the catalytic plasma anodization.

The highest energy of the UV photons was 5 eV, so the surface of the anodized material was not damaged.

Metal–insulator–semiconductor structures were formed by depositing aluminum contacts through a mask on the obtained oxides. We studied electrical and other parameters by optical methods, Auger spectroscopy, and by measuring the high-frequency capacitance–voltage characteristics.

3. RESULTS AND DISCUSSION

In Fig. 1, we show experimental dependences of the thickness *d* of oxide films on the time *t* of plasma anod-

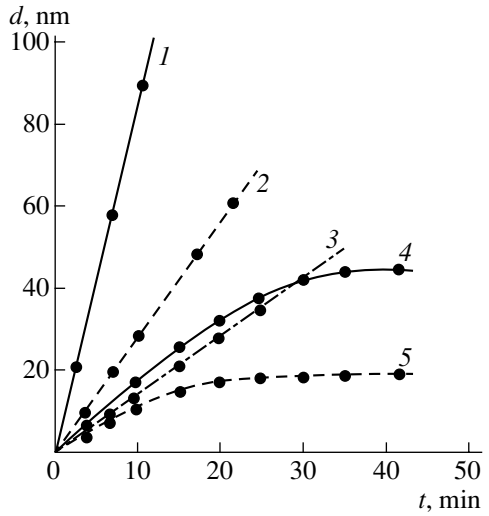

Fig. 1. Dependences of the thickness d of oxide films on the time t of plasma anodization of (*1*, *4*) Al, (*2*, *5*) Si, and (*3*) SiC using (*1*, *2*, *3*) and not using (*4*, *5*) a catalyst. The plasma anodization was carried out under the following conditions: the forming-current density was $I_f = 2$ mA/cm^2 and the substrate temperature was $T_s = 423$ K for aluminum; $I_f = 5$ mA/cm^2 and $T_s = 523$ K for silicon; and $I_f = 10$ mA/cm^2 and $T_s = 600$ K for silicon carbide.

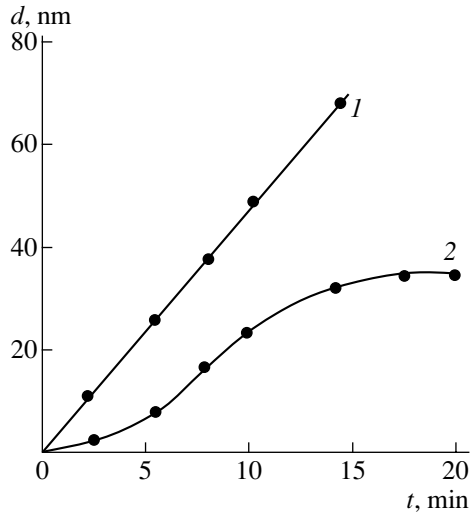

Fig. 2. Kinetics of oxidation of GaAs (*1*) in the presence of UV radiation in the course of plasma anodization and (*2*) in the absence of this radiation. The forming-current density was $I_f = 0.8$ mA/cm^2, and the substrate temperature was $T_s = 400$ K.

ization of Al, Si, and SiC. It can be seen that the oxide thickness increases rapidly and linearly if a catalyst is used. In contrast, the thickness increases much more slowly and the curves $d(t)$ level off if a catalyst is not used. Note that the SiO_2 oxide is not formed on the SiC surface without a catalyst.

The effect of UV radiation on the growth kinetics of the GaAs natural oxide is illustrated in Fig. 2. It is noteworthy that the use of UV radiation in the course of plasma anodization not only promotes oxidation but also increases the uniformity of the thickness of GaAs oxide and reduces the built-in charge in the oxide.

In developing a mechanism of catalytic plasma anodization of metals and semiconductors, we should take into account the specific features that distinguish this process from other methods for obtaining oxides. These features are as follows: (i) the catalytic effect is not observed if anodization is performed in an electrolyte; (ii) the catalytic effect is observed in the course of repeat anodization in plasma of structures that consist of a catalyst, the oxide, and the material to be anodized and were preliminarily grown in an electrolyte or plasma; (iii) the region of the negative space charge in plasma at the sample surface is not observed experimentally in catalytic plasma anodization; (iv) a metal whose oxide is the catalyst has unoccupied *d* or *f* orbitals; (v) the catalyst has superionic conduction of oxygen and a low electron conductivity (i.e., the catalyst is a solid electrolyte); (vi) the self-diffusion coefficient of oxygen is larger than that of the metal; (vii) the electronegativity of the material to be anodized is higher than that of the metal whose oxide serves as the catalyst; and (viii) an unusually high oxidation rate for a metal whose oxide is used as the catalyst.

We used the facts above to suggest a mechanism of catalytic plasma anodization. We used an Y catalyst in the anodization of silicon as an example. In the initial stage of the process, the primary Y oxide film is obtained owing to chemisorption of oxygen, since Y has a high adsorptivity and the process has a very high rate [11]. A further increase in the thickness of the Y oxide occurs owing to the diffusion and drift of oxygen atoms through the oxide film. This process also has a high rate since the diffusion coefficient of oxygen in Y_2O_3 is very large [12].

Since the electronegativity of oxygen is higher than that of Y [13], oxygen carries a negative effective charge and its motion is accelerated by an applied external electric field. In addition, the presence of the catalyst oxide above the silicon surface increases the surface density of oxygen by many orders of magnitude. As the electronegativity of Si is higher than that of Y, silicon atoms attract oxygen atoms from Y_2O_3 and react with them to form the SiO_2 oxide. The applied film is conducive to the formation of a new molecule that consists of an O atom and a Si atom, which ensures the growth of oxides. The oxygen vacancies at the catalyst surface are easily filled with oxygen atoms from the plasma.

When a voltage that is positive relative to the plasma is applied to the sample, the mutual migration of cations of the anodized material and oxygen anions from the plasma occurs, and the oxide of the anodized mate-

rial is formed as a result of a chemical reaction. Electrons also enter Y_2O_3 if an external field is applied. These injected electrons are antibonding quasiparticles, and they weaken the chemical bond between O and Y. However, it is well known that Y atoms have unoccupied *d* orbitals; as a result, electrons in the conduction band (an antibonding band) have a very large effective mass [14] and do not play a significant role in the electrical conductivity. Therefore, the forming current for SiO_2 under the catalyst consists predominantly of the ionic component. Cations do not migrate to the Y_2O_3–plasma interface since their coefficient of self-diffusion in Y_2O_3 is much smaller than that for oxygen [12]. This means that the anionic-transport number $\alpha = 1$ in the case under consideration; i.e., the catalyst is a solid electrolyte and its oxide exhibits anionic mobility.

Thus, the Y layer oxidizes very rapidly, holds electrons within its volume, transfers oxygen to Si, and easily takes oxygen again from the plasma. Yttrium is an effective source of oxygen ions for Si; i.e., it acts as the catalyst for the SiO_2 compound.

It is well known that the presence of a catalyst stimulates the appearance of intermediate complexes with an activation energy that is lower than that of complexes formed without a catalyst. Some of the ions whose energy is insufficient for overcoming the barrier are accumulated in the plasma near the sample [15]. These ions are inactive in the absence of a catalyst and become active if there is a catalyst. In that case, the space charge in the plasma is not observed, and, consequently, the reaction rate increases.

Catalytic plasma anodization develops owing to a reduction in the activation energy for oxidation of the material. In general, this reduction is caused by the formation of new intermediate complexes (Y–O complexes in the case under consideration), which changes the shape and lowers the height of the potential barrier; as a result, the reaction can proceed via a new channel that involves a barrier with a lower height.

Thus, unlike the widely accepted concepts that electrons hinder plasma anodization, in the catalytic plasma anodization electrons play a decisive role by weakening the chemical bonding of the metal to oxygen. Furthermore, electrons are held in the catalyst, are hardly involved in the forming current, and thus increase the ionic component of this current. This circumstance can be explained by the fact that there is no catalytic effect in an electrolyte where there are no electrons.

The mechanism described above accounts for the catalytic effect of ZrO_2 (and all REE oxides) since Zr has unoccupied *d* orbitals and REEs, unoccupied *f* orbitals; the electronegativity and self-diffusion coefficients are similar in the corresponding oxides.

We attribute the increase in the growth rate as a result of irradiation of the anodized surface with UV photons to the appearance of antibonding quasiparticles mainly in the bulk of the GaAs natural oxide at the levels of the tails in the density of states and at the semiconductor–oxide interface. These quasiparticles weaken the chemical bonds and facilitate the motion of ions. Irradiation with UV photons makes it possible to perform technological processes related to the breaking of chemical bonds at relatively low temperatures. Therefore, a plasma-induced anodic natural oxide of GaAs was formed in the course of plasma anodization of the sample exposed to UV radiation. The catalytic process of plasma anodization of GaAs is unproductive since, after the completion of the process and the removal of the catalyst from the surface of the GaAs natural oxide, the gallium arsenide oxide is also removed from the surface.

The improvement in the uniformity of thickness of the GaAs natural oxide is related to the fact that the surface concentration of nonequilibrium charge carriers generated by UV radiation in GaAs exceeds the doping-impurity concentration, which eliminates the effect of nonuniformity of the resistivity over the sample surface.

4. CONCLUSIONS

(1) In order to carry out the process of catalytic plasma anodization, the following conditions are necessary: electrons should be injected into the material to be anodized (electrons are antibonding particles and, as such, weaken the chemical bonds and facilitate the motion of atoms), the material used as the catalyst must have unoccupied *d* or *f* orbitals, and the electronegativity of the material to be anodized must exceed that of the material used as the catalyst.

(2) Increasing the concentration of antibonding quasiparticles in the material to be anodized as a result of irradiation with UV photons increases the mobility of drifting atoms, which is conducive to an increase in the anodization rate.

(3) In order to improve the uniformity of thickness of GaAs natural oxide, it is necessary to irradiate the sample with UV photons in the course of plasma anodization.

REFERENCES

1. V. P. Parkhutik and V. A. Labunov, *Plasma Anodization: Physics, Technology, and Application in Microelectronics* (Nauka i Tekhnika, Minsk, 1990), p. 276 [in Russian].
2. S. Gourrier, A. Mircea, and M. Bacal, Thin Solid Films **65**, 315 (1980).
3. M. Croset and G. Velasco, FR Patent No. 7,727,470 (1979).
4. J. Perriere, J. Siejka, and S. Rigo, Corros. Sci. **20** (1), 91 (1980).
5. S. Gourrier and J. B. Theeten, Appl. Phys. Lett. **38** (1), 33 (1981).

6. A. P. Bibilashvili, A. B. Gerasimov, and G. B. Chakhunashvili, Inventor's Certificate No. 551, 972 (1976).
7. S. V. Baras'ev, A. P. Bibilashvili, and A. B. Gerasimov, Inventor's Certificate No. 1 017 124 (1983).
8. A. P. Bibilashvili, M. T. Vepkhvadze, A. B. Gerasimov, *et al.*, Pis'ma Zh. Tekh. Fiz. **25** (15), 5 (1999) [Tech. Phys. Lett. **25**, 593 (1999)].
9. A. P. Bibilashvili, Fiz. Khim. Obrab. Mater., No. 5, 40 (2001).
10. S. V. Baras'ev, A. P. Bibilashvili, and A. B. Gerasimov, Inventor's Certificate No. 1 172 412 (1985).
11. K. N. R. Taylor and M. I. Darby, *Physics of Rare Earth Solids* (Chapman and Hall, London, 1972; Mir, Moscow, 1978).
12. V. I. Fistul', *Physics and Chemistry of Solids* (Metallurgiya, Moscow, 1995), Vol. 2 [in Russian].
13. L. Pauling and P. Pauling, *Chemistry* (Freeman, San Francisco, 1975; Mir, Moscow, 1978).
14. A. N. Kocharyan and D. I. Khomskiĭ, Zh. Vses. Khim. O-va im. D. I. Mendeleeva **26**, 39 (1981).
15. J. F. O'Hanlon and W. B. Pennebakei, Appl. Phys. Lett. **18**, 554 (1971).

Translated by A. Spitsyn

Semiconductors, Vol. 38, No. 11, 2004, pp. 1267–1274. Translated from Fizika i Tekhnika Poluprovodnikov, Vol. 38, No. 11, 2004, pp. 1308–1315.

ELECTRONIC AND OPTICAL PROPERTIES OF SEMICONDUCTORS

Impurity Centers of Rare-Earth Ions (Eu, Sm, Er) in GaN Wurtzite Crystals

V. V. Krivolapchuk*^, Yu. V. Kozhanova, V. V. Lundin*, M. M. Mezdrogina*, S. N. Rodin*, and Sh. A. Yusupova***

**Ioffe Physicotechnical Institute, Russian Academy of Sciences, Politekhnicheskaya ul. 26, St. Petersburg, 194021 Russia*
^e-mail: vlad.krivol@pop.ioffe.rssi.ru
***St. Petersburg State Polytechnical University, St. Petersburg, 195251 Russia*
Submitted February 16, 2004; accepted for publication February 16, 2004

Abstract—Gallium nitride (GaN) was doped with Eu, Sm, and Er impurities using the diffusion method. The behavior of rare-earth impurities (the formation of donor or acceptor levels in the GaN band gap) correlates with the total concentration of defects, which is determined from optical measurements, and with the position of the Fermi level in starting and doped crystals. The intensity of emission lines, which are characteristic of the intracenter *f–f* transition of rare-earth ions, is controlled by the total defect concentration in the starting semiconductor matrix. © *2004 MAIK "Nauka/Interperiodica".*

1. INTRODUCTION

Wide-gap GaN crystals doped with rare-earth ions (REIs) have attracted the attention of many researchers because of the possibility of developing light-emitting devices for various spectral regions. The crystals are doped with thulium (Tm) for the short-wavelength region, with erbium (Er) for the visible and mid-IR regions, and with europium and samarium (Eu, Sm) for the long-wavelength region [1–3]. The presence of a wide-gap semiconductor matrix allows *p–i–n* structures based on REI-doped GaN to operate at room temperature or above, since the wider the band gap of the semiconductor, the less pronounced is the thermal quenching of photoluminescence (PL) [4]. The wavelength of emission resulting from intracenter *f–f* transitions of the REIs is independent of the type of semiconductor matrix. This is another reason why research of this kind is of current interest. In addition, the technology of fabrication of structures with an REI-doped matrix for a specified spectral region, which corresponds to the emission wavelength of the intracenter *f–f* transition of the REIs, is considerably simpler than the technology of fabrication of multicomponent epitaxial structures [5]. In order to resolve such problems successfully, it is necessary to determine the nature of the REI-induced states and corresponding energy levels, since they control the kinetics of electron excitations of the system along with the defects of the matrix.

Despite extensive previous research in this field, it is not known whether REIs in semiconductor matrixes are donors or acceptors. It is known that REIs in a semiconductor matrix can be found in different charge states. When Eu, Sm, and Er are introduced, charge states (2^+) and (3^+) are most often observed. In this case, some ions of this type can be in charge state (2^+) and others in state (3^+); the ratio of their concentrations is controlled by the defect concentration in the semiconductor matrix [5]. Previously, it was shown using Er in GaN as an example that REIs are substitutional impurities [6]. Consequently, they should be donors or acceptors in this semiconductor matrix. However, until now, the nature of the REI impurity centers was not determined. The effect of methods of introduction of REIs into the GaN semiconductor matrix on the shape of the spectra of the near-edge PL and the intensity of the emission line characteristic of intracenter *f–f* transitions of Er was studied previously [7].

The purpose of this study was to determine the nature of impurity states (donors or acceptors) of rare-earth metals (Eu, Sm, Er) introduced into the GaN epitaxial layers and to determine the effect of correlation between these states and defects in the starting GaN matrix on the specific features of the PL spectra of REI-doped GaN crystals.

2. EXPERIMENTAL

In this study, REIs were introduced into the GaN crystals using the diffusion method, as in [8]. The Sm, Eu, and Er dopants were incorporated into each group of crystals under identical technological conditions. The films were deposited and subsequently annealed in an ammonia ambient in a single operation at 1000–1050°C for 1–1.5 h [8]. As in [7], we obtained crystals by two different methods, namely, by chloride–hydride vapor-phase epitaxy in an open system (HVPE) and by decomposition of metal–organic compounds (MOC-hydride epitaxy, MOCVD). This

allowed us to attain a wider variation of the defect concentration in the starting semiconductor matrix.

The main sources of data on the defect concentration in starting crystals (as in [8]) are the PL spectra, the results of measurements of the carrier concentration by the van der Pauw method (the Hall effect), the results of examining the surface morphology by scanning electron microscopy, the data of X-ray structural analysis (the width of the curve of the diffraction reflection), and the position of the Fermi level (determined from the carrier concentration, the density of states in the conduction band, and the tabulated data on the Fermi function) at temperatures T = 77 and 300 K in starting (undoped) and REI-doped GaN crystals.

For undoped GaN crystals obtained by the HVPE technique, the Fermi level is located 0.085 eV above the bottom of the conduction band at T = 300 K and 0.03 eV above the bottom of the conduction band at T = 77 K.

For the GaN crystals obtained by the MOCVD technique, the Fermi level is located 0.0173 eV above the bottom of the conduction band at T = 300 K and below the bottom of the conduction band at T = 77 K. The concentration and type of defects in starting and doped crystals were estimated using optical spectroscopy (PL spectra), specifically, by the intensity and position of emission lines D^0, x and A^0, x, which are caused by recombination at neutral donors and acceptors, by the full width at half-maximum (FWHM) line, and by the dependence of the PL spectra on the excitation intensity. The REIs used in this study had different charge states. The Er ion has a single charge state (3^+), while the Eu and Sm ions may be in the (2^+) and (3^+) charge states [1, 2]. The charge state of the Eu impurity ion was determined using Mössbauer spectroscopy.

When studying the effect of REI doping on the PL spectra of GaN crystals, it was shown that the method of introducing the impurity specifies the shape of the PL spectrum [7]. When REIs are introduced during growth, one can observe emission lines characteristic of near-edge PL and intracenter *f*–*f* transitions of REIs. When REIs are introduced by ion implantation, the near-edge PL is not observed. In that case, one can observe only emission lines characteristic of the *f*–*f* transitions of REIs, which may indicate that numerous defects are generated by implantation. In this study, we used the diffusion method to introduce REIs.

In order to compare the emission spectra of various GaN crystals correctly, the process parameters were kept constant: the angle of incidence of the beam, the intensity of excitation light, and the temperature.

Optical measurements were carried out using an SDL-2 diffraction spectrometer with an inverse linear dispersion of 1.3 nm/mm in the near-edge PL region of GaN. As emission sources for PL excitation, we used several types of laser. The sources of PL excitation in the steady-state mode were as follows.

(i) A continuous-wave He–Cd laser with an emission wavelength of λ = 3250 Å and an emission power of 5 mW (band-to-band excitation of GaN).

(ii) A continuous-wave Ar laser of the LG-106M4 type with an emission power density of 0.5 W/cm^2 and selection of the emission wavelength using a rotating prism mounted in the place of the totally reflecting mirror. This allowed us to attain lasing at several wavelengths, namely, λ_1 = 5145 Å, λ_2 = 4880 Å, and λ_3 = 4765 Å (excitation of intracenter transitions in rare-earth ions).

(iii) Xenon and halogen lamps with a set of optical filters (excitation of intracenter transitions in rare-earth ions).

3. RESULTS AND DISCUSSION

The undoped GaN crystals were divided into several groups, depending on the preliminary estimate of the type of defects in them.

(i) Crystals whose spectra contain only lines of the near-edge PL, but with different values of FWHM (27–300 meV).

(ii) Crystals with an inhomogeneously broadened line of the near-edge PL, which also have an emission line at 3.26–3.17 eV, the so-called donor–acceptor PL band, whose intensity can exceed the intensity of the near-edge PL by orders of magnitude.

(iii) Crystals that mainly have deep-level defects, which are the effective centers of nonradiative recombination. The existence of these centers is inferred from the low intensity of the near-edge PL line and small FWHM (7–9 meV, i.e., $< kT$) [8].

When analyzing the PL spectra, we paid most attention to the intensity of lines of intracenter *f*–*f* transitions at wavelengths of 1.54 and 0.54 μm (Er), 0.72 μm (Sm), 0.35 μm (Eu^{2+}), and 0.54 and 0.66 μm (Eu^{3+}), as well as to the evolution of the near-edge PL band, which is inhomogeneously broadened [8], and to variation in its width. According to [8], the carrier concentration in the crystals obtained by the HVPE technique exceeded $>10^{18}$ cm^{-3}, since the value of FWHM was 180–300 meV. For the crystals obtained by the MOCVD technique, the value of FWHM was 18–27 meV, i.e., the carrier concentration was approximately an order of magnitude lower.

To clarify the effect of the postgrowth treatment, namely, heat treatment in an ammonia atmosphere or doping with REIs with subsequent annealing in the same atmosphere, we divided the crystal into two parts. One part was only thermally treated in an ammonia atmosphere (NH_3, temperature T_a = 1050°C, duration t_a = 1 h). The other part was doped with Er (GaN⟨Er⟩)

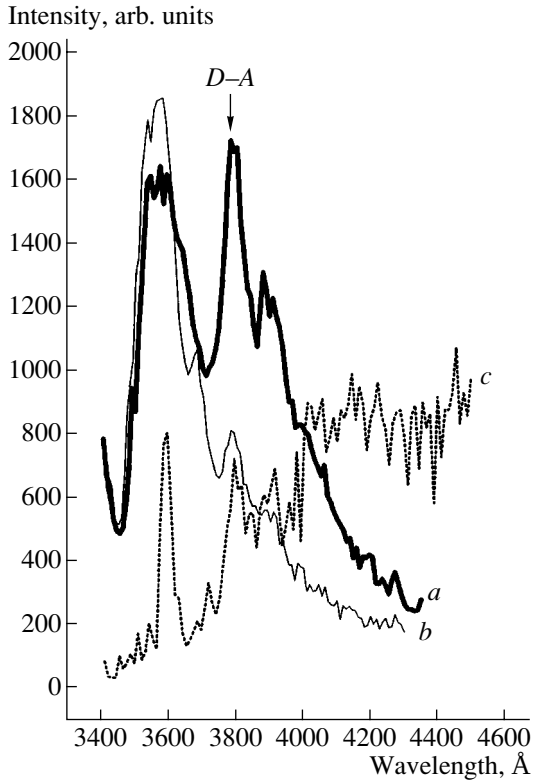

Fig. 1. Effect of heat treatment in an ammonia (NH_3) atmosphere and Er doping on the shape of spectra of the near-edge photoluminescence of GaN (HVPE): (*a*) starting crystal, (*b*) crystal annealed in ammonia, and (*c*) Er-doped crystal. $T = 77$ K.

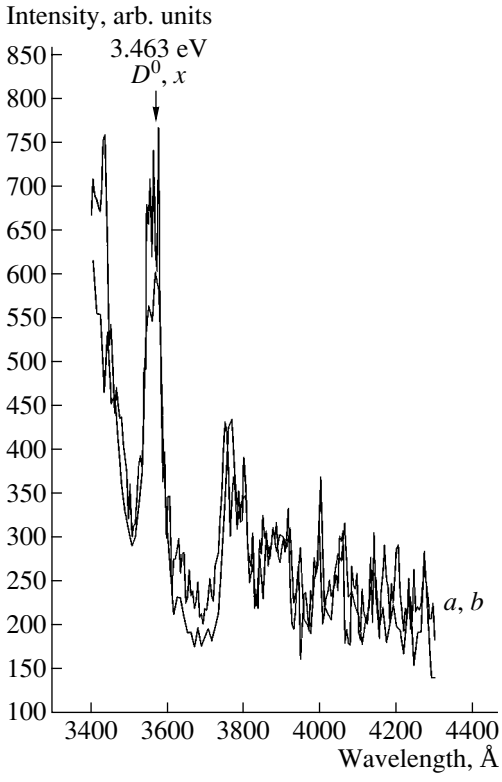

Fig. 2. Near-edge photoluminescence of GaN:Sm (MOCVD): (*a*) starting crystal and (*b*) Sm-doped crystal. $T = 77$ K.

with subsequent heat treatment under the same conditions. The PL spectra are shown in Fig. 1. One can see that the heat treatment affected the shape of the spectrum (compare curves *a* and *b*), specifically, the intensity of the donor–acceptor recombination band (D–A) decreased. However, no variation in intensity, no shift of the position of the near-edge PL peak, and no variation in FWHM were observed. After doping with Er and heat treatment (curve *c*), substantial variations were observed in the shape of the spectrum. The intensity of the near-edge PL decreased with a simultaneous decrease in FWHM, and the intensity of the donor–acceptor PL also decreased. We may assume that heat treatment only causes a decrease in the concentration of the donor–acceptor pairs, whereas doping with Er transforms shallow-level defects into deep-level defects [8].

3.1. Crystals of the First Group

Figure 2 shows the PL spectra with FWHM = 15–27 meV prior to and after doping with Sm for the crystals obtained by the MOCVD method. On doping with other REIs, the spectra had the same shape. One can see that the spectrum of the near-edge PL D^0, x is virtually unaffected by doping. The carrier concentration is also unaffected; consequently, the position of the Fermi level also remains unchanged.

In the long-wave spectral region, there are emission lines characteristic of intracenter *f–f* transitions of REIs: at 0.54 and 1.55 μm for Er, at 0.716 μm for Sm^{2+}, and at 0.66 μm for Eu^{3+} (see Fig. 3).

Figure 4 shows the spectra for the crystals obtained by the HVPE method (*a* is for the starting crystal, and *b* is for the Er-doped crystal). One can see that the spectra are broadened, and FWHM for various starting crystals varies from 120 to 300 meV. Inhomogeneous broadening emerges because the emission wavelengths, which correspond to the radiative recombination of carriers localized at various shallow-level centers, are somewhat different. The causes of inhomogeneous broadening of the spectra were considered in detail in [8]. A substantial spread in the values of FWHM for the near-edge PL line in starting samples is caused by the different concentrations of various defects in these samples. The intensity of emission of the near-edge PL line and its FWHM depend on the concentration of radiative and nonradiative centers and the carrier transport to these centers. The parameters of the carrier transport are in turn controlled by the tails in the density of states in the band gap and by the position of the percolation level [8]. Hence, it follows that, under identical experimental conditions, the samples with different PL intensities

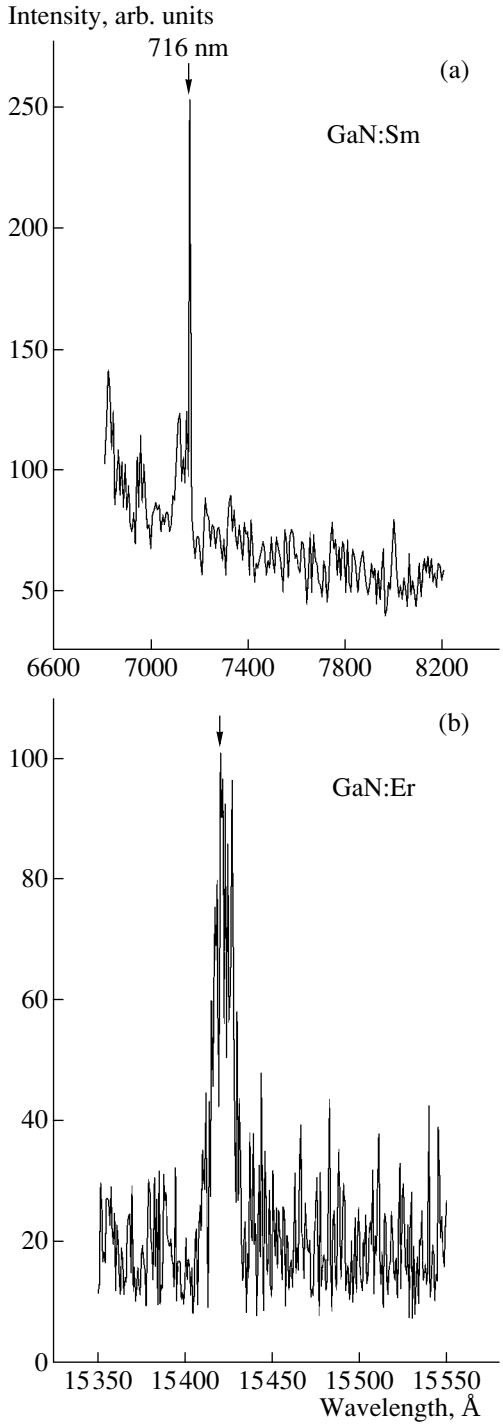

Fig. 3. Photoluminescence spectra in the longer-wavelength region: (a) GaN:Sm (MOCVD) and (b) GaN:Er (MOCVD). $T = 77$ K.

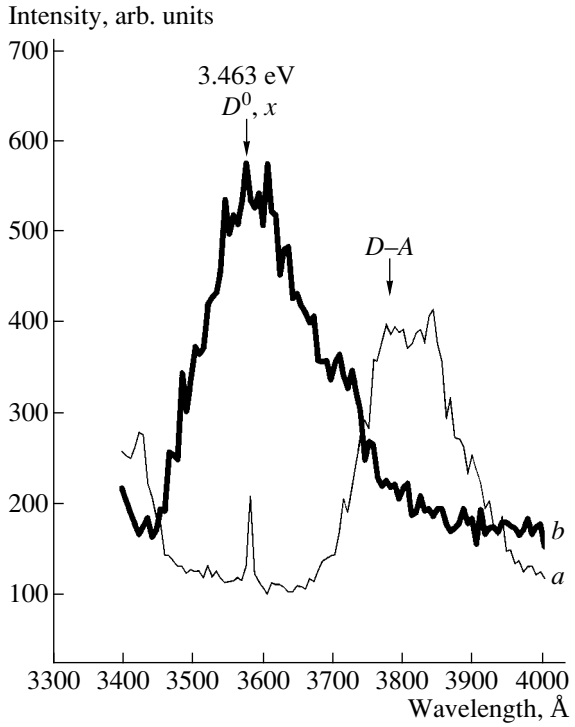

Fig. 4. Near-edge photoluminescence of GaN:Er (HVPE): (*a*) starting crystal and (*b*) Er-doped crystal. $T = 77$ K.

differ primarily in defect concentration. These defects induce both deep levels, which substantially shorten the lifetime of free carriers, and fluctuations in the density of band states.

In the case of doping with Er that has one charge state (3^+), the energy of the peak of the near-edge PL line is indistinguishable from the peak energy for the undoped crystal and corresponds to the emission line of excitons bound at neutral donors, D^0, x (3.463 eV, 3579 nm). The variation in the carrier concentration on doping at a level as high as 8×10^{18} cm^{-3} is insignificant (10^{19} cm^{-3} for the undoped crystal). Consequently, the variation in the position of the Fermi level due to doping is insignificant: 0.006 eV at $T = 77$ K. We may assume that the concentration of electrically active centers is lower than that of optically active centers. The cause of this behavior is the fact that the variations in the shape of the spectrum of the near-edge PL are more significant than the variations in the carrier concentration and, consequently, in the position of the Fermi level. Such a behavior of the introduced impurity may be caused by the formation of various complexes of REIs with impurities [5, 8] present in the crystal. However, the intensity of emission lines characteristic of intracenter *f*–*f* transitions of REIs is considerably lower for GaN crystals obtained by the HVPE method compared with crystals obtained by the MOCVD method. Thus, most likely, the mechanisms of excitation of rare-earth ions in GaN are different. For crystals with the Fermi level below the bottom of the conduction band at the measurement temperature of spectra ($T = 77$ K), the excitation of intracenter transitions is caused by carrier trapping at the REIs. When the Fermi level is located above the bottom of the conduction band, the excitation is caused by trapping at the REI–impurity complex.

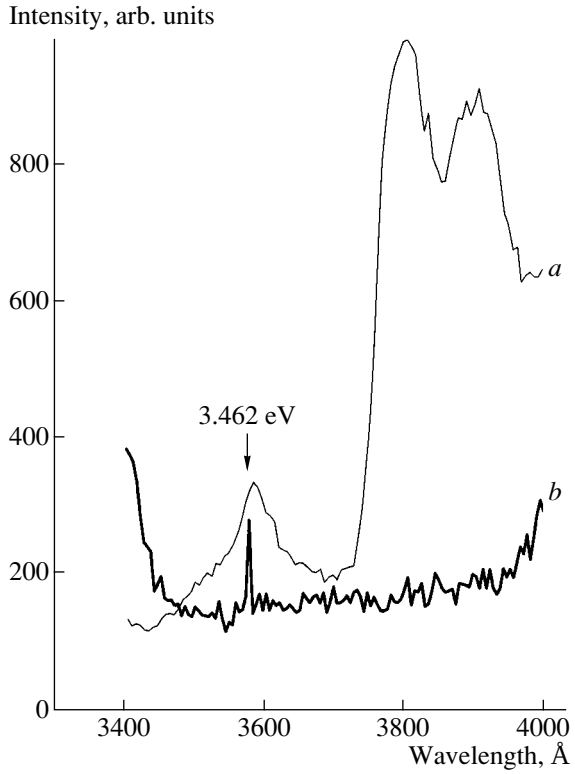

Fig. 5. Near-edge photoluminescence of GaN:Eu (HVPE): (*a*) starting crystal and (*b*) Eu-doped crystal. $T = 77$ K.

3.2. Crystals of the Second Group

Figure 5 illustrates the results of doping a GaN crystal with Eu. The intensity of the donor–acceptor PL in the undoped crystal was higher than that of the near-edge PL. After doping, the position of the near-edge PL peak changed. For the starting crystal, it was 358.4 nm; after doping, 357.8 nm. Thus, the peak shifts to longer wavelengths. In addition, the near-edge PL line narrows drastically, the donor–acceptor PL line completely vanishes, and a band in the region of 410–440 nm emerges. We may suggest two causes of such considerable variation in the shape of the spectrum. These are the transformation of shallow-level defects into deep-level defects, which is indicated by a decrease in intensity and narrowing of FWHM of the near-edge PL line, and the presence of the emission line, which is characteristic of intracenter *f–f* transitions in the Eu^{2+} ion.

To determine the charge state of the impurity Eu ion, we used Mössbauer spectroscopy at ^{151}Eu using a standard MS-2201 spectrometer. The measurements were carried out at room temperature. The studied crystals GaN:⟨Eu⟩ and $^{151}Sm_2O_3$ served as adsorbers. The spectra were the superposition of two lines, whose relative intensities varied considerably from sample to sample. The line with an isomer shift of 0.2 mm/s corresponds to the Eu^{3+} ions, while the line with an isomer shift of 9.5 mm/s corresponds to the Eu^{2+} ions. The spectra are noticeably broadened (the experimental width is

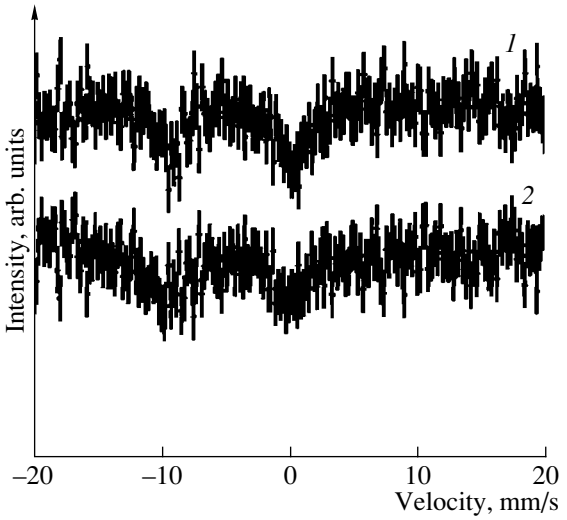

Fig. 6. Mössbauer spectra of GaN:⟨Eu + Eu⟩ crystals. (*1*) and (*2*) are crystals with substantially different Eu concentration.

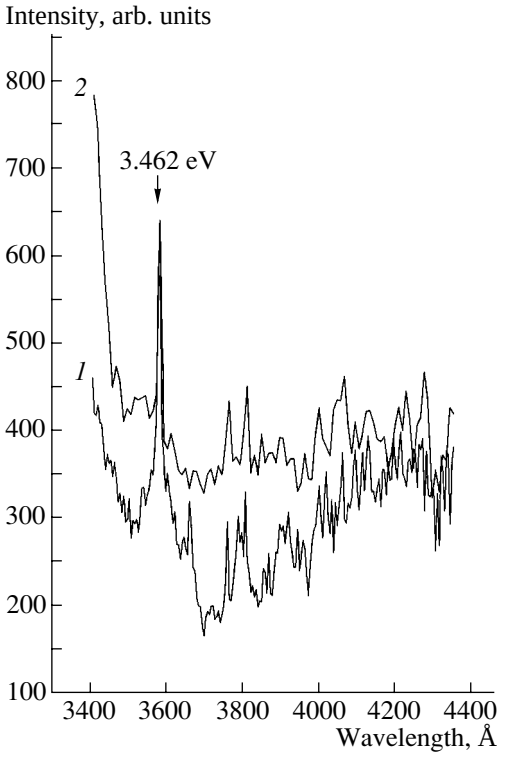

Fig. 7. Near-edge photoluminescence spectra of GaN:⟨Eu + Eu⟩ crystals. $T = 77$ K. Curves (*1*) and (*2*) are for the crystals with substantially different Eu concentration.

2.8 mm/s) compared with the doubled natural width (1.36 mm/s), which is typical of the Mössbauer spectra of ^{151}Eu. Note that the concentration of impurity ions in the samples for Mössbauer measurements was increased by a factor of no less than 2 (we introduce ⟨Eu + Eu⟩) compared with the concentration of impurity Eu ions in

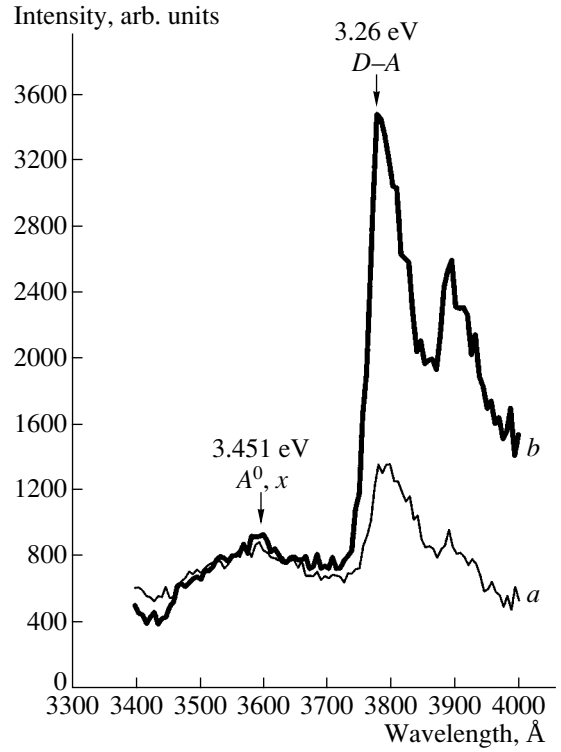

Fig. 8. Near-edge photoluminescence of the GaN:Er crystal, sample *N*1: (*a*) starting crystal and (*b*) Er-doped crystal. $T = 77$ K.

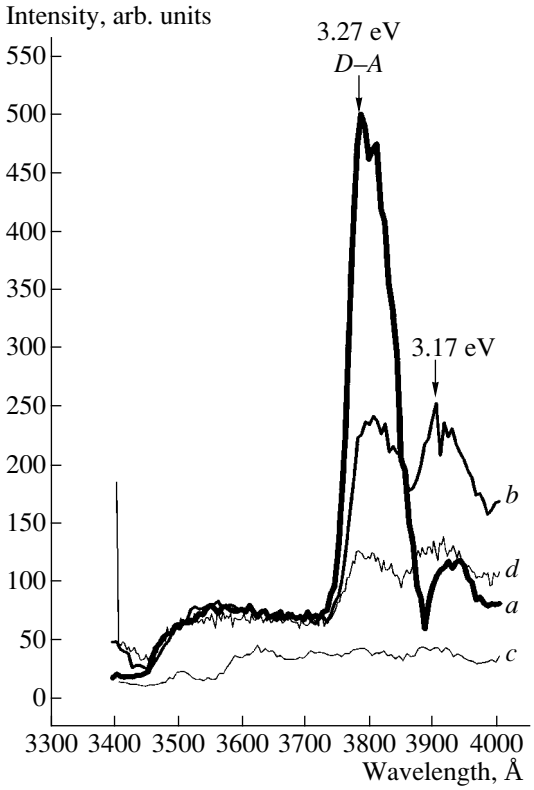

Fig. 9. Near-edge photoluminescence of the GaN:Er crystal, sample *N*2: (*a*) starting crystal, (*b*) Er-doped crystal, (*c*) crystal doped with Er and then ground to a depth of 20 μm, and (*d*) crystal additionally doped with Er after grinding. $T = 77$ K.

the GaN crystal, whose PL spectrum is shown in Fig. 5. This is caused by the lower resolution of Mössbauer spectroscopy compared with optical spectroscopy. Figure 6 shows Mössbauer spectra for two crystals with an increased but different Eu concentration. One can see that the Eu ion has two charge states: (2^+) and (3^+). The PL spectra of the same crystals with an increased Eu concentration are shown in Fig. 7. One can see that, under such heavy doping, the PL spectra of two crystals are virtually identical, similarly to the Mössbauer spectra; i.e., the data of the Mössbauer spectroscopy correlate with the data of optical investigations.

Figures 8 and 9 show the variations in the spectra of starting crystals *N*1 and *N*2 (which differ in the ratio between intensities of the donor–acceptor PL band and the near-edge PL line) and their spectra after doping with Er. The intensity of the donor–acceptor PL for crystal *N*1 increased after doping (Fig. 8). Consequently, the concentration of donor–acceptor pairs increased; thus, we may state that Er is the acceptor impurity, similarly to Mg, whose introduction gives rise to donor–acceptor PL in GaN [8]. In crystal *N*2, the intensity of the donor–acceptor PL decreased after doping (Fig. 9). One of the causes of such a sharp distinction in PL of two samples is the difference in the crystallite sizes, which are larger for crystal *N*1 than for *N*2. To verify this assumption, the sample surface was ground to a depth of more than 20 μm, which substantially exceeded the penetration depth of the dopant, and then polished. Figure 9 shows the spectra of the crystal after polishing (curve *c*) and after introduction of the doping ions (curve *d*). One can see that the intensities of both the near-edge PL and donor–acceptor PL after polishing are low, while the introduction of Er caused an increase only in the intensity of the donor–acceptor PL, which exceeded the intensity of the near-edge PL. Thus, a situation similar to that observed for crystal *N*1 occurred. In the spectrum of crystal *N*1, we observe emission lines at longer wavelengths; these lines are characteristic of intracenter *f*–*f* transitions in Er (1.54 μm). However, these lines are absent in the spectrum of crystal *N*2. The presence of donor–acceptor PL in the spectra of crystals indicates that an additional recombination channel exists, which apparently hampers the population of rare-earth centers; therefore, no emission is observed at a wavelength of 1.54 μm. The intensity of the emission line in the green spectral region (0.54 μm) is sufficient to detect with the sensitivity of the instrumentation used in this study.

3.3. Crystals of the Third Group

The PL spectra of the crystals that have only deep-level defects in the initial state are shown in Fig. 10.

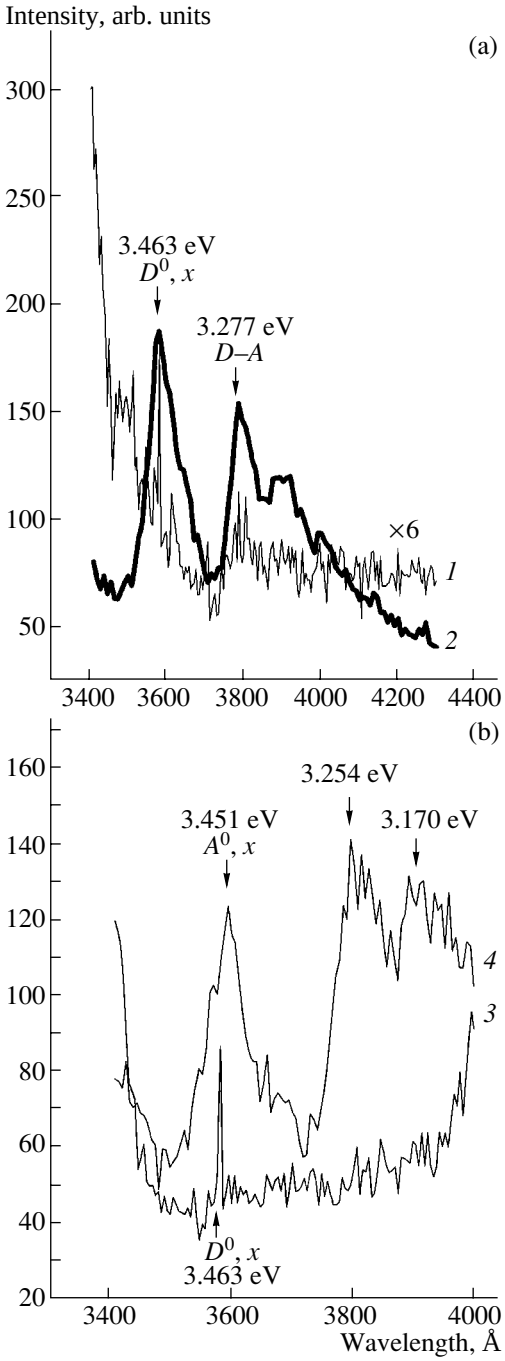

Fig. 10. Spectra of near-edge photoluminescence of (a) GaN:Sm and (b) GaN:Eu. (a): (*1*) starting crystal and (*2*) Sm-doped crystal; (b): (*3*) starting crystal and (*4*) Eu-doped crystal. $T = 77$ K.

The doping of such crystal with REIs generally leads to the transformation of deep-level defects into shallow-level defects [8]. Figure 10 shows the spectra of starting GaN crystals (curves *1*, *3*) and crystals doped with Sm (curve *2*) and Eu (curve *4*). We can see that doping causes an increase in FWHM and intensities of the near-edge PL and donor–acceptor PL, while the position of the near-edge PL peak is unchanged (3.463 eV), which corresponds to the emission related to recombination at a neutral donor (D^0, x). Since the intensity of the near-edge PL increases and donor–acceptor PL emerges, we may assume that the REIs are acceptors.

Based on all the data obtained, we may conclude that the REIs in the semiconductor matrix can be both donors and acceptors, depending on the concentration of defects in the starting crystals. At the same time, the defect concentration in the starting crystal governs the charge state of the introduced REIs, namely, whether the (2^+) or (3^+) states are realized, as is the case, for example, with the introduction of Eu.

We may assume that there is a spatial ordering of defects in REI-doped GaN crystals. In general, the control parameters of this process are as follows: (i) the charge state of the REIs, which causes changes in the type of bonds, from a covalent bond, which is characteristic of the Ga–N bond, to an ionic Er–N bond, since the REI is the substitutional impurity, as was shown previously [6]; and (ii) the concentration and the type of defects in a semiconductor matrix. These processes were observed only for crystals with a high carrier concentration, i.e., with a high impurity concentration. No such processes were observed for the crystals obtained by the MOCVD method.

5. CONCLUSIONS

We can draw the following conclusions from the results of our studies. (i) The REIs in wurtzite GaN crystals can be either donors or acceptors, depending on the total defect concentration in the starting semiconductor matrix. (ii) The intensity of emission lines characteristic of intracenter transitions in REIs in epitaxial layers correlates with the concentration of defects in the starting semiconductor matrix: the lower the concentration of defects, the higher the intensity of the lines that correspond to intracenter transitions.

In all probability, the diffusion mechanism of REIs in GaN depends on the defect concentration in the starting matrix. As the defect concentration in the matrix increases (the Fermi level is close to the bottom of the conduction band), REIs apparently reside in the interdomain space of the mosaic structure. In this case, all variations in the PL spectra are caused by the variations in these regions.

ACKNOWLEDGMENTS

This study was supported by the program of the Ministry of Science, Industry, and Technology of the Russian Federation “Optical and Nonlinear-Optical Properties of Nanostructures.”

REFERENCES

1. A. J. Steckel and R. Birkhahn, Appl. Phys. Lett. **73**, 1700 (1998).
2. A. J. Steckel, M. Garter, R. Birkhahn, and J. D. Scofield, Appl. Phys. Lett. **73**, 2450 (1998).
3. S. Kim, S. J. Rhee, and D. A. Turnbull, Appl. Phys. Lett. **71**, 2662 (1997).
4. A. J. Neuhalfen and B. W. Wessels, Appl. Phys. Lett. **60**, 2657 (1992).
5. M. M. Mezdrogina, E. I. Terukov, N. P. Seregin, *et al.*, Fiz. Tekh. Poluprovodn. (St. Petersburg) **36**, 1337 (2002) [Semiconductors **36**, 1252 (2002)].
6. V. V. Krivolavchuk, M. M. Mezdrogina, S. D. Raevskiĭ, *et al.*, Pis'ma Zh. Tekh. Fiz. **28** (7), 19 (2002) [Tech. Phys. Lett. **28**, 270 (2002)].
7. S. Kim, R. L. Henry, A. E. Wicken, *et al.*, J. Appl. Phys. **90**, 252 (2001).
8. V. V. Krivolapchuk, M. M. Mezdrogina, A. V. Nasonov, and S. N. Rodin, Fiz. Tverd. Tela (St. Petersburg) **45**, 1556 (2003) [Phys. Solid State **45**, 1634 (2003)].

Translated by N. Korovin

Semiconductors, Vol. 38, No. 11, 2004, pp. 1275–1279. Translated from Fizika i Tekhnika Poluprovodnikov, Vol. 38, No. 11, 2004, pp. 1316–1320.

ELECTRONIC AND OPTICAL PROPERTIES OF SEMICONDUCTORS

Effect of Proton Radiation on the Kinetics of Phosphorescence Decay in the Ceramic Material ZnS–Cu

T. A. Kuchakova^, G. V. Vesna, and V. A. Makara

Department of Physics, Shevchenko National University, Kiev, 03608 Ukraine

^e-mail: kuch@univ.kiev.ua

Submitted March 1, 2004; accepted for publication March 23, 2004

Abstract—The results of studying the dose dependences of the decay kinetics of phosphorescence excited by X-ray radiation in luminescent ZnS–Cu ceramic material before and after irradiation with 50-MeV protons are considered. An anomalous variation in the exponent of the hyperbolic phosphorescence curves was observed experimentally as the accumulated light sum increased. It is found from an analysis of the data obtained that two processes are involved in the decay: one of these is monomolecular and corresponds to the first-order kinetics; the other is bimolecular and corresponds to the second-order kinetics. Transitions of charge carriers delocalized from traps occur at the nonradiative-recombination centers induced by proton radiation. Recombination of these charge carriers at the emission centers in the course of decay is described by the second-order kinetics.

1. INTRODUCTION

A high-intensity afterglow is observed for several tens of minutes in the classical ZnS–Cu (FK-106) luminophor. This luminophor is widely used for visualization of X-ray radiation since it exhibits a high quantum yield in the green-emission band (~525 nm) [1]. A number of publications are devoted to studying the kinetics of phosphorescence in ZnS phosphor crystals subjected to photoexcitation (see, for example, [2, 3]). One special feature of X-ray excitation of a material is the appearance of local regions with a high density of electronic excitation. The spatial distribution of localized charge carriers of different types has a significant effect on the kinetics of the phosphorescence decay [4]. This type of excitation is also most informative in studying the radiation defects formed in the material as a result of irradiation with protons. The reason is that X-ray photons penetrate much more deeply into a material than optical photons, which makes it possible to gain more information about the changes that occur in the bulk of the material. The second special feature of X-ray excitation is its low efficiency in the emission of the accumulated light sum, since the probability of an X-ray photon interacting with a high-energy photoelectron with point defects does not exceed the probability of their interaction with ions of the matrix. In the case of generation of the same number of free electron–hole pairs, X-ray excitation nearly always yields a larger accumulated light sum than photoexcitation.

An analysis of variations in the X-ray luminescence, phosphorescence [5], and thermally stimulated luminescence (TSL) of zinc sulfide as a result of irradiation with protons shows that the radiation defects produced do not form new centers of emission or absorption; instead, these defects act as the nonradiative-recombination centers. The main factors affecting the properties of semiconductors after irradiation with protons are the formation of new impurities as a result of nuclear reactions, radiation-defect production, and the accumulation of hydrogen atoms [6]. Radiation defects produced in zinc sulfide as a result of irradiation with electrons, neutrons, or protons are diverse and complex if the energy of the incident particles is higher than the threshold energy. However, Frenkel pairs in the zinc and sulfur sublattices are dominant [7–9]. The vacancies produced by irradiation are not annealed out at temperatures lower than 400 K (V_{Zn}) and 450 K (V_S) [9]. One type of point defects (V'_{Zn}, a singly negatively charged zinc vacancy) is incorporated into an associative center of blue emission with a wavelength of λ = 465 nm [9, 10]. In the case of proton radiation with a dose of 10^{15} cm^{-2}, no increase in the intensity of the corresponding band was observed. At the same time, the intensity of green emission related to the V''_{Zn} vacancies decreased significantly. According to [10], the green-emission band can be almost completely quenched if the sample is heated in zinc vapors.

The aim of this study was to gain insight into the decay kinetics of luminescence in the powdered ceramic material ZnS–Cu as the dose of X-ray excitation varied; this decay was measured before and after irradiation with protons.

2. EXPERIMENTAL

We studied the luminescent ceramic ZnS–Cu obtained by hot pressing an FK-106 (ZnS–Cu) commercial powder phosphor crystal in graphite molders at

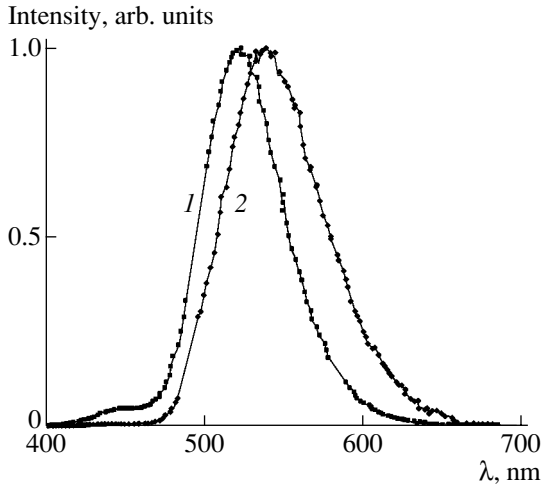

Fig. 1. Spectra of the (*1*) steady-state luminescence excited by X-ray radiation and (*2*) phosphorescence of the ZnS–Cu samples. $T = 85$ K.

a temperature of 1400 K and a pressure of 3×10^7 Pa. In order to study the afterglow, we chose two types of samples: unirradiated samples (type 1) and samples irradiated with protons at a dose of 10^{15} cm^{-2} (type 2). The samples were irradiated with 50-MeV protons in a U-240 cyclotron. Luminescence and phosphorescence were excited using radiation from an X-ray tube (Mo, 35 kV, 10 mA) at temperatures $T = 85$ and 295 K. Phosphorescence was detected simultaneously via two channels: integrally (luminescence emission was focused directly onto the sensitive area of an FÉU-106 photomultiplier) and spectrally (emission was directed to the photomultiplier through an MDR-2 wide-aperture monochromator). All the luminescence spectra were corrected taking into account the spectral sensitivity of the detecting system. The duration of excitation of the samples was varied from 2 s to 3 h; phosphorescence was detected for 10 min. Taking into account the technical characteristics of the detection system, we analyzed the phosphorescence data obtained after a lapse of at least 30 s from the completion of excitation.

3. RESULTS AND DISCUSSION

It was established that the time dependences of the phosphorescence intensity $J(t)$ are similar after excitation for identical time intervals. This inference is valid both for detection in integral light and for detecting the phosphorescence intensity at the peak of the green-emission band (520–529 nm). The spectrum of steady-state luminescence excited by X-ray radiation and that of phosphorescence are different (Fig. 1). The blue-emission band peaked at $\lambda = 465$ nm is not observed in the spectrum of low-temperature phosphorescence; furthermore, a shift of the green-emission band to longer wavelengths is clearly seen. The emission spectrum of steady-state luminescence of the ZnS–Cu ceramic in the green region apparently consists of several closely spaced and highly overlapping emission bands [11]. The shift of the resulting peak of the green-emission band in the phosphorescence spectrum with respect to the corresponding band in the spectrum of luminescence stimulated by X-ray radiation may be caused by the different contribution of the component bands mentioned above to the total emission intensity. For this center, a recombination mechanism is involved in emission, since emission is observed in both phosphorescence and TSL. This means that the emission center can remain in a recharged state for a very long time, which causes a variation in the spatial coordinates of the corresponding ligands. Naturally, the strength and possibly symmetry of the crystal field change for a recharged emission center. The energy gap between the ground and excited states should change (the Jahn–Teller effect [8]) as a result of the recombination of a free charge carrier in the crystal field mentioned above. In the case of steady-state luminescence, we will observe not only the emission due to the recombination of free charge carriers, but also the emission caused by excitonic recombination.

It was also established experimentally that long-term X-ray excitation ($t_0 = 3$ h) did not affect the number of recombination centers (radiative and nonradiative) and trapping centers. In order to draw this conclusion, we compared the phosphorescence and TSL curves measured after 5-s excitation and before and after 3-h excitation and the release of the accumulated light sum. The shape of the phosphorescence curve depends on the dose of excitation obtained for both types of sample. As the duration of excitation increases, the phosphorescence intensity increases steadily and attains a maximum in ~180 s at $T = 85$ K for both types of sample. At $T = 295$ K, the highest phosphorescence intensity is attained in ~60 s for the type-1 samples and in ~180 s for the type-2 samples. If the irradiated sample is excited for a longer time (from 10 min to 3 h), a slight increase in the light sum under the phosphorescence curve is observed in the final stage of the phosphorescence decay. Note that the value of accumulated light sum under the phosphorescence curve was found to be much smaller (especially at $T = 295$ K) for the samples irradiated with protons. In addition, a decrease in the emission intensity of steady-state luminescence by ~35% was observed for these samples; specifically, a decrease in the emission intensity for the main band peaked at $\lambda = 522$ nm was detected. In all cases (two types of samples and two temperatures of excitation), experimental curves of the intensity decay $J(t)$ after the elapse of the first minute of decay can be satisfactorily approximated using a hyperbolic dependence (the phenomenological Becquerel formula [12]):

$$J(t) = \frac{J_0}{(1 + \omega t)^{\alpha}}, \qquad (1)$$

where α and ω are constants (note that $1 \le \alpha \le 2$).

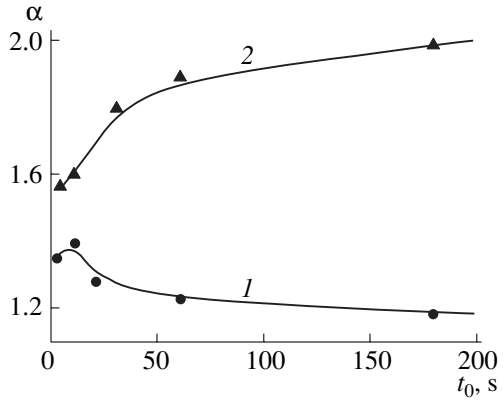

Fig. 2. Dependences of the hyperbola exponent α on the duration of excitation by X-ray photons for the samples (*1*) unirradiated and (*2*) irradiated with protons. T = 295 K.

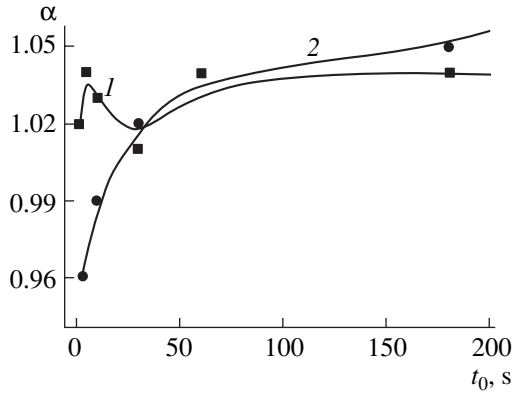

Fig. 3. Dependences of the hyperbola exponent α on the duration of excitation by X-ray photons for the samples (*1*) unirradiated and (*2*) irradiated with protons. T = 85 K.

Irradiation of the ceramics with protons induces changes in the dependence of the phosphorescence kinetics on the duration of excitation of the samples. If the phosphorescence is excited at the liquid-nitrogen temperature, these changes are less pronounced and the general trends are retained. In Figs. 2 and 3, we show the dependences of the exponent $\alpha = \ln(J)/\ln(t)$ (here, t is the detection time of phosphorescence) on the duration of excitation t_0 for both types of the samples at T = 85 and 295 K.

The method used for excitation requires that a number of factors be considered. First of all, the distribution of recharged traps over the volume should be taken into account. The deeper lying layers of the luminophor are excited to a lesser extent. The decay curves for each layer have specific initial slopes; the recorded decay curve is the sum of all these curves. We should also take into account the spatial distribution of electronic excitation that is typical of excitation with X-ray photons. Local regions with different excitation density are formed in the sample bulk.

In the samples of type 1, the decay characteristics at both the above temperatures do not change when leveling-off (saturation) is attained. The state of saturation corresponds to an equilibrium distribution of charges over the traps (the following condition is satisfied: the ratio between the concentrations of localized charges is found to be constant in the time interval from t_1 to t_2, i.e., n_i/n_k = const); the decay characteristics change only slightly when the samples are further excited. The condition n_i/n_k = const is not satisfied at a low level of excitation. The spread in the values of α is representative of these trends. For the samples of type 1, the decay curves obtained for different durations of excitation can be made to coincide by shifting to the right along the time axis the curve that corresponds to a lower excitation level. As the stored light sum increases, the exponent α decreases. The kinetics of phosphorescence decay in the type-1 samples in the case of X-ray excitation corresponds to the kinetics of the transition (Becquerel's) region in the theoretical decay curve obtained on the basis of the gas-kinetic theory of photoluminescence in phosphor crystals [2, 3].

An increase in the exponent α is observed in the samples of type 2 as the duration of excitation increases, i.e., as the stored light sum increases; this behavior cannot be explained in the context of the gas-kinetic theory of luminescence in phosphor crystals [2, 3]. At the same time, an increase in the exponent α as the light sum stored in the sample increases cannot be attributed to special features of excitation by the X-ray radiation either [4]. Variations in radiation had a greater effect on the decay at room temperature. At the same time, if the time instant of the phosphorescence decay (t_i) is fixed, the dose dependence of intensity is described adequately by the following expression that defines the light-sum accumulation and is known from the gas-kinetic theory of photoluminescence:

$$J(t_i) = J_0(t_i)\left[1 - \exp\left(-\frac{t_0}{\tau_i}\right)\right]. \qquad (2)$$

Here, t_0 is the duration of excitation of the sample, while τ_i is the characteristic time of saturation of the traps of the ith type and reflects the rate of light-sum accumulation. The obtained time dependences of the τ_i distribution within the detection range of phosphorescence are shown in Fig. 4. The values of τ_i were calculated using the smallest rms deviation of dependence (2) from experimental values. The found form of these dependences makes it possible to assume that the observed phosphorescence in the ZnS–Cu luminescent ceramic is a superposition of two emission curves related to different physical processes and dominant in different time intervals. The first process exhibits linear kinetics, while the second process features quadratic kinetics. We used the Alentsev–Fock method [12] to decompose the curves into two components. We took into account the following. The phosphorescence curve is a superposition of two curves that are dominant in

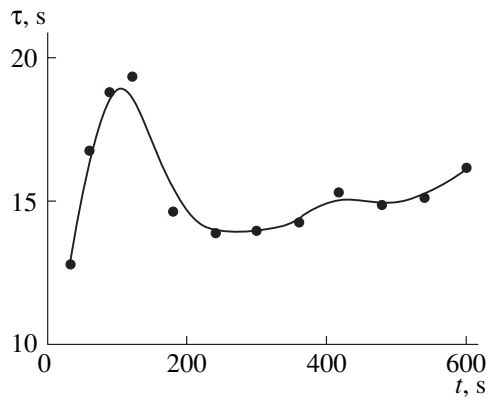

Fig. 4. Distribution of τ within the time interval of the phosphorescence detection. T = 295 K.

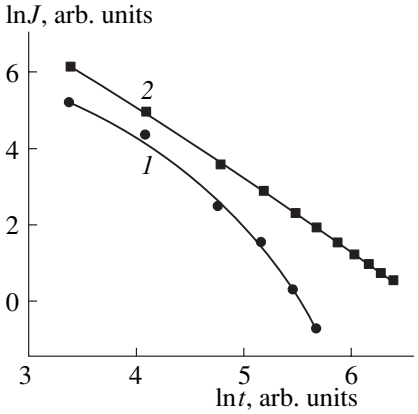

Fig. 5. Characteristic decomposition of the experimental phosphorescence curve into two elementary components at T = 295 K: (*1*) exponential component and (*2*) hyperbolic component.

different (although partially overlapping) time intervals. As a result, we obtain different decay curves with different durations of the phosphorescence excitation. If we assume that in this case the shape of the decay curves that represent different mechanisms remains unchanged, the difference between experimental curves is then caused by differences in the relative contributions of the components. We decomposed the experimental curves for both types of sample and for various combinations of excitation duration. Note that experimental curves of the phosphorescence decay in fact remain similar in the later stages of the process. An important advantage of this method is the existence of an experimental test for its applicability; this test relies on the presence of horizontal portions in the plot that shows the ratio between two decay curves. The substantial decrease in the detected light sum stored at the traps that are remote from the emission centers (i.e., those exhibiting the hyperbolic decay law) in the sample of type 2 made it possible to decompose the decay curve into two components more accurately. In Fig. 5, we show a typical set of two elementary components of the decay curve that were obtained as a result of decomposing the experimental curve. Using these data on the exponential component of the phosphorescence curve, we obtained values of τ (characteristic decay time) equal to ~70 and ~50 s at T = 85 and 295 K, respectively. The large value of τ can be explained if a polaron stabilized in the lattice by some defect acts as the metastable state, while the transition to the emission center is realized via a tunneling mechanism. The constant $\omega = 5\ s^{-1}$ at $\alpha = 1.8$ is obtained for the second component whose decay is described by the kinetics given by formula (1).

The presence of an exponential component in the decay may be caused by the following factors: (i) the presence of homologically related emission centers and traps in the material; (ii) the extremely low mobility of free charge carriers (formation of an intermediate metastable polaronic state); and (iii) an appreciable excess (by at least an order of magnitude) of the concentration of recharged emission centers over the concentration of the shallow-level traps that give rise to phosphorescence. It was previously assumed [13] that there are specific traps in ZnS–Cu that reside near the emission center or are part of a unified complex. The green-emission centers that are dominant in the material under consideration may be composed of intrinsic defects and the activator impurity (Cu) [9, 10]. The metastable state acts as the trap in this center, while the excited level of the center plays the role of a short-lived level [13]. A polaron localized in the vicinity of the defect may also play the role of the metastable state [14–16]. An intracenter mechanism is actually in effect in the complex under consideration; as is well known, this mechanism is described by an exponential decay dependence. A radiative transition in this center occurs regardless of the state of other centers and is controlled only by the corresponding probability. In this case, the decay intensity obeys the exponential law

$$J = J_0 \exp\left(-\frac{t}{\tau}\right), \qquad (3)$$

where J_0 is the highest emission intensity at $t = 0$ and τ is the characteristic decay time.

The dependences of the decay kinetics on the duration of excitation (see Figs. 2, 3) can be interpreted in the following way on the basis of the suggested mechanism of radiative transitions in afterglow. In the case of short-term excitation, the charge carriers are mainly captured by the traps responsible for the exponential decay, since the probability of charge-carrier recombination in this case is independent of both time and the state of other centers. Traps of the above type are therefore transformed more rapidly into the quasi-steady state. As the excitation duration increases, the contribution of the second component, whose decay obeys the hyperbolic law, increases. The nonradiative-recombination centers formed by proton radiation inhibit the

buildup of charge carriers at the traps that are located in space independently of the emission centers. The above recombination centers compete with recharged emission centers in the recombination-related transitions. Thus, an increase in the value of α with increasing excitation duration is related to the variation in the relation between the values of the light sums accumulated at traps of different types.

Thus, the shape of the emission curve for phosphorescence reflects the combined contribution of relaxation processes that occur in the crystal after termination of excitation. The radiation defects that are produced by irradiation with protons and which affect selectively the recombination processes in the ZnS–Cu ceramic made it possible to clarify the origin of the traps responsible for phosphorescence in this material. The anomalous behavior of the decay kinetics observed in ZnS–Cu after irradiation with protons allowed us to suggest a mechanism of phosphorescence and clarify the causes of the increase in the hyperbola exponent in the decay.

REFERENCES

1. A. M. Gurvich, *X-ray Phosphorescent Crystals and X-ray Fluorescent Screens* (Atomizdat, Moscow, 1976) [in Russian].
2. M. V. Fok, *Introduction to Kinetics of Luminescence of Phosphorescent Crystals* (Nauka, Moscow, 1964) [in Russian].
3. V. V. Antonov-Romanovskiĭ, *Kinetics of Photoluminescence of Phosphorescent Crystals* (Nauka, Moscow, 1966) [in Russian].
4. V. Ya. Degoda, Ukr. Fiz. Zh. **46** (1), 124 (2001).
5. V. Ya. Degoda and V. Ya. Proskura, Ukr. Fiz. Zh. **40**, 957 (1995).
6. V. V. Kozlovskiĭ, V. A. Kozlov, and V. N. Lomasov, Fiz. Tekh. Poluprovodn. (St. Petersburg) **34**, 129 (2000) [Semiconductors **34**, 123 (2000)].
7. A. A. Adrianov and F. F. Kodzhespirov, Fiz. Tekh. Poluprovodn. (Leningrad) **8**, 2043 (1974) [Sov. Phys. Semicond. **8**, 1330 (1974)].
8. G. Watkins, in *Point Defects in Solids* (Plenum, New York, 1975; Mir, Moscow, 1979).
9. N. K. Morozova and V. A. Kuznetsov, *Zinc Sulfide: Production and Optical Properties*, Ed. by M. V. Fok (Nauka, Moscow, 1987) [in Russian].
10. A. N. Georgobiani, L. S. Lepnev, E. I. Panasyuk, and V. F. Tunitskaya, Tr. Fiz. Inst. im. P. N. Lebedeva, Akad. Nauk SSSR **182**, 3 (1987).
11. A. G. Miloslavskiĭ and N. V. Suntsov, Fiz. Tekh. Vys. Davlenii **7** (2), 94 (1997).
12. M. V. Fok, Tr. Fiz. Inst. im. P. N. Lebedeva, Akad. Nauk SSSR **59**, 3 (1972).
13. D. Curie, *Luminescence of Crystals* (Dunod, Paris, 1960; Inostrannaya Literatura, Moscow, 1961; Wiley, New York, 1963).
14. M. V. Fok, Fiz. Tverd. Tela (Leningrad) **5**, 1489 (1963) [Sov. Phys. Solid State **5**, 1085 (1963)].
15. É. I. Adirovich, *Problems in the Theory of Luminescence in Crystals* (GITTL, Moscow, 1956) [in Russian].
16. Vu Kuang and M. V. Fok, Tr. Fiz. Inst. im. P. N. Lebedeva, Akad. Nauk SSSR **79**, 39 (1974).

Translated by A. Spitsyn

Semiconductors, Vol. 38, No. 11, 2004, pp. 1280–1283. Translated from Fizika i Tekhnika Poluprovodnikov, Vol. 38, No. 11, 2004, pp. 1321–1324.

ELECTRONIC AND OPTICAL PROPERTIES OF SEMICONDUCTORS

Photosensitivity of Thin Films of Semiconductor Nanocomposites Based on Metal–Organic Complexes with Cu^+ and Ru^{2+}

E. L. Aleksandrova* and N. N. Khimich**

**Ioffe Physicotechnical Institute, Russian Academy of Sciences, St. Petersburg, 194021 Russia*

***Grebenshchikov Institute of Silicate Chemistry, Russian Academy of Sciences, St. Petersburg, Russia*

Submitted April 6, 2003; accepted for publication April 19, 2004

Abstract—The photosensitivity of nanocomposites in a system constituted by an organic transition metal complex and silica was studied. It is shown that the photosensitivity of a nanocomposite is determined by the valence and the ionization potential of the metal atom, which is equal to $(3–8) \times 10^4$ cm^2/J (quantum yield of carrier photogeneration is 0.03–0.05) for the Cu^+ complex and 5×10^3 cm^2/J for the Ru^{2+} complex. The possibility of controlling the magnitudes and spectra of both the photosensitivity and luminescence of thin films of nanocomposites based on these complexes by varying the structure of metal complexes and the fact that the quantum efficiency of photogeneration can be raised by introducing transport molecules into the structure of a nanocomposite gives reason to believe that photosensitive and electroluminescent devices can be created on the basis of these nanocomposites. *© 2004 MAIK "Nauka/Interperiodica".*

1. INTRODUCTION

Organic–inorganic nanocomposites [1], which constitute one of the most intensively developing areas of materials science, have clearly pronounced semiconducting properties. Owing to the possibility of obtaining thin transparent layers of optical quality, they seem to be promising materials for creating recording media. In this context, organic complexes of a number of transition metals with bipyridyl ligands are of primary interest in this class of nanocomposites [2–5]. Composites of this kind have already found practical application: they are successfully used in luminescent sensors for determining the concentration of oxygen [5, 6]. The occurrence of an effective charge transfer between a metal atom and an organic aromatic ligand gives reason to believe that photosensitive recording media, including photorefractive media for holography [7], and materials for photovoltaic cells [8] can be created using these composites. Owing to their effective luminescence, whose spectral range can be varied by choosing the metal atom [2–4, 9], and the possibility of introducing transport molecules, which provide an effective carrier transport, these composites are certainly of interest as a new class of materials for electroluminescent devices.

The aim of this study was to examine the photosensitive properties of nanocomposites in a system constituted by an organic transition metal complex and silica and to analyze the mechanism of carrier photogeneration in the nanocomposites.

2. OBJECTS AND METHODS OF STUDY

As objects of study, we used thin films synthesized on the basis of complexes of Cu^+ and Ru^{2+} with 2,2'-bipyridyl (ligand L)–$[MeL_{2n}]^{+n}$, where $n = 1$ for Me = Cu^+ and $n = 2$ for Me = Ru^{2+} (L = bipy):

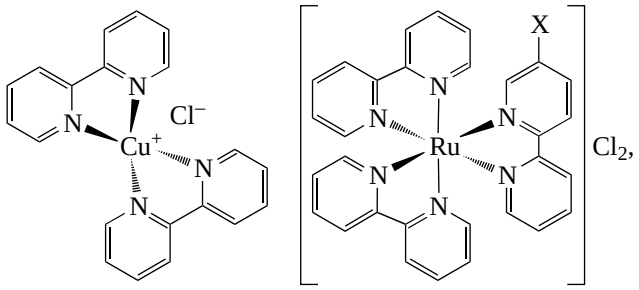

where X = –H and –CONH–$(CH_2)_3$–SiO–. The concentration of the complex was 1–20%. We used xerogels SiO_2 as a matrix, which were synthesized by the sol–gel method of hydrolytic polycondensation of tetramethoxysilanes in an acid medium [10]. In addition to the composites mentioned above, the matrix contained free bipyridyl molecules, which provided carrier transport. The films were annealed at 300 and 500°C. The organic complexes with Cu^+ and Ru^{2+} formed a nanohybrid with the silica matrix via molecular interaction between the components of the system in the case of the copper complex [11] and via chemical binding for the ruthenium complex [12]. The thickness of the film was 1–2 μm.

The photosensitivity and the quantum efficiency η of carrier photogeneration were measured in the electrophotographic mode by the procedure described in [13], in the spectral range 400–800 nm at an electric field strength $E = (0.1–1.0)E_0$, where E_0 is the limiting field strength for a given material. The field depen-

dences $\eta(E^{1/2})$ were used to evaluate the dielectric constant (ε) of the starting xerogel and the nanocomposites based on metal complexes in terms of the Pool–Frenkel model and to find the quantum efficiency of formation of bound pairs (η_0) and the thermalization length (r_t) using the Onsager model. The absorption spectra α were measured on a Perkin Elmer spectrophotometer. The photosensitivity $S_{0.1}$ was found from the criterion of a 10% decrease in the surface potential of a layer (V) relative to the initial value ($\Delta V/V = 0.1$) as a result of exposure to a monochromatic light or to that of a KGM-300 halogen lamp (integral photosensitivity).

3. RESULTS AND DISCUSSION

The nanocomposites obtained, with a content of metal complexes in the range 1–20%, had the structure shown in Fig. 1. All the composites in which the content of a complex was less than or equal to 15% were monolithic and transparent. Although the increase in hardness and mechanical strength of the sample with a 10% content of the complex compared to the starting gel is not very significant, it indicates that there is a certain physical interaction between the organic component and the silica matrix. The optimal structure of the composite is obtained at a content of the organic component in the range 5–10%. When the content of the organic component is raised to 15%, the density and hardness of the composite decrease, while a 20% content of this component leads to a dramatic decrease in the hardness of the composite, and it ceases to be monolithic. This change in the properties of the organic–inorganic hybrids synthesized can be understood by analyzing their micrographs (Fig. 1). The structure of a sample with a 10% content of the complex (Fig. 1b) is similar to the structure of the starting gel (Fig. 1a), which, however, is considerably more ordered, apparently because of the formation of a nanocomposite. The pore diameter in both the structures is 10–17 nm. The structure of a composite with a 20% content of the complex is looser and more porous (Fig. 1c). Presumably, the optimal content of the copper complex, the approximate size of whose molecules is 1.0–1.5 nm, is limited by the size and number of these pores in the matrix. Thus, the structure of the composite is optimal in the case of a 10% content of the complex, whereas the introduction of a greater amount of molecules of the complex dramatically impairs the mechanical properties of a sample and causes it to crack, because the silica matrix is formed under nonoptimal conditions.

The spectra of absorption $\alpha(\lambda)$ and photosensitivity $S_{0.1}(\lambda)$ of films that contain nanocomposites with Cu^+ and Ru^{2+} complexes in a SiO_2 matrix are shown in Figs. 2a and 2b (curves *1* and *2*, respectively). For comparison, the same figure shows, for comparison, the spectra of the starting xerogel (curves *3*). It can be seen from Fig. 2a that the absorption peak associated with the Cu^+ complex lies at 750 nm, i.e., in the longer-wavelength part of the spectrum as compared with the peak for the Ru^{2+} complex at 450 nm. The energy at

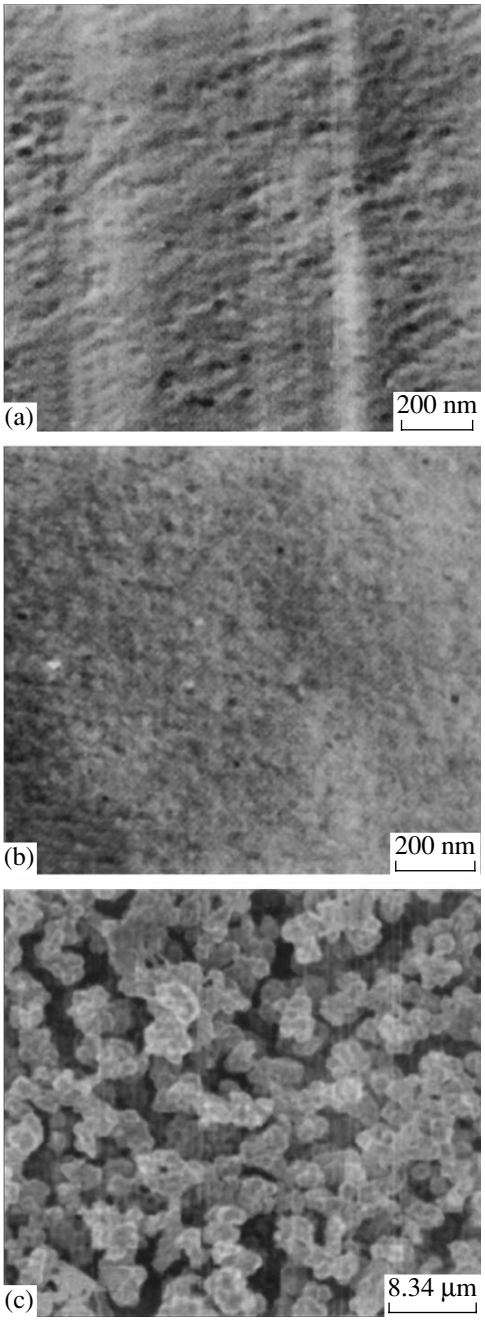

Fig. 1. Electron micrographs of (a) starting xerogel and (b, c) nanocomposites with different content of Cu^+ complexes: (b) 10 and (c) 20%.

which the absorption peak lies (1.69 eV for the Cu^+ complex and 2.76 eV for the Ru^{2+} complex) decreases as the valence of the metal becomes lower [14]. This correlates with the previously observed shift of the absorption peak to longer wavelengths on passing from Me^+ to Me^{2+} and with a decrease in the ionization potential of the metal atom, which is indicative of electron transfer from the metal atom to the ligand.

The luminescence spectra of the nanocomposites synthesized, which were measured [9] previously under

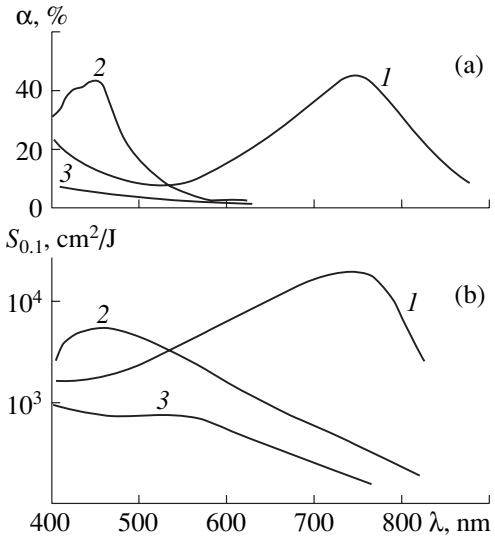

Fig. 2. Spectra of (a) absorption α(*a*) and (b) photosensitivity $S_{0.1}$ of composites based on (*1*) Cu^+ and (*2*) Ru^{2+} and that of (*3*) starting xerogel; content of the complexes, 5%.

excitation with light from a nitrogen laser (wavelength 337 nm, pulse width 6–8 ns) for 1 μs after the excitation pulse at temperature $T = 300$ K, coincide with the spectra of analogous nanocomposite structures [3–6]. Irrespective of the annealing temperature, there is a luminescence band peaked at 610–620 nm for the Ru^{2+} complex and a broad band at around 420 nm for the Cu^+ complex. The luminescence intensity for the Ru^{2+} complex exceeds that for the Cu^+ complex by more than a factor of 10. The luminescence band observed for the Cu^+ complex is apparently due to emission from only bipyridyl fragments, which absorb at 300–360 nm, rather than from the complex with the metal, which absorbs in the long-wavelength spectral range, as can be seen from Fig. 2.

The photosensitivity spectra of the nanocomposites (Fig. 2b) reproduce their absorption spectra (Fig. 2a). The photosensitivity of films of the nanocomposite with Cu^+ at a 5–10% content of the complex is $(3–8) \times 10^4$ cm²/J, with a quantum yield of 0.03–0.05. For the Ru^{2+} complex, the photosensitivity $S_{0.1}$ is about 5×10^3 cm²/J at 400–550 nm, with a quantum yield $\eta \approx 0.003 \pm 0.001$, which is more than an order of magnitude lower than that for the Cu^+ complex. The photosensitivity of layers of the starting xerogel is about 2×10^3 cm²/J, with a quantum yield $\eta \approx 0.001$. The thermalization length for the nanocomposite with Cu^+ is $r_t = 1.5 \pm 0.2$ nm, which is comparable with the size of the molecule of the complex (1.0–1.5 nm) and is somewhat smaller (by 25%) than the corresponding value for polymeric complexes of similar structure [15]. The quantum yield of formation of bound pairs is $\eta_0 = 0.08 \pm 0.03$.

The correlation between the absorption and photosensitivity spectra of the systems studied and the increase in the luminescence intensity observed as the value of $S_{0.1}$ decreases (on passing from the Cu^+ complex to the Ru^{2+} complex) indicate that the molecule of a complex, $[CuL_2]^+$ or $[RuL_3]^{2+}$, is involved in the primary photophysical processes. The absorption of a photon by the molecule leads to electron transfer from the metal atom to the ligand. Within the same molecule, the excess photon energy is lost and Coulombically bound carriers are thermalized. Further charge separation occurs as a result of temperature-and-field-assisted dissociation in an external electric field. Carriers become free at distances of 10–15 nm. This distance (Coulomb radius) is calculated from the dielectric constant ε, which is 6.5–7.0 for the complexes and 6.0 ± 0.5 for the starting xerogel.

The energy $\hbar\omega$ of the peak of the absorption band associated with the complex is determined by the metal atom, as is shown above. At the same time, if the ligand is varied from bipyridyl to biquinolyl and to phenanthroline derivatives for the nanocomposites with Ru^{2+}, the energy of the first charge-transfer band shifts from 4.64 eV for bipyridyl to 4.47 eV for nitrophenanthroline, 4.19 eV for aminophenanthroline, and 3.87 eV for phenanthroline-5,6-dione [16]. The presence of free (forming no complexes with the metal) bipyridyl molecules makes it possible to obtain rather high photosensitivities, which exceed the $S_{0.1}$ of structurally similar metal–organic complexes of the same metals in a polymeric matrix [15], and apparently high carrier mobilities, which are attained because of the hopping of free carriers via aromatic nitrogen-containing molecules of bipyridyl.

4. CONCLUSIONS

Thus, it was shown that, with the silica matrix used, it is possible to obtain rather high photosensitivities for thin films of nanocomposites with metal–organic complexes, which exceed the values of $S_{0.1}$ for structurally similar complexes of the same metals in a polymeric matrix. The fact that an effective luminescence from nanocomposites in the silica matrix is observed and the spectral position of the band of this luminescence can be varied by selecting an appropriate metal atom [9] or a ligand structure (replacing bipyridyl with biquinolyl or phenanthroline, which are also capable of complexation with metals, etc.) gives reason to believe that not only photosensitive materials, but also electroluminescent devices can be developed on the basis of these nanocomposites.

REFERENCES

1. A. D. Pomogaĭlo, Usp. Khim. **69**, 60 (2000).
2. F. N. Castellano, T. A. Heimer, and G. J. Meyer, Chem. Mater. **6**, 1041 (1994).
3. K. Matsui and F. Momose, Chem. Mater. **9**, 2588 (1997).
4. F. Momose, K. Maedo, and K. Matsui, J. Non-Cryst. Solids **244**, 74 (1999).

5. V. I. Zemskiĭ, A. V. Veresov, and L. Yu. Kolesnikov, Pis'ma Zh. Tekh. Fiz. **20** (9), 74 (1994) [Tech. Phys. Lett. **20**, 374 (1994)].
6. M. Ahmat, N. Mohammad, and J. Abdullah, J. Non-Cryst. Solids **290**, 86 (2001).
7. Z. Peng, A. R. Charavi, and L. Yu, Appl. Phys. Lett. **69**, 4002 (1996).
8. S. C. Yu, X. Gong, and W. K. Chan, Macromolecules **31**, 5639 (1998).
9. E. L. Aleksandrova, M. E. Kompan, and N. N. Khimich, in *Abstracts of International Conference on Amorphous and Microcrystalline Semiconductors* (St. Petersburg, 2004), p. 194.
10. N. N. Khimich, B. I. Venzel', I. A. Drozdova, and L. A. Koptelova, Zh. Prikl. Khim. (St. Petersburg) **75**, 1125 (2002).
11. N. N. Khimich, E. L. Aleksandrova, V. Ya. Goĭkhman, and L. A. Koptelova, Fiz. Khim. Stekla **29**, 555 (2003) [Glass Phys. Chem. **29**, 401 (2003)].
12. N. N. Khimich, M. P. Semov, and L. F. Chepik, Dokl. Akad. Nauk **394** (1), 1 (2004).
13. E. L. Aleksandrova and Yu. A. Cherkasov, Opt. Spektrosk. **64**, 1047 (1988) [Opt. Spectrosc. **64**, 624 (1988)].
14. Y. Mori and K. Maeda, J. Chem. Soc., Perkin Trans. **2**, 1969 (1997).
15. E. L. Aleksandrova, M. Ya. Goĭkhman, V. V. Kudryavtsev, *et al.*, Opt. Zh. **68** (11), 67 (2001) [J. Opt. Technol. **68**, 849 (2001)]; Fiz. Tekh. Poluprovodn. (St. Petersburg) **37**, 846 (2003) [Semiconductors **37**, 818 (2003)].
16. R. D. Gillard and R. E. Hill, J. Chem. Soc. **11**, 1217 (1974).

Translated by M. Tagirdzhanov

Semiconductors, Vol. 38, No. 11, 2004, pp. 1284–1290. Translated from Fizika i Tekhnika Poluprovodnikov, Vol. 38, No. 11, 2004, pp. 1325–1331.

ELECTRONIC AND OPTICAL PROPERTIES OF SEMICONDUCTORS

A Mechanism of Charge-Carrier Photogeneration in Polyamidine Supramolecular Structures

E. L. Aleksandrova*, M. M Dudkina, and A. V. Ten'kovtsev****

**Ioffe Physicotechnical Institute, Russian Academy of Sciences, Politekhnicheskaya ul. 26, St. Petersburg, 194021 Russia*

e-mail: 15lab@hq.macro.ru

***Institute of Macromolecular Compounds, Russian Academy of Sciences, Bol'shoi proezd 31, St. Petersburg, 199004 Russia*

Submitted April 29, 2004; accepted for publication May 11, 2004

Abstract—The photophysical properties and mechanism of charge-carrier photogeneration in supramolecular polyamidine structures (which form, as was shown previously, a promising class of materials for photosensitive and electroluminescent devices) are studied. Based on the analysis of the spectral, field, temperature, and concentration behavior of changes in the photosensitive and luminescence properties, it is shown that the carrier photogeneration in the systems under investigation is described by the Pool–Frenkel model, which takes into account strong interactions and collective effects in the supramolecular system arising due to the formation of a regular network of hydrogen bonds between functional groups of a polymer. © *2004 MAIK "Nauka/Interperiodica".*

1. INTRODUCTION

In recent decades, polymers have been widely used in the development of optical recording media and semiconductor optoelectronic devices. The traditional approach to the synthesis of photoconductive polymer systems is based on either the introduction of photosensitive low-molecular compounds into a polymer matrix (formation of "guest–host" systems; these compounds exhibit donor–acceptor interaction and can form charge-transfer complexes (CTCs) with monomeric units of the polymer) or the formation of polymers with covalently bonded photoactive fragments in the main or lateral chain. The primary photophysical processes that occur in such systems after absorption of a photon and subsequent charge transfer in a complex are generally limited by the monomeric unit of the polymer, and the polymer structure affects the transport of a photon-induced carrier that forms a Coulomb pair and subsequent transport of free charge carriers.

However, it was suggested recently that photosensitive polymer systems can be obtained by forming supramolecular ensembles of photoactive components, which arise due to the existence of a system of regular hydrogen bonds between the fragments of macromolecules [1]. Then, this suggestion was confirmed experimentally for one of the classes of these polymers—polyamidines [2]. The formation of supramolecular ensembles changes the properties of the ground and excited states of individual particles, and the collective character of this process leads to the occurrence of new photophysical properties and specific features of primary photophysical processes (in particular, the appearance of new absorption bands, which are absent in the spectra of monomeric analogs), the mechanisms of photogeneration of charge carriers and their transport, and so on. Obviously, the formation of networks of hydrogen-bonded systems with fragments characterized by significant π conjugation gives rise (due to the intense charge transfer in the chains of their components, i.e.,macromolecules) to high mobilities of free charge carriers (about 10^{-4} cm^2/(V s) [3]) and high luminescence efficiency (on the same order of magnitude as that of polyphenylenevinylenes [4]), which makes these materials promising for various applications in optoelectronics.

The possibility of introducing (due to the formation of complexes) chromophore molecules, which have high luminescence quantum yields and nonlinear optical properties, into a polyamidine matrix makes it possible to expand and vary their photosensitivity range and the efficiency of photophysical processes, which is of interest for developing nonlinear optical materials and recording media (in particular, for dynamic holography) and electroluminescent devices based on these systems.

The purpose of this study is to gain insight into the nature of primary photophysical processes, in particular, the mechanism of carrier photogeneration in polyamidine supramolecular structures, including structures with introduced chromophore molecules, and reveal the specific features caused by the formation of supramolecular ensembles.

1063-7826/04/3811-1284$26.00 © 2004 MAIK "Nauka/Interperiodica"

2. OBJECTS OF STUDY

It is well known that polymers containing amidine groups in the main chain exhibit efficient two-center bonding with the formation of cyclic and linear supramolecular ensembles [5] (Figs. 1a, 1b), which leads to the occurrence of a quasi-conjugate system. In addition, the high basicity of amidine groups makes it possible to obtain ionic complexes of these polymers with both low-molecular compounds with donor or acceptor properties and introduced low-molecular compounds forming complexes through nonvalent bonding. This circumstance makes it possible to systematically change the photophysical properties of molecular ensembles due to the occurrence of charge transfer in the chains of the component macromolecules as a result of the formation of network hydrogen-bonded systems with fragments characterized by strong π conjugation.

We investigated a series of polyamidines with the general formula

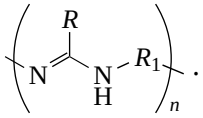

The above structures differ in both the structure of the main chain,

$$R_1 = (-CH_2-)_x, \quad x = 6, 7, 8, 10 \qquad \text{(I)}$$

or

$$R_1 = -C_6H_6-CH_2-C_6H_4-, \qquad \text{(II)}$$

and the type of substituents in the amidine fragment,

$$R = -CH_3 \qquad \text{(a)}$$

or

$$R = -C_6H_5. \qquad \text{(b)}$$

Hereinafter, we use the designations Ia and Ib for structures with a main chain of type I and substituents of types (a) and (b), respectively. Similar designations (IIa and IIb) are used for structures with a main chain of type II.

Polyamidines were synthesized by the conventional method [6]. These structures were chosen for the following reasons. On the one hand, they allow one to consider the relationship of the basicity and, respectively, the strength of hydrogen bonds both between amidine groups and between amidine groups and chromophore molecules with the photophysical properties of the complexes. On the other hand, the systematic increase in the number of π-conjugated fragments prone to the effect of π stacking, which leads to the transfer of an electron between noncovalent-bonded elements of the chain, makes it possible to determine the influence of this factor on the photoconductivity of the system as a whole.

Compounds with a developed π-conjugation chain that can form ionic bonds with polyamidine molecules

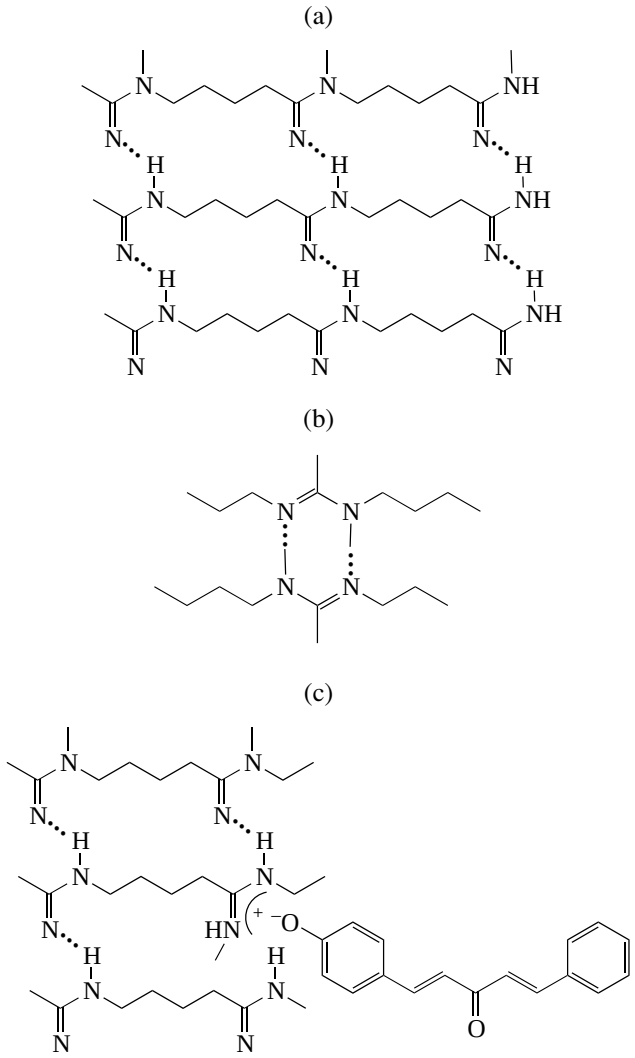

Fig. 1. Supramolecular (a) linear and (b) cyclic structures of polyamidines; (c) destruction of the structure as a result of the formation of a complex with a chromophore.

were used as chromophores introduced into the polymer matrix. The general formula of these compounds is

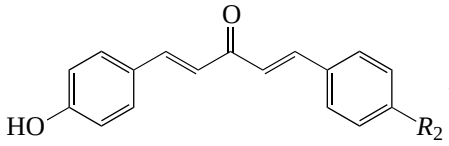

(III)

where R_2 = H, F, OCH_3, NO_2, $N(CH_3)_2$, OH, $NHCOCH_3$.

The energy of interaction between these compounds and the polymer matrix depends on the structure of the substituent R_2 and can be characterized their Hammet σ constants. These constants characterize the donor ($\sigma < 0$) or acceptor ($\sigma > 0$) character of the functional group. These compounds, which can form ionic bonds with polyamidines, were chosen because, according to the data of [7], their complexes with polydecamethylene-

acetamidine have a low Schottky barrier, which manifests itself in nonlinear optical effects of the second and third orders in these complexes [4]. It is noteworthy that the efficiency of the second-harmonic generation linearly increases as the donor properties of the substituent are enhanced (decreasing the values of σ).

As low-molecular compounds capable of nonvalent formation of complexes with polyamidines (a guest in the guest–host system), we used the molecules with strong donor or acceptor properties. As donors, we used nitrogen-containing molecules of indole, carbazole, and diphenylamine with low ionization potentials I_D (7.9, 7.4, and 7.1 eV, respectively [8]) and their analogs without a nitrogen atom (which plays an important role in the formation of complexes with aromatic polymers—phenanthrene and anthracene with I_D = 7.8 and 7.3 eV, respectively [8]). Fullerene molecules (C_{60} : C_{70} = 87 : 13) were used as acceptors. The content of the introduced compounds was 1 mol %.

Complexes of polymers were obtained by mixing polyamidine solutions with solutions of the noted compounds in ethanol. The thus obtained solutions were poured onto a rotating substrate (glass with an In_2O_3(Sn) (ITO) coating, 3000 rpm, 30 s) to form films with their subsequent drying in vacuum at room temperature to constant mass. The film thickness was in the range 1–5 μm.

3. MEASURING TECHNIQUE

The photosensitivity $S_{0.1}$ and the quantum yield of carrier photogeneration η were determined in the electrophotographic mode [9, 10]. The measurements were carried out in the equienergy spectrum with an average photon-flux density of 10^{13} cm^{-2} s^{-1} in the spectral range 400–900 nm at an electric field strength E = (0.2–1.0)E_0, where E_0 is the limiting field strength for this material in the temperature range T = 300–420 K, i.e., above and below the glass-transition temperatures of the polymers T_{gl}. Samples were heated by passing an electric current through the ITO layer on the substrate (which is necessary for measurements in the electrophotographic mode). Temperature was measured with an accuracy of about 1% by liquid-crystal indicators.

The complete collection of the charge carriers photogenerated in the polymer layer was monitored by the "photogeneration-wedge" method [11] and by measuring the field dependences of the quantum yield $\eta/\varepsilon = f(V/d)$ for layers of thickness d in the range 1–5 μm (where ε is the permittivity). The error in measuring $S_{0.1}$ and η was 10%.

The absorption spectra were measured on a Perkin-Elmer spectrophotometer in the wavelength range 400–1200 nm. The spectra obtained were used to determine the optical energy gap ΔE_G^{opt} (the band gap) according to [12].

The photosensitivity $S_{0.1}$ was determined by the criterion of the decrease in the surface potential of a layer by 10% with respect to the initial value ($\Delta V/V$ = 0.1) as a quantity inverse to the exposure necessary to attain a critical change in the surface potential. The total photosensitivity $S_{0.1}$ was determined by the same criterion ($\Delta V/V$ = 0.1) for illumination of layers by a KGM-300 halogen lamp with a power of 300 W.

The value of permittivity, which is necessary for the calculation, was estimated from the slopes of the field dependences of the quantum yield $\eta(E)$ and the carrier mobility $\mu(E)$, according to the Pool–Frenkel model ($d\eta(E)/dE = (e^2/4\pi\varepsilon\varepsilon_0)^{1/2}$ [9]), and the ultimate potentials of the layer charging, as well as by comparing the data on ε obtained for aliphatic and aromatic polymers [13]. The activation energy of photogeneration W_a was determined from the slopes of the temperature dependence $\eta(T)$, and the field dependences $\eta(E)$ were used to determine (according to the Onsager model) the thermalization length $r_t \approx 1/W_a$ [10].

4. RESULTS AND DISCUSSION

Investigation of the dark characteristics of polymers at temperatures below the glass-transition temperature showed almost complete absence of dark conductivity for all objects under investigation (the resistance was about 10^{13} Ω cm^{-2}). However, after heating to temperatures above T_{gl}, the resistance decreased significantly (to 10^9 Ω cm^{-2}). Measurements of the electronic absorption spectra of the polymer films under study, $\alpha(\lambda)$, showed that the intrinsic absorption edge of the polymers, $\hbar\omega$, lies in the range 350–420 nm. It is noteworthy that the energies $\hbar\omega$ and ΔE_G^{opt} correlate with the degree of π conjugation in a polymer, which manifests itself in the bathochromic shift of the absorption band and the energy of the optical band gap ΔE_G^{opt} in the Ia–Ib–IIa–IIb series (see table). In addition, weak long-wavelength bands peaked at 505–510 and 635–640 nm for Ia and at 490–525 and 750–850 nm for IIb are observed in the spectra $\alpha(\lambda)$ beyond the intrinsic-absorption region. These bands are absent in the spectra of the polymer solutions in ethanol. These bands can be assigned to the forbidden transitions in the quasi-conjugate system of hydrogen-bonded amidine groups (Fig. 1) (this system cannot exist in solutions of proton-donor solvents, in particular, ethanol). This suggestion is confirmed by the calculations of electronic spectra of a trimer of the model compound—N,N'-dimethylacetamidine—by the ZINDO/S method with optimization of the geometric characteristics by the *ab initio* STO-3G method. According to these calculations, the prohibition of the transition at 420 nm is removed in this case.

As the analysis of the photosensitivity spectra $S_{0.1}(\lambda)$ showed [2], the value of $S_{0.1}$ steadily decreases from 2×10^4 to 3×10^3 cm^2/J with increasing λ from 400 to 950 nm. In this case, the total photosensitivity is equal to 0.03–0.08 (lx s)$^{-1}$ and is independent of the number of methylene units x in the main chain of the

Photophysical characteristic of the polymers under study and their complexes

Polymer or complex	ΔE_G^{opt}, eV	$T < T_{gl}$						$T > T_{gl}$	
		Absorption $\hbar\omega_{max}$, eV	Luminescence $\hbar\omega_{max}$, eV	I/I_0	$S_{0.1}/(S_{0.1})_0$	ε	η, %	ε	η, %
Ia	3.3	5.86	2.98	1.0	1.0	3.2–3.3	4.5	3.1–3.3	4.5
Ib	3.2	5.01	2.95	1.25	0.85	3.3–3.5	4.8	3.1–3.3	4.5
IIa	3.0	3.86	2.48	3.0	2.3	4.1–4.3	8.6	2.8–3.0	<0.1
IIb	2.7	4.10	2.48	0.75	4.0	4.2–4.5	9.4	2.8–3.0	≤0.03
Ia + III (R = OH)	2.71	2.54	2.45	3.5	0.75	3.5–4.0	3.4	–	–
Ia + III (R = OCH_3)	2.59	2.45	2.03	–	0.6	3.5–4.0	2.9	–	–

polymer I. When a chromophore is introduced, the photosensitivity increases in the chromophore absorption region (at 450–550 nm) due to the increase in the absorption.

The spectrum of the quantum yield of carrier photogeneration η(λ) shows that the quantum yield is almost constant (only weakly depends on λ) in the visible spectral range (Fig. 2) and steadily decreases in the long-wavelength region: at λ > 750 nm for Ia and Ib (curves *1*, *2*) and at λ > 620 nm for IIa and IIb (curves *3*, *4*). The introduction of chromophores into Ia leads to a decrease in η by a factor of 2–2.5 (curve *5*). For the monomeric analog (N,N'-didecylacetamidine), unlike the spectra considered above, there is no region with a constant quantum yield and η begins to decrease at λ = 400 nm (curve *6*). For all the polymers under study, the found values of activation energies are 0.1–0.2 eV, which corresponds to thermalization lengths (calculated within the Onsager model for ε = 3) of 2–3 nm. However, the strong interaction between amidine groups and the presence of collective effects cast doubt on the validity of the Onsager model for the systems under investigation because the Onsager model assumes that the absorbing centers—monomeric units (for most polymers)—are noninteracting and retain their individuality (which manifests itself, in particular, in the insignificant difference between the spectrum of a polymer and the spectrum of its monomeric analog) [9, 12, 14]. Most likely, polyamidines can be adequately described by the Pool–Frenkel model, which considers the escape of a bound carrier from a Coulomb center as a result of overcoming the potential barrier reduced by 0.1–0.2 eV by an applied external electric field. After the carrier becomes free at a distance of about 15 nm, it begins to move over the network of alternating single and double bonds (similar to the structure of polyphenylenevinylene) formed by the arising supramolecular structure.

As was shown previously [1, 2], the photosensitivity and quantum yield η systematically increase in the Ia(x = 10)–Ia(x = 6)–Ib–IIb–IIa series, whereas the positions and the intensity of the luminescence bands of the objects studied are determined not so much by the chemical structure of the monomeric unit of a polymer and the π-conjugation length [4] as the cooperative absorption and emission of the ensemble of supramolecular structures with a π–*n*–H-conjugation system, which arise during the ordering of the system caused by the formation of a network of hydrogen bonds between nitrogen-containing functional groups.

We should also note the significant dependence of the photosensitivity of the polymers under study on the thermal history of the samples. At temperatures above the glass-transition temperature, the dielectric properties (ε) and photosensitivity ($S_{0.1}$) of polymers Ia and Ib hardly change, whereas a relative decrease in ε by a factor of almost 2 for polymer IIb and a significant decrease in η are observed for polymer IIa (see table). It is likely that the noted features are related to the decrease in the basicity of polymers in the Ia–Ib–IIb–IIa series. This circumstance leads to a weakening of intermolecular hydrogen bonds and the degradation of the supramolecular structure, which is responsible for the occurrence of photoconductivity.

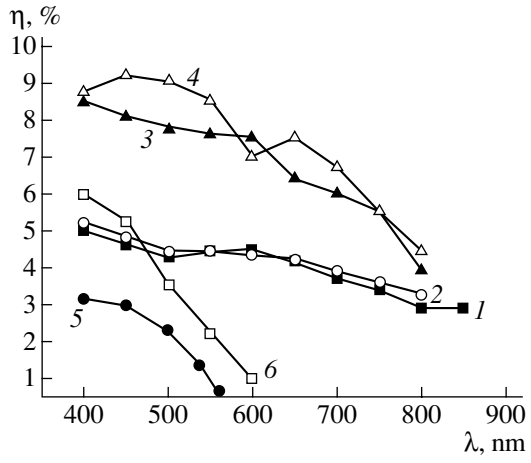

Fig. 2. Spectra of the quantum yield of carrier photogeneration η for polyamidines of different structure: (*1*) Ia, (*2*) Ib, (*3*) IIa, (*4*) IIb, (*5*) Ia+ III (R = OH), and (*6*) N,N'-didecylacetamidine.

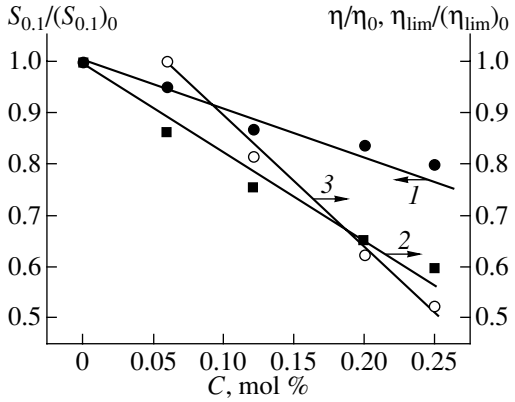

Fig. 3. Dependences of the (*1*) photosensitivity $S_{0.1}$ and quantum yields of (*2*) photogeneration η and (*3*) luminescence η_{lum} on the concentration of III in the Ia + III (R = OCH_3) complex; $I_0 = 9.445 \times 10^{22}$ s^{-1}.

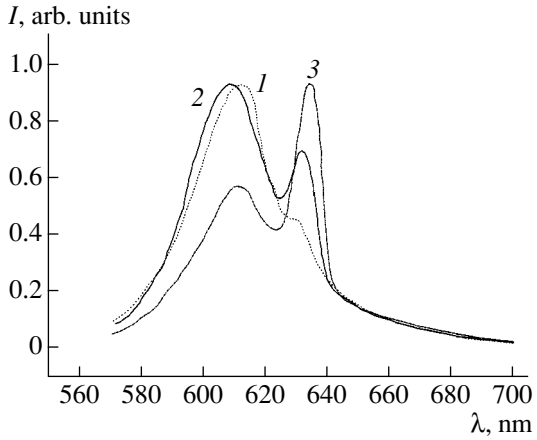

Fig. 4. Luminescence spectra of the Ia+ III (R = OCH_3) complex for different chromophore concentrations: (*1*) 1, (*2*) 5, and (*3*) 10 mol %.

As can be seen from the data listed in the table, the values of both the quantum yield η and $S_{0.1}$ increase in going from aliphatic polyacetamidines to aromatic benzamidines, which could be explained by the enhanced π conjugation. However, above the glass-transition temperature (under conditions corresponding to the destruction of the supramolecular structure), the value of η drops for polymers containing aromatic groups, remaining almost constant for aliphatic polyamidines. This fact indicates that the increase in the degree of conjugation due to the introduction of aromatic groups is not a major factor leading to the occurrence of photosensitivity. We can suggest that such behavior is related to a change in the system of hydrogen bonds and the transformation of the linear structures responsible for carrier transport (Fig. 1a) into cyclic structures (Fig. 1b), which govern the photosensitivity of the system.

The decisive role of the supramolecular organization of the system is confirmed by the significant decrease in the photosensitivity of polyamidines caused by the introduction of chromophores. Specifically, the photosensitivity of the Ia + III (R = OH) system decreases by a factor of 1.7. In this case, the acidity of the introduced admixture is sufficient for the protonation of the amidine groups of the polymer, which leads to the destruction of the system of hydrogen bonds and, accordingly, to quasi-conjugation in the supramolecular system (Fig. 1c). This is also confirmed by the fact that, with an increase in the relative chromophore concentration, a steady decrease in the photosensitivity and quantum yield is observed (Fig. 3, curves *1* and *2*, respectively). The decrease in the photosensitivity with increasing concentration correlates with the decrease in the luminescence quantum yield η_{lum} in the Ia+ III (R = OCH_3) system (Fig. 3, curve *3*). Note that, with an increase in the chromophore concentration, the intensity of the chromophore luminescence is redistributed between the short- and long-wavelength bands (Fig. 4). Apparently, this phenomenon is due to the specific features of chromophores of the dibenzalidenealkanone class, for which the long-wavelength absorption peak is associated with the π–π^* rather than the n–π transition, which occurs in the well-studied carbazolyl-containing polymers [14]. As is well known [9, 14], the photogeneration quantum yield of polymers is independent of the concentration of absorbing centers (chromophores in the case under study). The observed concentration dependences of the photophysical processes also indicate that both competing processes—carrier photogeneration and the release of the photoexcitation energy—are not related to the polyamidine monomeric unit but are controlled by the supramolecular structure of the ensemble of polymer chains.

This is also confirmed by the results of studying the effect of the donor–acceptor properties of the substituent R_2 in a chromophore (which are characterized by the Hammet σ constants) on the photosensitivity (Fig. 5a). It can be seen that S correlates with the σ constants of the substituent in III. It should be noted that, when polyamidines are exposed to light with a wavelength corresponding to the region of intrinsic absorption of chromophore ions (Fig. 5a, curve *1*), the dependence $S(\sigma)$ correlates with the dependence of the efficiency of the third harmonic generation on the same parameter [7], whereas, at λ = 600 nm (which corresponds to the absorption of supramolecular ensembles), the dependence $S(\sigma)$ demonstrates antibatic behavior (Fig. 5a, straight line *2*). The regularities established confirm that the increase in the degree of conjugation in a chromophore leads to a decrease in the carrier photogeneration efficiency.

The introduction of fullerene C_{60} (which is known [8] as an efficient acceptor capable of forming nonvalent complexes) as a dopant into a polymer matrix leads to a significant (by a factor of 5) increase in the dark conductivity and a twofold decrease in the photosensitivity of the polymers Ia and IIa. Such behavior of the systems under study is indicative of the predominantly

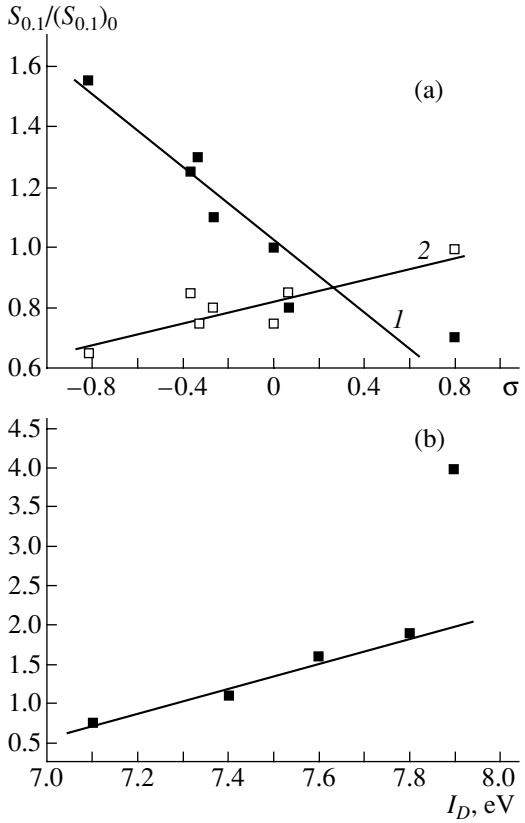

Fig. 5. Dependences of the photosensitivity $S_{0.1}$ at λ = (*1*) 500 and (*2*) 600 nm on the (a) σ constants of the substituent in the compound III and (b) the ionization potential I_D of the introduced low-molecular donor.

acceptor character of the functional groups of polyamidines.

The use of indole (a typical representative of donors prone to nonvalent complex formation) as a low-molecular admixture leads to an increase in the photosensitivity of the Ia + indole system by a factor of 5 (Fig. 5b). At the same time, the introduction of a nitrogen-free representative of this class of low-molecular donors—anthracene—into a polymer does not change its photophysical properties. Obviously, this difference is due to the different features of interaction of admixture molecules with fragments of the polymer matrix. When anthracene is used as an admixture, the absorption spectrum of the composite is a superposition of the spectra of polyamidine and anthracene, whereas the introduction of indole leads to the appearance of a new absorption band at 400–480 nm in the spectrum of the composite. The introduction of carbazole and diphenylamine results in the appearance of a broad (up to 600 nm) band. The appearance of such bands, whose position depends on the ionization potential I_D of the donor molecule, indicates the formation of a complex (specifically, polymer–indole). It is likely that the formation of the complex is facilitated by the presence of NH groups in the indole molecule that are capable of forming hydrogen bonds with functional groups of the polymer. Thus, the introduction of low-molecular impurities exhibiting donor–acceptor interaction with monomeric fragments of polyamidines does not play a key role in the photogeneration, as occurs in the sensitization of most aromatic polymers [9, 10, 14]. The introduction of such polymers into polyamidines leads to an increase in the photosensitivity by several orders of magnitude with a significant red shift of the photosensitivity region [10].

The data on the behavior of the changes in the photophysical properties of polyamidines and their sensitization by chromophores show that the mechanism of photogeneration in polyamidines differs from that typical of most polymers and confirm our suggestion that the Pool–Frenkel model is valid for supramolecular systems in the stage of carrier photogeneration and the subsequent transport of free carriers over the network of alternating single and double bonds formed by the supramolecular structure.

5. CONCLUSIONS

Thus, we may conclude that the proposed approach to the development of photosensitive polymer systems, based on the formation of supramolecular structures originating from the ordered network of hydrogen bonds between functional groups of the polymer chain, is an efficient method for preparing photoconductive media with a high photosensitivity ($\geq 10^4$ cm^2/J). Taking into account the rather high values of carrier mobility and luminescence efficiency at low glass-transition temperatures, modulus elasticity, and melt viscosity, we believe that such systems are promising for the development of photosensitive and transport layers of electrophotographic devices and thermoplastic materials for recording media.

REFERENCES

1. J.-M. Lehn, *Supramolecular Chemistry: Concepts and Perspectives* (VCH, Weinheim, 1995; Nauka, Novosibirsk, 1998).
2. E. L. Aleksandrova, M. M. Dudkina, and A. V. Ten'kovtsev, Fiz. Tekh. Poluprovodn. (St. Petersburg) **37**, 282 (2003) [Semiconductors **37**, 266 (2003)].
3. E. L. Aleksandrova, L. P. Kazakova, M. M. Dudkina, and A. V. Ten'kovtsev, *Abstracts of II International Conference on Amorphous and Microcrystalline Semiconductors* (Fiz.–Tekh. Inst., St. Petersburg, 2002), p. 107.
4. E. L. Aleksandrova, M. E. Kompan, A. V. Ten'kovtsev, and M. M. Dudkina, Fiz. Tekh. Poluprovodn. (St. Petersburg) **38**, 1110 (2004) [Semiconductors **38**, 1074 (2004)].
5. F. Böehme, C. Klinger, H. Komber, *et al.*, J. Polym. Sci. **36**, 929 (1997).

6. A. V. Tenkovtsev, A. V. Yakimansky, M. M. Dudkina, *et al.*, Macromolecules **34**, 7100 (2001).
7. A. V. Ten'kovtsev, M. M. Dudkina, A. E. Trofimov, *et al.*, Zh. Prikl. Khim. (St. Petersburg) **74**, 1147 (2001).
8. L. V. Gurvich, G. V. Karachentsev, V. N. Kondrat'ev, Yu. A. Lebedev, V. A. Medvedev, V. K. Potapov, and Yu. S. Khodeev, *Energies of Chemical Bond Breaking. Ionization Potentials and Electron Affinity*, Ed. by V. N. Kondrat'ev (Nauka, Moscow, 1974) [in Russian].
9. I. A. Akimov, Yu. A. Cherkasov, and M. I. Cherkashin, *Sensitized Photoeffect* (Nauka, Moscow, 1980) [in Russian].
10. E. L. Aleksandrova and Yu. A. Cherkasov, Opt. Spektrosk. **64**, 1047 (1988) [Opt. Spectrosc. **64**, 624 (1988)].
11. E. L. Aleksandrova and Yu. A. Cherkasov, Zh. Nauchn. Prikl. Fotogr. Kinematogr. **31** (1), 61 (1986).
12. É. A. Silin'sh, M. V. Kurik, and V. Chapek, *Electronic Processes in Organic Molecular Crystals* (Zinatne, Riga, 1988), p. 195 [in Russian].
13. A. R. Eleva and L. G. Zherdeva, in *Abstracts of III All-Union Conference on Unusual Photographic Processes* (Kiev. Gos. Univ., Kiev, 1972), p. 47.
14. A. V. Vannikov and A. D. Grishina, *Photochemistry of Polymer Donor–Acceptor Complexes* (Nauka, Moscow, 1984) [in Russian].

Translated by Yu. Sin'kov

Semiconductors, Vol. 38, No. 11, 2004, pp. 1291–1297. Translated from Fizika i Tekhnika Poluprovodnikov, Vol. 38, No. 11, 2004, pp. 1332–1338.

SEMICONDUCTOR STRUCTURES, INTERFACES, AND SURFACES

Photosensitive Structures Based on $HgGa_2S_4$ Single Crystals: Preparation and Properties

V. Yu. Rud'*^, Yu. V. Rud', B. Kh. Baĭramov**, G. A. Il'chuk***, V. O. Ukrainets***, N. Fernelius****, and P. G. Shunemann*****

**Ioffe Physicotechnical Institute, Russian Academy of Sciences, Politekhnicheskaya ul. 26, St. Petersburg, 194021 Russia*
^e-mail: rudvas@spbstu.ru
***St. Petersburg State Technical University, ul. Politekhnicheskaya 29, St. Petersburg, 195251 Russia*
****National University Lvivska Politekhnika, Lviv, 79013 Ukraine*
*****Wright Laboratory, Wright-Patterson AFB, 45433 Ohio, USA*
******Lockheed Sanders, Nashua, 03061 New Hampshire, USA*
Submitted February 18, 2004; accepted for publication March 26, 2004

Abstract—Photosensitive structures based on *n*-$HgGa_2S_4$ single crystals were prepared and investigated. It was concluded that $HgGa_2S_4$ crystals are promising for the fabrication of photodetectors of natural and linearly polarized light in the short-wavelength spectral region. © *2004 MAIK "Nauka/Interperiodica".*

Mercury thiogallate $HgGa_2S_4$ belongs to ternary semiconductor compounds of the $A^{II}B_2^{III}C_4^{VI}$ type, where A^{II} is Zn, Cd, or Hg; B^{III} is B, Ga, or In; and C^{VI} is S, Se, or Te. Although these semiconductors have not been adequately studied, they are increasingly of interest for application in solid-state electronics and nonlinear optics [1–4] because their fundamental properties can be controlled by changing the nature and positional ordering of the component atoms. In this paper, we report the results of the first investigations of the electrical properties and optical absorption of homogeneous *n*-$HgGa_2S_4$ single crystals, the preparation of new photosensitive structures based on them, and the study of photoelectric processes in these structures.

1. The research was carried out with $HgGa_2S_4$ single crystals grown by planar crystallization from a stoichiometric melt of mercury thiogallate under conditions of an ultralow temperature gradient (T/l = 1–3 K/cm) along the crucible containing the compound and rates of motion of the crystallization front of 0.1–0.3 K/h [5]. The single crystals obtained under different processing conditions showed a homogeneous light orange color when exposed to white light. They are described by the space group S_4^2 (typical of $A^{II}B_2^{III}C_4^{VI}$ compounds) and their unit-cell parameters are consistent with the data in the literature [6].

2. According to the sign of thermopower, all nominally undoped crystals grown by planar crystallization had *n*-type conductivity. It is noteworthy that, as for most $A^{II}B_2^{III}C_4^{VI}$ compounds, the conductivity type of $HgGa_2S_4$ cannot be controlled by changing the crystallization conditions, which is related to the features of the defect structure of ternary semiconductors of this type [1].

The samples for measuring the kinetic coefficients were limited in size (no larger than $0.6 \times 0.9 \times 4$ mm^3). Hall measurements showed that the growth technique we used makes it possible to obtain single crystals with a rather low concentration of free electrons (n = 10^8–10^9 cm^{-3}) and high resistivity (ρ = 10^9–10^{10} Ω cm) at $T \cong 300$ K; the sign of the Hall coefficient indicates that the majority carriers are electrons.

Figure 1 (curve *1*) shows a typical temperature dependence of the resistivity of one of the *n*-$HgGa_2S_4$ samples in the range from room to liquid-nitrogen temperature. It can be seen that the resistivity of *n*-$HgGa_2S_4$ single crystals obeys the Arrhenius law in a wide temperature range (which is typical of semiconductors):

$$\rho = \rho_0 \exp\left(-\frac{E}{kT}\right). \quad (1)$$

Here, E is the activation energy, k is the Boltzmann constant, and T is the sample temperature. The activation energy of the resistivity of the crystals grown found from the dependences $\rho(T)$ was E = 37–40 meV, which is much lower than the band gap of $HgGa_2S_4$ ($E_G \cong$ 2.8 eV) [6]. In this case, the Arrhenius law (Fig. 1, curve *1*) may be related to the excitation of electrons from donor levels to the conduction band (on the assumption of high compensation of donors by acceptors [7]). Note that such shallow-level centers have not been observed in $A^{II}B_2^{III}C_4^{VI}$ compounds until now. Hence, we may conclude that the study of $HgGa_2S_4$ single crystals made it possible to obtain important experimental proof that shallow levels of lattice defects may

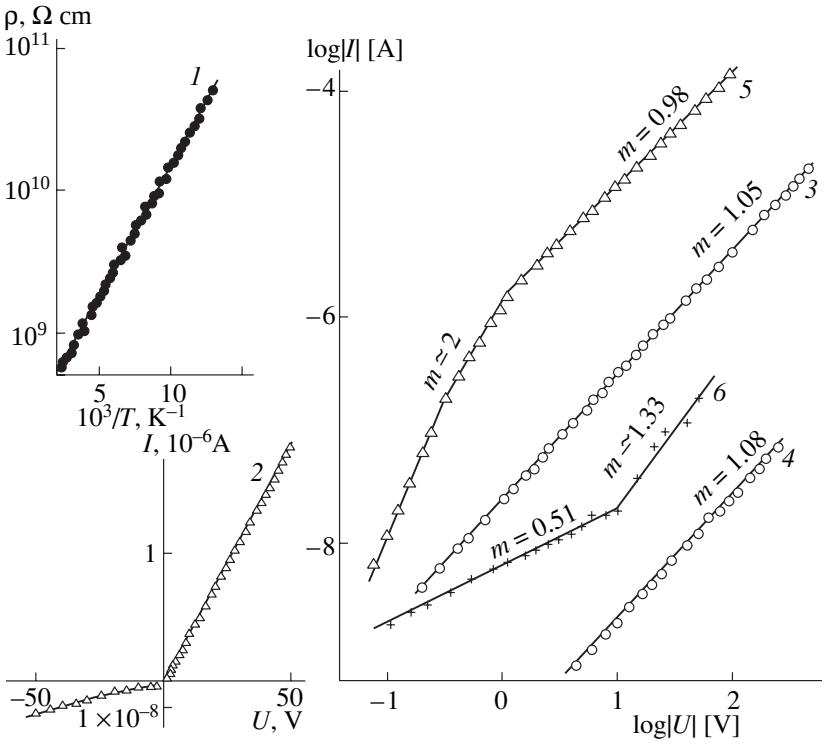

Fig. 1. Temperature dependence of the resistivity of a *n*-$HgGa_2S_4$ single crystal (curve *1*, sample 7*n*), the steady-state current–voltage characteristic of an In–*n*-$HgGa_2S_4$ surface-barrier structure (curve *2*, sample 17*n*), the steady-state (curves *3*, *4*) and optical (curves *5*, *6*) current–voltage characteristics of an In–*n*-$HgGa_2S_4$ surface-barrier structure (sample 17*n*) in the logarithmic coordinates $\log|I|$–$\log|U|$ at $T = 300$ K at a (*3*, *5*) forward and (*4*, *6*) reverse bias. The values of the exponent *m* are indicated for curves *3*–*6*. Positive polarity of the barrier contact corresponds to the forward direction. Illumination from the barrier contact; the light intensity is about 1 mW/cm^2.

exist in crystals of ternary compounds of the $A^{II}B_2^{III}C_4^{VI}$ group.

3. Measurements of current–voltage (*I*–*V*) characteristics of contacts formed by vacuum deposition or chemical deposition of some pure metals showed for the first time that In [2], Au, and Ag layers on cleaved or mechanically and chemically treated surfaces of electrically homogeneous *n*-$HgGa_2S_4$ crystals exhibit pronounced rectification. Figure 1 (curve *2*) shows the steady-state *I*–*V* characteristic of one of the surface-barrier In–*n*-$HgGa_2S_4$ structures of the highest quality. The rectification coefficient, which is the ratio of the forward to reverse current at fixed biases $|U| \approx 20$ V is as high as $K \approx 200$ for the structures of highest quality. Small sizes of available crystals impede further improvement of the quality of the peripheral area of such structures. In our opinion, increasing the sizes of the single crystals will make it possible to obtain significantly higher values of *K* compared to those cited in this paper.

The initial portions ($U < 1$ V) of the forward steady-state *I*–*V* characteristics ($T = 300$ K) of the In–*n*-$HgGa_2S_4$ and Ag–*n*-$HgGa_2S_4$ surface-barrier structures obey the well-known diode equation. The diode factor for such structures turned out to be rather high ($\beta \approx 10$), whereas, when the structures are illuminated from the side of the barrier contact, its value drops to $\beta \approx 2$. We believe that the high value of $\beta \approx 10$ indicates a tunneling-recombination mechanism of the forward current, whereas, under illumination, the recombination mechanism is dominant ($\beta \approx 2$).

In a wide range of forward biases (0.1–500 V), the power dependence $I \propto U^m$ is observed. The exponent *m* is close to unity (Fig. 1, curve *3*), which indicates either the tunneling of charge carriers or current limitation by the space charge in the velocity-saturation mode. According to [8, 9], the current density in this case can be written as

$$J = \frac{2\varepsilon\varepsilon_0 v_s A}{L^2} U, \qquad (2)$$

where ε and ε_0 are the permittivities of the semiconductor and free space, respectively; v_s is the saturation velocity; *A* is the area of the structure; and *L* is the thickness of the $HgGa_2S_4$ wafer.

The reverse steady-state *I*–*V* characteristic, as can be seen from Fig. 1 (curve *4*), also follows a power law and its exponent *m* almost coincides with the value characteristic of the forward current. This circumstance

suggests that a change in the direction of current does not affect its nature.

It can also be clearly seen from Fig. 1 (curves *5*, *6*) that the forward and reverse currents increase by 1.5–2 orders of magnitude under illumination from the barrier contact. In this case, a portion described by a quadratic law arises in the power dependence of the forward current on bias in the range $0.2 < U < 1$ V (Fig. 1, curve *5*). This feature indicates the possible presence of currents limited by the space charge in the mobility mode:

$$J = \frac{9\varepsilon\varepsilon_0\mu A}{8L^3}V^2, \quad (3)$$

where μ is the electron mobility in $HgGa_2S_4$. The forward current at $U > 1$ V is characterized by the exponent $m \approx 1$, as in the absence of illumination. Therefore, the mechanism of the forward-current transport at $U >$ 1 V turns out to be insensitive to the photogeneration of charge carriers.

For illuminated structures, the dependence of the reverse current on bias retains a power character. However, the presence of photogenerated charge carriers changes the exponent as follows: $m \approx 0.5$ at biases $U <$ 10 V, while at $U > 10$ V, the exponent becomes as high as $m \approx 1.33$. The increase in m at $U > 10$ V can be explained by the increase in the contribution of currents limited by the space charge in the mobility mode (trapless quadratic law) [8, 9].

The illumination of In–*n*-$HgGa_2S_4$ and Ag–$HgGa_2S_4$ surface-barrier structures gives rise to the photoelectric effect. As a rule, the open-circuit photoelectric voltage is dominant in these structures under their illumination from the barrier contact, which, under these conditions, acquires a negative charge and retains its sign with changes in the photon energy, the light intensity, and the location of the light probe (0.2 mm in diameter) on the surface. The sign of the photoelectric voltage is consistent with the direction of rectification. Therefore, the rectification and photoelectric effect in such structures should be attributed to the energy barrier formed at the contact of $HgGa_2S_4$ with In and Ag.

Some parameters of the structures obtained are listed in the table. It can be seen from the table that the highest photovoltaic sensitivity of the surface-barrier structures is $S_u^m \approx 2100$ V/W, which significantly exceeds the result of [2].

The typical spectral dependences of the relative quantum photoconversion efficiency $\eta(\hbar\omega)$ of a surface-barrier structure and the optical absorption coefficient of a $HgGa_2S_4$ crystal for exposure to unpolarized light at $T = 300$ K are shown in Fig. 2. It can be seen that, in the structures of highest quality illuminated from the barrier contact, photosensitivity is observed in a wide spectral range (from 0.9 to 3.6 eV) (Fig. 2, curve *1*). Its value changes within four to five orders of magnitude and is peaked in the region of photon energies $\hbar\omega^m = 3$–3.6 eV, which, according to [1, 6], corresponds to the fundamental absorption band of $HgGa_2S_4$. When such a structure is illuminated from the side of the substrate at $\hbar\omega > 2.25$ eV, a drop in η is observed in the short-wavelength region of the spectrum $\eta(\hbar\omega)$ (Fig. 2, curve *2*). This drop is consistent with the beginning of the sharp increase in the optical absorption coefficient α of the $HgGa_2S_4$ crystal (Fig. 2, curve *3*) on which the surface-barrier structure was formed. Figure 2 (curve *3*) demonstrates that the sharp increase in α occurs specifically at a photon energy of $\hbar\omega \geq 2.3$ eV, which can be considered a preliminary estimate of the band gap width E_G of the ternary compound $HgGa_2S_4$. In this case, the observed decrease in

Photoelectric properties of the structures based on *n*-$HgGa_2S_4$ single crystals at $T = 300$ K

Structure	$\hbar\omega^m$, eV	δ, eV	S_u^m, V/W	P_N^m, %
In–$HgGa_2S_4$	3.05–3.65	>0.8	2100	–40
Ag–$HgGa_2S_4$	2.1	0.55	35	–16
pr–$HgGa_2S_4$	3.06–3.27	>0.6	2900	–38
H_2O–$HgGa_2S_4$	3.0–3.3	>0.6	15000	–48

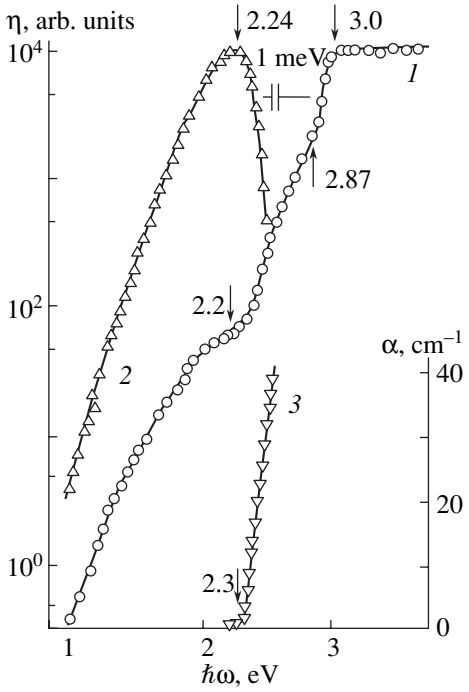

Fig. 2. Spectra $\eta(\hbar\omega)$ of an In–*n*-$HgGa_2S_4$ structure (sample *17*; curves *1*, *2*) and $\alpha(\hbar\omega)$ (curve *3*) of an *n*-$HgGa_2S_4$ single crystal (sample *17-1*, $0.64 \times 2.1 \times 4.3$ mm^3 in size) at $T = 300$ K. Geometric conditions of illumination: (*1*) from the barrier contact and (*2*) from the substrate (substrate thickness $d \approx 0.64$ mm).

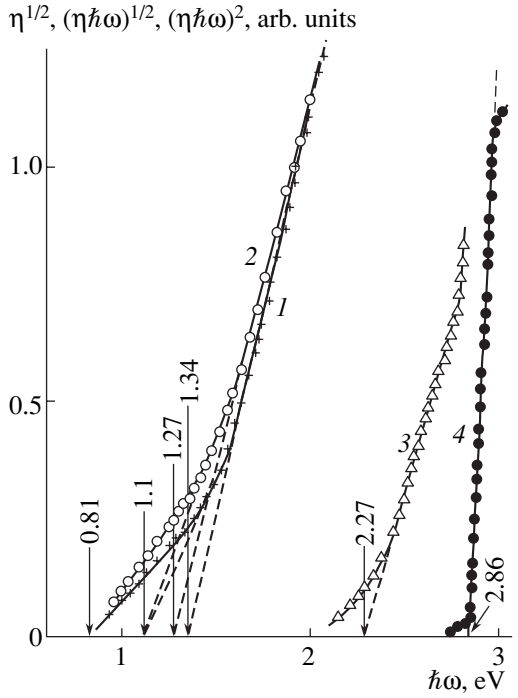

Fig. 3. Spectral dependence of the relative quantum efficiency of photoconversion of (*1*, *3*, *4*) In–*n*-$HgGa_2S_4$ and (*2*) Ag–*n*-$HgGa_2S_4$ structures in the coordinates (*1*, *2*) $\eta^{1/2}$–$\hbar\omega$, (*3*) $(\eta\hbar\omega)^{1/2}$–$\hbar\omega$, and (*4*) $(\eta\hbar\omega)^2$–$\hbar\omega$. Illumination from the barrier contact. The values of cutoff energies for the corresponding curves are indicated by arrows (T = 300 K). Samples (*1*, *3*, *4*) *17* and (*2*) *17-4*.

η (Fig. 2, curve *2*) can be attributed to the increase in α in the $HgGa_2S_4$ substrate. As a result of this increase, the region of the carrier photogeneration becomes more and more removed from the active region of the structure with increasing α to be finally located in the thin surface layer of the semiconductor. We may suggest that, due to the small diffusion displacement in $HgGa_2S_4$ crystals, the concentration of photogenerated carriers that reach the active region rapidly decreases at $\hbar\omega \geq 2.3$ eV and, as a result, the photosensitivity decreases as well.

It can also be seen from Fig. 2 that the spectra $\eta(\hbar\omega)$ at $\hbar\omega < 2.2$ eV are almost insensitive to the geometric parameters of illumination of the surface-barrier structure (Fig. 2, curves *1*, *2*), which is due to the bulk character of the carrier photogeneration in $HgGa_2S_4$ crystals.

The long-wavelength edge of the photosensitivity spectra of the surface-barrier structures ($\hbar\omega < 2.2$ eV) obeys the Fowler law, which represents a linear dependence in the coordinates $\eta^{1/2}$–$\hbar\omega$ (Fig. 3, curve *1*). This fact makes it possible to relate the long-wavelength photosensitivity of the In–$HgGa_2S_4$ and Ag–$HgGa_2S_4$ structures to the emission of photoelectrons from the metal to the semiconductor. The heights of the surface potential barrier estimated from these dependences are $\varphi_B \cong 1.35$ and 1.27 eV for indium and silver, respectively, at T = 300 K. It is noteworthy that, for some energy barriers obtained by plotting the dependences $\eta^{1/2}$–$\hbar\omega$, several slopes were observed, which can be attributed to the complexity of the energy spectrum of $HgGa_2S_4$ crystals.

The increase in the photosensitivity of the surface-barrier structures of highest quality at $\hbar\omega > 2.3$ eV under illumination from the barrier contact (Fig. 2, curve *1*) may be related to the interband optical absorption in $HgGa_2S_4$ crystals. We failed to detect this absorption in such small crystals by conventional absorption spectroscopy (Fig. 2). It can be seen from Fig. 3 (curve *3*) that, in the range of photon energies 2.3–2.8 eV, the spectral dependence of the photosensitivity follows a linear law in the coordinates $(\eta\hbar\omega)^{1/2}$–$\hbar\omega$. On the basis of the existing theory of interband absorption in semiconductors [10], the extrapolation $(\eta\hbar\omega)^{1/2} \longrightarrow 0$ makes it possible to determine the energy of indirect interband optical transitions E_G^{in} in ≈2.27 eV for *n*-$HgGa_2S_4$ crystals at T = 300 K. The sharper increase in the photosensitivity in the surface-barrier structures at $\hbar\omega > 2.8$ eV (Fig. 3, curve *1*) obeys the quadratic law ($(\eta\hbar\omega)^2$–$\hbar\omega$), which is characteristic of direct interband transitions, and the extrapolation $(\eta\hbar\omega)^2 \longrightarrow 0$ makes it possible to determine the energy of direct interband transitions in *n*-$HgGa_2S_4$ crystals: $E_G^{\text{dir}} \approx 2.86$ eV at T = 300 K. This value is in agreement with the data of [6].

The large total width of the spectra $\eta(\hbar\omega)$ at half-height $\delta > 0.8$ eV for the In–$HgGa_2S_4$ structures (see table) indicates their fairly high quality with respect to the recombination processes. At the same time, the drop in the photosensitivity at $\hbar\omega < 3$ eV indicates the possibility of using such structures as photodetectors operating in the short-wavelength spectral region and insensitive to long-wavelength radiation ($\lambda > 0.44$ eV).

4. We also studied the possibility of preparing photosensitive structures based on a direct contact of natural protein with the surface of a *n*-$HgGa_2S_4$ single crystal. The technique of preparation of structures composed of a semiconductor wafer and a protein (*pr*) layer with thickness $d \approx 0.1$ mm is similar to that used by us previously [11]. A layer of molybdenum (d = 2–4 μm) deposited on a glass plate was generally used as a current-collecting contact.

All the *pr*–*n*-$HgGa_2S_4$ structures we obtained showed rectifying characteristics ($K \approx 5$ at $U \approx 10$ V and T = 300 K). The forward direction is implemented at positive polarity of the external voltage on the Mo layer, which is in direct contact with the protein. Illumination of the *pr*–*n*-$HgGa_2S_4$ heterocontacts is accompanied by the appearance of a photovoltage, the sign of which is in agreement with the direction of rectification. The conservation of the photovoltage sign as the photon energy changes in the entire range of photosensi-

tivity and the position of the light probe on the surface of the structure give grounds to believe that the photovoltaic effect is controlled by the separation of photogenerated pairs by the only active region formed near the heterocontact between the semiconductor and protein.

Illumination of *pr*–*n*-$HgGa_2S_4$ structures from the protein layer gave rise to the highest photosensitivity: $S_u^m \approx 2900$ V/W, which is significantly higher than for In–$HgGa_2S_4$ surface-barrier structures (see table). It is also important that the photosensitivity of *pr*–*n*-$HgGa_2S_4$ structures shows no degradation phenomena, as for structures of the same type on compound diamond-like substances [11].

A typical spectral dependence of the relative quantum photoconversion efficiency for one of the *pr*–$HgGa_2S_4$ structures exposed to unpolarized light from the protein layer is shown in Fig. 4 (curve *1*). The spectral profile $\eta(\hbar\omega)$ and its features are similar to those observed for the In–$HgGa_2S_4$ solid-state structures of highest quality (Fig. 2, curve *1*). The long-wavelength falloff at $\hbar\omega < 2.3$ eV is, apparently, controlled by the photoactive absorption at the levels of lattice defects in *n*-$HgGa_2S_4$ crystals.

5. We also investigated for the first time the photosensitivity of the contact of an electrolyte (using H_2O as an example) with the surface of an *n*-$HgGa_2S_4$ single crystal. The technique of preparation of the structures was the same as in [12]. A platinum-wire mesh (with a wire diameter of 0.05 mm) was used as a counterelectrode. In the absence of illumination, the photoelectrochemical cells obtained show a pronounced diode characteristic ($K \approx 10^2$ at U = 10–20 V). No signs of degradation were observed for the H_2O–$HgGa_2S_4$ cells.

Figure 4 (curve *2*) shows a typical spectral dependence of the relative quantum efficiency of photoconversion for an H_2O–*n*-$HgGa_2S_4$ cell. It can be seen that the photosensitivity of such structures is dominant in the intrinsic-absorption region of $HgGa_2S_4$, attaining maximum values at $\hbar\omega^m \approx 3$ eV. H_2O–$HgGa_2S_4$ cells make it possible to obtain the highest (in comparison with the other types of structures) photovoltaic sensitivity: $S_u^m \approx 1.5 \times 10^4$ V/W at T = 300 K. This value is much higher than that for the solid-state surface-barrier structures (see table).

It should also be noted that analysis of the spectra $\eta(\hbar\omega)$ of the *pr*–$HgGa_2S_4$ and H_2O–$HgGa_2S_4$ structures in the fundamental-absorption region of $HgGa_2S_4$ yields the same values of E_G^{in} and E_G^{dir} for $HgGa_2S_4$ as for the In–$HgGa_2S_4$ structures (Fig. 3, curves *3*, *4*).

6. Since $HgGa_2S_4$ crystals are anisotropic (space group S_4^2) and characterized by strong tetragonal compression $\tau = 1 - c/2a \approx 7\%$, one might expect natural photopleochroism to appear in photosensitive structures based on them [13]. Therefore, photosensitive

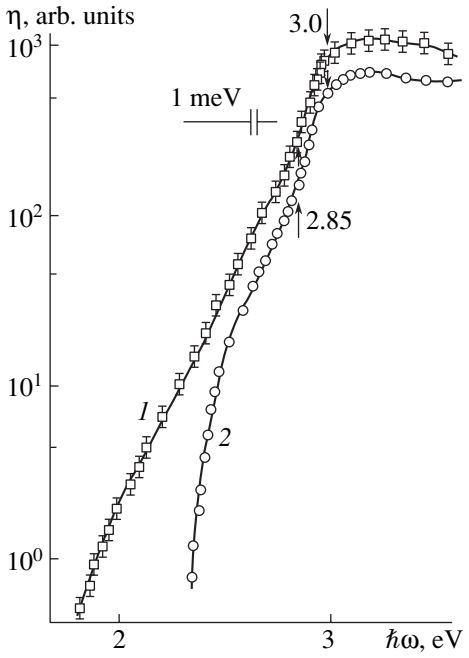

Fig. 4. Spectral dependences of the relative quantum efficiency of photoconversion of *pr*–*n*-$HgGa_2S_4$ (curve *1*, sample *17-5*) and H_2O–*n*-$HgGa_2S_4$ (curve *2*, sample *17-2*) structures in unpolarized light at T = 300 K. To exclude superpositions, the spectra are shifted relative to each other along the ordinate axis.

structures were deliberately formed on *n*-$HgGa_2S_4$ wafers of two crystallographic orientations of the photodetection plane: (100) and (001). It was found that, when linearly polarized light propagates perpendicularly to the illuminated (001) plane of the In–$HgGa_2S_4$, *pr*–$HgGa_2S_4$, and H_2O–$HgGa_2S_4$ structures, the photocurrent is independent of the spatial orientation of the electric field vector of the light wave, whereas for the (100) photodetection plane, the photocurrent through the above structures obeys Malus's law [13], which corresponds to the space group S_4^2.

Figure 5 shows typical spectral dependences of the relative quantum efficiency of photoconversion of the *pr*–$HgGa_2S_4$ structure for two polarizations of light: $\mathbf{E} \parallel \mathbf{c}$ and $\mathbf{E} \perp \mathbf{c}$, where $\mathbf{c}$ is the unit vector directed along the tetragonal axis of the crystal. As can be seen from Fig. 5 (curves *1*, *2*), with an increase in the photon energy, the sign of the polarization difference of the quantum efficiency $\Delta\eta = \eta^{\parallel} - \eta^{\perp}$ changes. Here, the symbols $\parallel$ and $\perp$ indicate the orientation of $\mathbf{E}$ with respect to $\mathbf{c}$ ($\mathbf{E} \parallel \mathbf{c}$ and $\mathbf{E} \perp \mathbf{c}$) for the normal incidence of light on a $HgGa_2S_4$(100) crystal. For example, for photon energies of up to $\hbar\omega \approx 2.3$ eV, the inequality $\eta^{\parallel} > \eta^{\perp}$ is valid for *pr*–$HgGa_2S_4$ structures; therefore, the sign of $\Delta\eta$ is positive. Then, at a particular photon energy (specific for each structure), the polarization difference $\Delta\eta$ becomes zero (the photoisotropic point), after which it remains negative in the entire short-wave-

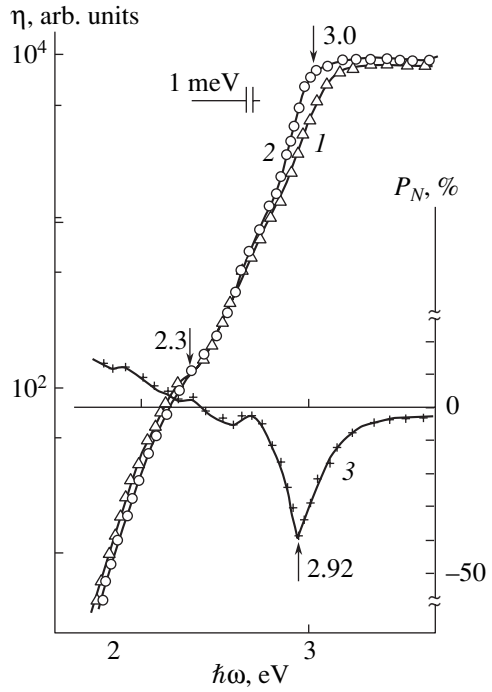

Fig. 5. Spectral dependences of the relative quantum efficiency of photoconversion of a *pr*–*n*-$HgGa_2S_4$ structure at $T = 300$ K ((*1*) **E** ∥ **c** and (*2*) **E** ⊥ **c**) and the natural-photopleochroism coefficient (*3*). Illumination in the direction perpendicular to the plane of the protein layer, which is in contact with the $HgGa_2S_4$(100) single crystal.

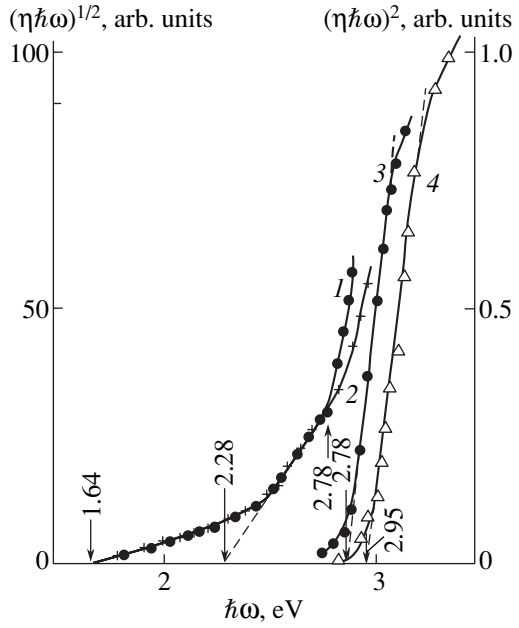

Fig. 6. Dependences $(\eta^{\parallel,\perp}\hbar\omega)^{1/2}$–$\hbar\omega$ ((*1*) **E** ⊥ **c** and (*2*) **E** ∥ **c**) and $(\eta^{\parallel,\perp}\hbar\omega)^2$–$\hbar\omega$ ((*3*) **E** ⊥ **c** and (*4*) **E** ∥ **c**)) for a *pr*–*n*-$HgGa_2S_4$ structure at $T = 300$ K.

length region of photosensitivity (2.4–3.7 eV). This behavior was observed for all three types of structures under consideration, which gives additional grounds for attributing this behavior to the absorption processes in $HgGa_2S_4$.

Analysis of the spectra $\eta(\hbar\omega)$ of the *pr*–*n*-$HgGa_2S_4$ structure exposed to polarized light (Fig. 6) in the context of the theory of interband optical absorption in semiconductors [10] shows that the dependences $(\eta^{\parallel,\perp}\hbar\omega)^{1/2}$–$\hbar\omega$, which are characteristic of indirect optical transitions, only slightly depend on polarization and, therefore, their extrapolation $(\eta^{\parallel,\perp}\hbar\omega)^{1/2}$–$\hbar\omega \longrightarrow 0$ yields a similar value of E_G^{in} for both polarizations (≅2.28 eV), which was also obtained when the same structures were exposed to unpolarized light. With an increase in the photon energy ($\hbar\omega > 2.8$ eV), a polarization dependence arises in the spectra $\eta(\hbar\omega)$, for which $\Delta\eta = \eta^{\parallel} - \eta^{\perp} < 0$. The change in the polarization from **E** ⊥ **c** and **E** ∥ **c** is accompanied by an almost simultaneous blue shift of the spectral dependence $\eta(\hbar\omega)$ (Fig. 5, curves *1*, *2*). The spectral dependences $\eta^{\parallel,\perp}(\hbar\omega)$, as follows from Fig. 6 (curves *3*, *4*), are flattened in the coordinates $(\eta^{\parallel,\perp}\hbar\omega)^2$–$\hbar\omega$. As a result, the direct energy gap $E_G^{\text{dir}} \approx 2.87$ eV for the polarization **E** ⊥ **c**, and, in going to the polarization **E** ∥ **c**, it increases by ~80 meV: $E_G^{\text{dir}} \approx 2.95$ eV at $T = 300$ K. Unfortunately, the energy-band spectrum of $HgGa_2S_4$ has not been calculated [14, 15]. Therefore, more a detailed analysis of the polarization dependences of the photosensitivity cannot yet give definitive results.

The typical spectral dependence of the natural photopleochroism coefficient [13]

$$P_N = (\eta^{\parallel} - \eta^{\perp})/(\eta^{\parallel} + \eta^{\perp}) \qquad (4)$$

for *pr*–*n*-$HgGa_2S_4$ structures is shown in Fig. 5 (curve *3*). It follows from this dependence that the sign of the coefficient P_N is positive only in the region of impurity absorption in $HgGa_2S_4$ at $\hbar\omega < 2.3$ eV. Its inversion occurs in going to the short-wavelength spectral region ($\hbar\omega > 2.5$ eV). The highest coefficient of negative photopleochroism is obtained near the energy of direct interband optical transitions, as for pseudodirect-gap ternary $A^{II}B^{IV}C_2^V$ semiconductors with a chalcopyrite structure [16].

7. Thus, based on single crystals of the ternary compound $HgGa_2S_4$, we prepared for the first time photosensitive heterocontacts between a natural protein and semiconductor and photosensitive photoelectrochemical cells. In addition, the characteristics of surface-barrier structures based on $HgGa_2S_4$ were significantly improved. The physical properties of $HgGa_2S_4$ single crystals and several types of photosensitive structures based on them were investigated. Natural photopleochroism was found and studied in $HgGa_2S_4$-based pho-

tosensitive structures. The perspectives for applying the new semiconductor in the development of photodetectors of natural and linearly polarized light in the short-wavelength spectral range were outlined.

ACKNOWLEDGMENTS

This study was supported by the International Science and Technology Center, grant no. 2008.

REFERENCES

1. A. N. Georgobiani, S. I. Radautsan, and N. M. Tiginyanu, Fiz. Tekh. Poluprovodn. (Leningrad) **19**, 193 (1985) [Sov. Phys. Semicond. **19**, 121 (1985)].
2. V. Yu. Rud', Yu. V. Rud', M. C. Ohmer, and P. G. Schunemann, Fiz. Tekh. Poluprovodn. (St. Petersburg) **33**, 1217 (1999) [Semiconductors **33**, 1108 (1999)].
3. P. C. Ricci, A. Aneda, R. Corping, *et al.*, in *Abstracts of 13th International Conference on Ternary and Multinary Compounds* (Paris, 2002), p. 189.
4. M. C. Ohmer and R. Pandey, MRS Bull. **23**, 16 (1998).
5. P. G. Schunemann and T. M. Pollak, MRS Bull. **23**, 23 (1998).
6. *Physicochemical Properties of Semiconductors*, Ed. by A. V. Novoselova, V. B. Lazarev, Z. S. Medvedeva, N. P. Luzhina, and A. A. Levin (Nauka, Moscow, 1978) [in Russian].
7. J. S. Blakemore, *Semiconductor Statistics* (Pergamon, Oxford, 1962; Mir, Moscow, 1964).
8. E. Hernandez, Cryst. Res. Technol. **33**, 285 (1998).
9. M. A. Lampert and P. Mark, *Current Injection in Solids* (Academic, New York, 1970; Mir, Moscow, 1973).
10. S. Sze, *Physics of Semiconductor Devices*, 2nd ed. (Wiley, New York, 1981; Mir, Moscow, 1984).
11. Yu. V. Rud', V. Yu. Rud', I. V. Bodnar', *et al.*, Fiz. Tekh. Poluprovodn. (St. Petersburg) **33**, 1201 (1999) [Semiconductors **33**, 1093 (1999)].
12. V. Yu. Rud', Yu. V. Rud', and M. Serginov, Phys. Status Solidi A **121**, K171 (1990).
13. F. P. Kesamanly, V. Yu. Rud', and Yu. V. Rud', Fiz. Tekh. Poluprovodn. (St. Petersburg) **33**, 513 (1999) [Semiconductors **33**, 483 (1999)].
14. V. L. Panyutin, B. É. Ponedel'nikov, A. É. Rozenson, and V. I. Chizhikov, Izv. Vyssh. Uchebn. Zaved., Fiz. **22** (8), 57 (1979).
15. F. M. Gashimzade, D. A. Guseĭnova, and V. Ya. Shteĭnshraĭber, Preprint No. 21, IF AN AzSSR (Inst. of Physics, Academy of Sciences of Azerbaijan, Baku, 1980).
16. Yu. V. Rud', Izv. Vyssh. Uchebn. Zaved., Fiz. **29** (8), 68 (1986).

Translated by Yu. Sin'kov

Semiconductors, Vol. 38, No. 11, 2004, pp. 1298–1301. Translated from Fizika i Tekhnika Poluprovodnikov, Vol. 38, No. 11, 2004, pp. 1339–1342.

SEMICONDUCTOR STRUCTURES, INTERFACES, AND SURFACES

Effect of Modifying a Bi Nanolayer on the Charge Transport in Sb–*n*-Si–Bi–$Ge_{33}As_{12}Se_{55}$–Sb Heterostructures

A. B. Kondrat^, N. I. Popovich, and N. I. Dovgoshej

Uzhgorod National University, Uzhgorod, 88000 Ukraine

^e-mail: moshenec@rambler.ru

Submitted February 24, 2004; accepted for publication February 26, 2004

Abstract—The current–voltage characteristics of the Sb–*n*-Si–$Ge_{33}As_{12}Se_{55}$–Sb and Sb–*n*-Si–Bi–$Ge_{33}As_{12}Se_{55}$–Sb heterostructures are studied. It is found that the presence of bismuth atoms in the transition region causes the current through the structure to increase. The width of the space-charge region and, correspondingly, the extent of penetration of the contact field into the *p*-type region are in the range from 0.2 to 0.5 μm. The introduction of a modifying bismuth layer also leads to radical changes in the current–voltage characteristic, which indicates that the mechanism of the charge-carrier transport in the structure is changed. The introduction of the Bi nanolayer leads to the transformation of an abrupt heterojunction into a gradient heterojunction. A soft breakdown is not observed in the structures with the modified transition layer. The soft breakdown is observed at a reverse bias; the cutoff voltage of ~0.62 V corresponds to the barrier height of 0.65 eV for electrons. © *2004 MAIK "Nauka/Interperiodica".*

1. INTRODUCTION

At present, a search is under way to find new film–crystal combinations with the aim of developing heterostructures with new functional capabilities, as well as heterostructures with a higher radiation resistance. Some of the studies concerned with these types of heterostructures were performed using films of binary chalcogenide vitreous semiconductor compounds. The use of these compounds widens the range of combinations of heterostructure pairs that consist of an amorphous film and a crystal. The choice of the Sb–*n*-Si–$Ge_{33}As_{12}Se_{55}$–Sb heterostructure as the object of study is motivated by the results of calculating the threshold of photoemission for the glasses of a GeAsSe system. This analysis shows that the offset of the conduction band for this heterostructure is close to zero. In addition, $Ge_{33}As_{12}Se_{55}$ films are used as optical coatings in infrared electronics due to their transparency in the wavelength range 1–12 μm and their stability against the impact of aggressive media. These films were also used to reduce the reverse currents in silicon-based diode structures [1].

One of the differences between homojunctions and heterojunctions consists in the fact that a transition layer forms at the interface between different semiconductors in a heterojunction. These layers have a considerable effect on the characteristics of heterojuctions, generally degrading them. The formation of the transition layer depends on the technological conditions of fabrication of the structures. One way of improving the properties of the heterostructure is to modify the transition layer, e.g., by introducing a small amount of impurity into the interface region. The choice of material for modification is crucial. We considered the use of bismuth as the modifier. It is well known that bismuth exhibits the largest diffusion coefficient among metals and can also induce conductivity-type conversion in chalcogenide vitreous semiconductors [2]. The modification of the transition region in the *p*-Si–$Ge_{33}As_{12}Se_{55}$ heterostructure using the metals Cu, Pb, Sb, In, and Bi was studied previously [3]. The modification of the transition region using Bi atoms yields the largest value of the rectification factor; however, in that case, one serious disadvantage is the appearance of soft breakdown at reverse bias voltages.

The effect of the transition layer on the electrical properties of the *n*-Si–$Ge_{33}As_{12}Se_{55}$ heterojunction has not been adequately studied. Therefore, the objective of this study was to gain insight into the effect of modifying the transition layer on the electrical properties of a heterostructure that consists of *n*-Si and a $Ge_{33}As_{12}Se_{55}$ amorphous film.

2. EXPERIMENTAL

Sputtering-assisted deposition of $Ge_{33}As_{12}Se_{55}$ amorphous films onto silicon substrates was carried out in a VUP-5M setup. The $Ge_{33}As_{12}Se_{55}$ glasses were evaporated from quasi-closed evaporators (Knudsen cell) made of a thin ($d < 0.1$ μm) tantalum foil [4]. In order to satisfy the conditions for effusive evaporation of material, we chose the following relation between the effective area of orifices S_1 and the total area S_0 of the cell:

$$100S_1 < S_0. \quad (1)$$

In order to study the current–voltage (*I–V*) characteristics of experimental samples, we applied alternat-

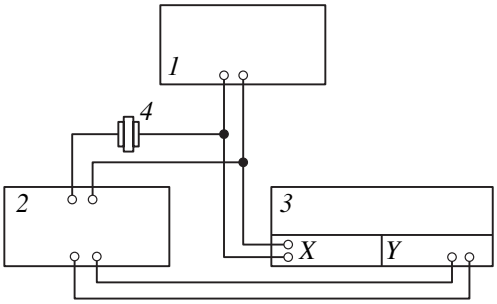

Fig. 1. Block diagram of the setup for measuring the *I–V* characteristics of experimental samples: (*1*) G6-15 generator of special-form signals, (*2*) U5-9 amplifier, (*3*) N307/1 *x–y* recorder, and (*4*) the sample under study.

ing voltage in the form of triangular pulses to the structure under study. This voltage was generated by a signal generator and was recorded using a chart recorder. The signal generator made it possible to vary both the repetition frequency and the amplitude of the pulses. Separate points in the *I–V* characteristics were formed using a constant-voltage source, a voltmeter, and an amplifier. The voltage was measured within the range from 0.001 to 5 V with an error of 2%, while the current was measured in the range from 10^{-13} to 10^{-4} A with an error of 3%. A schematic diagram of the setup for measuring the *I–V* characteristics is shown in Fig. 1.

3. RESULTS AND DISCUSSION

In Fig. 2, we show the *I–V* characteristics of a Sb–*n*-Si–$Ge_{33}As_{12}Se_{55}$–Sb structure (a) without modification of the transition layer and (b) with the transition layer modified by Bi atoms (i.e., in the latter case, we have the Sb–*n*-Si–Bi–$Ge_{33}As_{12}Se_{55}$–Sb structure). The thickness of the $Ge_{33}As_{12}Se_{55}$ film was 0.2 μm. The reason for choosing Sb as the material for electrodes was the fact that Sb forms injecting contacts with both the $Ge_{33}As_{12}Se_{55}$ film and *n*-Si [5–8]. The choice of bismuth as the modifier is based on the fact that Bi can convert the *p*-type conductivity of a chalcogenide vitreous semiconductor into *n*-type conductivity [2]. In order to clarify the effect of the Sb–*n*-Si–Bi structure on the properties of the heterojunction in general, we studied the *I–V* characteristics of this structure (Fig. 3). It is evident that the effect of this structure is not significant; the Bi nanolayer indeed plays the role of the modifier.

As can be seen from Fig. 2, bismuth causes the current through the structure to increase, which can be attributed partially to a decrease in the effective thickness of the high-resistivity $Ge_{33}As_{12}Se_{55}$ film and a decrease in the thickness (or complete disappearance) of the SiO_2 layer at the Si surface as a result of Bi diffusion. The introduction of a modifying Bi layer also has a significant effect on the shape of the *I–V* characteristic, which may indicate that the mechanism of the

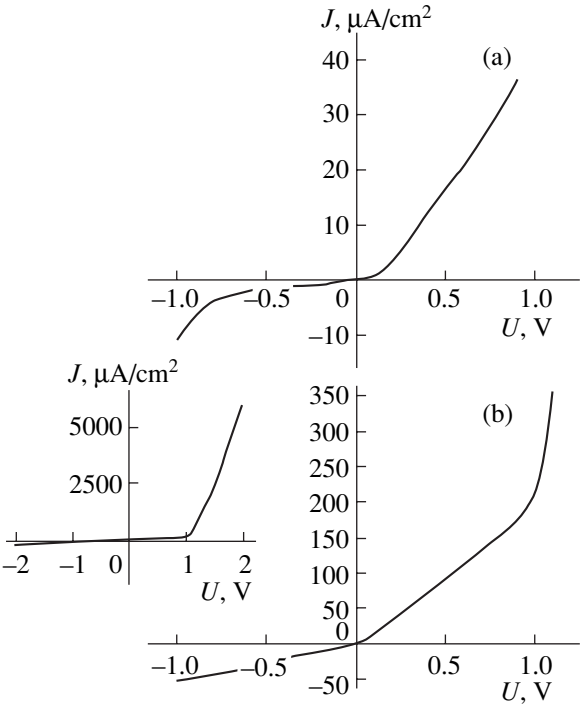

Fig. 2. Current–voltage characteristics of the Sb–*n*-Si–$Ge_{33}As_{12}Se_{55}$–Sb structure with positive voltage applied to Si (the thickness of the $Ge_{33}As_{12}Se_{55}$ film is 0.2 μm) (a) without modification of the transition layer and (b) with a modified transition layer (on different scales).

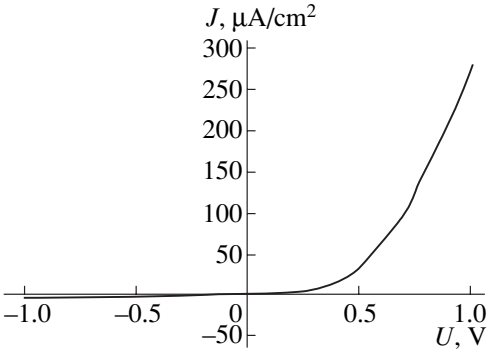

Fig. 3. *I–V* characteristic of the Sb–*n*-Si–Bi structure with a positive bias voltage applied to Bi.

charge-carrier transport in the structure under study changes.

Since Bi has a large diffusion coefficient, the actual thickness of the $Ge_{33}As_{12}Se_{55}$ film in the structure with a modified transition layer is smaller than that without a Bi layer. Therefore, we studied the Sb–*n*-Si–Bi–$Ge_{33}As_{12}Se_{55}$–Sb structures with an 0.5-μm-thick $Ge_{33}As_{12}Se_{55}$ film. The *I–V* characteristic of this structure is shown in Fig. 4. The available published data on the diffusion coefficients of metals in chalcogenide vitreous semiconductors are lacking; therefore, we could

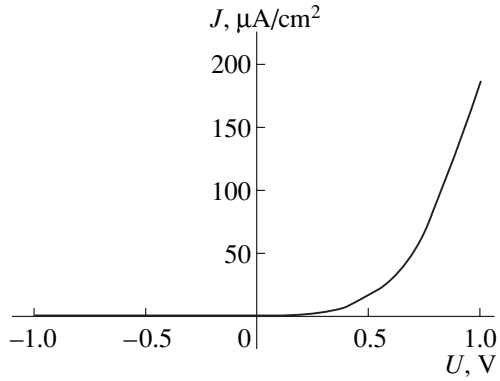

Fig. 4. *I–V* characteristic of a Sb–*n*-Si–Bi–$Ge_{33}As_{12}Se_{55}$–Sb with a positive bias voltage applied to Bi. The thickness of the $Ge_{33}As_{12}Se_{55}$ film is 0.5 μm.

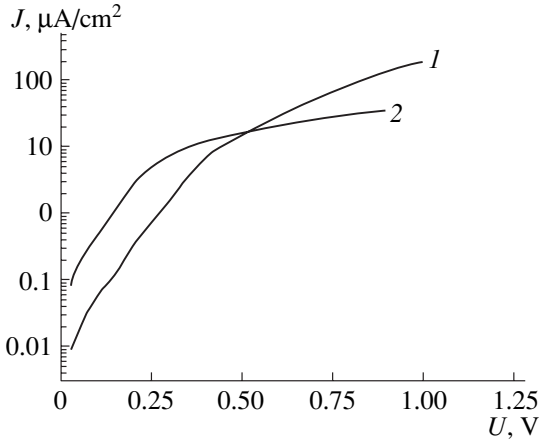

Fig. 5. Positive portions of *I–V* characteristics plotted on the semilogarithmic scale for (*1*) the Sb–*n*-Si–Bi–$Ge_{33}As_{12}Se_{55}$–Sb structure and (*2*) the Sb–*n*-Si–$Ge_{33}As_{12}Se_{55}$–Sb structure. The thickness of the $Ge_{33}As_{12}Se_{55}$ film is 0.2 μm.

not calculate accurately the depth of penetration of Bi into the $Ge_{33}As_{12}Se_{55}$ film.

The differences between the *I–V* characteristics of the Sb–*n*-Si–Bi–$Ge_{33}As_{12}Se_{55}$–Sb structures with $Ge_{33}As_{12}Se_{55}$ films with different values of thickness can be interpreted in the following way. It is well known that the rectification factor depends on the film thickness [9], which is caused by the position of the space-charge region in the film. The rectification factor attains a maximum in the situation where the entire space charge caused by the contact potential difference is located within the thickness of the film. As the thickness of the film increases further, the series resistance of the junction increases and limits the forward current; as a result, the rectification factor decreases.

Rectification factors in the structures under study at a voltage of 0.3 V

Structure	Thickness of the $Ge_{33}As_{12}Se_{55}$ film, μm	Rectification factor
Sb–*n*-Si–$Ge_{33}As_{12}Se_{55}$–Sb	0.2	7
Sb–*n*-Si–Bi–$Ge_{33}As_{12}Se_{55}$–Sb	0.2*	2.7
Sb–*n*-Si–Bi–$Ge_{33}As_{12}Se_{55}$–Sb	0.5*	82.4

Note: An asterisk indicates that the correction for Bi diffusion is introduced.

On analyzing the *I–V* characteristics (Figs. 2b, 4) and rectification factors (see table), we may conclude that the width of the space-charge region (and, accordingly, the extent of penetration of the contact field into the *p*-type region) is in the range 0.2–0.5 μm with correction for the Bi diffusion. If the thickness of the $Ge_{33}As_{12}Se_{55}$ film is equal to 0.2 μm, the rectification factor is smaller than that for a 0.5-μm-thick film. Consequently, we may state that, in the former case, the thickness of the film is not sufficient to accommodate the entire space charge. The forward current in the heterostructures with a 0.5-μm-thick $Ge_{33}As_{12}Se_{55}$ film is lower than that in the heterostructures with a 0.2-μm-thick film. Thus, the film thickness in the former case is larger than the width of the space-charge region; i.e., we may take $d \approx 0.4$ μm as the extent of penetration of the contact field into the *p*-type region of the heterojunction.

This fact is inconsistent with the theory that disregards the transition regions in heterojunctions. According to this theory, the calculated thickness of the space-charge region in a $Ge_{33}As_{12}Se_{55}$ film is $W_1 = 2.74$ nm in the absence of an external field. The discrepancy is attributed to the presence of a transition layer, in particular, the nonuniformity of the layer of the $Ge_{33}As_{12}Se_{55}$ film with a thickness on the order of several tens of nanometers and the presence of a SiO_2 silicon-oxide layer with a thickness of 5–10 nm on the silicon surface. In addition, introducing a bismuth nanolayer transforms an abrupt heterojunction into a gradient heterojunction in the structure under study.

In Fig. 5, we show the *I–V* characteristics of the structures under study using the semilogarithmic scale. In this case, an exponential voltage dependence of the current is observed. This dependence can be approximated using the following expression:

$$I = I_{01}\exp(\beta_1 U) + I_{02}\exp(\beta_2 U). \qquad (2)$$

It is important that the coefficient β_1 is the same for both curves, whereas the coefficient β_2 is different for each of the curves. It is also worth noting that the ohmic portion at small values of applied positive voltage is not observed in the *I–V* characteristics of the structures (Fig. 2a, 4). This circumstance indicates that there is no barrier at the interface between silicon and the film of a chalcogenide vitreous semiconductor.

For a Sb–*n*-Si–Bi–$Ge_{33}As_{12}Se_{55}$–Sb structure with a 0.2-μm-thick $Ge_{33}As_{12}Se_{55}$ film, the *I–V* characteristics are linearized in logarithmic (rather than semilogarith-

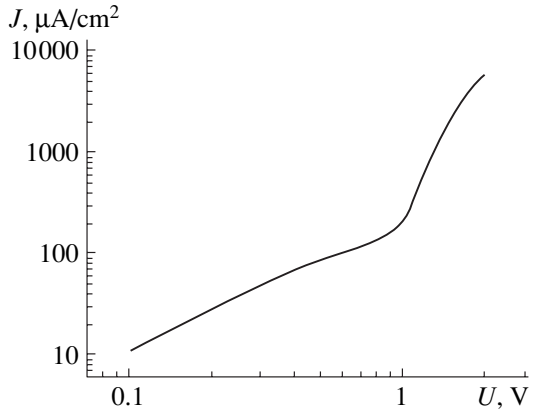

Fig. 6. Positive portion of the *I–V* characteristic for a Sb–*n*-Si–Bi–$Ge_{33}As_{12}Se_{55}$–Sb structure; the log–log scale is used. The thickness of the $Ge_{33}As_{12}Se_{55}$ film is 0.2 μm.

mic) coordinates (Fig. 6); i.e., a power-law dependence of the current on the voltage $I \propto V^m$ is observed. Several portions of the characteristic with different values of m can be distinguished. The dependence under consideration is characteristic of heterojunctions with a high-resistivity layer at the interface [9]. In order to interpret these results, we can use the theory of currents limited by the space charge in the case of monopolar injection [9, 10].

In modifying the transition region, an interesting and useful feature is the absence of soft breakdown in the structures with a modified transition layer (Figs. 2, 4), which improves the characteristics of the heterojunction. The absence of soft breakdown can also be attributed to the elimination of electrons from the charge transport when the transition region is modified by a bismuth nanolayer. Soft breakdown is observed at reverse bias voltages; a cutoff voltage of ~0.62 V (Fig. 2a) corresponds to a barrier height of 0.65 eV for electrons.

4. CONCLUSIONS

(i) We developed a method for modifying the transition layer in the *n*-Si–$Ge_{33}As_{12}Se_{55}$ heterostructure using bismuth atoms.

(ii) It is shown that soft breakdown caused by electron transport under a reverse-bias voltage is not observed in the structures with a modified layer. The barrier height for electrons at the interface is 0.62 eV.

(iii) It is shown that an abrupt junction is transformed into a gradient junction when the transition region is modified with a bismuth nanolayer. This effect may be attributed to the diffusion of metal into surface layers with a resulting increase in the width of the space-charge region.

REFERENCES

1. S. V. Svechnikov, V. V. Khiminets, and N. I. Dovgosheĭ, *Complex Noncrystalline Chalcogenides and Chalcohalides and Their Application in Optoelectronics* (Naukova Dumka, Kiev, 1992) [in Russian].
2. A. A. Aĭvazov, B. G. Budagyan, S. P. Vikhrov, and A. I. Popov, *Unordered Semiconductors* (Mosk. Énerg. Inst., Moscow, 1995) [in Russian].
3. N. D. Savchenko, A. B. Kondrat, N. I. Dovgoshej, and Yu. I. Bertsik, Funct. Mater. **1** (3), 432 (1999).
4. *Technology of Thin Films: A Handbook* (Sovetskoe Radio, Moscow, 1974), Vol. 1 [in Russian].
5. N. I. Dovgoshej, O. B. Kondrat, and R. M. Povch, Funct. Mater. **1** (3), 437 (1999).
6. A. B. Kondrat, N. D. Savchenko, and N. I. Dovgosheĭ, Vopr. At. Nauki Tekh. **6** (7), 248 (1998).
7. N. I. Dovgosheĭ, A. B. Kondrat, N. D. Savchenko, and Yu. Ĭ. Sidor, Fiz. Khim. Tverd. Tela **1** (1), 119 (2000).
8. *Materials for Semiconductor Devices and Integrated Circuits* (Vysshaya Shkola, Moscow, 1975) [in Russian].
9. A. V. Simashkevich, *Heterojunctions Based on II–VI Semiconductor Compounds* (Shtiintsa, Kishinev, 1980).
10. A. G. Milns and J. J. Feucht, *Heterojunctions and Metal–Semiconductor Junctions* (Academic, New York, 1972; Mir, Moscow, 1975).

Translated by A. Spitsyn

Semiconductors, Vol. 38, No. 11, 2004, pp. 1302–1303. Translated from Fizika i Tekhnika Poluprovodnikov, Vol. 38, No. 11, 2004, pp. 1343–1344.

SEMICONDUCTOR STRUCTURES, INTERFACES, AND SURFACES

The Effect of a Thermoelectric Field on a Current–Voltage Characteristic of the *p*-Ge–*n*-GaAs Heterojunction

M. M. Gadzhialiev^, Z. Sh. Pirmagomedov, and T. N. Éfendieva

Amirkhanov Institute of Physics, Dagestan Scientific Center, Russian Academy of Sciences, ul. 26 Bakinskikh Komissarov 94, Makhachkala, 367003 Dagestan, Russia

^e-mail: ziyav@yandex.ru

Submitted February 4, 2004; accepted for publication March 16, 2004

Abstract—Current–voltage characteristics, which emerge under the effect of oppositely directed temperature gradients, are investigated for "long" Ge–GaAs *p–n* junctions. The rectification factor increases depending on counter heat flows. This effect is attributed to a thermoelectric field forming at the heterointerface.

1. INTRODUCTION

The thermoelectric power of the Ge–GaAs heterostructure was previously investigated as a function of the temperature gradient [1, 2]. It was found that the thermoelectric power of the heterostructure at a high temperature gradient is controlled by nonequilibrium charge carriers generated under the effect of a gradient.

It is interesting to investigate the effect of the thermoelectric field emerging under the effect of a high temperature gradient on the current–voltage (*I–V*) characteristic of heterostructures. The thermoelectric field that interacts with the diffusion field of the heterostructure emerges under the effect of counter heat flows that meet each other at the boundary plane of the heterointerface, which is kept at a constant temperature by a liquid refrigerant.

2. EXPERIMENTAL

"Long" *p*-Ge–*n*-GaAs junctions were fabricated using the procedure suggested in [3]. The junction was fabricated using an external high temperature gradient directed such that the refractory material was positioned at the high-temperature side of a thermal field.

We refer to heterojunctions as long if the sizes of their base regions x_1x_3 and x_2x_4 on both sides of the junction are much larger than the extent of space-charge regions x_0x_1 and x_0x_2, i.e., $x_1x_3 \geqslant x_1x_0$ and $x_2x_4 \geqslant x_0x_2$ (Fig. 1).

Rectangular wafers with identical sizes $0.1 \times 1 \times 3$ mm were fabricated from *n*-GaAs and *p*-Ge. The wafers were ground, etched, and superimposed on each other so that the total length was 4 mm. Then the samples were placed into a vacuum chamber, and a high temperature gradient was induced in a near-contact region in a He flow. We consider the temperature gradient as high if the carrier concentration in the sample varies along a free-path length. As the temperature gradient increased and Ge started to melt at the plane of the wafer adjoining GaAs, heating was immediately switched off. As a result, the molten layer crystallized and formed the heterojunction. X-ray structural analysis showed that the crystallized boundary region between Ge and GaAs is single-crystal, and the boundary planes are rotated relative to each other by no more than 3°.

The *I–V* characteristic of resulting Ge–GaAs junction is similar to the *I–V* characteristic obtained in [3] for a heterojunction fabricated by Ge epitaxy onto a GaAs surface, which indicates the high quality of the heterojunction.

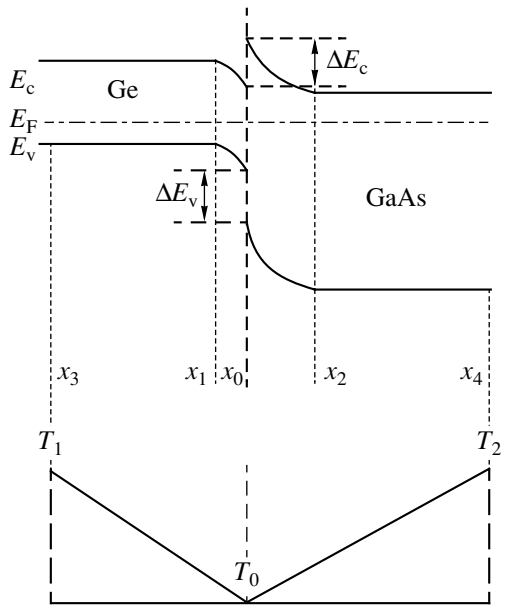

Fig. 1. Energy-band diagram of the *p–n* Ge–GaAs heterojunction in the absence of a temperature gradient. The temperature distribution over the heterojunction length under the effect of counter heat flows is shown in the lower panel.

The setup for measuring thermoelectric-power under a high temperature gradient was described in [4]. The measurements were carried out by the following scheme. Initially, the *I–V* characteristic was measured at a certain temperature of the boundary region of the heterojunction in the absence of heat flows. Then, maintaining the same temperature of the boundary region, we induced counter heat flows using heaters arranged at the ends of long diodes, and the *I–V* characteristic was measured as a function of the magnitude of counter heat flows, while the temperature of the boundary region was retained. Heaters at both ends made it possible to induce identical temperature gradients at both sides of the heterojunction. The temperature distribution along the heterojunction length under counter heat flows is shown at the bottom of Fig. 1.

3. RESULTS AND DISCUSSION

Figure 2 shows the *I–V* characteristics at a temperature of the boundary region of the heterojunction T_0 = 150 K both in the absence of the temperature gradient and at $\Delta T = T_1 - T_0 = T_2 - T_0$ equal to 80 and 120 K, respectively.

We can see from a comparison of the *I–V* characteristics that both the forward-voltage drop, at which the experimental value of the current starts to increase, and the limiting prebreakdown reverse voltage decrease due to the thermoelectric field induced by counter heat flows. The calculation shows that the rectification factor increases (η_0 = 100, η_1 = 130, η_2 = 330) as the counter heat flows increase. The quantities η_0, η_1, and η_2 are the rectification factors at various differences in temperature $\Delta T = T_{1,2} - T_0$ between the ends and the junction region. In our case, η_0 is obtained at ΔT = 0, η_1 is obtained at ΔT = 80 K, and η_2 is obtained at ΔT = 120 K.

The variations observed in the parameters of the *I–V* characteristics can be qualitatively explained as follows. Due to the counter heat flows, thermoelectric fields E_T^n (in the *n*-type region) and E_T^p (in the *p*-type region) emerge in the base regions of the heterojunction. These fields compensate the built-in field E_d, which appears in the heterojunction under the thermodynamic equilibrium due to the contact potential of the *p–n* junction. As we can see from Fig. 2 (inset), the field E_d is weakened because of the partial compensation of charges of a double electric field. The positive charges on the *n*-type side are compensated by electrons, and the negative charges on the *p*-type side are compensated by holes. Electrons and holes enter the *p–n* junction region from the ends due to the counter heat flows. It is clear that an increase in heat flows from the ends to the junction region is accompanied by an increase in the degree of weakening of the field of the contact potential difference E_d. This in turn leads to the variation in the *I–V* characteristic. As we can see from Fig. 2, the onset of an exponential increase in the forward current decreased from 2 to 1 V.

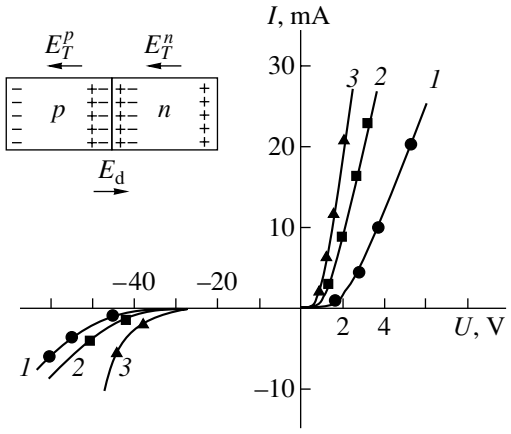

Fig. 2. Current–voltage characteristics of the *p*-Ge–*n*-GaAs heterojunction with the temperature difference between the ends and the junction region $\Delta T = T_1 - T_0 = T_2 - T_0$: (*1*) 0, (*2*) 80, and (*3*) 120 K.

The experimental prebreakdown reverse voltage decreases as ΔT increases, which is explained as follows. The initiation of counter heat flows is accompanied by an increase in the average temperatures of the base *n*- and *p*-type regions. It is known that the elevation of the temperature leads to a decrease in the reverse voltage that corresponds to the breakdown of the heterojunction.

REFERENCES

1. N. S. Lidorenko, I. I. Balmush, Z. M. Dashevskiĭ, *et al.*, Dokl. Akad. Nauk SSSR **272**, 855 (1983) [Sov. Phys. Dokl. **28**, 888 (1983)].
2. M. M. Gadzhialiev and Z. Sh. Pirmagomedov, Fiz. Tekh. Poluprovodn. (St. Petersburg) **37**, 1334 (2003) [Semiconductors **37**, 1296 (2003)].
3. R. L. Anderson, Solid-State Electron. **5**, 341 (1962).
4. M. M. Gadzhialiev and V. A. Elizarov, Fiz. Tekh. Poluprovodn. (St. Petersburg) **32**, 1313 (1998) [Semiconductors **32**, 1168 (1998)].

Translated by N. Korovin

Semiconductors, Vol. 38, No. 11, 2004, pp. 1304–1307. Translated from Fizika i Tekhnika Poluprovodnikov, Vol. 38, No. 11, 2004, pp. 1345–1348.

SEMICONDUCTOR STRUCTURES, INTERFACES, AND SURFACES

The Effect of γ-Ray Radiation on the Characteristics of the Interface between Silicon and Lead–Borosilicate Glass

P. B. Parchinskiĭ^, S. I. Vlasov, and A. A. Nasirov

National University of Uzbekistan, Tashkent, 700174 Uzbekistan

^e-mail: pavelphys@mail.ru

Submitted February 16, 2004; accepted for publication April 13, 2004

Abstract—The effect of γ-ray radiation on the density of surface states at the interface between silicon and lead–borosilicate glass is studied. It is established that, at radiation doses higher than 10^6 rad, a local peak in the surface-state density at $E = E_c - (0.32 \pm 0.04)$ eV is observed. It is shown that the interface between Si and lead–borosilicate glass is more resistant to irradiation with γ-ray photons than is the Si–SiO_2 interface obtained by thermal oxidation of the silicon surface. © *2004 MAIK "Nauka/Interperiodica".*

The low-melting lead–borosilicate (LBS) glasses are widely used in semiconductor device technology to passivate the surfaces of semiconductor devices and structures and to encapsulate these devices and structures [1, 2]. It is well known that the variation in the characteristics of semiconductor devices under the effect of radiation is largely controlled by the processes of accumulation of the radiation-induced charge in the bulk of insulating layers and at the semiconductor–insulator interface [3, 4]. However, the processes of formation of the radiation-induced charge in the bulk of insulating layers based on LBS glasses have hardly been studied until now. This circumstance has stimulated interest in studying the effect of radiation on the characteristics of passivating and insulating layers based on LBS glasses, as well as the effect on the characteristics of the interface between the semiconductor and the LBS glass. It was established previously that irradiation with γ-ray photons causes the density of the effective surface charge at the interface between silicon and the LBS glass to increase. This effect is caused both by the accumulation of the radiation-induced charge in the glass bulk and by an increase in the concentration of surface states N_{ss} at the Si–glass interface [5, 6]. The objective of this study was to determine the dose dependence of N_{ss} and to gain insight into the effect of γ-ray radiation on the special features of the spectrum of the energy distribution of the surface states over the silicon band gap dN_{ss}/dE.

The samples under study were fabricated by depositing the LBS glass onto the substrate of *n*-Si that was grown by the floating-zone method and had the ⟨111⟩ crystallographic orientation. The composition and electrical characteristics of the glass and the method for depositing the glass onto the silicon substrate were similar to those described by Vlasov *et al.* [7]. The temperature of formation of the Si–glass interface was 700°C. In order to determine the values of N_{ss} and dN_{ss}/dE, we used the method of high-frequency capacitance–voltage (*C–V*) characteristics [8]. To this end, we fabricated the test metal–insulator–semiconductor (MIS) structures using vacuum deposition of the aluminum control electrode onto the glass surface. The area of the control electrode in the structures obtained was 0.01 cm^2. The insulator-layer thickness determined from the capacitance of the MIS structure in the depletion mode was equal to $(2 \pm 0.1) \times 10^{-4}$ cm.

The MIS structures under study were irradiated with γ-ray photons using a ^{60}Co source without applying a bias voltage to the field electrode. The radiation dose was successively increased from 10^4 to 2×10^7 rad.

In Fig. 1 we show the typical *C–V* characteristics obtained for one of the MIS structures before and after irradiation with γ-ray photons. The structure capacitance was normalized to the insulator capacitance C_0 = 35 pF. As can be seen from the dependences shown, irradiation with γ-ray photons causes the *C*(*V*) curves to shift to negative voltages, which indicates that a positive radiation-induced charge Q_i is introduced into the glass. Simultaneously, a change in the slope of the *C*(*V*) curves is observed; this change may be a result of an increase in the density of states N_{ss} at the interface between Si and LBS glass [8]. At the same time, note that the radiation dose of 10^4 rad does not significantly affect the shape of the *C–V* characteristics of the studied MIS structures and, consequently, the value of N_{ss}. A slight decrease in the values of the smallest capacitance in irradiated MIS structures is observed at radiation doses of 5×10^6 rad or higher. This decrease may be a consequence of partial compensation of the substrate in the course of production of radiation defects [4]. For example, the effective charge-carrier concentration determined according to [9] was $n_0 = (1 \pm 0.05) \times 10^{14}$ cm^{-3} in the initial MIS structures and $n_0 = (1.2 \pm 0.05) \times 10^{14}$ cm^{-3} in the MIS irradiated at a dose of 10^7 rad.

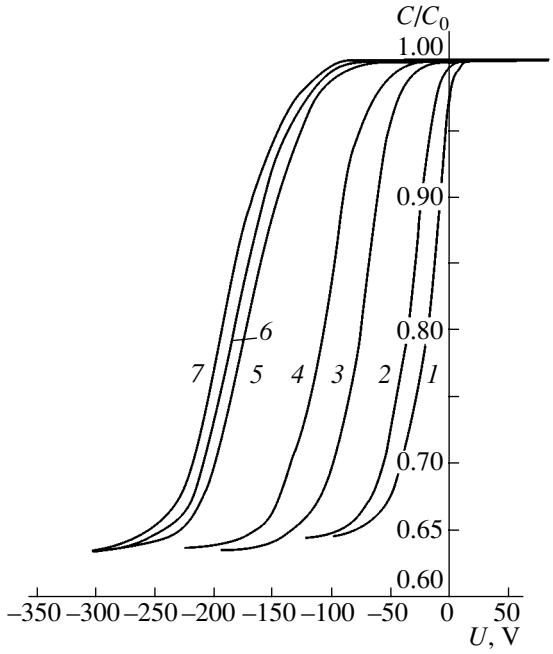

Fig. 1. Capacitance–voltage characteristics of the structures under study: (*1*) before irradiation with γ-ray photons and (*2–7*) after irradiation with γ-ray photons at doses of (*2*) 10^5, (*3*) 5×10^5, (*4*) 10^6, (*5*) 5×10^6, (*6*) 10^7, and (*7*) 2×10^7 rad.

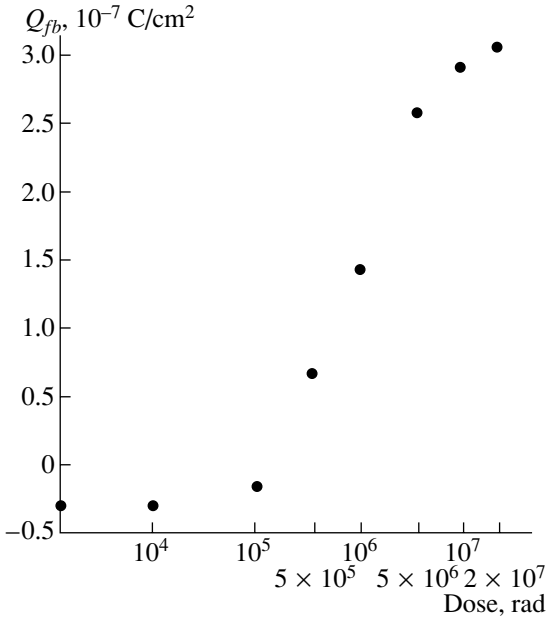

Fig. 2. Dependence of the effective surface charge Q_{fb} measured at the flat-band voltage on the dose of γ-ray radiation.

In Fig. 2 we show the dependence of the effective surface charge measured at the flat-band voltage Q_{fb} on the dose of γ-ray photons. It is noteworthy that a negative charge $Q_{fb} = (3.5–4.5) \times 10^{-8}$ C/cm^2 was detected in insulators of unirradiated MIS structures; the origin of this charge was considered previously [10]. We can see from the dependences shown that the highest rate of changes in Q_{fb} is observed at γ-radiation doses of 5×10^5–5×10^6 rad. At radiation doses higher than 5×10^6 rad, variations in the value of Q_{fb} become much smaller, which indicates that the radiation-induced charge is close to saturation.

In Fig. 3 we show representative spectra of the surface-state density at the interface between silicon and LBS glass in the structure under study; the spectra were measured before and after irradiation with γ-ray photons. We determined the values of dN_{ss}/dE by comparing the experimental *C–V* characteristics with theoretical characteristics calculated according to [11]. It is noticeable that the value of dN_{ss}/dE increases nonuniformly in irradiated structures. The value of the surface-state density increases much more rapidly in the upper half of the Si band gap than in the lower half. In addition, a local peak in the values of dN_{ss}/dE is observed in the upper half of the band gap at energy $E = E_c - (0.32 \pm 0.04)$ eV. In Fig. 4 we show the radiation-dose dependence of the value of dN_{ss}/dE at the midgap ($E = E_c - 0.56$ eV) and in the lower and upper halves of the band gap at energies $E = E_c - 0.7$ eV and $E = E_c - 0.32$ eV, respectively. It can be seen from the dependences shown that the rate of variations in the values of dN_{ss}/dE is nearly the same for all values of the energy if the radiation dose is no higher than 10^6 rad. An abrupt increase in the rate of the surface-state density in the upper half of the band gap (at $E = E_c - 0.32$ eV) is observed at radiation doses 10^6–5×10^6 rad. Thus, the effect of a nonmonotonic increase in the density of surface states exhibits a threshold and only appears at radiation doses that exceed 10^6 rad. However, the rate of variations in the value of dN_{ss}/dE decreases for all values of energy if the dose exceeds 10^7 rad; this behavior indicates that the density of surface states is saturated.

A similar nonuniform increase in the density of surface states over the Si band gap and the appearance of a local peak in the energy spectrum of the surface-state density in the upper half of the band gap (at energies $E = E_c - 0.3–0.4$ eV) were observed previously in studies of the effect of various types of radiation on the Si–SiO_2 interface obtained as a result of thermal oxidation of the Si surface [3, 12–16]. The data reported in [13, 14] indicate that the effects under consideration manifest themselves only if the radiation doses exceed 5×10^5 rad. Thus, there is qualitative agreement between the radiation-induced variations in the spectra of the surface-state density at the Si–SiO_2 interface and at the interface between Si and the LBS glass. Moreover, there is a threshold dose for the appearance of the local peak in the energy spectrum of dN_{ss}/dE. It may be assumed from the above that the physical processes that cause the surface states at the interfaces between Si and SiO_2 and between Si and the LBS glass have a common origin.

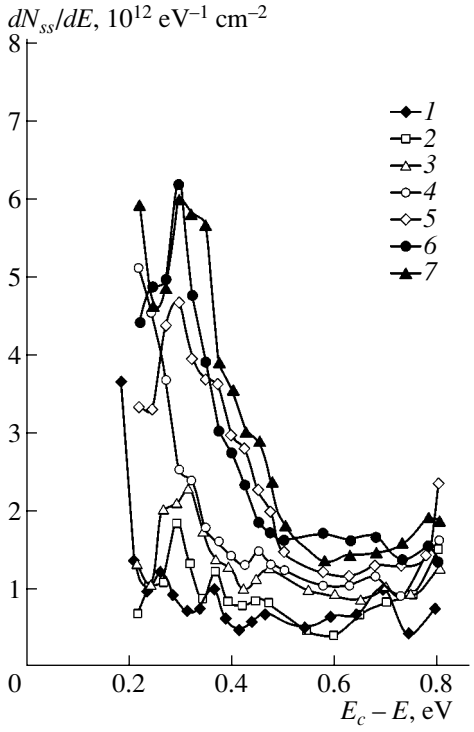

Fig. 3. Energy spectra of the surface-state density in the structures under study: (*1*) before irradiation with γ-ray photons and (*2–7*) after irradiation with γ-ray photons at doses of (*2*) 10^5, (*3*) 5×10^5, (*4*) 10^6, (*5*) 5×10^6, (*6*) 10^7, and (*7*) 2×10^7 rad.

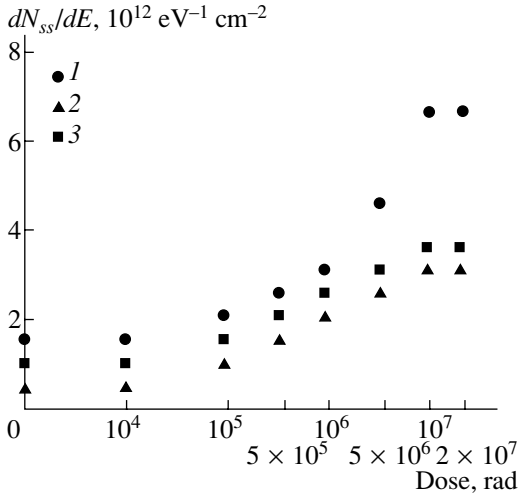

Fig. 4. Dependences of the density of surface states on the dose of γ-ray radiation at (*1*) $E = E_c - 0.32$ eV, (*2*) $E = E_c - 0.56$ eV, and (*3*) $E = E_c - 0.7$ eV.

The data reported in [14, 15] indicate that the appearance of a peak in the dN_{ss}/dE spectrum at energies $E = E_c - (0.3–0.4)$ eV at the Si–SiO_2 interface is caused by the production of radiation defects at this interface. According to [15], these defects may be nonsaturated valence bonds of Si atoms and appear as a result of the breakage of stressed bonds at the Si–SiO_2 interface. Apparently, a similar process of breaking stressed bonds also occurs at the interface between Si and the LBS glass.

At the same time, it is worth noting that the radiation resistance of the Si–(LBS glass) interface that we studied is higher than that of the Si–SiO_2 interface. For example, according to [3, 17, 18], the density of surface states at the Si–SiO_2 interface increases by a factor of 7–12 as a result of irradiation with γ-ray photons with doses ranging from 10^5 to 10^6 rad. Our data indicate that the surface-state density at the interface between Si and the LBS glass increases by no more than fivefold (even in the region of the local peak) after irradiation with similar doses. In this case, the value of dN_{ss}/dE at the Si midgap only increases by a factor of 2.5–3.

The higher radiation resistance of the interface between Si and the LBS glass can be interpreted in the following way. The coefficients of the linear thermal expansion for Si ($\alpha = 4.5 \times 10^{-6}$ K^{-1}) and SiO_2 ($\alpha = 0.4 \times 10^{-6}$ K^{-1}) differ from one another by more than an order of magnitude [2]. Therefore, significant stresses exist at the Si–SiO_2 interface formed by thermal oxidation of the Si surface; these stresses give rise to a large number of stressed bonds that can be easily broken under the effect of radiation [3]. The coefficient of linear thermal expansion of the LBS glass studied by us, $\alpha = 5.1 \times 10^{-6}$ K^{-1}, is similar to the corresponding coefficient for Si. Furthermore, the temperature that corresponds to the formation of the interface between Si and the LBS glass is much lower than the temperatures at which thermal oxidation of the silicon surface typically occurs. The result of these factors is that mechanical stresses at the interface between Si and the LBS glass are much lower than those at the Si–SiO_2 interface. Accordingly, the number of stressed bonds whose breakage causes the surface-state density to increase is also smaller.

Thus, the fact that there are quantitative differences between variations in the values of dN_{ss}/dE at equal radiation doses are not inconsistent with the previous assumption that the processes of defect production at the Si–SiO_2 interface and the interface between Si and the lead–borosilicate (LBS) glass have a common origin. At the same time, the higher radiation resistance of the interface between Si and the LBS glass creates prospects for the use of LBS to passivate and protect the surfaces of semiconductor devices that operate under severe-radiation conditions.

REFERENCES

1. M. Shimbo, K. Furukava, K. Nanzava, and K. Fukada, J. Electrochem. Soc. **134**, 156 (1987).
2. I. G. Pichugin and Yu. M. Tairov, *Technology of Semiconductor Devices* (Vysshaya Shkola, Moscow, 1984) [in Russian].

3. V. S. Pershenkov, V. D. Popov, and A. V. Shal'nov, *Surface Radiation Effects in Integrated Microcircuits* (Énergoatomizdat, Moscow, 1988) [in Russian].
4. V. S. Vavilov, B. M. Gorin, N. S. Danilin, A. E. Kiv, Yu. A. Nurov, and V. I. Shakhovtsev, *Radiation Methods in Solid-State Electronics* (Radio i Svyaz', Moscow, 1990) [in Russian].
5. P. B. Parchinskiĭ, Pis'ma Zh. Tekh. Fiz. **28** (22), 17 (2002) [Tech. Phys. Lett. **28**, 932 (2002)].
6. P. B. Parchinskiĭ, S. I. Vlasov, S. Z. Zaĭnabidinov, *et al.*, Uzb. Fiz. Zh. **4**, 200 (2002).
7. S. I. Vlasov, P. B. Parchinskiĭ, and B. A. Olmatov, Neorg. Mater. **36**, 608 (2000).
8. S. M. Sze, *Physics of Semiconductor Devices*, 2nd ed. (Wiley, New York, 1981; Mir, Moscow, 1984), Vol. 1.
9. K. H. Zaineger and F. P. Heiman, Solid State Technol. **13**, 49 (1970).
10. P. B. Parchinskiĭ, S. I. Vlasov, A. A. Nasirov, and T. P. Adilov, Pis'ma Zh. Tekh. Fiz. **22** (2), 46 (1996) [Tech. Phys. Lett. **22**, 67 (1996)].
11. J. R. Brews, Solid-State Electron. **20**, 607 (1977).
12. S. K. Lai, Appl. Phys. Lett. **39**, 58 (1981).
13. T. P. Ma, G. Scogan, and R. Leone, Appl. Phys. Lett. **27**, 61 (1975).
14. T. P. Ma, Appl. Phys. Lett. **27**, 615 (1975).
15. S. N. Kozlov, A. N. Nevzorov, and T. G. Chaĭkovskaya, Mikroélektronika **15**, 283 (1986).
16. G. N. Galkin, R. U. Abasova, E. A. Bobrova, and V. S. Vavilov, Fiz. Tekh. Poluprovodn. (Leningrad) **16**, 2158 (1982) [Sov. Phys. Semicond. **16**, 1390 (1982)].
17. S. Z. Zaĭnabidinov, S. I. Vlasov, E. G. Zaugol'nikova, *et al.*, Fiz. Tekh. Poluprovodn. (Leningrad) **19**, 1191 (1985) [Sov. Phys. Semicond. **19**, 730 (1985)].
18. V. Ya. Kiblik, R. O. Litvinov, V. G. Litovchenko, and N. M. Litovchenko, Ukr. Fiz. Zh. **22**, 1097 (1977).

Translated by A. Spitsyn

Semiconductors, Vol. 38, No. 11, 2004, pp. 1308–1311. Translated from Fizika i Tekhnika Poluprovodnikov, Vol. 38, No. 11, 2004, pp. 1349–1352.

SEMICONDUCTOR STRUCTURES, INTERFACES, AND SURFACES

Photoelectric Properties of ZnO/CuPc/Si Structures

G. A. Il'chuk*, S. E. Nikitin*, Yu. A. Nikolaev*, V. Yu. Rud', Yu. V. Rud'*, and E. I. Terukov***

**Ioffe Physicotechnical Institute, Russian Academy of Sciences, Politekhnicheskaya ul. 26, St. Petersburg, 194021 Russia*

***St. Petersburg State Polytechnical University, Politekhnicheskaya ul. 29, St. Petersburg, 195251 Russia*

Submitted April 12, 2004; accepted for publication April 19, 2004

Abstract—*n*-ZnO:Al/CuPc/*n*(*p*)-Si structures were formed using vacuum-evaporation deposition of copper phthalocyanine (CuPc) layers on the surface of *n*- and *p*-Si wafers with subsequent magnetron-sputtering deposition of ZnO:Al layers on the CuPc surface. It is shown that the structures obtained exhibit a high photosensitivity (~80 V/W at $T = 300$ K) in the spectral range 1.65–3.3 eV. The rectification factor and photovoltaic effect in these structures are discussed in relation to the properties of silicon substrates. It is concluded that the contact of phthalocyanine with diamond-like semiconductors (e.g., silicon) are promising for application in wide-band high-efficiency photovoltaic converters. © *2004 MAIK "Nauka/Interperiodica".*

1. INTRODUCTION

Even early studies of electrical conductivity and photoconductivity of phthalocyanine of various metals made it possible to classify these materials as electronic semiconductors [1–3]. This circumstance indicated that a wide range of new synthetic materials could in principle be used in the development of photosensitive and emitting structures, as well as other next-generation devices of molecular electronics [4–7]. It is worth noting that the photoconversion efficiency of thin-film solar cells based on the films of copper phthalocyanine CuPc is now as high as ~3.6% [7]. Recently, we showed that photosensitive ZnO/CuPc/*n*-Si structures can be formed [8]. This study is a continuation of our research in this field and is concerned with the formation of photosensitive ZnO/CuPc/Si structures using both *n*- and *p*-Si crystals.

2. EXPERIMENTAL

We used silicon crystals oriented in the (111) crystallographic plane with *n*- and *p*-type conductivity as the substrates; KÉF-0.01 (*n*-Si, $\rho = 0.01\ \Omega$ cm) and KDB-0.03 (*p*-Si, $\rho = 0.03\ \Omega$ cm) crystals were used. CuPc layers with a thickness of ~0.5 μm were obtained using thermal evaporation of phthalocyanine powder in vacuum with the subsequent deposition of the evaporation products onto the polished surface of the silicon substrate at a temperature of about 50°C. The deposited CuPc films had a specular surface; the ZnO:Al layers were then deposited onto this surface using magnetron sputtering of the target in the presence of high-purity Al and in an argon atmosphere. By varying the argon pressure during the deposition process (2–4 h), we attained the required gradient of resistivity within the ZnO film thickness ($d \leq 1$ μm). These conditions of deposition ensured a high adhesion of the ZnO layer to the CuPc surface. As a result, we obtained two types of structures: *n*-ZnO:Al/CuPc/*p*-Si and *n*-ZnO:Al/CuPc/*n*-Si.

3. RESULTS AND DISCUSSION

1. Measurements of the steady-state current–voltage (*I*–*V*) characteristics showed that distinct rectification was observed for both types of structures at $T = 300$ K (Figs. 1a, 1b). The rectification factor K for typical structures as defined as the ratio between the forward current and the reverse current at specified bias voltages U is listed in the table. The largest values of $K \approx 50$ at $U = 6$ V are obtained for the best structures based on *p*-Si. It is worth noting that, in the structures whose substrates had different types of conductivity, the conducting direction was found to be the same and corresponded to the positive external bias voltage applied to the *n*-ZnO:Al layer. This circumstance reflects a specific feature of the energy-band diagram for the structures obtained, which calls for further research.

Photoelectric properties of ZnO/CuPc/Si structures at $T = 300$ K

Type of structure	K	R_0, Ω	U_0, V	$S_U^{\max}$, V/W	δ, eV
n-ZnO : Al/CuPc/*p*-Si	30–50 ($U \approx 6$ V)	300–400	4.5	80	1.73
n-ZnO : Al/CuPc/*n*-Si	20 ($U \approx 2$ V)	10^3–10^4	4.0	20	1.80

1063-7826/04/3811-1308$26.00

The initial portion of the steady-state *I–V* characteristics of the structures at forward-bias voltages $U \le 0.5$ V can be described by the well-known diode equation [9]. The smaller diode exponent ($\beta \approx 3$) is characteristic of the *n*-ZnO:Al/CuPc/*p*-Si structures, whereas this exponent turns out to be even larger ($\beta \approx 20$) for the structures formed on the *n*-Si substrates. The values of β obtained make it possible to assume that there is a tunneling–recombination mechanism of charge transport in the structures under consideration in the case of forward-bias voltages.

For both types of structures subjected to forward-bias voltages $U > 4.5$–5 V, the forward portion of the steady-state *I–V* characteristics obeys a linear law:

$$I = (U - U_0)/R_0; \quad (1)$$

typical values of the cutoff voltage U_0 and residual resistance R_0 for both types of structures are listed in the table. The cutoff voltages were found to be nearly the same in both structures, whereas the lower residual resistance was typical of structures based on *p*-Si.

As a rule, the reverse currents of the structures under study exhibit the power-law dependence $I \propto U^m$. The exponent $m \approx 2.5$ for the *n*-ZnO:Al/CuPc/*p*-Si structures in the voltage region $U < 8$ V; this circumstance makes it possible to relate this value of the exponent to the contribution of the currents limited by the space charge in the mobility mode [10]. As the voltage increases ($U > 8$ V), the value of the exponent increases to $m = 6$, which is apparently related to the development of a soft breakdown. The value of the exponent $m \cong 1$–1.3 for reverse *I–V* characteristics in the structures based on Si crystals in the range of reverse bias voltages used, which may be caused by tunneling of charge carriers or may be related to the current limited by the space charge in conditions of saturation of the charge-carrier velocity [10].

2. The photovoltaic effect is clearly pronounced in the *n*-ZnO:Al/CuPc/*p*-Si and *n*-ZnO:Al/CuPc/*n*-Si structures obtained. As a rule, the photovoltage sign is independent of the radiation intensity, the energy of incident photons, and the location of the excitation optical probe (with a diameter of ~0.3 mm) on the photosensitive surface of the structures. The absence of inversion of the sign of the photovoltaic effect makes it possible to assume that one of the two active regions in each of the types of structure makes the major contribution to the observed photosensitivity. The voltage photosensitivity was always found to be highest if the thin wide-gap *n*-ZnO:Al layer of the structure was illuminated. The highest voltage photosensitivity $S_U^{\max}$ was observed in the *n*-ZnO:Al/CuPc/*p*-Si structures. It can be seen from the table that the photosensitivity of the structures obtained by deposition of thin CuPc and ZnO layers on the *p*-Si substrates is indeed higher.

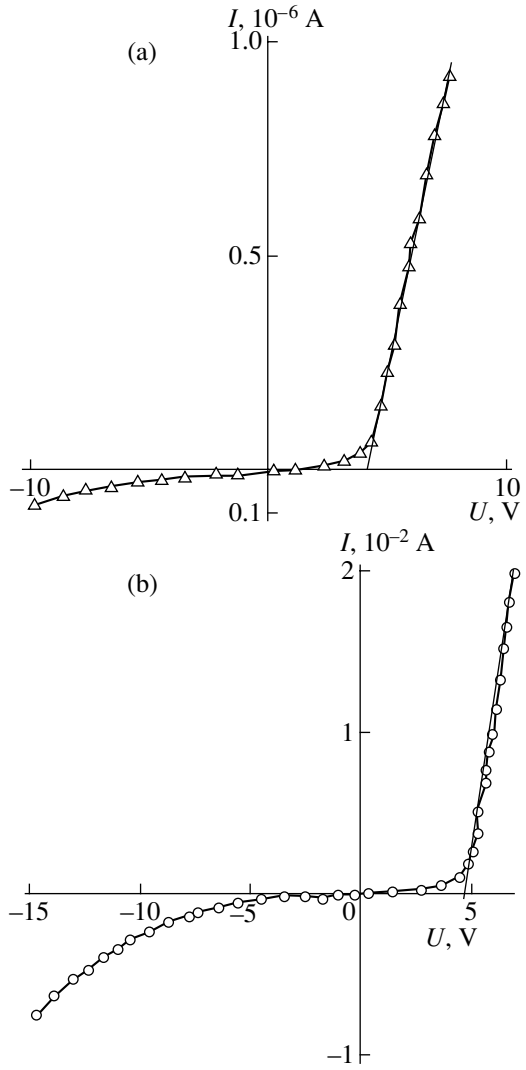

Fig. 1. Steady-state current–voltage characteristics of the (a) *n*-ZnO:Al/CuPc/*p*-Si and (b) *n*-ZnO:Al/CuPc/*n*-Si structures at $T = 300$ K.

It is important to note that the photovoltage sign in the two types of structures obtained was found to be different. For structures on the *n*-Si substrates, positive polarity of the photovoltage corresponds to the *n*-ZnO:Al layer and is consistent with the rectification direction. If the structures formed on the *p*-Si substrates are illuminated, the *n*-ZnO:Al layer is also charged positively, which does not correspond to the rectification direction. Apparently, this special feature of the photovoltage sign is caused by differences in the actual energy-band models for these structures.

In Fig. 2 we show typical spectral dependences of relative quantum efficiency of photoconversion $\eta(\hbar\omega)$ for both types of structures at $T = 300$ K in the situation where the wide-gap (*n*-ZnO:Al) side of the structures is illuminated. The main conclusion that can be drawn from Fig. 2 is that, despite the differences in the polarity

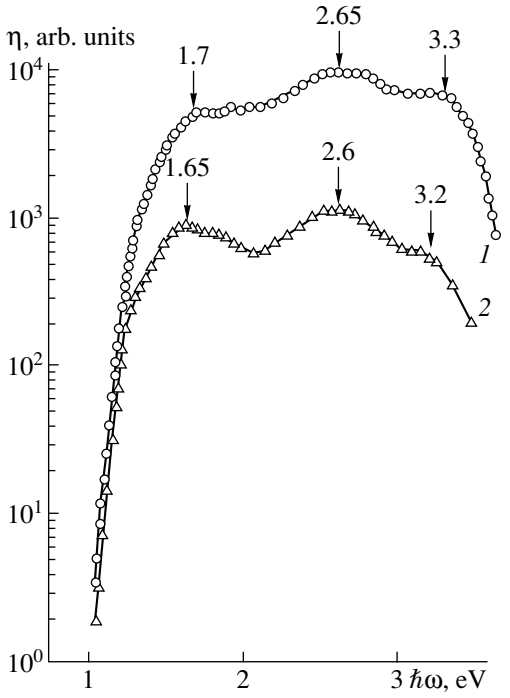

Fig. 2. Spectral dependences of relative quantum efficiency of photoconversion in the *n*-ZnO:Al/CuPc/*p*-Si (curve *1*) and *n*-ZnO:Al/CuPc/*n*-Si (curve *2*) structures exposed to nonpolarized excitation light. The *n*-ZnO:Al side of the structures was illuminated; $T = 300$ K.

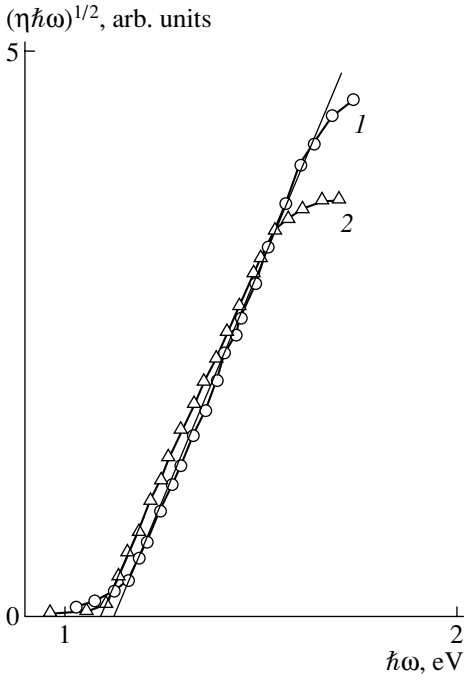

Fig. 3. The $(\eta\hbar\omega)^{1/2} = f(\hbar\omega)$ dependences for the (*1*) *n*-ZnO:Al/CuPc/*p*-Si and (*2*) *n*-ZnO:Al/CuPc/*n*-Si structures at $T = 300$ K.

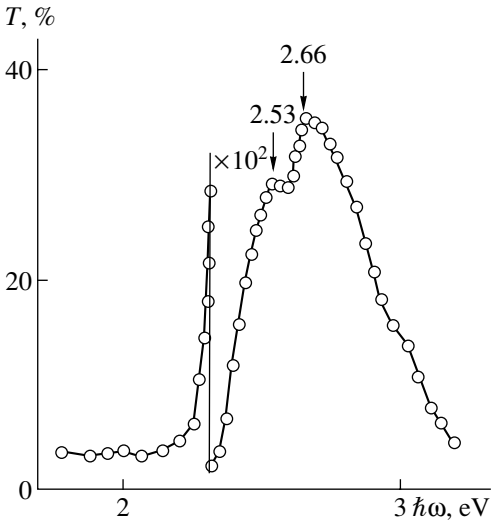

Fig. 4. Spectral dependence of the optical-transmission coefficient for the CuPc film ($d \approx 1$ μm) at $T = 300$ K.

of the photovoltaic effect, the spectral contour of the $\eta(\hbar\omega)$ curves for both types of structures is found to be nearly the same. Indeed, for both types of structures (Fig. 2, curves *1*, *2*) the photosensitivity has almost coincident energy positions of both the onset of the increase in photosensitivity at the photon energy $\hbar\omega > 1$ eV and the short-wavelength falloff of η at $\hbar\omega > 3.3$ eV. According to Fig. 3, the long-wavelength increase in photosensitivity at $\hbar\omega > 1$ eV obeys the following law characteristic of indirect band-to-band optical transitions [9]:

$$\eta\hbar\omega = A'(\hbar\omega - E_G)^2. \quad (2)$$

Here, A' is a constant coefficient and E_G is the semiconductor band gap. Extrapolating dependence (2) as $(\eta\hbar\omega)^{1/2} \longrightarrow 0$, we obtain nearly the same values of E_G for both types of structures (Fig. 3); in turn, these values are close to that of the silicon band gap [11]. This circumstance makes it possible to relate the energy position of the long-wavelength photosensitivity edge in the structures of both types to the interband absorption in the narrow-gap component (*n*- or *p*-Si) of these structures. In turn, the energy position of the short-wavelength falloff of η at $\hbar\omega > 3.3$ eV is consistent with the band gap of the top layer of the structures under consideration and, thus, can be related to the interband absorption in ZnO [11].

The highest photosensitivity for both types of structures (see Fig. 2) is indeed attained in the interval between the band gaps of the narrow-gap (Si) and wide-gap (ZnO) components of the ZnO:Al/CuPc/Si structures, which is a characteristic attribute of an ideal heterojunction [11]. In addition to the above, there is another special feature: a maximum at $\hbar\omega^{max} = 2.6$ eV is observed in the $\eta(\hbar\omega)$ spectra in the range of the high-

est photosensitivity of the structures (at 1.7–3.3 eV) (Fig. 2). The spectral position of the maximum ($\hbar\omega^{max}$ = 2.6 eV) in the $\eta(\hbar\omega)$ dependences obtained is in qualitative agreement with the optical-transmission spectrum of the CuPc layer deposited onto the quartz substrate simultaneously with the formation of the heterojunction (Fig. 4). Therefore, the maximum in the $\eta(\hbar\omega)$ spectra of the ZnO/CuPc/Si structures should be attributed to the presence of a transmittance band in the optical spectra of the CuPc film.

The broad-band type of photosensitivity of the structures is represented in the table by the full width of the $\eta(\hbar\omega)$ spectra at their half-maximum δ. As can be seen from the data listed, both types of structures have large and nearly coincident values of δ: δ = 1.7–1.8 eV. This circumstance leads us to believe that both heteroboundaries (Si/CuPc and ZnO/CuPc) in the structures based on the contact of CuPc layers with Si and ZnO semiconductors are of good quality with respect to the recombination processes. It is also evident that the structures based on the heterocontact of phthalocyanine with diamond-like semiconductors (e.g., Si) may be quite promising for the development of wide-band high-efficiency photoconverters.

REFERENCES

1. A. T. Vartanyan, Zh. Fiz. Khim. **22**, 769 (1948).
2. D. D. Elay, Nature **162**, 869 (1948).
3. E. K. Putseĭko, Dokl. Akad. Nauk SSSR **39**, 471 (1948).
4. J. F. Nierengarten, G. Hadziioannon, and N. Armaroli, Mater. Today **4**, 16 (2001).
5. J. Wang, G. Yu, A. J. Heeger, and G. Stradanov, Org. Electron. **1**, 33 (2000).
6. N. Folman and W. R. Salaneck, Surf. Sci. **500**, 904 (2002).
7. P. Penmans and S. R. Forrest, Appl. Phys. Lett. **79**, 126 (2001).
8. G. A. Il'chuk, N. V. Klimova, O. I. Kon'kov, *et al.*, Fiz. Tekh. Poluprovodn. (St. Petersburg) **38**, 1056 (2004) [Semiconductors **38**, 1018 (2004)].
9. S. Sze, *Physics of Semiconductor Devices*, 2nd ed. (Wiley, New York, 1981; Mir, Moscow, 1984).
10. M. A. Lampert and P. Mark, *Current Injection in Solids* (Academic, New York, 1970; Mir, Moscow, 1979).
11. *Physicochemical Properties of Semiconductors*, Ed. by A. V. Novoselova, V. B. Lazarev, Z. S. Medvedeva, N. P. Luzhina, and A. A. Levin (Nauka, Moscow, 1979) [in Russian].

Translated by A. Spitsyn

Semiconductors, Vol. 38, No. 11, 2004, pp. 1312–1315. Translated from Fizika i Tekhnika Poluprovodnikov, Vol. 38, No. 11, 2004, pp. 1353–1357.

LOW-DIMENSIONAL SYSTEMS

Transformation Kinetics of Electric Field Domains in Weakly Coupled GaAs/AlGaAs Superlattices in a Transverse Electric Field

Yu. A. Mityagin^, V. N. Murzin, Yu. A. Efimov, A. A. Pishchulin, and V. N. Pyrkov

Lebedev Physical Institute, Russian Academy of Sciences, Moscow, 119991 Russia

^e-mail: mityagin@maill.lebedev.ru

Submitted March 1, 2004; accepted for publication March 4, 2004

Abstract—Transformation kinetics of the resonant-tunneling domain structure in a superlattice in a rapidly varying electric field is investigated using real-time studies of current response. It is shown that the kinetics is mainly determined by a lag in redistribution of the space charge that forms the domain boundary. A nonmonotonic oscillatory dependence of the transient-process duration on the amplitude of a voltage pulse is observed, as well as the effect of the weak dependence of the transformation time on the displacement of the domain boundary, which indicates that the transformation processes is discrete. Possibilities for controlling the switching processes in a multistable system of current states in weakly coupled semiconductor superlattices are discussed. © *2004 MAIK "Nauka/Interperiodica".*

For weakly coupled superlattices (SLs), the resonant tunneling responsible for the negative differential conductivity results in instabilities and the formation of a homogeneously ordered resonant-tunneling structure, in which each lowest level in a single quantum well (QW) corresponds to a certain excited level in the neighboring QW. For intermediate fields, such a structure is found to be unstable and is divided into regions with different electric fields, so the field is constant within each region (domains with high and low electric fields) [1]. A variation in the voltage applied to the ends of an SL results in the reconstruction of the resonant-tunneling structure, which is accompanied by the detuning of the resonances, the displacement of boundaries between the domains, and, as a consequence, a variation in the relative volumes of domains of high and low electric fields [1–5]. The features of the reconstruction largely depend on the observation conditions, i.e., whether the observation is made with an increasing or decreasing voltage applied to the SL [3]. In the first case, the features of formation of the resonant-tunneling structure are determined by the highest possible resonance current in the low-field domain. Accordingly, the resonant levels must be matched in this domain and be appreciably detuned in the high-field domain. In the second case, the conditions for formation of the resonant-tunneling structure are determined by the lowest possible (nonresonant) conductivity in the region of the high-field domain, and therefore all resonances, both in the high-field domain and the low-field domain, are found to be substantially detuned. The result is the appearance of a current hysteresis, multistability, and a fine periodic structure in both branches of the hysteresis [2, 3].

All these features of domain formation and transformation in a slowly varying electric field are well known and have been studied in detail [1–5]. At the same time, until recently there were no such studies in a rapidly varying field, which would allow one to obtain direct information about the characteristics of the transformation process.[1] On the other hand, such information is rather important both in order to understand the physics of the formation of the domain structure and its modification in an electric field and to obtain information about the time characteristics that determine the rate of switching processes in multilevel switching (and other) devices based on these effects [7]. The first experimental studies in pulsed fields [7–9] showed the basic possibility of switching between stable current states in a system with multistability and made it possible to estimate the characteristic switching times. However, it was difficult to obtain more detailed information about the transformation processes of the resonant tunneling structure in an electric field. Using the real-time detection method of the current response, we studied for the first time the transformation kinetics of the resonant-tunneling structure in an SL in a rapidly varying electric field. Simulation of the time variation of transverse transport, distribution of the space charge, and other characteristics of SLs in pulsed fields was performed. Comparing the experimental data with the results of the simulation, we established the general pattern of transformation of the resonant-tunneling structure and

[1] The research into current instabilities and the phenomena of self-sustaining current oscillations in some laboratories deal with a rather specific case of lightly doped SLs, in which the formation of a domain boundary appears to be difficult because of the insufficient concentration of charge carriers [4, 6].

1063-7826/04/3811-1312$26.00 © 2004 MAIK "Nauka/Interperiodica"

accounted for the observed features of the electronic properties, including the transverse transport, in weakly coupled SLs to which short and long electric field pulses are applied.

We studied long-period GaAs/$Al_{0.3}Ga_{0.7}As$ SL structures that include wide QWs and involve a set of quantum-confinement subbands. Superlattices (with a QW width of 25 nm, barrier width of 10 nm, and number of periods 30) located between two heavily doped *n*-GaAs layers (2×10^{18} cm^{-3}) were grown by molecular-beam epitaxy on GaAs substrates and were intentionally doped with a silicon donor impurity to a concentration of 1.2×10^{16} cm^{-3}. Electrical measurements were performed on mesa structures with a mesa diameter of 500 μm and Cr/Au contacts formed by vacuum sputtering. A change in the transverse conductivity of the structure was studied for certain fixed voltages at the SL, when rectangular voltage pulses of different polarities with quite sharp edges (shorter than 10 ns) were applied. Measurements were performed in real-time mode, and they allowed us to record the time dependence of the current through the structure at different instants following the leading edge of the voltage pulse, during the pulse, and after termination of the pulse. The amplitude and duration of the pulse varied within the range ΔU_p = 0–0.5 V and $\tau_p = 10^{-4}$–10^{-7} s, respectively. Measurements were performed at a temperature of T = 4.2 K.

We can see from Fig. 1, where a fragment of the current–voltage characteristic $I(U)$ is shown, that the fabricated structures feature a pronounced current hysteresis, whose upper and lower current branches have a fine periodic structure, and current multistability branches within the hysteresis region. These data correspond to voltages in the range 1.6–3.0 V, where a low-field domain (resonant-tunneling transitions 1 ⟶ 2 between subband 1 in the previous QW and subband 2 in the successive QW) and a high-field domain (resonant-tunneling transitions 1 ⟶ 3) are formed in the SL. In Fig. 1b a typical example of the measured current I through the SL is shown as a function of time t as a rectangular voltage pulse is applied to the SL. The point $I_A(U_A)$ at U_A = 2.040 V in the lower branch of the hysteresis is chosen as a starting point. When a pulse ΔU_p of negative polarity corresponding to a decrease in the voltage at the SL is applied, the operation point should be shifted along the lower branch of the hysteresis towards smaller values of U to the point $U = U_A - \Delta U_p$. After the pulse is switched off, the voltage at the SL should return to the initial value $U = U_A$. However, the operation point cannot shift along the lower branch of the hysteresis to the initial current state and must shift at once upwards along the new current branch of multistability towards higher currents to a new steady current state at $U = U_A$ [3, 8, 9]. Such a situation is observed experimentally for quite long pulses (τ_p = 10 μs), whose duration is much greater than the characteristic reconstruction times for the resonant-tunneling structure. In

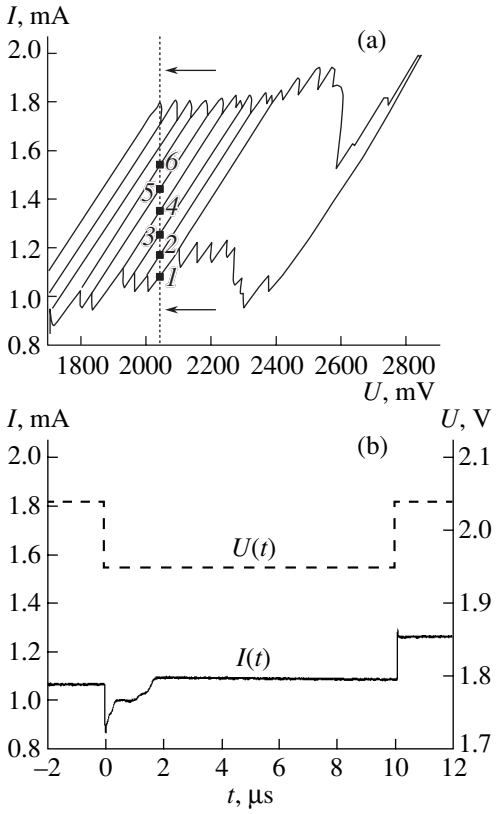

Fig. 1. (a) Fragment of the current–voltage characteristic $I(U)$ and (b) time dependence of the current $I(t)$ measured when rectangular voltage pulses of negative polarity are applied to a superlattice (SL). The numbers denote stable current states of the system with multistability at a fixed voltage of U_A = 2.040 V. The data were obtained for a pulse amplitude of 0.092 V, which induced the 1 ⟶ 3 transition. (b) Variation of the voltage on the SL when the pulse is applied (τ_p = 10 μs).

Fig. 1 we can see that, during the action of the pulse (for a pulse amplitude of ΔU_p = 0.092 V), the steady-state value of the current I = 1.07 mA (attained after some transition region) exactly corresponds to the current on the lower hysteresis branch at $U = U_A - \Delta U_p$ ($U = U_A - \Delta U_p$ = 1.948 V). After the termination of the pulse, the current practically instantaneously increases to a new stationary value of $I \approx 1.25$ mA, which corresponds to the point of intersection of the corresponding current branch of multistability with the straight line $U = U_A$ = 2.040 V (in this case, 1 ⟶ 3). The measurements show that, with increasing pulse amplitude, the domain boundary is shifted by a greater number of SL periods and, accordingly, the operation point shifts to higher current states of the system with multistability.

In addition to the quite obvious fact that all stages of the switching processes, which are caused by the displacement of the operation point in the current–voltage characteristic along the branches of multistability and are not related to a change in the fields in the SL, are instantaneous, the data obtained allow us to draw the

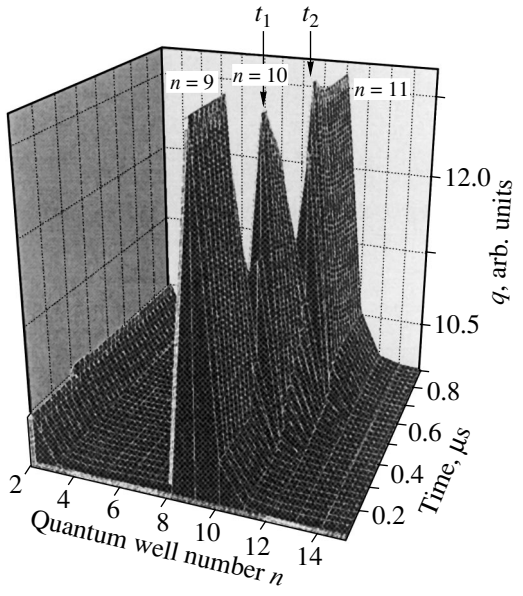

Fig. 2. Calculated distribution of the space charge q over the QWs of the SL at different times after a sharp decrease in voltage at the ends of the SL by ΔU_p = 100 mV (transition 1 ⟶ 3 in Fig. 1). Arrows show the instants at which the space charge is displaced to the first neighboring QW (t_1 = 0.280 μs) and to the next QW (t_2 = 0.476 μs).

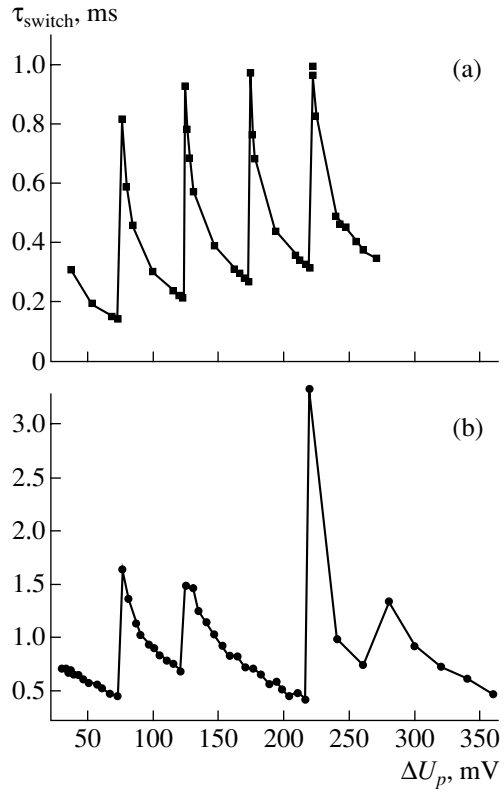

Fig. 3. Transient-process duration as a function of the amplitude of the voltage pulses (τ_p = 10 μs): (a) simulation data, (b) experimental values.

basic conclusion that the characteristic time of the transformation of the resonant-tunneling structure in the SL in an electric field is practically entirely determined by the lag of the processes related to the space-charge redistribution and formation of domain boundaries. In Fig. 1 we can see that this fact manifests itself in the appearance of a transition region (a spike) on the $I(t)$ curves just after the leading pulse edge. The duration of this region, measured from the beginning of the pulse to the point where the steady-state value of the current is attained, is ~10^{-7} s, which is consistent with the rough estimates of the resonant-tunneling time obtained from the measurements of the resonance current [10].

A more detailed study of the dependence $I(t)$ in this transition region allows us to trace the kinetics of redistribution of the space charge and the transformation of the resonant-tunneling structure in the fields that displace the domain boundary over several periods of the SL. It can be seen in Fig. 1 that, in the transition region, the $I(t)$ curve has a complicated nonmonotonic run with several inflection points. The measurements show that the number of such points increases with increasing number of SL periods over which the domain boundary is displaced [11]. Comparing these data with the results of simulation performed for a discrete model of transverse transport in weakly coupled SLs [3], we may conclude that the transformation has a discrete character. It follows from the simulation data (Fig. 2), which agree well with the experiment, that the displacement of the space charge and domain boundary to the final QW with varying voltage at the SL is not a single event but includes several steps, which are caused by the subsequent detuning and tuning of the resonant levels as the space charge flows over to the final state through a sequence of QWs. This process is accompanied by the appearance of current instabilities and such features as the inflection points in the transition region of the time dependence of the current $I(t)$.

The discrete character of the processes of transformation of the resonant tunneling structure in an SL in an electric field is also confirmed by the results of studies performed with varying amplitude and duration of the voltage pulses applied to the SL. It can be seen in Fig. 3 that the transient-process time (τ_{switch}) depends nonmonotonically (oscillatory) on the pulse amplitude. With increasing amplitude, the duration of the transient periodically first monotonically decreases, then sharply grows, and then again decreases. Comparing these data with the results of simulation, we can uniquely connect the observed spikes with the situations where the pulse amplitude attains values that are sufficient for the transition of the domain boundary to the neighboring QW. The monotonic decrease in the duration of the transient and in the transformation time within each period of $I(\Delta U_p)$ can be clearly attributed to the acceleration of the electronic processes that determine the displacement of the space charge with increasing pulse ampli-

tude and magnitude of the field produced by the pulse in the SL.

This interpretation is supported by the data obtained in the study of the features of transformation of a resonant-tunneling structure under short applied pulses, whose duration is on the order of the characteristic reconstruction times or shorter. The main result obtained in these studies is the experimental observation of the fact that, for short pulses whose duration is insufficient for the transition of the domain boundary to the final state, the transformation process is only partially completed: the domain boundary passes to some intermediate QW to which it has time to move during the pulse action. Accordingly, the system passes to the corresponding intermediate current state, which is different from the final state in the case of long pulses. This result, which is confirmed by the simulation data, shows that in principle one can control switching in a multistable system of current states [7, 9] by changing not only the amplitude, but also the duration of the voltage pulse of required polarity applied to the SL.

We also obtained a rather unexpected result related to the characteristic transformation time of the resonant tunneling structure, which required special study. It turned out that, in the experiments with domain boundary displacement over several periods, the average characteristic transformation time remained almost unchanged as the number of transition periods and, accordingly, the total displacement of the domain boundary increased. At first sight, one might expect an increase in transformation time in this situation. However, the results of direct measurements of the duration of the transition region of $I(t)$ in the vicinity of the leading pulse edge, confirmed by the simulation data, showed that the recorded change in the transient-process duration when the domain boundary is displaced over a greater number of SL periods is actually extremely small (Fig. 3). The simulation shows that the cause of this weak dependence of the transient-process duration on the magnitude of the displacement of the domain boundary is the fact that a transition over several SL periods requiring higher amplitudes of the voltage pulse occurs under conditions where the field gradient in the SL is greater than that for domain boundary displacement over smaller distances.

To sum up, we note the following. In our experimental and simulation studies, we showed that the transformation kinetics of the resonant tunneling structure with varying voltage applied to the SL is almost entirely determined by the lag in the redistribution of the space charge that forms the electric-field domains. This lag manifests itself in the appearance of a transition region of the $I(t)$ dependence near the leading edge of the electric-field pulse applied to the SL. We showed that the $I(t)$ dependence in the transition region is nonmonotonic and is characterized by the presence of a structure reflecting the discrete character of the transformation of the resonant-tunneling structure when the domain boundary moves through a sequence of several QWs in an SL. We observed an oscillatory dependence of the duration of the transient process on the amplitude of the change in voltage. We showed experimentally and by simulation that the lag in transformation of the resonant-tunneling structure to a final state is hardly affected by an increase in both the number of periods and the distances over which the domain boundary moves in the SL under the effect of a change in external voltage. In short-pulse experiments, we showed that one can interrupt the processes of transformation at any intermediate stage; this opens up the possibility of controlling the switching between current states not only by changing the amplitude, but also by changing the duration of the voltage pulses applied to the SL.

This study was supported by the Russian Foundation for Basic Research (project nos. 02-02-16977 and 03-02-06534); the program "Physics of Solid State Nanostructures" of the Ministry of Science, Technology, and Industry (grant no. 97-1048); and the Presidium of the Russian Academy of Sciences (the program "Low-Dimensional Quantum Nanostructures").

REFERENCES

1. L. Esaki and L. L. Chang, Phys. Rev. Lett. **33**, 495 (1974).
2. J. Kastrup, H. T. Grahn, K. Ploog, *et al.*, Appl. Phys. Lett. **65**, 1808 (1994).
3. Yu. A. Mityagin and V. N. Murzin, Pis'ma Zh. Éksp. Teor. Fiz. **64**, 146 (1996) [JETP Lett. **64**, 155 (1996)].
4. A. Wacker, in *Theory of Transport Properties of Semiconductor Nanostructures*, Ed. by E. Scholl (Chapman and Hall, London, 1998), p. 321.
5. V. N. Murzin and Yu. A. Mityagin, Usp. Fiz. Nauk **169**, 464 (1999) [Phys. Usp. **42**, 396 (1999)].
6. Yu. A. Efimov, Yu. A. Mityagin, V. N. Murzin, and A. A. Pishchulin, Kratk. Soobshch. Fiz., No. 5, 13 (2000).
7. Yu. A. Mityagin, Yu. A. Efimov, V. N. Murzin, and A. A. Pishchulin, Physica E (Amsterdam) **13**, 961 (2002).
8. V. N. Murzin, Yu. A. Mityagin, *et al.*, in *Proceedings of International Symposium on Nanostructures: Physics and Technology* (St. Petersburg, 1994), p. 285; in *Proceedings of International Symposium on Nanostructures: Physics and Technology* (St. Petersburg, 1995), p. 151.
9. Yu. A. Efimov, Yu. A. Mityagin, V. N. Murzin, and A. A. Pishchulin, Kratk. Soobshch. Fiz., No. 7, 24 (2001).
10. Yu. A. Mityagin, V. N. Murzin, I. P. Kazakov, *et al.*, Nanotechnology **11** (4), 211 (2000).
11. V. N. Murzin, Yu. A. Mityagin, A. A. Pishchulin, and Yu. A. Efimov, in *Proceedings of International Symposium on Nanostructures: Physics and Technology* (St. Petersburg, 2003) p. 188.

Translated by I. Zvyagin

Semiconductors, Vol. 38, No. 11, 2004, pp. 1316–1322. Translated from Fizika i Tekhnika Poluprovodnikov, Vol. 38, No. 11, 2004, pp. 1358–1363.

LOW-DIMENSIONAL SYSTEMS

Vibration Modes and Electron-Phonon Interaction in Semiconductor Nanotubes

A. I. Vedernikov*^ and A. V. Chaplik^^**

**Novosibirsk State University, Novosibirsk, 630090 Russia*

^e-mail: ahtoh@ngs.ru

***Institute of Semiconductor Physics, Siberian Division, Russian Academy of Sciences, Novosibirsk, 630090 Russia*

^^e-mail: chaplik@isp.nsc.ru

Submitted January 19, 2004; accepted for publication April 21, 2004

Abstract—Vibration eigenmodes of a III–V semiconductor nanotube are found taking into account the crystal structure and piezoelectric effect. Electron–phonon interaction is studied, and it is shown that, in contrast to bulk samples, its piezoelectric part has a complicated dependence on the phonon frequency. *© 2004 MAIK "Nauka/Interperiodica".*

1. INTRODUCTION

Nanotubes (NTs) continue to be one of the most promising objects of study in the physics of low-dimensional systems. The majority of publications in this field are concerned with carbon NTs (e.g., see [1] and references therein). However, recent years have seen progress in the technology of the preparation of semiconductor NTs of III–V compounds, Ge, and Si. The method for rolling up double layers [2–4] suggested by Prinz and coworkers makes it possible to obtain NTs in which the radius and wall thickness are controllable parameters and can be varied over rather wide limits. Despite the similarity between the electronic processes in semiconductor NTs and the corresponding processes in carbon NTs, they also have a number of substantial differences. In this paper, we study the electron–phonon interaction in semiconductor III–V NTs, for which we must naturally first find the vibration eigenmodes of an NT. For carbon NTs, this problem was considered in a recent study by Suzuura and Ando [5]. Our study differs from [5] in a number of significant ways. First, due to elastic isotropy of a layer of two-dimensional graphite, the vibration problem for carbon NTs can be solved in the isotropic-continuum approximation, as was done in [5] (the medium was described by only two elastic moduli). In the case of rolled-up III–V quantum wells, we take into account three elastic moduli of a cubic crystal. Second, both for the vibration problem and for the problem of electron–phonon interaction, we make allowance for the piezoelectric effect, which is important for III–V crystals. Third, it will be shown that the piezoelectric interaction of acoustic phonons with two-dimensional electrons "attached" to the surface of a hollow cylinder differs significantly from the electron–phonon interaction in bulk samples. As far as we know, this problem has not yet been discussed in the literature.

2. EIGENVIBRATIONS OF A HOLLOW CYLINDER

We consider an NT obtained by rolling up a quantum film of a cubic crystal. The normal to the film surface corresponds to the [100] direction and the tube axis, to the [001] direction (Fig. 1). We introduce a cylindrical system of coordinates in which the z axis coincides with the axis of the cylindrical shell and r and α are the polar coordinates in the plane perpendicular to the cylinder axis. Let R be the radius of the median surface of the tube and h be its thickness. Thus, in the absence of vibrations, the tube occupies the volume bounded by $-h/2 \le r \le h/2$ (the coordinate r is measured from the median surface) and $0 \le z \le L$, where L is the tube length. A cylindrical shell obtained by rolling the film up is, strictly speaking, stressed, and there is uniaxial tensile–compressive strain in it (the sign of the strain is different on different sides of the median surface). Clearly, for $R \gg a_0$ (a_0 is the lattice constant), these strains are small. From obvious considerations of symmetry, it follows that the relation between the stress tensor and the strain tensor is the same as in a flat film of a cubic crystal: there are only three independent components of the tensor of elastic moduli and one independent component of the tensor of piezoelectic

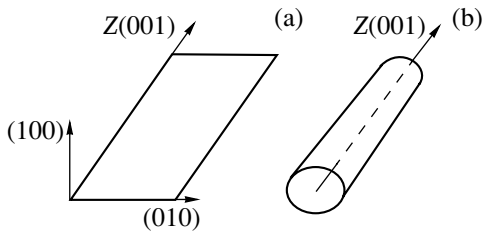

Fig. 1. (a) A quantum film, (b) a rolled-up nanotube.

1063-7826/04/3811-1316$26.00 © 2004 MAIK "Nauka/Interperiodica"

moduli, although the absolute values of the constants may differ from those for a flat film (the difference is small for $R \gg a_0$). Therefore, the stress tensor can be written as

$$\sigma_{ij} = \lambda_{ijkl} u_{kl} - e_{kij} E_k, \tag{1}$$

where λ_{ijkl} is the tensor of elastic moduli, e_{kij} is the tensor of piezoelectic moduli, E_k is the electric-field vector, and u_{kl} is the strain tensor. The independent components of the tensor of elastic moduli are $\lambda_{iiii} \equiv \lambda_{11}$, $\lambda_{iijj} \equiv \lambda_{12}$, and $\lambda_{ijij} \equiv \lambda_{44}$, where the indices i and j may assume any of the three values z, r, and α ($i \neq j$). The independent component of the tensor of piezoelectic moduli is $e_{ijk} \equiv e_{14}$, where i, j, and k may also assume any of the three values z, r, and α and all three indices should be different.

Generally, the solution to the complete three-dimensional problem is extremely complicated. Nevertheless, there are methods for reducing the three-dimensional problem to a two-dimensional one, which are valid for quite thin shells ($h \ll R$). One such method is based on the use of the hypothesis of nondeformable normals (the Kirchhoff–Love hypothesis; for example, see [6]). According to this hypothesis, any fiber normal to the median surface before deformation remains straight and normal to the modified median surface after deformation as well. At the same time, the length of the fiber perpendicular to the shell remains unchanged.

We consider a layer in the shell at a distance r from the median surface ($-h/2 \le r \le h/2$). We take into account the variation in the curvature of this layer compared to the curvature of the median surface. Then we obtain the following expressions for the strain:

$$\begin{aligned}
u^r_{\alpha\alpha} &= \frac{1}{R+r}\frac{\partial u^r}{\partial \alpha} + \frac{w^r}{R+r}, \\
u^r_{zz} &= \frac{\partial v^r}{\partial z}, \\
u^r_{z\alpha} &= \frac{1}{2}\left(\frac{\partial u^r}{\partial z} + \frac{1}{R+r}\frac{\partial v^r}{\partial \alpha}\right), \\
u^r_{r\alpha} &= \frac{1}{2}\left(\frac{\partial u^r}{\partial r} - \frac{u^r}{R+r} + \frac{1}{R+r}\frac{\partial w^r}{\partial \alpha}\right), \\
u^r_{rr} &= \frac{\partial w^r}{\partial r}, \\
u^r_{rz} &= \frac{1}{2}\left(\frac{\partial v^r}{\partial r} + \frac{\partial w^r}{\partial z}\right).
\end{aligned} \tag{2}$$

Here, u^r_{ij} are components of the strain tensor and (u^r, v^r, w^r) are the components of the displacement vector over the azimuthal angle, along a tube, and over the tube radius, respectively. The same values without the superscript r refer to the median layer.

According to the hypothesis of nondeformable normals, we must set $\sigma_{r\alpha} = \sigma_{rz} = \sigma_{rr} = 0$. Expanding these expressions, we obtain

$$\begin{aligned}
2\lambda_{44} u^r_{r\alpha} + e_{14}\frac{\partial \varphi}{\partial z} &= 0, \\
2\lambda_{44} u^r_{rz} + e_{14}\frac{1}{R+r}\frac{\partial \varphi}{\partial \alpha} &= 0, \\
\lambda_{11} u^r_{rr} + \lambda_{12}(u^r_{zz} + u^r_{\alpha\alpha}) &= 0,
\end{aligned} \tag{3}$$

where φ is the electrostatic potential. We rewrite the first two equations of system (3) in terms of the displacement vector:

$$\begin{aligned}
\lambda_{44}\left(\frac{\partial u^r}{\partial r} - \frac{u^r}{R+r} + \frac{1}{R+r}\frac{\partial w^r}{\partial \alpha}\right) + e_{14}\frac{\partial \varphi}{\partial z} &= 0, \\
\lambda_{44}\left(\frac{\partial w^r}{\partial z} + \frac{\partial v^r}{\partial r}\right) + e_{14}\frac{1}{R+r}\frac{\partial \varphi}{\partial \alpha} &= 0.
\end{aligned} \tag{4}$$

For the points of a straight fiber, normal to the median surface, the derivatives $\frac{\partial u^r}{\partial r}$ and $\frac{\partial v^r}{\partial r}$ must remain constant and equal to

$$\frac{\partial u^r}{\partial r} = \frac{u^r - u}{r}, \quad \frac{\partial v^r}{\partial r} = \frac{v^r - v}{r}. \tag{5}$$

We substitute expressions (5) into Eqs. (4). If we also take into account that, in the first approximation, we can set $w^r = w$, we obtain

$$\begin{aligned}
u^r &= \left(1 + \frac{r}{R}\right)u - \frac{r}{R}\frac{\partial w}{\partial \alpha} - \frac{r(R+r)}{R}\frac{e_{14}}{\lambda_{44}}\frac{\partial \varphi}{\partial z}, \\
v^r &= v - r\frac{\partial w}{\partial z} - \frac{r}{R+r}\frac{e_{14}}{\lambda_{44}}\frac{\partial \varphi}{\partial \alpha}.
\end{aligned} \tag{6}$$

We express the components of the strain tensor in terms of the displacement at the median surface:

$$\begin{aligned}
u^r_{\alpha\alpha} &= \frac{1}{R}\frac{\partial u}{\partial \alpha} - \frac{r}{R(R+r)}\frac{\partial^2 w}{\partial \alpha^2} - \frac{r}{R}\frac{e_{14}}{\lambda_{44}}\frac{\partial^2 \varphi}{\partial z \partial \alpha} + \frac{w}{R+r}, \\
u^r_{zz} &= \frac{\partial v}{\partial z} - r\frac{\partial^2 w}{\partial z^2} - \frac{r}{R+r}\frac{e_{14}}{\lambda_{44}}\frac{\partial^2 \varphi}{\partial z \partial \alpha}, \\
u^r_{z\alpha} &= \frac{1}{2}\left(\frac{1}{R+r}\frac{\partial v}{\partial \alpha} + \left(1 + \frac{r}{R}\right)\frac{\partial u}{\partial z} - \frac{r(2R+r)}{R(R+r)}\frac{\partial^2 w}{\partial z \partial \alpha}\right. \\
&\quad \left. - \frac{r}{(R+r)^2}\frac{e_{14}}{\lambda_{44}}\frac{\partial^2 \varphi}{\partial \alpha^2} - \frac{r(R+r)}{R}\frac{e_{14}}{\lambda_{44}}\frac{\partial^2 \varphi}{\partial z^2}\right), \\
u^r_{r\alpha} &= -\frac{e_{14}}{2\lambda_{44}}\frac{\partial \varphi}{\partial z}, \\
u^r_{rr} &= -\frac{\lambda_{12}}{\lambda_{11}}\left(\frac{1}{R}\frac{\partial u}{\partial \alpha} + \frac{\partial v}{\partial z} - r\frac{\partial^2 w}{\partial z^2} - \frac{r}{R(R+r)}\frac{\partial^2 w}{\partial \alpha^2}\right.
\end{aligned} \tag{7}$$

$$+\frac{w}{R+r}-\frac{r(2R+r)}{R(R+r)}\frac{e_{14}}{\lambda_{44}}\frac{\partial^2\varphi}{\partial z\partial\alpha}\Big),$$

$$u_{rz}^r = -\frac{e_{14}}{2\lambda_{44}}\frac{1}{R+r}\frac{\partial\varphi}{\partial\alpha}.$$

Now we can find the nonzero components of the stress tensor,

$$\sigma_{\alpha\alpha}^r = \frac{\lambda_{11}^2-\lambda_{12}^2}{\lambda_{11}}\Big(\frac{1}{R}\frac{\partial u}{\partial\alpha}+\frac{w}{R+r}-\frac{r}{R(R+r)}\frac{\partial^2 w}{\partial\alpha^2}$$
$$-\frac{r}{R}\frac{e_{14}}{\lambda_{44}}\frac{\partial\varphi}{\partial z\partial\alpha}\Big)+\frac{\lambda_{12}(\lambda_{11}-\lambda_{12})}{\lambda_{11}}$$
$$\times\Big(\frac{\partial v}{\partial z}-r\frac{\partial^2 w}{\partial z^2}-\frac{r}{R+r}\frac{e_{14}}{\lambda_{44}}\frac{\partial^2\varphi}{\partial z\partial\alpha}\Big),$$

$$\sigma_{zz}^r = \frac{\lambda_{11}^2-\lambda_{12}^2}{\lambda_{11}}\Big(\frac{\partial v}{\partial z}-r\frac{\partial^2 w}{\partial z^2}-\frac{r}{R+r}\frac{e_{14}}{\lambda_{44}}\frac{\partial\varphi}{\partial z\partial\alpha}\Big)$$
$$+\frac{\lambda_{12}(\lambda_{11}-\lambda_{12})}{\lambda_{11}}\Big(\frac{1}{R}\frac{\partial u}{\partial\alpha}+\frac{w}{R+r}$$
$$-\frac{r}{R(R+r)}\frac{\partial^2 w}{\partial\alpha^2}-\frac{r}{R}\frac{e_{14}}{\lambda_{44}}\frac{\partial^2\varphi}{\partial z\partial\alpha}\Big), \quad (8)$$

$$\sigma_{z\alpha}^r = \lambda_{44}\Big(\Big(1+\frac{r}{R}\Big)\frac{\partial u}{\partial z}+\frac{1}{R+r}\frac{\partial v}{\partial\alpha}-\frac{r(2R+r)}{R(R+r)}\frac{\partial^2 w}{\partial z\partial\alpha}\Big)$$
$$-\frac{r}{(R+r)^2}e_{14}\frac{\partial^2\varphi}{\partial\alpha^2}-\frac{r(R+r)}{R}e_{14}\frac{\partial^2\varphi}{\partial z^2}+e_{14}\frac{\partial\varphi}{\partial r}.$$

Next, we have to find the relation between the displacement of the median layer and the potential φ. Deformations of piezoelectric semiconductors are accompanied by polarization **P**, which is related to the strain tensor as

$$P_i = e_{ikj}u_{ik}. \quad (9)$$

The electric potential φ(**r**) can be found from the Poisson equation div**D** = 0, where the electric displacement vector is $D_i = \varepsilon E_i + 4\pi e_{ijk}u_{jk}$. Thus, the Poisson equation becomes

$$-\varepsilon\Delta\varphi + 4\pi e_{ijk}\frac{\partial u_{jk}}{\partial x_i} = 0. \quad (10)$$

We assume that, in an NT, an acoustic wave with a quasi-momentum q directed along the NT with azimuthal quantum number m is excited. The displacement vector in this case is $(u, v, w)\exp(iqz + im\alpha - i\omega t)$. Taking into account that the NT wall thickness is much smaller than its radius, we search for the solution in the form of the expansion

$$\varphi = \Big(\varphi_0(q,m)+\varphi_1(q,m)\frac{r}{R}+\varphi_2(q,m)\frac{r^2}{R^2}\Big)$$
$$\times\exp[iqz+im\alpha-i\omega t]. \quad (11)$$

After substituting the potential in the form (11) into the Poisson equation (10), we obtain in the zeroth approximation in r

$$-\Big(\varepsilon+\frac{8\pi e_{14}^2}{\lambda_{44}}\Big)\Big(q^2+\frac{m^2}{R^2}\Big)\varphi_0+\varepsilon\frac{\varphi_1+2\varphi_2}{R^2}$$
$$=4\pi e_{14}\Big(-\frac{im}{R^2}v+\frac{iq}{R}u+\frac{2mq}{R}w\Big). \quad (12)$$

This equation must be supplemented by boundary conditions:

$$q\frac{I_m'(qR-qh/2)}{I_m(qR-qh/2)}\Big(\varphi_0-\varphi_1\frac{h}{2R}+\varphi_2\frac{h^2}{4R^2}\Big)$$
$$=\varepsilon\Big(\frac{\varphi_1}{R}-\varphi_2\frac{h}{R^2}\Big)-8\pi e_{14}u_{\alpha z}\big|_{r=-h/2}, \quad (13)$$

$$q\frac{K_m'(qR+qh/2)}{K_m(qR+qh/2)}\Big(\varphi_0+\varphi_1\frac{h}{2R}+\varphi_2\frac{h^2}{4R^2}\Big)$$
$$=\varepsilon\Big(\frac{\varphi_1}{R}+\varphi_2\frac{h}{R^2}\Big)-8\pi e_{14}u_{\alpha z}\big|_{r=h/2}. \quad (14)$$

Here, I_m and K_m are the Bessel functions of imaginary argument of the first and third kind, respectively, and I_m' and K_m' are their derivatives. The components of the strain tensor $u_{\alpha z}$ in Eqs. (13) and (14) are taken on the inner ($r = -h/2$) and outer ($r = h/2$) surfaces of the NT, respectively. Using Eqs. (12)–(14), we find φ_0, φ_1, and φ_2 in the leading approximation in h:

$$\varphi_0 = \frac{2\pi e_{14}h}{\varepsilon}(qR(I_m'K_m+I_mK_m')+2\varepsilon I_mK_m)$$
$$\times\Big(\frac{im}{R}v+iqu\Big),$$
$$\varphi_1 = \frac{4\pi e_{14}R}{\varepsilon}\Big(\frac{im}{R}v+iqu\Big), \quad (15)$$
$$\varphi_2 = -\frac{4\pi e_{14}R}{\varepsilon}\Big(\frac{im}{R}v-mqw\Big).$$

In (15), the product qR appears in the arguments of the Bessel functions and their derivatives. By substituting (15) into (11), we obtain the final expressions for φ. Next, we use the formulas for the stress, moments, and the equations of motion of an element of the shell known in the theory vibrations of elastic shells (see, e.g., [6]). We then obtain the equations of motion (with

allowance for the piezoelectric effect), where the only unknowns are the displacements of the median layer:

$$\frac{\lambda_{11}^2-\lambda_{12}^2}{\lambda_{11}}\left(\frac{1}{R^2}\frac{\partial^2 u}{\partial\alpha^2}+\frac{1}{R^2}\frac{\partial w}{\partial\alpha}\right)$$
$$+\frac{\lambda_{12}(\lambda_{11}-\lambda_{12})}{\lambda_{11}}\left(\frac{1}{R}\frac{\partial^2 v}{\partial z\partial\alpha}-\frac{h^2}{12R^2}\frac{\partial^3 w}{\partial z^2\partial\alpha}\right)$$
$$+\lambda_{44}\left(\frac{1}{R}\frac{\partial^2 v}{\partial z\partial\alpha}+\left(1+\frac{h^2}{4R^2}\right)\frac{\partial^2 u}{\partial z^2}-\frac{h^2}{4R^2}\frac{\partial^3 w}{\partial z^2\partial\alpha}\right)$$
$$+\frac{4\pi e_{14}^2}{\varepsilon}\left(\frac{1}{R}\frac{\partial^2 v}{\partial z\partial\alpha}+\frac{\partial^2 u}{\partial z^2}\right)=\rho\frac{\partial^2 u}{\partial t^2},$$

$$\frac{\lambda_{11}^2-\lambda_{12}^2}{\lambda_{11}}\left(\frac{\partial^2 v}{\partial z^2}-\frac{h^2}{12R^2}\frac{\partial^3 w}{\partial z^3}\right)$$
$$+\frac{\lambda_{12}(\lambda_{11}-\lambda_{12})}{\lambda_{11}}\left(\frac{1}{R}\frac{\partial^2 u}{\partial z\partial\alpha}+\frac{1}{R}\frac{\partial w}{\partial z}\right)$$
$$+\lambda_{44}\left(\frac{1}{R}\frac{\partial^2 u}{\partial z\partial\alpha}+\left(1+\frac{h^2}{12R^2}\right)\frac{1}{R^2}\frac{\partial^2 v}{\partial\alpha^2}+\frac{h^2}{12R^3}\frac{\partial^3 w}{\partial z\partial\alpha^2}\right) \quad (16)$$
$$+\frac{4\pi e_{14}^2}{\varepsilon}\left(\frac{1}{R}\frac{\partial^2 u}{\partial z\partial\alpha}+\frac{1}{R^2}\frac{\partial^2 v}{\partial\alpha^2}\right)=\rho\frac{\partial^2 v}{\partial t^2},$$

$$\frac{\lambda_{11}^2-\lambda_{12}^2}{\lambda_{11}}\left(-\frac{h^2}{12}\left(\frac{1}{R^4}\frac{\partial^4 w}{\partial\alpha^4}+\frac{\partial^4 w}{\partial z^4}\right)-\frac{h^2}{6R^4}\frac{\partial^2 w}{\partial\alpha^2}\right.$$
$$\left.-\frac{1}{R^2}\left(1+\frac{h^2}{12R^2}\right)w-\frac{1}{R^2}\frac{\partial u}{\partial\alpha}+\frac{h^2}{12R}\frac{\partial^3 v}{\partial z^3}\right)$$
$$+\frac{\lambda_{12}(\lambda_{11}-\lambda_{12})}{\lambda_{11}}\left(-\frac{1}{R}\frac{\partial v}{\partial z}-\frac{h^2}{6R^2}\frac{\partial^4 w}{\partial z^2\partial\alpha^2}+\frac{h^2}{12R^2}\frac{\partial^3 u}{\partial z^2\partial\alpha}\right)$$
$$+\lambda_{44}\left(-\frac{h^2}{3R^2}\frac{\partial^4 w}{\partial z^2\partial\alpha^2}+\frac{h^2}{4R^2}\frac{\partial^3 u}{\partial z^2\partial\alpha}-\frac{h^2}{12R^3}\frac{\partial^3 v}{\partial z\partial\alpha^2}\right)$$
$$=\rho\frac{\partial^2 w}{\partial t^2}.$$

Thus, we reduced the three-dimensional problem to a two-dimensional one. These equations completely define small vibrations of crystalline thin cylindrical shells. Substituting the solution in the form of plane waves, we obtain three linear algebraic equations for amplitudes of displacements of the median layer (u, v, w). The condition of existence of a nontrivial solution of the obtained homogeneous system of equations determines the dispersion relation for acoustoelectric vibrations. The general expression is rather complicated; here we consider two special cases, $m = 0$ and 1, where m is the azimuthal quantum number of acoustic phonons that determines the dependence of the displacements on α in terms of the factor $\exp(im\alpha)$.

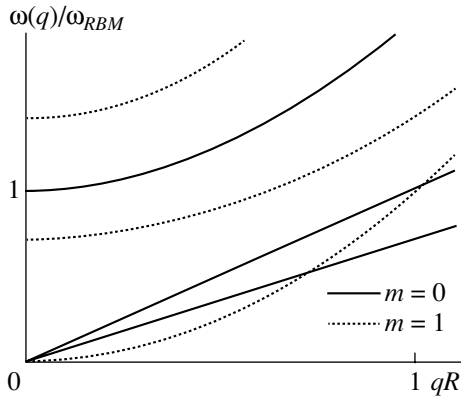

Fig. 2. Frequencies of vibration modes as functions of q in the long-wavelength limit for $m = 0$ and 1.

For $m = 0$, the frequency of a transverse (in-plane) wave in the long-wavelength limit is equal to $\omega_1 = q\sqrt{\lambda_{44}/\rho + 4\pi e_{14}^2/\varepsilon\rho}$. The displacement eigenvector of such a torsional mode is directed along the azimuth, $\xi = (1, 0, 0)$. The frequency of the radial ("breathing") mode also remains finite in the long-wavelength limit and is equal to $\omega_2 = 1/R\sqrt{(\lambda_{11}^2-\lambda_{12}^2)/\rho\lambda_{11}}$. The polarization vector of this mode is directed along the radius, $\xi = (0, 0, 1)$. Finally, the third mode is a longitudinal acoustic wave, whose frequency is equal to $\omega_3 = q\sqrt{(\lambda_{11}-\lambda_{12})(\lambda_{11}+2\lambda_{12})/\rho(\lambda_{11}+\lambda_{12})}$. The corresponding eigenvector is directed along the tube axis, $\xi = (0, 1, 0)$.

For $m = 1$ in the long-wavelength limit ($qR \ll 1$), three independent vibration modes are also obtained:

$$\omega_1 = \frac{1}{R}\sqrt{2\frac{\lambda_{11}^2-\lambda_{12}^2}{\rho\lambda_{11}}},\quad \xi = (1/\sqrt{2}, 0, i/\sqrt{2});$$
$$\omega_2 = \frac{1}{R}\sqrt{\frac{\lambda_{44}}{\rho}+\frac{4\pi e_{14}^2}{\varepsilon\rho}},\quad \xi = (0, 1, 0);$$
$$\omega_3 = \sqrt{\frac{(\lambda_{11}-\lambda_{12})(\lambda_{11}+2\lambda_{12})}{\rho(\lambda_{11}+\lambda_{12})}}q^2R, \quad (17)$$
$$\xi = (1/\sqrt{2}, 0, -i/\sqrt{2}).$$

All these branches are doubly degenerate, since in the case $m = -1$ we have the same result, except for the polarization vectors, which have to be replaced by their complex conjugate values. The result for ω_3 in (17) corresponds to the dispersion relation of flexural waves in elastic rods (see [7]). Equations (16) with $e_{14} = 0$ and

$h = 0$ coincide with Eqs. (2.5) in [5] if the following relations are satisfied (in the notation of [5]):

$$\frac{\mu}{M} = \frac{\lambda_{44}}{\rho}, \quad \frac{B+\mu}{M} = \frac{\lambda_{11}^2 - \lambda_{12}^2}{\rho\lambda_{11}}, \quad \frac{B}{M} = \frac{\lambda_{12}(\lambda_{11}-\lambda_{12})}{\rho\lambda_{11}} + \frac{\lambda_{44}}{\rho}. \tag{18}$$

The compatibility condition for these relations is $\lambda_{11} - \lambda_{12} - 2\lambda_{44} = 0$, which corresponds to the transition to an isotropic elastic medium.

Figure 2 shows the spectra of vibration modes with $m = 0; 1$ in the long-wavelength limit. We can see that there is a wave with quadratic dispersion at small q. At extremely low temperatures $T \ll s/R$, where s is a quantity on the order of the velocity of sound, these vibrations play a dominant role in NT thermodynamics and kinetics. In contrast to flexural waves in a thin plate that also have a quadratic relation between ω and q, the obtained solution ω_3 does not contain the shell thickness h.

Now we will discuss the solutions with $m > 1$. For $k = 0$, the characteristic determinant is given by

$$\begin{Vmatrix} \frac{\lambda_{11}^2 - \lambda_{12}^2}{\lambda_{11}}\frac{m^2}{R^2} - \rho\omega^2 & 0 & -\frac{im}{R^2}\frac{\lambda_{11}^2 - \lambda_{12}^2}{\lambda_{11}} \\ 0 & \left(\lambda_{44}\left(1 + \frac{h^2}{12R^2}\right) + \frac{4\pi e_{14}^2}{\varepsilon}\right)\frac{m^2}{R^2} - \rho\omega^2 & 0 \\ \frac{im}{R^2}\frac{\lambda_{11}^2 - \lambda_{12}^2}{\lambda_{11}} & 0 & \frac{\lambda_{11}^2 - \lambda_{12}^2}{\lambda_{11}}\left(\frac{h^2(m^2-1)^2}{12R^4} + \frac{1}{R^2}\right) - \rho\omega^2 \end{Vmatrix} = 0. \tag{19}$$

In the limit $h/R \ll 1$, we readily obtain

$$\omega_1 = \sqrt{\frac{\lambda_{44}}{\rho}\left(1 + \frac{h^2}{12R^2}\right) + \frac{4\pi e_{14}^2}{\varepsilon\rho}}\frac{m}{R}, \quad \omega_2 = \sqrt{\frac{\lambda_{11}^2 - \lambda_{12}^2}{\rho\lambda_{11}}}\frac{\sqrt{m^2+1}}{R}, \quad \omega_3 = \sqrt{\frac{\lambda_{11}^2 - \lambda_{12}^2}{\rho\lambda_{11}}}\frac{m(m^2-1)}{\sqrt{m^2+1}}\frac{h}{2\sqrt{3}R}. \tag{20}$$

Thus, all waves with $m > 1$ exhibit a gap dispersion (with $\omega \neq 0$ for $k = 0$), although the gap in ω_3 has an additional smallness in h/R.

3. ELECTRON–PHONON INTERACTION

Now we consider the interaction of acoustic phonons with electrons via the piezoelectric potential. The interaction Hamiltonian has the form $H_{\text{piezo}} = -e\varphi(\mathbf{r})$. This expression must be averaged over the ground state for the radial motion of electrons in the NT. As a result, the contribution linear in r in (11) vanishes and the quadratic contribution is relatively small for $h/R \ll 1$; i.e., in the principal order of magnitude, we have $\langle\varphi\rangle = \varphi_0$.

The operator of the relative displacement in the interaction representation is written as

$$\boldsymbol{\eta}(\mathbf{r}) = \sum_{q,m,s}\sqrt{\frac{\hbar}{2S\rho\omega_s(q,m)}}c_s(q,m)\xi(q,m) + \text{c.c.}, \tag{21}$$

where ξ is the vibration eigenvector normalized to unity. For different modes, its components are written out in (17). Now we can find the interaction Hamiltonian

$$H_{\text{piezo}} = \sum_{q,m,s} V(q,m)c_s(q,m) + \text{c.c.},$$

where

$$V(q,m) = \frac{2\pi e e_{14} h}{\varepsilon}(qR(\mathrm{I}'_m\mathrm{K}_m + \mathrm{I}_m\mathrm{K}'_m) + 2\varepsilon\mathrm{I}_m\mathrm{K}_m) \times\left(qu_0 + \frac{m}{R}v_0\right)\sqrt{\frac{\hbar}{2S\rho\omega_s(q,m)}}. \tag{22}$$

Here, u_0 and v_0 are the components of the polarization vector $\xi = (u_0, v_0, w_0)$. We can see from (22) that, in contrast to a bulk situation, piezoelectric interaction in NTs depends on the phonon wave vector in a rather complicated way.

Electron–phonon interaction via deformation potential has the usual form, $H_{\text{def}} = E_a\text{div}\boldsymbol{\eta}$, where E_a is the deformation-potential constant. Substituting $\boldsymbol{\eta}(\mathbf{r})$ into this expression, we obtain

$$H_{\text{def}} = \sum_{q,m,s}\Gamma(q,m)c_s(q,m) + \text{c.c.},$$

where

$$\Gamma(q,m) = \left(iqv_0 + i\frac{m}{R}u_0\right)\sqrt{\frac{\hbar E_a^2}{2S\rho\omega_s(q,m)}}. \tag{23}$$

For an axially symmetric ($m = 0$) vibration mode, electrons interact by the piezoelectric mechanism only with transverse phonons (the polarization vector $\xi = (1, 0, 0)$). There is no interaction with such phonons via deformation potential ($\mathrm{div}\xi = 0$), but there is a deformation electron–phonon interaction for other branches of the vibration spectrum. For $m = 1$, electrons interact with all phonon branches both via the deformation potential and by the piezoelectric mechanism.

Let us consider piezoelectric interaction in the limiting cases $qR \gg 1$ and $qR \ll 1$ and compare its contribution with the contribution of the deformation interaction. In addition, we shall be interested in the difference of the piezoelectric interaction in an NT from that in the 3D case.

In the limit of large radii, $qR \gg 1$, electrons interact with transverse phonons ($m = 0, 1$). Matrix element (22) assumes the asymptotic form

$$V(q, m) = \frac{\pi e e_{14} h}{R}\frac{2\varepsilon - 1}{\varepsilon}\sqrt{\frac{\hbar}{2S\rho\omega_s(q, m)}}. \quad (24)$$

It follows from (24) that the frequency dependence of the interaction amplitude is the same as in the 3D case,

$$V_{3D} = \frac{4\pi e e_{14}}{\varepsilon}\sqrt{\frac{\hbar}{2V\rho_{3D}\omega}}; \quad (25)$$

here, V is the volume and ρ_{3D} is the bulk density.

In this limiting case, the interaction via the piezoelectric potential is less important than the interaction via the deformation potential. The ratio of the corresponding matrix elements is on the order of $\frac{2\pi e e_{14} h}{qRE_a}$. For a GaAs-based NT with a wall thickness of $h = 10$ Å, this parameter is on the order of $1/qR \ll 1$. At $h/R \longrightarrow 0$, the piezoelectric interaction vanishes, as in the case of a plate.

We now consider the case $qR \ll 1$. For an axially symmetric phonon ($m = 0$) in this long-wavelength limit, electrons interact via the deformation potential only with longitudinal waves and via the piezoelectric potential only with transverse waves. In this case, we use (22) to obtain the following expression for the quantity $V(q, 0)$:

$$V(q, 0) \approx 4\pi e e_{14} h\left(\ln\frac{2}{qR} - C - \frac{1}{2\varepsilon}\right)q\sqrt{\frac{\hbar}{2S\rho\omega_1(q, 0)}}. \quad (26)$$

Here, C is the Euler constant. It follows from (24) and (26) that, in the long-wavelength limit, the frequency dependence differs from that for the bulk case. The ratio of the amplitude of electron–phonon interaction via piezoelectric potential in an NT to the corresponding quantity in a bulk sample is

$$\frac{V_{NP}}{V_{3D}} = \varepsilon q h \ln\frac{2}{qR}. \quad (27)$$

Thus, the piezoelectric interaction in an NT is weaker than in the bulk. Nevertheless, with increasing wavelength, the role of piezoelectric interaction increases relative to the deformation interaction. Indeed, the amplitude of the deformation potential is given by

$$\Gamma(q, 0) = iq\sqrt{\frac{\hbar E_a^2}{2S\rho\omega_s(q, 0)}}. \quad (28)$$

The ratio of the amplitudes is

$$\left|\frac{V}{\Gamma}\right| \approx \frac{4\pi e e_{14} h}{E_a}\left(\ln\frac{2}{qR} - C - \frac{1}{2\varepsilon}\right)\sqrt{\frac{s_\parallel}{s_\perp}}, \quad (29)$$

where $s_\parallel$ and $s_\perp$ are the longitudinal and transverse velocities of acoustic phonons.

For phonons with $m = 1$ in the long-wavelength limit, the electrons interact via the deformation potential only with the flexural wave and via the piezoelectric potential with both flexural and longitudinal waves. In these three cases, we obtain expressions for the amplitudes of the deformation potential and of the piezoelectric potential:

$$\Gamma(q, 1) = \frac{i}{R\sqrt{2}}\sqrt{\frac{\hbar E_a^2}{2S\rho\omega_3(q, 1)}},$$
$$V_b(q, 1) \approx 2\pi e e_{14} h\frac{q}{\sqrt{2}}\sqrt{\frac{\hbar}{2S\rho\omega_3(q, 1)}}, \quad (30)$$
$$V_\parallel(q, 1) \approx 2\pi e e_{14} h\frac{1}{R}\sqrt{\frac{\hbar}{2S\rho\omega_3(q, 1)}}.$$

At $T \ll s/R$, the electrons interact only with the flexural wave, since its frequency tends to zero quadratically in k. We then obtain the following expression for the ratio of amplitudes:

$$\left|\frac{V}{\Gamma}\right| = \frac{2\pi e e_{14} h}{E_a}qR. \quad (31)$$

We can see from (29) and (31) that, in the long-wavelength limit at low temperatures ($T \ll s/R$), the contribution to electron–phonon interaction related to the piezoelectric potential is much smaller for intersubband transitions than for intrasubband transitions.

Thus, we found vibration eigenmodes of a semiconductor NT taking into account the crystal structure of III–V compounds and the piezoelectric effect. We also clarified the features of the piezoelectric electron–phonon interaction that distinguish NTs from bulk samples.

ACKNOWLEDGMENTS

This study was supported by the Russian Foundation for Basic Research (project no. 02-02-16377), a grant from the President of the Russian Federation for the Support of Leading Scientific Schools (grant no. NSh-593.2003.2), and the Ministry of Education of the Russian Federation (grant no. A03-2.9-861).

REFERENCES

1. H. Ajiki and T. Ando, J. Phys. Soc. Jpn. **62**, 1255 (1993).
2. V. Ya. Prinz, V. A. Seleznev, and A. K. Gutakovsky, *The Physics of Semiconductors* (World Sci., 1999).
3. A. K. Gutakovsky, V. V. Preobrazhenskii, M. A. Putyato, *et al.*, Physica E (Amsterdam) **6**, 828 (2000).
4. V. Ya. Prinz, Microelectron. Eng. **69**, 466 (2003).
5. H. Suzuura and T. Ando, Phys. Rev. B **65**, 235412 (2002).
6. A. S. Vol'mir, *Nonlinear Dynamics of Plates and Shells* (Nauka, Moscow, 1972) [in Russian].
7. L. D. Landau and E. M. Lifshitz, *Course of Theoretical Physics*, Vol. 7: *Theory of Elasticity*, 4th ed. (Pergamon, New York, 1986; Nauka, Moscow, 1987), Sect. 25.

Translated by I. Zvyagin

Semiconductors, Vol. 38, No. 11, 2004, pp. 1323–1325. Translated from Fizika i Tekhnika Poluprovodnikov, Vol. 38, No. 11, 2004, pp. 1364–1367.

LOW-DIMENSIONAL SYSTEMS

MOCVD-Grown AlGaN/GaN Heterostructures with High Electron Mobility

V. V. Lundin*^, E. E. Zavarin*, A. I. Besulkin*, A. G. Gladyshev*, A. V. Sakharov*, M. F. Kokorev, N. M. Shmidt*, A. F. Tsatsul'nikov*, N. N. Ledentsov*, Zh. I. Alferov*, and R. Kakanakov*****

**Ioffe Physicotechnical Institute, Russian Academy of Sciences, St. Petersburg, 194021 Russia*

^e-mail: lundin.vpegroup@mail.ioffe.ru

***St. Petersburg State Electrotechnical University, St. Petersburg, 197376 Russia*

****Institute of Applied Physics, Bulgarian Academy of Sciences, Plovdiv, Bulgaria*

Submitted March 10, 2004; accepted for publication March 16, 2004

Abstract—Specific features of MOCVD growth of AlGaN/GaN heterostructures have been studied. In the structures obtained, the 2D electron gas in the channel had a density of 1.2×10^{13} cm^{-2} and a mobility of 1290 cm^2/(V s) at room temperature. The effect of the purity of starting components on the properties of the structure is studied. *© 2004 MAIK "Nauka/Interperiodica".*

1. INTRODUCTION

Recently, field-effect transistors with high electron mobility in the channel (HEMT), based on AlGaN/GaN heterostructures with graded doping, has been the subject of a number of research projects in Japan, USA, and Europe [1–6]. The large values of the band gap, the band offset at the AlGaN–GaN heterointerface, the breakdown voltage, and some other specific features of the III–N system open up prospects for the design of transistors with parameters superior to those attained in III–V structures. Very high (on the order of 10^6 V/cm) built-in piezo- and pyroelectric fields exist in AlGaN/GaN heterostructures when the configuration of the structure is chosen correctly, which enhances the bending of the conduction band at the AlGaN/GaN interface, thus raising the carrier density in the channel. However, this specific feature, combined with the lattice mismatch typical of the AlN–GaN system, makes it difficult to optimize the configuration of the device's structure.

Several research centers have now demonstrated GaN-based HEMTs. Devices with a working frequency of several tens of gigahertz and a power of more than 100 W have been presented [7]. These devices are now leaving the laboratory research stage, and their mass production can be expected in the near future. At the same time, many specific features of graded-doped AlGaN/GaN heterostructures, both in epitaxial growth and physical processes, require thorough research.

2. EXPERIMENT

The structures under study were grown by MOCVD on (0001) sapphire substrates in a modified Epiquip VP 50-RP installation under reduced pressure. The installation was equipped with a horizontal quartz reactor with an inductively heated graphite substrate holder. The carrier gas was hydrogen; the precursors were ammonia, monosilane, trimethylgallium, and trimethylaluminum. All the listed compounds were of Russian manufacture. Ammonia of different purity was used, in accordance with the following rating: 99.999% (below, 5N) and 99.9999% (below, 6N). The growth temperature of epitaxial layers was 1070°C. Details of the epitaxial growth were published in [8].

The sequence of layers in the grown heterostructures was:

—undoped GaN with a thickness of 3 μm;

—undoped $Al_{0.25}Ga_{0.75}N$ with thickness d_1;

—Si-doped $Al_{0.25}Ga_{0.75}N$ with thickness d_2;

—undoped GaN with thickness d_3.

The thickness of layers d_1, d_2, and d_3 and molar flow rates of SiH_4 for the structures under study are listed in the table.

The grown structures were studied by measuring capacitance–voltage (C–V) characteristics with a mercury probe. The carrier density and mobility were determined from the Hall effect measurements using the van der Pauw method. The numerical modeling of the structures was performed by a self-consistent solution of the Poisson and Schrödinger equations taking into account the built-in piezo- and pyroelectric fields, with subsequent calculation of C–V characteristics using the weak-signal method [8–10].

3. RESULTS AND DISCUSSION

The electron density and mobility in the grown structures are listed in the table and shown in Fig. 1

Configuration of AlGaN/GaN structures and the data of the Hall effect measurements

Structure no.	NH_3	d_1, nm	d_2, nm	d_3, nm	SiH_4, nmol min^{-1}	300 K		77 K	
						μ, cm^2 V^{-1} s^{-1}	N_{2D}, 10^{13} cm^{-2}	μ, cm^2 V^{-1} s^{-1}	N_{2D}, 10^{13} cm^{-2}
1	6N	2.5	7.5	10	0.4	980	1.5	3460	1.6
2	6N	10	–	10	–	800	0.9	3050	0.8
3	6N	2.5	7.5	10	0.14	1209	1.1	5000	1.2
4	6N	5	15	10	0.4	990	2.1	2770	2.1
5	6N	12.5	7.5	10	0.4	900	1.9	3160	1.8
6	6N	2.5	7.5	10	0.3	1290	1.2	4800	1.3
7	5N	2.5	7.5	10	0.4	1060	1.5	4500	1.4
8	5N	10	–	10	–	660	1.6	3800	0.95

Note: The thickness of layers was determined from the results of preliminary calibration: d_1, $Al_{0.25}Ga_{0.75}N$; d_2, $Al_{0.25}Ga_{0.75}N$: Si; d_3, GaN.

(compared with the results of other studies). The high mobility, which significantly exceeds the carrier mobility in GaN epitaxial layers grown in similar conditions, indicates the formation of a 2D electron channel at the GaN–AlGaN interface.

To study the effect of ammonia purity on the electronic properties of (Al)GaN layers and graded-doped AlGaN/GaN heterostructures, we investigated nominally undoped GaN layers grown with 5N and 6N ammonia. It appeared that the density N_d–N_a in these layers was 10^{16} and 10^{14} cm^{-3}, respectively. In undoped AlGaN epitaxial layers grown using 5N ammonia, the background density N_d–N_a did not exceed 5×10^{17} cm^{-3}. So the strong variation of the background density in (Al)GaN layers is the source of the extremely strong effect of the purity of ammonia on the room-temperature electron density in undoped AlGaN/GaN structures. As follows from the data obtained in the Hall effect measurements, the use of 5N instead of 6N ammonia leads to a doubling of the electron density in the channel and a significant decrease in the room-temperature mobility (see table, structure nos. 2 and 8). The decrease in temperature to 77 K has virtually no influence on the carrier density in the undoped structure grown using 6N ammonia, nor on the carrier density in the doped structures. However, the carrier density in the undoped structure grown using 5N ammonia decreases by a factor of 1.5 as the temperature decreases from 300 to 77 K. At the same time, the difference in the density and mobility values between structure nos. 2 and 8 is not so strong. Thus, these data show that the use of 5N ammonia raises the background doping level in the GaN layer, which agrees with the above data for undoped GaN layers.

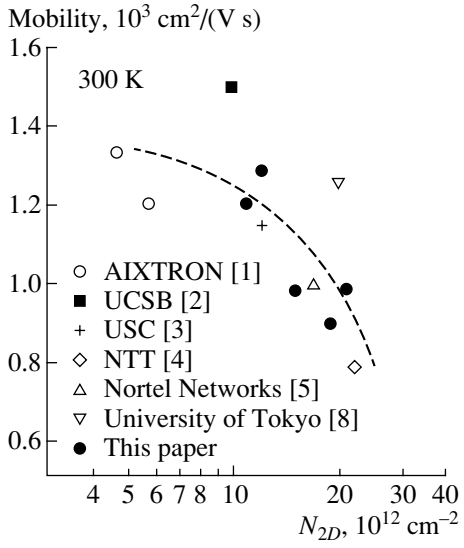

Fig. 1. Carrier mobility vs. carrier density in structures with 2D electron gas; comparison of results of the present study with the published data.

The doping of AlGaN with Si with the use of 5N ammonia (structure no. 7) results in a considerable increase (by a factor of 1.5) in the carrier density at T = 77 K, as compared to undoped structure no. 8. In this case, the room-temperature carrier mobility significantly decreases, while the carrier density remains virtually unchanged. These results also confirm the conclusion that the shunting conductance in the GaN layer makes a considerable contribution to the measured room-temperature conductance of structure no. 8. The results of the experiments performed suggest that it becomes virtually impossible to control carrier density by doping if 5N ammonia is used.

Note that, by using 5N ammonia, we had earlier successfully grown different types of light-emitting InGaN/GaN/AlGaN structures [11], including those with *p*–*n* junctions. Thus, AlGaN/GaN structures with a 2D electron gas are more sensitive to the purity of the ammonia used than light-emitting structures.

The analysis of carrier density and mobility dependences on the parameters of the structure has shown

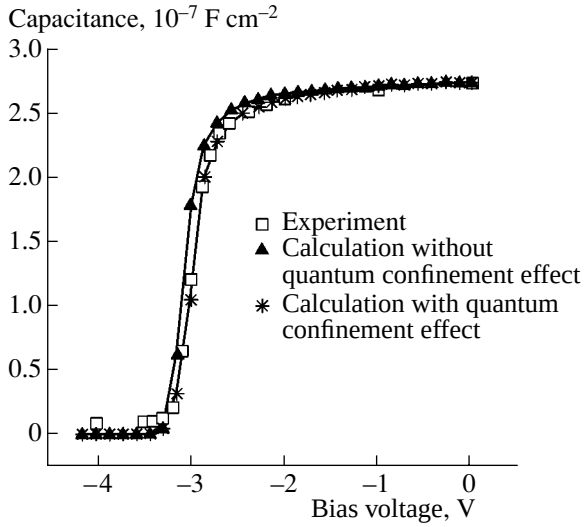

Fig. 2. Experimental and simulated *C–V* characteristics for structure no. 2 (see table).

that the carrier density in the channel depends not only on the doping level and thickness of the doped layer, but also on the thickness of the undoped AlGaN barrier layer (structure nos. 1, 5). An increase in the thickness of the undoped AlGaN layer results in an increase in the carrier density and a decrease in mobility in the channel. This behavior may be related to different factors: ionization of the background donor impurities in the AlGaN layer or an increase in the effective thickness of the 2D electron channel, which leads to the penetration of the electron wave function into the GaN layer and, accordingly, to an increase in scattering on the background impurities. In sample no. 3 with optimal structure parameters (thicknesses d_1–d_3, doping level), a mobility of 5000 cm^2/(V s) at T = 77 K was obtained.

It is evident that the ultimate optimization of transistor structures is possible only if it is based on the study of finished devices. Based on the structures grown, we fabricated prototypes of transistors that had demonstrated the possibility of controlling the source–drain current–voltage characteristics by varying the gate bias. Figure 2 shows experimental C–V characteristics and those calculated with and without taking into account the quantum confinement effect. This effect influences the shape of the C–V characteristic in the range in which the channel is shut off. The results obtained in determining the structure parameters by modeling for structure no. 2 demonstrate the high sensitivity of C–V characteristics to variations in the thickness of layers. Assuming that the effective barrier height is Φ_B = 0.5 eV, the thickness of layers is determined as d_1 = 14.3 nm and d_3 = 12.7 nm, which differs somewhat from the values set during the growth of the structure ($d_1 = d_3 =$ 10.0 nm). The calculated density of 2D electrons in the channel is 5×10^{12} cm^{-2}.

4. CONCLUSION

AlGaN/GaN heterostructures with a high mobility of carriers in the channel have been grown and investigated. A comparison between the results obtained and data reported earlier shows that the structure parameters are on a level with the highest world standards. It is also shown that the properties of these structures are to a significant extent dependent both on the design of the structure and on the purity of the precursors used (ammonia).

ACKNOWLEDGMENTS

This study was supported by the program of scientific cooperation between the Russian and Bulgarian Academies of Sciences (project no. 57, “New AlGaN/GaN Heterostructures for High-Power, High-Temperature, and High-Frequency Microelectronics”), “NATO for Peace” (grant SfP-972614), the Russian Foundation for Basic Research (project nos. 01-02-18011, 03-02-16657, 01-02-17646), and grants from the President of the Russian Federation for the support of young scientists and leading scientific schools.

REFERENCES

1. M. Marso, P. Javorka, A. Alam, *et al.*, Phys. Status Solidi A **188**, 199 (2001).
2. N. Zhang, B. Moran, S. P. DenBaars, *et al.*, Phys. Status Solidi A **188**, 213 (2001).
3. G. Simin, A. Tarakji, X. Hu, *et al.*, Phys. Status Solidi A **188**, 219 (2001).
4. N. Maeda, T. Saitoh, K. Tusubaki, and N. Kobayashi, Phys. Status Solidi A **188**, 223 (2001).
5. Y. Liu, J. A. Bardwell, S. P. McAlister, *et al.*, Phys. Status Solidi A **188**, 233 (2001).
6. B. Shen, T. Someya, and Y. Arakawa, Appl. Phys. Lett. **76**, 2746 (2000).
7. www.compoundsemiconductor.net/articles/news/7/12/12/1.
8. W. V. Lundin, A. V. Sakharov, A. F. Tsatsul’nikov, *et al.*, Phys. Status Solidi A **188**, 885 (2001).
9. M. F. Kokorev and N. A. Maleev, Semicond. Sci. Technol. **15**, 301 (2000).
10. M. F. Kokorev, N. A. Maleev, D. V. Pakhnin, *et al.*, in *Proceedings of 9th International Symposium on Nanostructures: Physics and Technology*, Ed. by Zh. Alferov and L. Esaki (St. Petersburg, Russia, 2001), p. 230.
11. A. S. Usikov, W. V. Lundin, B. V. Pushnyi, *et al.*, in *Proceedings of 7th International Conference on Silicon Carbide, III Nitrides and Related Materials, 1997* (Stockholm, 1997), Part 2, p. 1393.

Translated by D. Mashovets

Semiconductors, Vol. 38, No. 11, 2004, pp. 1326–1331. Translated from Fizika i Tekhnika Poluprovodnikov, Vol. 38, No. 11, 2004, pp. 1368–1373.

LOW-DIMENSIONAL SYSTEMS

Electron Magnetotransport in Coupled Quantum Wells with Double-Sided Doping

G. B. Galiev*, V. É. Kaminskiĭ*^, I. S. Vasil'evskiĭ, V. A. Kul'bachinskiĭ**, and R. A. Lunin****

**Institute of Ultrahigh Frequency Semiconductor Electronics, Russian Academy of Sciences, Moscow, 117105 Russia*

^e-mail: kamin@zelnet.ru

***Moscow State University, Moscow, 119992 Russia*

Submitted February 16, 2004; accepted for publication March 23, 2004

Abstract—Magnetoresistance in a weak magnetic field was measured in $Al_xGa_{1-x}As/GaAs/Al_xGa_{1-x}As$ structures with coupled quantum wells separated by a thin AlAs central barrier. The experimental data on negative magnetoresistance were analyzed in terms of the weak-localization model and in the kinetic approach using the density matrix. In some cases, the kinetics approach allows a more accurate description of the experimental data. © *2004 MAIK "Nauka/Interperiodica".*

1. INTRODUCTION

Currently, $Al_xGa_{1-x}As/GaAs/Al_xGa_{1-x}As$ structures are widely used in the fabrication of photodetectors, tunnel diodes, high-power transistors, and optoelectronic devices. Quite often, the desired characteristics of these structures are obtained using coupled quantum wells (QW), which are produced by dividing a GaAs QW with a thin AlAs barrier about three to four monolayers (ML) thick [1, 2]. In optoelectronic devices, a QW located between symmetrical $Al_xGa_{1-x}As$ barriers makes it possible to obtain the desired spectral characteristics. During the transverse (normal to the heterostructure plane) transport of electrons in these structures, the insertion of a barrier allows one to control the energy of the resonant level and, accordingly, the shape of the current–voltage characteristic. In FETs for microwave applications, the double-sided doping of $Al_xGa_{1-x}As/GaAs/Al_xGa_{1-x}As$ structures makes it possible to considerably enhance the output power [3–5].

The electrical characteristics of $Al_xGa_{1-x}As/GaAs/Al_xGa_{1-x}As$ QWs are of great interest also for fundamental physics. The study of magnetotransport in these structures makes it possible to understand better the mechanisms and parameters of electron scattering. For example, in longitudinal transport (in the plane of the structure), the variation of the barrier thickness changes the coupling between the wells and the electron scattering parameters [6, 7].

Galvanomagnetic effects in semiconductors are conventionally described using the method of the kinetic equation for the electron distribution function. In most cases, this approach is justified in a weak magnetic field. However, a great number of experimental data obtained up to now cannot be explained in terms of the classical approach. One of the examples is negative magnetoresistance (longitudinal and transverse). This effect is observed in various semiconductor objects not only in a weak, but also in a strong magnetic field. For example, both positive and negative magnetoresistance was observed at low temperatures in *n*-$Al_xGa_{1-x}As/GaAs$ heterostructures [8] and $Al_xGa_{1-x}As/GaAs/Al_xGa_{1-x}As$ QWs [9]. In structures with high mobility and density of electrons, the magnetoresistance was positive. In structures with low electron mobility, the magnetoresistance was first negative, but changed its sign as the magnetic field increased further.

In structures with low mobility and density of electrons, the magnetoresistance remains negative up to the field at which quantum oscillations arise. For example, in *n*-$GaAs/In_{0.07}Ga_{0.93}As/n$-GaAs heterostructures δ-doped with Si in the middle of the QW, negative magnetoresistance was observed up to ~6 T field in the temperature range 0.4–40 K [10]. At the same time, in $InP/In_{0.53}Ga_{0.47}As$ structures with higher mobility [11], positive magnetoresistance (antilocalization) was observed in the range of very weak magnetic fields in samples with a high surface density of electrons. For low electron densities, negative magnetoresistance was observed in the whole range of magnetic fields.

For the case of 2D degenerate electron gas with one filled subband, the classical magnetoresistance $\delta = \rho_{xx}(B)/\rho_0 - 1$ is zero. The well-known mechanism of positive magnetoresistance involves the filling of several subbands with different mobilities or the presence of several conducting layers in the structure. To explain negative magnetoresistance, Altshuler *et al.* [12] proposed the theory of quantum corrections to conductivity.

Recently [13, 14], another interpretation of negative magnetoresistance was proposed. Magnetotransport was described using the density matrix method, and the expressions for the conductivity tensor in an arbitrary

magnetic field were obtained. It was shown that negative magnetoresistance can be described without introducing concepts of weak localization.

To verify the theory [13, 14], we present the experimental data on magnetotransport in $Al_{1-x}Ga_xAs/GaAs/Al_{1-x}Ga_xAs$ structures with different QW widths. For comparative analysis, similar structures without a barrier and with a thin AlAs barrier in the middle of the QW were grown. Dependences of the resistivity tensor components on magnetic field B were measured at 4.2 K for these structures.

2. SAMPLE PREPARATION AND MEASUREMENT PROCEDURE

The samples under study were grown by MBE on semi-insulating (100) GaAs substrates misoriented by 2° in the [110] direction. First, a 0.5-μm-thick GaAs buffer layer was grown. Then an $Al_{0.2}Ga_{0.8}As$ barrier, GaAs QW, AlAs barrier, GaAs QW, and $Al_{0.2}Ga_{0.8}As$ barrier were grown. Finally, an 8-nm-thick GaAs capping layer was grown. Both QWs in a structure had the same width. Several parameters of the samples under study, including the AlAs barrier thickness b and the QW width W (the total width on both sides of the AlAs barrier) are listed in the table. The thickness of the $Al_{0.2}Ga_{0.8}As$ barriers that form the QW was also the same: 33 nm in all the structures. One half (across the thickness) of each barrier, adjacent to the QW, remained undoped, whereas the other half was doped with Si to ~$(1–2) \times 10^{18}$ cm^{-3}. The concentration of Si in the capping layer was the same. The GaAs and AlAs layers were grown at a temperature of 600°C; $Al_{0.2}Ga_{0.8}As$, at 640°C. The ratio of As to Ga flow rates in the growth zone was 30. Figure 1 shows the band diagram calculated for sample no. 3.

Samples in the shape of Hall bridges were prepared for galvanomagnetic measurements. For all samples, the resistance in magnetic field, $\rho_{xx}(B)$, and the Hall resistivity, $\rho_{xy}(B)$, were measured at 4.2 K in the magnetic field up to 1 T. The Hall density of electrons n_H and the Hall mobility μ_H were determined from these measurements. These parameters for each structure are listed in the table, along with $\rho_0 = \rho_{xx}(0)$.

3. DISCUSSION OF RESULTS OF GALVANOMAGNETIC MEASUREMENTS

As can be seen from the table, the insertion of an AlAs barrier into a narrow QW with W = 13 nm raises the Hall mobility, whereas in a wide QW with W = 35 nm, the insertion of the central barrier reduces the mobility, compared to samples without a barrier. The effect of this barrier on mobility was analyzed in detail in [7].

As can be seen from the band diagram (Fig. 1), the conductance of samples can be represented as the sum of conductances of the potential well on the substrate side, $Al_{0.2}Ga_{0.8}As$ barriers, QW, and the buffer. At a temperature of 4.2 K, the mobility in the doped

Experimental and calculated parameters of the studied samples at a temperature of 4.2 K

Sample no.	2	3	4	5	6	7
W, nm	13	13	26	26	35	35
b, nm	0	1.8	0	1.8	0	1.8
ρ_0, Ω	468	373	300	328	218	249
n_H, 10^{12} cm^{-2}	1.33	1.31	2.07	2.09	2.02	2.01
μ_H, m^2 V^{-1} s^{-1}	1	1.28	1	1.25	1.69	1.25
B_{tr}, T	0.009	0.006	0.005	0.004	0.003	0.004
B_1, T	0.39	0.32	0.55	0.22	0.17	0.4
μ_1, m^2 V^{-1} s^{-1}	0.88	1.23	0.75	1.1	1.62	1.33
μ_2, m^2 V^{-1} s^{-1}	0.63	0.37	0.41	0.57	0.49	0.4
μ_3, m^2 V^{-1} s^{-1}	4.84	4.92	4.2	7.92	8.91	6
n_1, 10^{12} cm^{-2}	1.06	1.13	1.76	1.54	1.68	1.42
n_2, 10^{12} cm^{-2}	0.53	0.57	1.23	1.08	1.18	1.41
n_3, 10^{10} cm^{-2}	1.27	1.47	1.41	1.23	1.34	1.14
τ_φ, ps	0.7	0.8	1.1	1.1	1.1	1.1
τ, ps	0.24	0.14	0.16	0.22	0.19	0.15

$Al_{0.2}Ga_{0.8}As$ barrier is very low, and the carrier density is low in the buffer; therefore, the conduction in these layers can be disregarded. As is well known, the Hall

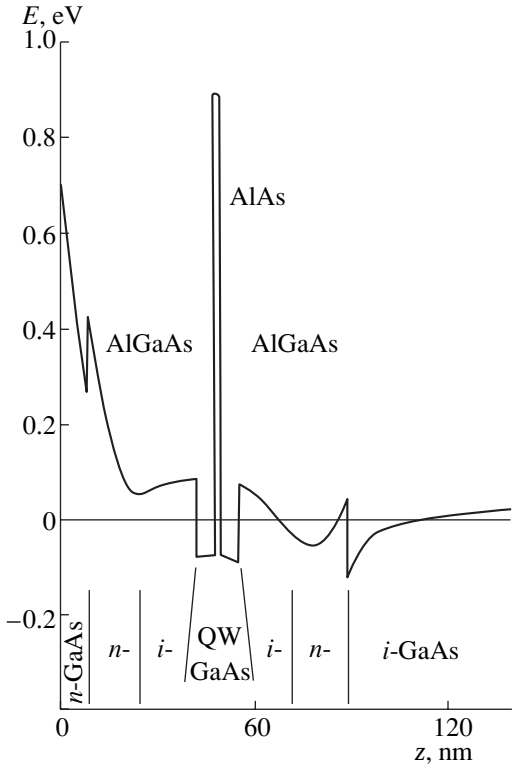

Fig. 1. Band diagram of the AlGaAs/GaAs/AlGaAs structure (sample no. 3). The energy is reckoned from the Fermi level.

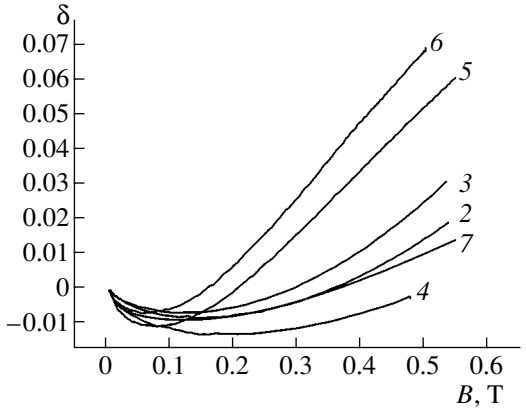

Fig. 2. Experimental dependences of magnetoresistance δ on magnetic field in the structures under study at $T = 4.2$K. The curve numbers correspond to sample numbers in the table.

mobility and density in layered structures are determined from the relations

$$\mu_H = \frac{\sum_i \gamma_i \mu_i^2 n_i}{\sum_i \mu_i n_i}, \quad n_H = \frac{\left(\sum_i \mu_i n_i\right)^2}{\sum_i \gamma_i \mu_i^2 n_i}, \qquad (1)$$

where μ_i and n_i are the mobility and surface density of electrons in the ith layer; γ_i, the Hall factor; and i, the index of summation over layers. The system of self-consistent Kohn–Sham equations for the potential and quantum wells was solved as in [15]. This solution to the system allows one to calculate the electron density in QWs for preset structure parameters and the dopant concentration in the barriers (N_d). The calculation shows that the electron gas is degenerate in almost filled subbands in the potential and quantum wells. Therefore, in the calculations using Eq. (1) for these wells, we assumed that $\gamma_i = 1$; below, indices 1 and 2 correspond to these wells. In another QW, on the substrate side, there are also almost empty subbands in which the electron gas is nondegenerate and $\gamma_i > 1$. Hereinafter, index 3 will correspond to carriers in this well. However, $n_3 \ll n_1, n_2$, and the conduction in these bands only affects the magnetoresistance. Then, the relation $n_1 < n_H < n_1 + n_2$ follows from (1). The proximity of the n_H value to one or other limit depends on the mobility ratio $p = \mu_2/\mu_1$. The calculated electron densities in the wells, n_1 and n_2, are listed in the table. The samples under study were grown in similar conditions; the electron density and mobility in the potential wells in all structures must therefore be nearly equal.

The resistance $\rho_{xx}(B)$ and Hall resistance $\rho_{xy}(B)$ dependences for these samples were measured in strong magnetic field earlier [7]. In all the samples, Shubnikov–de Haas oscillations were observed. The Fourier analysis of oscillations has revealed two series of oscillations that are periodic in the inverse magnetic field, which are related to electrons in the quantum and potential wells. In all the samples, the monotonic portion of the $\rho_{xx}(B)$ dependence increased nearly linearly as the magnetic field increased in the range $1 < B < 8$ T.

For structures with two conducting layers, the classical magnetoresistance was calculated using the relation [16]

$$\delta = \frac{\rho_{xx}(B)}{\rho_0} - 1 = \frac{a}{p}\frac{x^2(p-1)^2}{(1+ap)^2 + x^2(1+a)^2}, \qquad (2)$$

where $a = n_2/n_1$, $x = \mu_2 B$. This dependence is quadratic in magnetic field at $x \ll 1$; in high fields the magnetoresistance reaches a constant value, and

$$\delta_{max} = \frac{a}{p}\left(\frac{p-1}{a+1}\right)^2. \qquad (3)$$

For sample nos. 6 and 7, the calculation yields $\delta_{max} \approx 0.4$. At the same time, the experiment has shown virtually linear $\rho_{xx}(B)$ dependences; the magnetoresistance at $B = 5$ T was $\delta = 2.7$ and 1.6 for sample nos. 6 and 7, respectively. The source of such a high magnetoresistance and the disagreement with the results of classical theory was not discussed in [7].

To reveal the mechanisms of the observed effect, we studied the magnetoresistance at $B < 1$ T. Figure 2 shows the experimental results. As can be seen in this figure, negative magnetoresistance is observed in the magnetic field range $0 < B < B_1$, where B_1 is different for different samples.

According to the theory of weak localization [12], the magnetic field increases the longitudinal component of the conductivity tensor. The additional conductivity is determined by the relation

$$\Delta\sigma_{xx}^{WL} = G_0\left[\psi\left(\frac{1}{2} + \frac{\tau B_{tr}}{\tau_\varphi B}\right) - \psi\left(\frac{1}{2} + \frac{B_{tr}}{B}\right) - \ln\left(\frac{\tau}{\tau_\varphi}\right)\right], \qquad (4)$$

where $G_0 = q^2/2\pi^2\hbar$; q is the elementary charge; $\psi(x)$, di-gamma function; $B_{tr} = q^2\rho_0/4\pi\hbar\mu$; μ, the electron mobility; and τ_φ, the phase-breaking time. In [12], the results were calculated for one type of charge carrier. In [17], the theory was generalized for the case of several filled quantum-well subbands. It was shown that, to a first approximation, the contributions of all subbands to negative magnetoresistance are independent.

As can be seen from the table, in our structures $B_1 \gg B_{tr}$. According to the weak localization theory [12], quantum corrections to conductivity must be completely suppressed at $B > B_{tr}$. If we use classical relations for conductivity and Eq. (4), good agreement between the calculated and experimental curves for sample nos. 4 and 7 is obtained in the range $0 < B < 0.25$ T. For the other curves, this agreement can be achieved only in the initial portions of $\delta(B)$ dependences, at $B <$ 0.07 T. It is noteworthy that the experimental and calcu-

lated data agree well for all samples for $B \gg B_{tr}$. The phase-breaking time τ_φ corresponding to the best agreement between the calculation and experiment is also listed in the table. The calculation was done in terms of the model of conducting layers for several filled subbands in each layer. As can be seen from the table, the τ_φ values obtained are considerably less than the times typical of all known mechanisms of inelastic scattering on phonons in GaAs at the given temperature. Quite often, the phase breaking of the wave function in the weak localization theory is attributed to electron–electron scattering. In this case, τ_φ must decrease as the electron density increases. However, this dependence was not found in experimental studies of *n*-GaAs/$In_{0.07}Ga_{0.93}As$/*n*-GaAs [10] and $Al_xGa_{1-x}As$/GaAs [18] structures and δ-doped GaAs [19] with different electron densities and similar values of other parameters. A study of the *n*-GaAs/$In_{0.2}Ga_{0.8}As$/*n*-GaAs structure with a gate [20] has shown that there is no evident functional dependence of τ_φ on the electron density *n*. Moreover, analysis of experimental data shows that, for absolutely different materials with different densities and types of carrier, τ_φ differs no more than tenfold. For example, for electron transport this time was 5.9 ps [10], 2.5 ps [18], and 10 ps [19]. For *p*-type conduction, a value of 1 ps was obtained for $Al_xGa_{1-x}As$/GaAs [21] and Si/$Si_{0.85}Ge_{0.15}$/Si [22]. In a carbon film with both carrier types [23], the phase-breaking time was 1.8 ps. The data obtained in the literature cannot be attributed to inelastic scattering on phonons either, because the above materials have fundamentally different phonon spectra. The characteristic time τ of the momentum relaxation for the layer with lower electron mobility is also listed in the table.

Figure 3 shows the calculated magnetoresistance for sample nos. 4 and 6. As can be seen in Fig. 2, the experimental dependences for these samples occupy extreme positions. This allows us to estimate the accuracy of fitting. For other curves, the accuracy has intermediate values. In the case of calculation in terms of the weak localization model for three conducting layers, none of the curves demonstrated good agreement in a wide range of magnetic field. This may be related to the conventional large magnetoresistance of nondegenerate electron gas. Furthermore, as can be seen in the table, the condition for the applicability of the weak localization theory in the diffusion limit $\tau_\varphi \gg \tau$ [24] is satisfied for none of the samples. In this situation, the theory of quantum corrections to conductivity by Wittman and Schmid [25] can be used, which is valid when the diffusion limit is not reached. In some cases, this approach made it possible to describe negative magnetoresistance [23].

In this study, we compare the accuracy of describing the experimental dependences of magnetoresistance in terms of the weak localization theory and of the theory derived in [13, 14]. In these studies, the transport kinetics was described in terms of the density matrix, and it

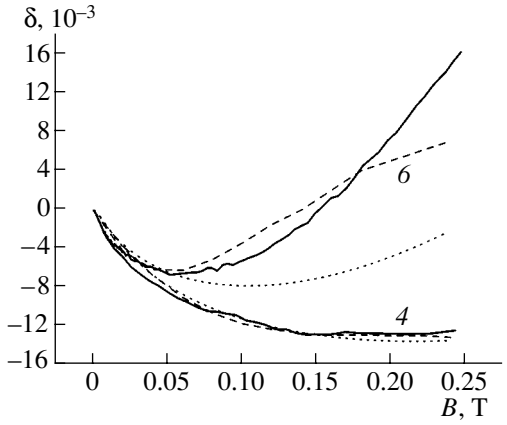

Fig. 3. Experimental (solid lines) and calculated dependences of magnetoresistance for sample nos. 4 and 6. Dotted lines: calculation in terms of the weak localization theory by Eq. (4); dashed lines, by Eq. (7).

was shown that, in a weak magnetic field satisfying the condition $\alpha = \hbar\omega/kT \ll 1$ ($B \ll 0.2$ T at $T = 4.2$ K), the integration may be, strictly speaking, substituted for summation over the magnetic quantization levels, and the conductivity tensor can be represented as

$$\sigma_{xx} = \sigma_{Bxx} + \frac{2q^2}{\sqrt{\pi}m} N_c \alpha \int \sqrt{x}\,dx \frac{\nu}{\omega^2 + \nu^2}\left(-\frac{\partial F}{\partial x}\right),$$

$$\sigma_{xy} = \sigma_{Bxy} + \frac{2q^2}{\sqrt{\pi}m} N_c \alpha \int \sqrt{x}\,dx \frac{\omega}{\omega^2 + \nu^2}\left(-\frac{\partial F}{\partial x}\right), \quad (5)$$

where σ_{Bxx}, σ_{Bxy} are the values calculated using the Boltzmann equation; N_c is the density of states in the conduction band; *F*, the Fermi–Dirac distribution function; $x = E/kT$; $\omega = qB/m$; and ν is the scattering frequency, which is generally energy-dependent. It can be seen that, at $\omega \longrightarrow 0$, formulas (5) are transformed into standard equations of the theory of semiconductors. Note here that, in common practice, the condition $\alpha < 0.7$ is sufficient to allow one to use integration instead of summation. As follows from (5), in a strongly degenerate electron gas, when the δ function can be substituted for the derivative of the distribution function as a first approximation, the magnetoresistance $\delta = -\hbar\omega/E_F$, where E_F is the Fermi energy. An exact calculation shows that the $\delta(B)$ dependence may have an alternating sign in the range of weak fields. In nondegenerate electron gas at low temperatures, the magnetoresistance can be much higher, and its sign is determined by the mobility. In our case, the sign of δ is different in different samples. It can be shown from (5) that, if $n_3 \ll n_0 = mkT/\pi\hbar^2$, the conduction in almost empty subbands can be disregarded. The calculation for GaAs yields $n_0 = 9.7 \times 10^9$ cm^{-2} at 4.2 K. Thus, the last condition is not satisfied for our structures (see table). Therefore, the conduction in almost empty subbands can have a significant effect on the field dependence of magnetoresis-

tance in heterostructures at low temperatures. The lower the temperature at which transport in a 2D gas is studied, the lower must be the electron density in almost empty subbands.

Numerical calculations [7] have shown that the potential well contains two quantum-well levels with high occupancy, and several almost unoccupied levels. The number of levels in the QW varies in different structures; it depends on the width of the well and the presence of a barrier. The electron density and mobility at each level is different. However, below we restrict our analysis to the model of three conducting layers. In terms of this model, the conductance is the sum of conductance in the QW between the heterojunctions, that of the potential well on the interface between $Al_{1-x}Ga_xAs/GaAs$ and the buffer, and the total conductance of almost empty quantum-well subbands. Each layer is described by an effective mobility and density of electrons. The Hall mobility and electron density can be expressed in terms of the layer parameters as

$$\mu_H = \frac{\mu_1}{S}\sum \alpha_i g_i^2, \quad n_H = n_1\frac{\mu_1}{\mu_H}S, \tag{6}$$

where

$$\alpha_i = n_{si}/n_{s1} \quad (i = 1, 2), \quad \alpha_3 = \frac{n_{s3}}{n_{s1}}\frac{e^d - 1}{d},$$

$$d = n_{s3}/n_{s0},$$

$$n_{s0} = \frac{mkT}{\pi\hbar^2}, \quad g_i = \mu_i/\mu_1, \quad S = \sum \alpha_i g_i.$$

The values of n_1 and n_2 were obtained in [7]. The electron densities in almost empty subbands in the potential well depend on the parameters of the buffer. Therefore, their calculated occupancies are only approximate. Evidently, μ_H and n_H are determined mainly by the parameters of nearly filled subbands in the quantum and potential wells. This fact allows us to determine the electron mobility in the wells using Eq. (1). Thus, only the electron parameters of almost empty subbands remain unknown. In the buffer region, the electron wave functions in these subbands are widely extended. Therefore, the mobility of electrons in these subbands is rather high. The fitting of the magnetoresistance is done by varying these parameters within narrow limits. This problem is quite enough.

It can be easily shown using (1) and (5) that for our heterostructure

$$\sigma_{xx} = \frac{\sigma_0}{S}\sum \alpha_i g_i \frac{1 + \beta_i}{1 + g_i^2 x^2},$$

$$\sigma_{xy} = x\frac{\sigma_0}{S}\sum \alpha_i g_i^2 \frac{1 + \beta_i}{1 + g_i^2 x^2}, \tag{7}$$

where

$$x = \mu_1 B, \quad \sigma_0 = 1/\rho_0, \quad \beta_i = 2\frac{\rho_0}{R_Q}x\sum \alpha_i g_i,$$

$$\beta_2 = \beta_1\frac{\alpha_1}{\alpha_2}, \quad \beta_3 = \frac{n_{s1}}{n_{s3}}d\beta_1, \quad R_Q = \frac{2\pi\hbar}{q^2}.$$

These relations can be used to fit the experimental dependences of magnetoresistance. The calculated data are listed in the table. Figure 3 shows experimental and calculated $\delta(B)$ dependences for two samples in the range of fields corresponding to $0 < \alpha < 1.2$. As can be seen from Fig. 3, very good agreement with the experiment is obtained in the case of negative magnetoresistance (sample no. 4). For sample no. 6, fair agreement is obtained for $\alpha < 0.9$ ($B < 0.18$ T). At $\alpha > 1.2$, the discrepancy becomes significant. One possible source of the discrepancy is the fact that, at these values of α, the replacement of summation by integration is not quite correct. In this case, exact formulae from [13, 14] must be applied, where the summation over the magnetic quantization levels is carried out. However, an even more significant factor for the accuracy of calculation is the following: when Eq. (7) was derived in [13, 14], terms containing the function $Z(\omega)$ were dropped from the general expressions for the conductivity tensor. As shown in [13, 14], $Z(0) = 0$, and it increases as the magnetic field increases. In strong magnetic fields, the behavior of magnetoresistance is defined precisely by $Z(\omega)$. This is especially important for an adequate description of positive magnetoresistance. Therefore, these terms must be taken into account in our case for sample no. 6.

4. CONCLUSION

Magnetoresistance in heterostructures with coupled QWs of different widths has been studied in weak magnetic field. The negative magnetoresistance observed in the magnetic field range from 0 to 0.2–0.6 T can be satisfactorily described in terms of the quantum kinetic approach. Calculations show that in complex heterostructures the relations between carrier densities and mobilities in all the layers define the dependence of magnetoresistance on magnetic field. Specifically, in the samples under study the negative magnetoresistance is largely due to the contribution of nondegenerate electron gas in almost empty quantum-well subbands.

ACKNOWLEDGMENTS

This study was supported by the Ministry of Industry, Science, and Technology of the Russian Federation (state contract no. 40.072.1.1.1178).

REFERENCES

1. W. Trzeciakowski and B. D. McCombe, Appl. Phys. Lett. **55**, 891 (1989).
2. A. Lorke, U. Merkt, F. Malcher, *et al.*, Phys. Rev. B **42**, 1321 (1990).
3. J.-L. Cazaux, N. G. Geok-Ing, D. Pavlidis, and H.-F. Chau, IEEE Trans. Electron Devices **35**, 1223 (1988).
4. M. Nawaz, Solid-State Electron. **43**, 687 (1999).
5. C. S. Whelan, W. E. Hoke, R. A. McTaggart, *et al.*, IEEE Trans. Electron Devices **21**, 5 (2000).
6. J. E. Hasbun, J. Phys.: Condens. Matter **14**, R143 (2003).
7. G. B. Galliev, V. É. Kaminskiĭ, V. G. Mokerov, *et al.*, Fiz. Tekh. Poluprovodn. (St. Petersburg) **37**, 711 (2003) [Semiconductors **37**, 686 (2003)].
8. A. de Visser, V. I. Kadushkin, V. A. Kul'bachinskiĭ, *et al.*, Zh. Éksp. Teor. Fiz. **105**, 1701 (1994) [JETP **78**, 918 (1994)].
9. V. A. Kul'bachinskiĭ, R. A. Lunin, V. G. Kytin, *et al.*, Zh. Éksp. Teor. Fiz. **110**, 1517 (1996) [JETP **83**, 841 (1996)].
10. G. M. Minkov, S. A. Negashev, O. E. Rut, *et al.*, Phys. Rev. B **61**, 13172 (2000).
11. A. M. Kreshchuk, S. V. Novikov, T. A. Polyanskaya, and I. G. Savel'ev, Fiz. Tekh. Poluprovodn. (St. Petersburg) **31**, 459 (1997) [Semiconductors **31**, 391 (1997)].
12. B. L. Altshuler, D. Khmelnitzkii, A. I. Larkin, and P. A. Lee, Phys. Rev. B **22**, 5142 (1980).
13. V. É. Kaminskiĭ, Fiz. Tekh. Poluprovodn. (St. Petersburg) **36**, 1360 (2002) [Semiconductors **36**, 1276 (2002)].
14. V. E. Kaminskii, Phys. Rev. B **67**, 085201 (2003).
15. V. É. Kaminskiĭ, Fiz. Tekh. Poluprovodn. (Leningrad) **23**, 662 (1989) [Sov. Phys. Semicond. **23**, 414 (1989)].
16. A. Isihara and L. Smrčka, J. Phys. C: Solid State Phys. **19**, 6777 (1986).
17. N. S. Averkiev, L. E. Golub, and G. E. Pikus, Fiz. Tekh. Poluprovodn. (St. Petersburg) **32**, 1219 (1998) [Semiconductors **32**, 1087 (1998)].
18. M. Y. Simmons, A. R. Hamilton, M. Pepper, *et al.*, Phys. Rev. Lett. **84**, 2489 (2000).
19. G. M. Min'kov, S. A. Negashev, O. É. Rut, *et al.*, Fiz. Tekh. Poluprovodn. (St. Petersburg) **32**, 1456 (1998) [Semiconductors **32**, 1299 (1998)].
20. G. M. Minkov, A. V. Germanenko, O. E. Rut, *et al.*, Phys. Rev. B **64**, 193309 (2001).
21. Y. Yaish, O. Prus, E. Buchstaf, *et al.*, cond-mat/0109469 (2001).
22. M. S. Kagan, G. M. Min'kov, N. G. Zhdanova, *et al.*, in *Proceedings of 11th International Symposium on Nanostructures: Physics and Technology* (St. Petersburg, Russia, 2003), p. 279.
23. R. T. F. van Schaijk, A. de Visser, S. G. Ionov, *et al.*, Phys. Rev. B **57**, 8900 (1998).
24. V. F. Gantmakher, *Electrons in Disordered Media* (Fizmatlit, Moscow, 2003), Chap. 2, p. 24 [in Russian].
25. H. P. Wittman and A. Schmid, J. Low Temp. Phys. **69**, 131 (1987).

Translated by D. Mashovets

Semiconductors, Vol. 38, No. 11, 2004, pp. 1332–1339. Translated from Fizika i Tekhnika Poluprovodnikov, Vol. 38, No. 11, 2004, pp. 1374–1381.

LOW-DIMENSIONAL SYSTEMS

Formation of Two- and One-Dimensional Solid-Phase Quantum Nanostructures in the CdHgTe–Electrolyte System

V. B. Bozhevolnov, A. M. Yafyasov^, and P. P. Konorov

Fock Institute of Physics, St. Petersburg State University, St. Petersburg, 198504 Russia

^e-mail: yafyasov@desse.phys.spbu.ru

Submitted September 25, 2003; accepted for publication April 15, 2004

Abstract—It is shown experimentally and theoretically that structures that exhibit properties of two- and one-dimensional electron gas at room temperature can be formed on the basis of CdHgTe compounds in a semiconductor–electrolyte system. The methods for fabricating the quantum-confinement structures and in situ monitoring of the physical properties of such structures are described. *© 2004 MAIK "Nauka/Interperiodica".*

1. INTRODUCTION

Recently, interest in quantum electronic effects that are observed in samples of geometrical size comparable to the electron wavelength λ_e has increased [1]. In this regard, the most significant result of recent decades is the discovery of the phenomena of weak localization and the quantum Hall effect [2]. Applications of quantum effects have resulted in the development of electronics in which systems with two-dimensional, one-dimensional (quantum wires), and zero-dimensional (quantum dots) electron gas are used as separate functional elements.

At present, systems with low-dimensional electron gas are formed mainly in heterostructures synthesized by molecular-beam epitaxy on the basis of SiGe–Si and (AlGa)As–GaAs compounds [1, 2]. A decrease in the dimensionality of the electron gas is caused by its localization in the space-charge region (SCR) of an abrupt heterojunction. The manifestation of quantum properties of electron gas is obscured by the effects of thermal and collisional broadening of discrete energy levels. As a rule, these effects become significant at room temperature. In this respect, the development of methods for fabricating structures whose properties are governed by quantum confinement effects up to room temperature has become an important physical and technical problem. We may single out two main areas of research that might solve this problem:

(i) the use of materials that have a small electron effective mass m_e^* and high mobility μ and, accordingly, large wavelength and mean free path of charge carriers;

(ii) the development of new methods for forming low-dimensional structures with *in situ* monitoring of their electronic properties.

Mercury–cadmium–tellurium (MCT) materials are promising for the fabrication of structures with quantum confinement; these materials are continuous solid solutions with isovalent substitution [3–6]. The main parameters of these materials for three different compositions x are listed in Table 1. A specific feature of MCT compounds is the strong composition dependence of their electronic characteristics. Therefore, it is possible to form heterostructures by making a contact between regions of MCT material with different compositions. Since the lattice constant a_0 of MCT material depends weakly on composition (Table 1) and, hence, the periodicity of the atomic structure in the heterojunction region is violated only slightly, the density of surface states is low and, as a consequence, electron capture and scattering are weakly pronounced.

The field effect in electrolytes is based on the change in the potential of the semiconductor electrode V during its polarization in electrolyte and, therefore, of the semiconductor surface potential V_s. This effect can

Table 1. Main parameters of the $Cd_xHg_{(1-x)}Te$ materials for three stoichiometric compositions (x). The data correspond to room temperature [5–8]

$Cd_xHg_{(1-x)}Te$	a_0, nm	$\frac{m_e}{m_0}$	$\frac{m_h}{n_0}$	E_g, eV	μ_e, $cm^2/(V\ s)$	λ_{ph}, μm	ε_{sc}	χ, eV	n_i, cm^{-3}	E_C–E_F, eV	L_D, nm	L_{mov}, nm	λ_e, nm
$x = 0.15$	0.64633	0.007	0.50	0.080	32×10^3	15	18	5.40	2.3×10^{16}	−0.035	13	300	59
$x = 0.20$	0.64641	0.020	0.45	0.150	20×10^3	8.1	17	5.33	7.1×10^{15}	+0.012	20	200	55
$x = 0.32$	0.64663	0.030	0.45	0.320	7×10^3	3.9	16	5.18	2.5×10^{14}	+0.105	76	80	45

1063-7826/04/3811-1332$26.00 © 2004 MAIK "Nauka/Interperiodica"

be used to change the MCT composition and simultaneously measure electrical properties of the fabricated structures [3].

For MCT compounds, the feasibility of such a way of changing the material composition has been proven in [8–12].

2. EXPERIMENTAL

As an original MCT material, we used samples with composition corresponding to $x = 0.32$ (Table 1). The surface of the samples was subjected preliminarily to dynamic chemical etching in an 8% bromine solution in methanol [3]. In order to change the MCT composition, we introduced a complexing agent into the measurement cell that contained an aqueous electrolyte. The complexing agent was chosen so that the formed cadmium complexes were stable in a larger interval of potentials than mercury complexes. As a result, at certain electrode potentials, the surface was depleted of cadmium, since cadmium complexes were the first to leave the solution, thus forming a near-surface layer that had a composition of $x = 0.20$, was enriched with mercury, and had a narrower band gap than the original material. Hence, a two-layer heterostructure containing a layer of a narrow-gap semiconductor at the surface of the original MCT sample was formed. The layer composition and thickness were determined from the capacitance–voltage (C–V) characteristics using the methods suggested in [13]. In addition, the parameters of the surface layer were monitored using the IR absorption method.

The C–V characteristics of the structure were measured directly in the electrochemical cell by the four-electrode method with controlled electrode potential [3, 14, 15]. Measurements were made using a pulsed signal of duration ~1.0 μs with averaging over no less than 32 pulses at each value of the applied potential. In addition, for each test pulse, the potential-relaxation time constant $\tau(V)$ of the electrode–electrolyte interface system was measured. Using $\tau(V)$ and the measured interface capacitance $C_{inf}(V)$, the shunting resistance of the structure $R_{inf}(V) = \tau(V)/C_{inf}(V)$ was estimated.

IR absorption was measured in a "dry" structure at room temperature in a dry nitrogen atmosphere. An optical system with modulation of a monochromatic beam at a frequency of 10–15 Hz was used. The signal was recorded using a differential bolometer with an ac bridge. The accumulation time of the signal was as long as 32 s for each value of the wavelength.

3. RESULTS AND DISCUSSION

3.1. A Method of Formation and Electrical Properties of Heterostructures with Two-Dimensional Electron Gas

Figure 1 shows C–V curves of the MCT-electrode surface for two samples (the curves were obtained by varying the electrode potentials in the controlled potential mode) as well as the calculated surface-potential dependence of the capacitance of the SCR for the MCT with $x = 0.32$. We can distinguish several specific regions in the characteristics; these regions correspond to different stages of the structure formation.

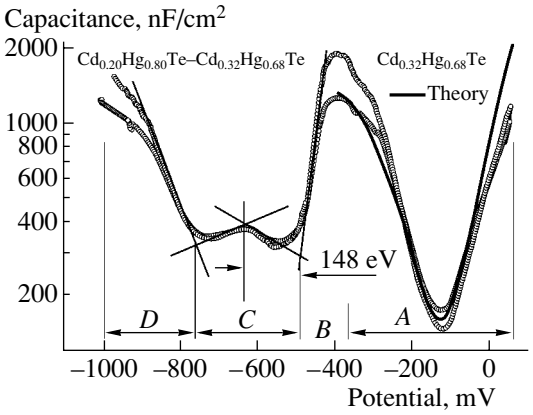

Fig. 1. Capacitance–voltage characteristics $C_{inf}(V)$ of the MCT–electrolyte system for two samples. The theoretical dependence of the capacitance of the space-charge region of MCT ($x = 0.32$) on the surface potential V_s is displaced along the potential axis to attain agreement with the experimental dependences of $C_{inf}(V)$ on the electrode potential V.

The region of electrode potentials from +50 to –250 mV corresponds to the polarization of the MCT electrode at which the electrode surface is dissolved, while the original relation between all components of the ternary compound remains unchanged (Fig. 1, region A). This inference is confirmed by the reversibility of the C–V curves and their conformity to the variation of the SCR capacitance in the MCT material of original composition ($x = 0.32$).

In the region of electrode potentials lower than –250 mV, the mercury complexes start to be discharged at the surface of the MCT electrode, whereas the cadmium complexes remain stable and continue to pass easily to the electrolyte. As a result, the electrode surface is enriched with mercury. This process is accompanied by the redistribution of potential jumps at the interphase boundary and by a sharp irreversible decrease in the capacitance in the region of electrode potentials from –350 to –550 mV (Fig. 1, region B), with the subsequent stabilization of the C–V characteristics.

In the range of potentials from –600 to –750 mV, a region of reversible variation of C–V characteristics (Fig. 1, region C) is again observed.

For electrode potentials smaller than –800 mV, an irreversible destruction of the electrode material occurs (Fig. 1, region D).

A decrease in the capacitance as one passes to region C and the reversibility of the variation in the C–V characteristics in this region can be attributed to the appearance of a stable structure that contains an insulating layer. The estimation of the thickness of this layer, using experimental values of capacitance, yields

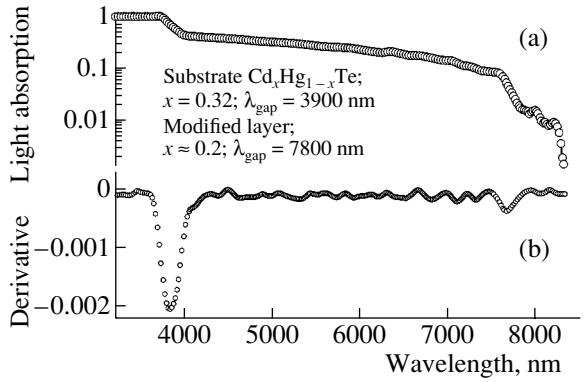

Fig. 2. (a) IR absorption spectrum of the structure consisting of MCT, substrate, and modified surface layer; (b) the result of differentiation of the spectrum of IR absorption.

36–41 nm under the assumption that the layer permittivity ε_{sc} is in the range characteristic of MCT materials (Table 1). We note that the thickness of this layer is comparable to the electron wavelength λ_e in an MCT material (Table 1), which may give rise to quantum confinement of electron gas at the heterojunction considered.

Figure 2 shows the measured IR absorption spectrum of the fabricated structure. In this spectrum (Fig. 2a), there are two features at wavelengths of 3900 and 7800 nm. These features indicate that a two-layer structure is formed that consists of a substrate with x = 0.32 and a semitransparent layer with x = 0.20. The thickness of this layer estimated taking into account the refractive index of MCT (n = 3.6 [16]) varied from 200 to 400 nm, which is five times greater than the thickness of the insulator layer calculated from the *C–V* characteristics. The result of differentiation of the spectral absorption curve is shown in Fig. 2b. The fine structure at the edge of the absorption spectrum indicates the existence of a quantum-confined electron gas in the region of the semitransparent layer.

The data obtained show that a heterojunction is formed at the contact between the substrate and the surface layer of MCT with x = 0.20. Figure 3 illustrates the process of heterostructure formation. The surface potential of the substrate is controlled by the electrochemical reaction of dissolution of $Cd_{0.32}Hg_{0.68}Te$. A change in the potential during polarization is limited by the potential of discharge of the mercury complex at the electrode surface with the formation of atomic mercury Hg^0 (Fig. 3a), which penetrates easily into the near-surface region of the MCT material and changes its composition. A similar process of the change in MCT composition was described previously [11, 12]. A change in the composition of the MCT electrode at the surface results in a change in its corrosion potential, which affects the surface potential. Thus, in the electrolyte–$Cd_{0.20}Hg_{0.80}Te$–$Cd_{0.32}Hg_{0.68}Te$ system, the potentials in the electrode bulk ($Cd_{0.32}Hg_{0.68}Te$) and at its surface ($Cd_{0.20}Hg_{0.80}Te$) are found to be fixed. The energy-band structure of the (surface layer of the $Cd_{0.20}Hg_{0.80}Te$ composition)–(substrate of the $Cd_{0.32}Hg_{0.68}Te$ composition) system corresponds either to a graded-gap (Fig. 3b) or to an abrupt heterostructure (Figs. 3c, 3d). The graded-gap character of the structure is at odds with the IR absorption data (Fig. 2) and the formation of an insulating layer that manifests itself in the *C–V* characteristics (Fig. 1). At the same time, in the model of an abrupt heterojunction, both the presence of oscillations near the absorption edge of the film (Fig. 2b) and the decrease in capacitance in region *C* of the *C–V* charac-

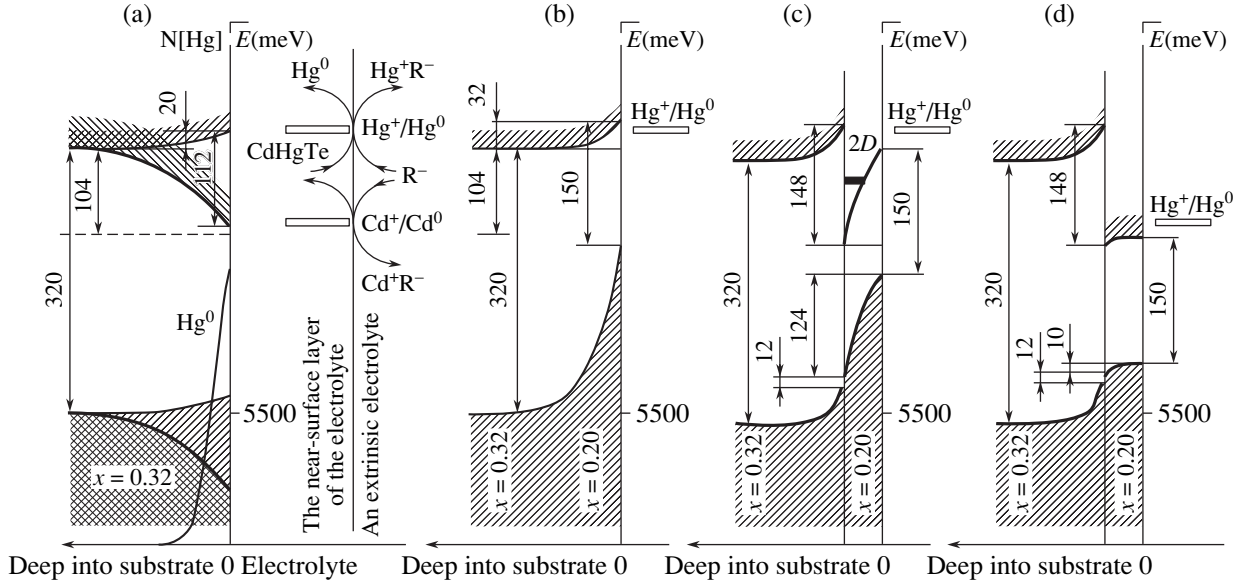

Fig. 3. Process of formation of a heterostructure and its possible types. (a) Enrichment of the substrate surface with mercury; (b) graded-gap, (c) abrupt biased, and (d) unbiased heterojunctions. The energy E (meV) is plotted on the vertical axis.

teristics can be attributed to quantum confinement of electron gas localized near the energy-band offset at the heterojunction.

Returning to Fig. 1, we note that the right-hand portions of *C–V* characteristics in region *C* extrapolated by straight lines reflect the process of formation of the surface $Cd_{0.20}Hg_{0.80}Te$ layer, while the left-hand portions indicate the change in total capacitance of the heterojunction during its polarization. The potential $V_1 = -480$ mV, corresponding to the intersection of the straight lines that extrapolate the *C–V* characteristics, differs from the potential of unbiased junction $V_2 = -628$ mV by $V = |V_1 - V_2| = 148$ mV, which coincides with the magnitude of the band offset at the heterojunction (Fig. 3c). Thus we may state that the process of formation of the surface $Cd_{0.20}Hg_{0.80}Te$ layer (Figs. 3a, 3b) comes to a halt when a band offset appears (Fig. 3c).

Thus, the measurements of IR absorption and *C–V* characteristics show that electrochemical modification of the MCT surface produces a heterostructure formed by the contact of two MCT regions of different compositions. The energy-band offset appearing at the contact results in the dimerization of the electron gas in the region of the heterostructure. Note that, for this method of heterostructure formation, the involvement of the electronic subsystem in modification of MCT material is important. The MCT material with $x = 0.20$ appearing at the surface of the original sample has a smaller m_e^* and, accordingly, larger λ_e compared to the original material with $x = 0.32$. The formation of a layer with $x = 0.20$ by the electrochemical dissolution reaction automatically comes to a halt when the layer thickness attains a value of about λ_e and quantum confinement of the electronic subsystem in the layer becomes important. We believe that the following two mechanisms may play the most substantial role in this process:

(1) In the prepared material, we have $\lambda_e \gg a_0$. In this case, the probability density (per atom) of finding an electron is low, and therefore the electrochemical process that is caused by electron–atom interaction and results in the formation of a new material composition is slowed down.

(2) The electron is localized at a quantum-confinement level, so there is an additional decrease in the electron density at the surface and the probability of electronic exchange decreases even more.

Both mechanisms, related to the wave nature of an electron, seem to inhibit electrochemical reactions, which makes it possible to form layers with a thickness comparable to λ_e in the material under study.

3.2. Preparation Technique and Properties of a One-Dimensional Conductor

A one-dimensional (1D) electronic quantum structure (a quantum wire) was formed by electrochemical modification of the MCT substrate ($x = 0.32$) while being simultaneously exposed to ultrasound vibrations

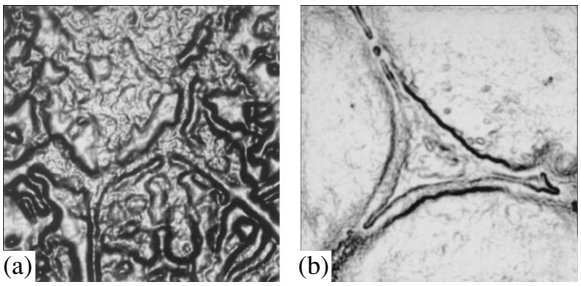

Fig. 4. Microphotographs: (a) a fragment of a "honeycomb structure" at the final stage of its evolution, (b) a node of the honeycomb structure of area $S_{knot} = 10^{-4}$ cm^2. The photos are taken in the electrolyte in dark blue light of a GaN light-emitting diode.

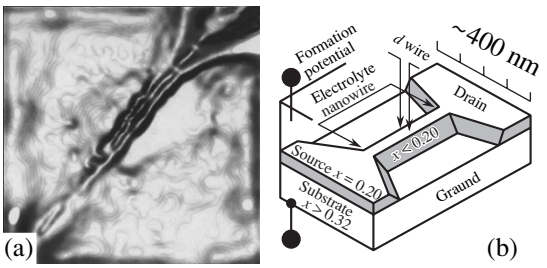

Fig. 5. (a) A microphotograph of a wirelike fragment of a node in honeycomb structure, (b) a sketch of the fragment of the wirelike structure containing a quantum wire.

on the interphase boundary, which led to the formation of vortex-type microflows in the electrolyte at the boundary. These flows gave rise to a strong lateral inhomogeneity of the conditions for the electrochemical reaction due to local removal of diffusion restrictions, which facilitated an additional cadmium transfer to the solution with the formation of geometrical microinhomogeneities. In turn, these inhomogeneities stabilized the vortex-type flows that formed them. As a result, in addition to the modification of the MCT composition described in Section 3.1, extended regions of the MCT material with $x < 0.20$ were formed in the region of contact between two electrolyte microflows.

Thus, under the self-stabilization conditions of the electrochemical reaction, which, in our opinion, are in some respects analogous to the formation of Bénard–Taylor cells (which represent a typical example of self-organization) [17], the honeycomb structure shown in Fig. 4 was formed. At the initial stage of formation, "nodes" appeared (see Fig. 4b); they had a characteristic transverse size of geometrical inhomogeneities containing extended fragments less than 5 μm in size.

In the region of the narrowing of filament-like fragments of the structure (whiskers, Fig. 5a), one-dimensional quantum conduction appeared provided that the electron gas was additionally compressed by the electric field related to external polarization. The length of such a quantum wire, which represented a fragment of

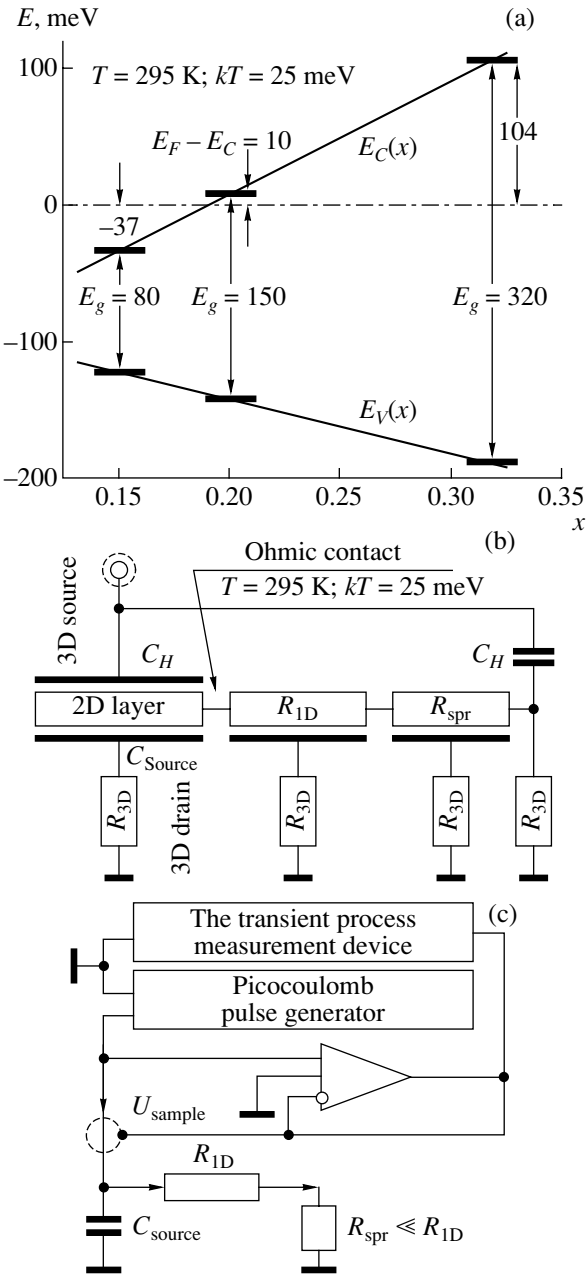

Fig. 6. (a) Positions of the bottom of the conduction band and the top of the valence band with respect to the Fermi level as functions of the composition of the $Cd_xHg_{1-x}Te$ material, which determine electric properties of contacts between the elements of the structure; (b) the electric equivalent circuit of a fragment of the structure containing a quantum wire; and (c) a circuit for the conductivity measurements by the method of potential relaxation (schematically).

the honeycomb structure (Fig. 5), was comparable to the electron mean free path in $Cd_{0.15}Hg_{0.75}Te$ (L_{mov} = 300 nm at room temperature). This resulted in ballistic transport of electrons along the wire.

The possibility of separating the one-dimensional conductivity and, in particular, the conductivity of a fragment of the honeycomb structure, from the total impedance of the structure determined from the $C_{inf}(V)$ and $R_{inf}(V)$ measurements is based on the following reasoning. The elements of the structure consisting of the MCT materials with $x = 0.32$ and $x \approx 0.20$ are found to be separated by potential barriers, whose height at room temperature is much larger than $kT \approx 25$ meV (Fig. 6a). At the same time, potential barriers between the elements of structure with $x \approx 0.20$ and $x \le 0.2$ are smaller than kT, and the contact between them is ohmic. Figure 6b shows the equivalent electric circuit of a fragment of the structure that contains a quantum wire, while Fig. 6c shows schematically a circuit for conductivity measurements by the method of potential relaxation. The quantum wire in this circuit is represented by the impedance that includes the resistance R_{1D} shunted by a distributed capacitance C_{1D} (not shown in Fig. 6c). The auxiliary forming platinum electrode placed in the bulk of the electrolyte played the role of an input contact (3D source), and the bulk of the original MCT sample played the role of an output contact (3D drain). The electric charge supplied to a node of the honeycomb structure drains through the impedance of a quantum wire and a spreading impedance Z connected in series. The impedance Z represents a combination of the resistances of the $Cd_{0.20}Hg_{0.80}Te$ and $Cd_{0.32}Hg_{0.68}Te$ regions ($R_{spr} = R_{2D} + R_{3D} \approx R_{2D}$) and the heterostructure capacitance of $C_{source} = C_{2D}S_{knot} = 200 \pm 10$ pF, where $C_{2D} = \sum C_{quant}$ is the specific capacitance of the system of quantum levels and S_{knot} is the area of the node of the honeycomb structure. The quantity C_H is the capacitance of the electrolytic contact (capacitance of the Helmholtz layer), which is $C_H \approx 10^4$ nF/cm^2 [3, 14].

One-dimensional conductivity can be determined by measuring the relaxation (spreading) time of the charge supplied to the system and using the formula $G = C_{source}/\tau = -\alpha(C_{source}/t_i)$, where t_i is the duration of the test pulse of the measuring setup, $\alpha = \ln(U(t)/U_0) < 0$, $U(t)$ is the function of potential relaxation of the structure measured after the application of the test pulse, U_0 is the measurement scale, and $\tau = R_{1D}C_{source} \approx 2.3 \times 10^{-6}$ s is the time constant related to charge spreading in a one-dimensional structure (Figs. 6b, 6c). The electrical characteristics of all other regions of the structure remain unmeasured, since their time constants are much greater than the time τ.

The values of the spreading resistances in quantum subbands were estimated from the formula

$$R_{spr} = 1/(e\mu_e N_i),$$

where the mobility μ_e is taken to be equal to the bulk mobility for $Cd_{0.20}Hg_{0.80}Te$, $\mu_e \approx 2 \times 10^4$ cm^2/(V s) [5, 6, 8]; the quantities N_i were obtained from the self-consistent solution of the Schrödinger and Poisson equations for semiconductors with a nonparabolic dispersion relation for the conduction band using the method suggested in [18]. In Table 2, the energies and

densities of electrons localized in quantum subbands are listed, as well as the results of estimation of R_{spr} and C_{quant} required for the analysis of the equivalent circuit used. From these data we can see that, for a surface potential of 150 mV, coinciding with the potential at the biased heterojunction (see Section 3.1), the entire electronic charge is localized at the first quantum level, which crosses the Fermi level at this potential.

The resistance of a quantum wire was determined from the relation [2]

$$R_{1D} = h/(n2e^2) = 12.9/n \text{ k}\Omega,$$

where $n = 1, 2, 3, \ldots$. Comparing the quantities R_{1D} and R_{spr}, we see that $R_{spr} \ll R_{1D}$ for all attainable values of n.

The capacitance of a quantum wire was estimated using the following approximate formula [1]:

$$C_{1D} = e^2\Gamma_i/(E_i - E_F).$$

Here, Γ_i is the electron concentration in the ith one-dimensional quantum subband with energy E_i.

For a quantitative estimation of the parameters Γ_i and E_i, we chose the model of a one-dimensional quantum conductor in the shape of a rectangular MCT bar with $x = 0.15$ and with the linear dimensions L_x and L_y (along the x and y axes, respectively) on the order of the electron wavelength ($\lambda_e = 59$ nm). In the calculation, we used the nonparabolic dispersion relation for electrons in the conduction band in the form [6]

$$k^2(E) = \frac{1}{P^2}\frac{(E - E_0)(E - E_0 + E_g)(E - E_0 + E_g + \Delta)}{(E - E_0 + E_g + 2/3\Delta)},$$

where k is the quasi-momentum, P is the matrix element of the quasi-momentum operator, $E_0 = \hbar^2k^2/(2m_0)$ is the free-electron energy, and Δ is the energy of spin–orbit splitting.

In the single-particle Hartree approximation, the wave functions can be written as $\varphi(x, y, k_z)\exp(ik_z z)$, where $\varphi(x, y, k_z)$ is the envelope function that describes the electron states $E_i(k_z)$ of the quantum subband $x \in [0, L_x]$, $y \in [0, L_y]$, and $z \in [-\infty, +\infty]$. Generally, we can find the energies of bound electron states $E_i(k_z)$ from the Schrödinger equation that, in the absence of an external electric field, is written as

$$-\frac{\partial^2\varphi(x, y, k_z)}{\partial x^2} - \frac{\partial^2\varphi(x, y, k_z)}{\partial y^2} = [k^2(E_i(k_z)) - k_z^2]\varphi(x, y, k_z).$$

It follows from the solution of this equation that the largest spacing between the quantum levels in a wire is attained at $L_x = L_y$. The ratio of the number of electrons in the first quantum subband to the total number of electrons, as well as the electron concentrations in quantum subbands, is shown in Fig. 7.

Setting $L_x = L_y = \lambda_e = 59$ nm and using the data in Fig. 7 and the formula for C_{1D}, we can estimate the capacitance of a quantum wire. In the limit of filling of one quantum subband, we have $C_{1D} = 1.1$ pF/cm, and for three quantum subbands filled, $C_{1D} = 3.4$ pF/cm. Comparing the capacitances shown in the equivalent circuit with the capacitance of a quantum wire, we can see that the latter may be disregarded. For this reason, the capacitance C_{1D} is not shown in the circuit in Fig. 6c.

Table 2. Calculated values of the energy and electron density in quantum subbands in the $Cd_{0.2}Hg_{0.8}Te$ material at room temperature

V_s, V	$\frac{E_i - E_F}{e}$, mV	$\frac{E_i - E_F}{k_0T}$	n_i, cm^{-2}	R_{spr}, Ω	C_{quant}, nF/cm^2
0.025	71	2.7	0.9×10^{10}	34800	0.62
0.050	66	2.5	1.5×10^{10}	20000	0.66
0.100	23	0.9	4.5×10^{10}	6800	0.80
0.150	0	0.0	11.0×10^{10}	2800	1.10
0.200	–28	–1.1	21.0×10^{10}	1440	1.20

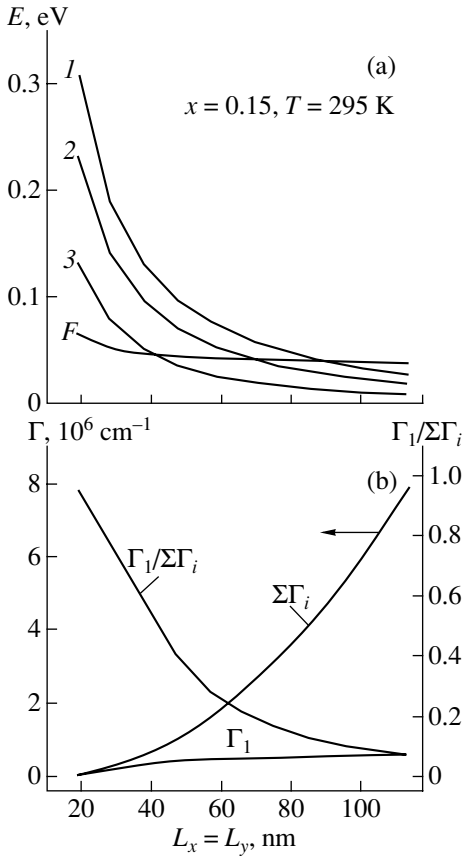

Fig. 7. (a) Dependences of the energies of quantum subbands and (b) electron concentrations in quantum subbands on the dimensions of the quantum wire L_x and L_y. F stands for the Fermi level E_F, (*1*) corresponds to E_1, (*2*) corresponds to E_2, and (*3*) corresponds to E_3.

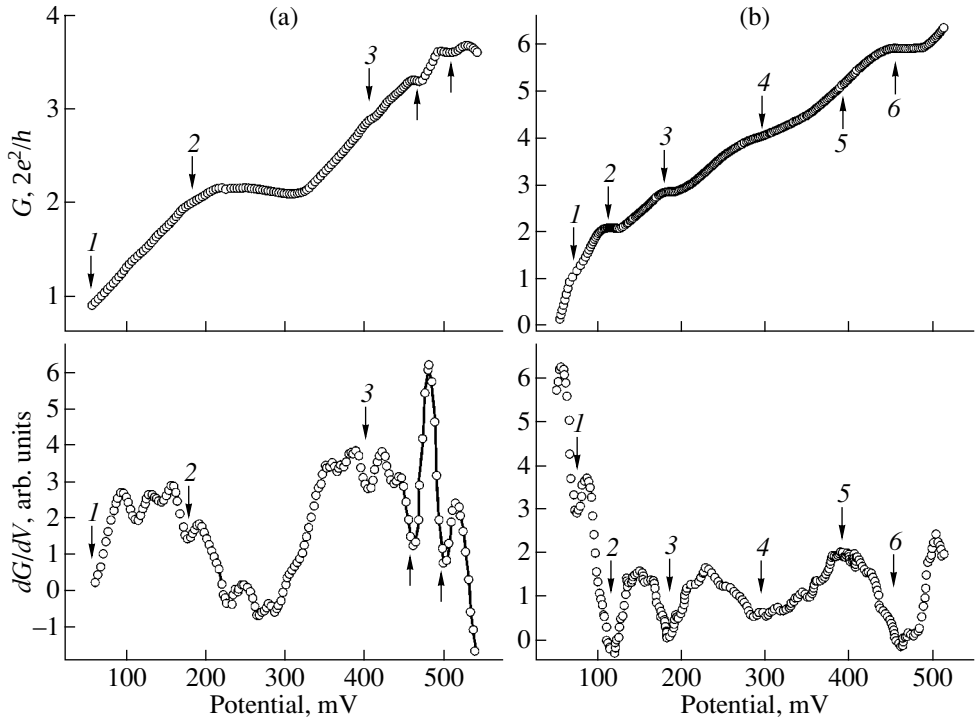

Fig. 8. Conductivities $G(V)$ (in units of $2e^2/h$) as a function of the voltage applied to the forming auxiliary electrode for two whiskers containing a quantum wire and the derivatives of these conductivities.

Figure 8 shows the dependence of the conductivity on the voltage at the field electrode $G(V) = n(2e^2/h)$ measured in quanta of the one-dimensional conductivity (n is the number of quanta) for two quantum-wire samples. In the $G(V)$ curves, we clearly see several first steps (Figs. 8a, 8b) for each of the samples. Figure 8b shows the dependence corresponding to the highest attained accuracy of measurements of the potential relaxation $U(t)$. Due to the insufficient accuracy (Fig. 8a), the first step is barely resolved and the $G(V)$ curve is distorted for large values of the conductivity quanta. The analysis of the corresponding derivatives shows that the $G(V)$ curves have a more complicated structure than $n(2e^2/h)$. This circumstance can be related either to the processes of quantum interference between whiskers connected to a node or to the effects of fractional quantization [2].

4. CONCLUSIONS

Thus, in the MCT–electrolyte system, structures can be fabricated exhibiting quantum properties both of two- and one-dimensional electron gas at room temperature if both the electrolyte and polarization conditions are chosen properly. Processes of self-organization can play an important role in the preparation of such structures. Our results show that low-dimensional quantum structures can be fabricated in semiconductor–electrolyte systems, using the field effect in the electrolyte both as the forming factor and as a method of in situ quality monitoring.

ACKNOWLEDGMENTS

This study was supported by the program "Universities of Russia," grant no. UR.06.01.021 (2004).

We are grateful to Prof. R. Compana (Brussels, Belgium), Prof. M.J. Kelly (University of Surrey, UK), Prof. A. Forchel (Würzburg), and Prof. V.I. Safarov (University Aix-Marseille, France) for helpful discussions.

REFERENCES

1. M. J. Kelly, *Low-Dimensional Semiconductors. Materials, Physics, Technology, Devices* (Clarendon, Oxford, 1995).
2. T. Ando, Y. Arakawa, K. Furuya, S. Komiyama, and H. Nakashima, *Mesoscopic Physics and Electronics* (Springer, Berlin, 1998).
3. P. P. Konorov and A. M. Yafyasov, *Physics of Semiconductor Electrode Surface* (S-Peterb. Gos. Univ., St. Petersburg, 2003), Chap. 6, p. 111 [in Russian].
4. A. M. Yafyasov, P. P. Konorov, and V. B. Bozhevol'nov, in *Fundamental Studies of New Materials and Processes in Matter* (Mosk. Gos. Univ., Moscow, 1994), p. 129 [in Russian].
5. *Semiconductors and Semimetals*, Vol. 18: *Mercury Cadmium Telluride*, Ed. by R. K. Willardson and A. C. Beer (Academic, New York, 1981), p. 388.

6. R. Dornhaus and G. Nimts, Springer Tracts Mod. Phys. **98**, 309 (1983).
7. M. W. Scot, J. Appl. Phys. **43**, 1055 (1972).
8. J. C. Shim, Y. G. Kim, Y. T. Song, *et al.*, J. Cryst. Growth **214–215**, 260 (2000).
9. V. Sakashito, B. Lochek, and H. H. Streblov, J. Electroanal. Chem. **140**, 75 (1982).
10. D. R. Rhiser and R. E. Kvaas, J. Vac. Sci. Technol. **21**, 168 (1982).
11. R. Kumaresan, S. Moorthy Babu, and P. Ramasamy, J. Cryst. Growth **198–199**, 1165 (1999).
12. Jong-Hwa Choi and Hee Chul Lee, Semicond. Sci. Technol. **17**, 266 (2002).
13. I. M. Ivankiv, A. M. Yafyasov, V. B. Bozhevol'nov, and A. D. Perepelkin, Fiz. Tekh. Poluprovodn. (St. Petersburg) **35**, 546 (2001) [Semiconductors **35**, 525 (2001)].
14. M. D. Krotova, B. I. Lendtsner, L. L. Knou, and Yu. V. Pleskov, Élektrokhimiya **5**, 291 (1969).
15. Yu. Ya. Gurevich and Yu. V. Pleskov, *Photoelectrochemistry of Semiconductors* (Nauka, Moscow, 1983), p. 312 [in Russian].
16. I. M. Nesmelova, *Optical Properties of Narrow-Gap Semiconductors* (Nauka, Novosibirsk, 1992), p. 158 [in Russian].
17. G. Nicolis and I. Prigogine, *Exploring Complexity* (Freeman, New York, 1989; Mir, Moscow, 1990).
18. A. M. Yafyasov, I. M. Ivankiv, and V. B. Bogevolnov, Appl. Surf. Sci. **142**, 629 (1999).

Translated by I. Zvyagin

Semiconductors, Vol. 38, No. 11, 2004, pp. 1340–1343. Translated from Fizika i Tekhnika Poluprovodnikov, Vol. 38, No. 11, 2004, pp. 1382–1385.

LOW-DIMENSIONAL SYSTEMS

Laser-Induced Resonant Electron Transitions in a Structure with Three Quantum Dots

A. V. Tsukanov

Institute of Physics and Technology, Russian Academy of Sciences, Moscow, 117218 Russia

e-mail: tsukanov@ftian.oivta.ru

Submitted April 8, 2004; accepted for publication April 15, 2004

Abstract—The effect of a resonance laser pulse on the quantum dynamics of electrons in a system of three semiconductor boxlike quantum dots is theoretically analyzed. It is shown that, in an asymmetric structure, the electron transfer between the two outer dots can be described in terms of a two-level scheme with diagonal transitions. The energies of the operating electron levels and the matrix elements for the corresponding electron transitions are found in the high-barrier approximation. The parameters of the laser pulse corresponding to the highest probability of resonance electron transitions between the ground states of two quantum dots are determined. © *2004 MAIK "Nauka/Interperiodica".*

1. INTRODUCTION

In [1] the dynamics of electrons in a semiconductor structure consisting of two similar quantum dots (QDs) under the action of a resonant laser field was considered. It was shown that the parameters of the laser pulse could be chosen so that the probability of electron transfer from one dot to the other is unity. Until now, however, the fabrication of two identical QDs has been practically impossible. The most "natural" source of errors in the production of such structures is the fact that it is difficult to control the heterolayer thickness with an accuracy exceeding several atomic layers. Accordingly, the QDs forming the potential in the direction of the structure growth may differ in width. The effect of the QD width on electron dynamics was studied analytically in [2]. According to the calculations, the probability of electron transfer between the ground states of two dots with different widths is always smaller than unity. Apart from purely technological problems, a substantial limitation on the parameters of the nanostructure is imposed by the mechanism of electron transport in delocalized states corresponding to the level in the vicinity of the edge of the barrier.

In this study, we suggest a mechanism of electron transport in a three-dot structure (between two outer dots) under the action of two resonance pulses. The main difference between this mechanism and the mechanisms considered in [1, 2] is that the electron transfer can be described in terms of diagonal transitions using only *localized* states. This possibility allows one to avoid a number of technical difficulties encountered in the previous approaches. Our aim is to choose the parameters of the system so that the electron that is initially localized in the ground state of one operating dot can pass to one of the excited levels of the central dot and then to the ground state of the other operating dot in a time that is short compared to the characteristic relaxation times. As in the case considered in [2], we assume the simplest nanostructure geometry with a boxlike shape of the dots. This model allows us to calculate the electron spectrum near the bottom of the conduction band, to find the matrix elements of transitions between the states of interest, and to obtain the time dependence of occupancies of these states. The analysis of the results obtained indicates that the probability of electron transitions between the ground states of the outer dots is close to unity and its deviation from unity is primarily due to the detuning of the field frequency from the transition frequency.

2. ELECTRON ENERGY SPECTRUM IN AN ASYMMETRIC STRUCTURE OF THREE QUANTUM DOTS

Let us consider a structure consisting of three QDs (A_1, A_2, and C) separated by the potential barriers B_1 and B_2 and connected via electron tunneling in the x direction (Fig. 1). We assume that there exist two deep levels localized in the outer dots and a level in the central (buffer) dot. Let us take the structure size to be L along both y and z directions. The dots are surrounded by a barrier that has a finite height U along the x direction and is infinite in the y and z directions. We assume that the outer dots are formed from semiconductors with identical band gaps and the conduction-band offsets between the central and outer dots are $V < U$. The thicknesses of the QDs (as well as those of the barriers) in the x direction can be different, $\tilde{a} = a + \delta a$ and $\tilde{b} = b + \delta b$. Then, without loss of generality, we set $\delta a < 0$ and, for the sake of simplicity, consider the electron effective mass m^* to be the same in the QDs and in the barriers.

1063-7826/04/3811-1340$26.00 © 2004 MAIK "Nauka/Interperiodica"

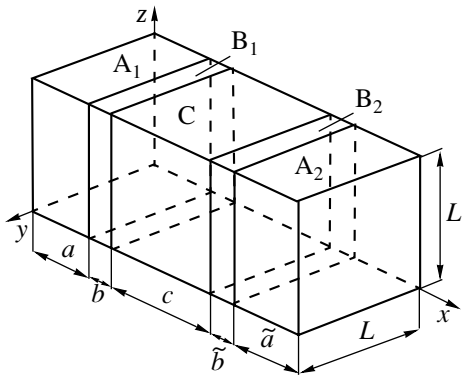

Fig. 1. A model of the nanostructure consisting of three quantum dots (A_1, A_2, and C) separated by barriers B_1 and B_2 of thicknesses b and $\tilde{b}$, respectively. The origin of coordinates is at the center of dot C. The quantum dot A_1 occupies the space region $-(c/2 + a + b) < x < -(c/2 + b)$, $|y|, |z| < L/2$; the dot A_2, $c/2 + \tilde{b} < x < c/2 + \tilde{a} + \tilde{b}$, $|y|, |z| < L/2$; and the dot C, $-c/2 < x < c/2$, $|y|, |z| < L/2$. The electron potential energy $U(\mathbf{r}) = 0$ for $\mathbf{r} \in A_{1,2}$; $U(\mathbf{r}) = V$ for $\mathbf{r} \in C$; $U(\mathbf{r}) = U$ for $\mathbf{r} \in B_{1,2}$ and for $x < -(c/2 + a + b)$, $x > c/2 + \tilde{a} + \tilde{b}$, $|y|$, $|z| < L/2$; and $U(\mathbf{r}) = +\infty$ at $|y|, |z| > L/2$.

In this model, the time-independent Schrödinger equation admits the separation of variables. The electron wave function has the form

$$\Psi(\mathbf{r}) = \frac{2}{L}\Psi(x)\cos\left(\frac{\pi n_2 y}{L}\right)\cos\left(\frac{\pi n_3 z}{L}\right), \qquad (1)$$

where $n_2 \geq 1$ and $n_3 \geq 1$ are integers. The energy eigenvalues measured from the bottom of the outer well are equal to

$$\varepsilon = \varepsilon_x + \frac{\hbar^2\pi^2(n_2^2 + n_3^2)}{2m^*L^2}. \qquad (2)$$

The value of ε_x can be determined from the dispersion relation that follows from the continuity condition for both the wave function $\Psi(x)$, which is a solution to the one-dimensional Schrödinger equation with the potential $U(x)$ (see Fig. 2), and its derivative.

We now consider the subband corresponding to $n_2 = 1$ and $n_3 = 1$. Let us take the quantity $\hbar^2\pi^2/m^*L^2$ as the new reference energy; then, $\varepsilon = \varepsilon_x$. We are interested in states with energies $\varepsilon_x \ll U$. In this approximation, we find that the energies of the operating levels are

$$\varepsilon_1 \approx U\frac{\pi^2}{\xi_a^2}\left[1 - 2\frac{\exp(br_a/a)}{r_a\sinh(br_a/a)}\right], \qquad (3)$$

$$\varepsilon_2 \approx \frac{\varepsilon_1}{1 + 2\delta a/a}, \qquad (4)$$

where

$$\xi_a = (2m^*a^2U/\hbar^2)^{1/2} \gg 1, \quad r_a = \sqrt{\xi_a^2 - \pi^2}.$$

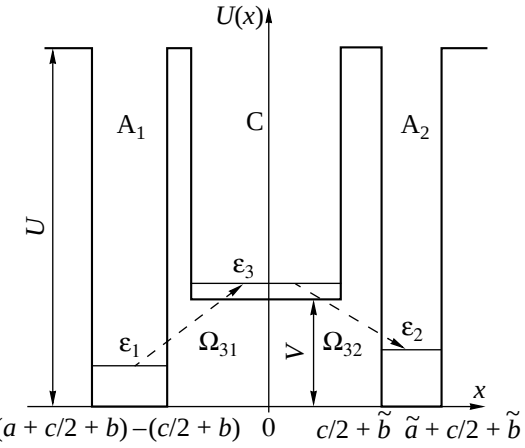

Fig. 2. Energy levels of the nanostructure consisting of three quantum dots (A_1, A_2, and C); ε_1 and ε_2 are the energy levels of the states localized in the outer dots and ε_3 is the transport level; U is the height of the energy barrier surrounding the dots; V is the conduction-band offset for the dots C, A_1, and A_2; and Ω_{31} and Ω_{32} are the transition frequencies.

As a transport level, we choose the first excited level, whose wave function has a maximum in the central dot. Setting

$$\xi_c = (2m^*c^2(U - V)/\hbar^2)^{1/2} \gg 1,$$

we find the energy of the transport level in the form

$$\varepsilon_3 \approx V + (U - V)\frac{\pi^2}{\xi_c^2}\left\{1 - \frac{2\sinh[(b + \tilde{b})r_c/c]}{r_c\sinh(br_c/c)\sinh(\tilde{b}r_c/c)}\right\},$$

$$r_c = \sqrt{\xi_c^2 - \pi^2}. \qquad (5)$$

We calculated the energies ε_1, ε_2, and ε_3 for a nanostructure with the parameters $a = 20$ nm, $b = 3$ nm, $c = 60$ nm, $\delta a = -1$ nm, $\delta b = 0$, $U = 1$ eV, $V = 0.045$ eV, and $m^* = 0.067m_0$, where m_0 is the free-electron mass. Using formulas (3) and (5), we obtain $\varepsilon_1 = 0.0118$, $\varepsilon_2 = 0.0132$, and $\varepsilon_3 = 0.0465$ eV. Simulation shows that ε_1 and ε_2 differ from the exact values by approximately 1% and the expression for ε_3 is valid with an accuracy of 0.01%. Indeed, since $\xi_c \approx 3\xi_a$, the approximation of high barriers performs better for the deeper central well. The wave functions $\Psi_1(x)$, $\Psi_2(x)$, and $\Psi_3(x)$ closely resemble the wave functions of the lower level in the corresponding isolated wells and are localized in the dots A_1, A_2, and C, respectively.

3. MATRIX ELEMENTS FOR OPTICAL DIPOLE TRANSITIONS AND THE PROBABILITY OF ELECTRON TRANSFER BETWEEN QUANTUM DOTS

Let us consider an electron that is initially localized on the lower level of the dot A_1. What will happen if we apply an external electric field with frequency Ω_{m1} that

is close to the frequency of transition between this state and one of the excited ones? If the matrix element of the electron–field interaction for these two states is nonzero, then electron transitions between them are induced. In the dipole approximation, the interaction with the field is characterized by the matrix element of the dipole transition between levels i and j,

$$\mathbf{d}_{ij} = -e\int \Psi_i^*(\mathbf{r})\mathbf{r}\Psi_j(\mathbf{r})d\mathbf{r}, \quad (6)$$

where e is the elementary charge.

Generally, the time dependence of the occupancy $p_i(t) = |\Psi_i(\mathbf{r}, t)|^2$ of level i is oscillatory. Using the resonance approximation, we can obtain the functions $p_i(t)$ in explicit form for a two-level system. The behavior of the occupancy of the ith level in the vicinity of the maximum $p_i^{\max}$ is of practical interest; we associate this maximum with the *probability of electron transfer* to the ith state.

In the energy diagram of the structure shown in Fig. 2, each operating state is mainly localized in one of the outer dots. The transfer itself occurs in two stages (two-level scheme, Rabi transitions). This process requires *two* laser pulses with frequencies corresponding to the frequencies of the *diagonal* electron transitions $|1\rangle \rightleftharpoons |3\rangle$ and $|3\rangle \rightleftharpoons |2\rangle$:

$$\Omega_{31} = \frac{(\varepsilon_3 - \varepsilon_1)}{\hbar}, \quad \Omega_{32} = \frac{(\varepsilon_3 - \varepsilon_2)}{\hbar}.$$

The laser field whose strength varies with time as

$$\mathbf{E}(t) = \mathbf{E}_1[\Theta(T_1 - t) - \Theta(-t)]\cos[(\Omega_{31} + \delta_1)t]$$
$$+ \mathbf{E}_2[\Theta(T_1 + T_2 - t) - \Theta(T_1 - t)]\cos[(\Omega_{32} + \delta_2)t]$$

generates two successive π pulses with the durations T_1 and T_2, respectively, where

$$T_i = \frac{0.5\pi}{\sqrt{(0.5\delta_i)^2 + |\lambda_i|^2}}.$$

Here, $\Theta(x)$ is the theta function, δ_i is the detuning of the ith pulse frequency from the transition frequency, and

$$\lambda_i \equiv \lambda_{i3} = \frac{\mathbf{E}_i\mathbf{d}_{i3}}{2}.$$

The occupancies of the operating levels depend on time as

$$p_1(t) = [\cos^2(\omega_1 t) + (\delta_1/2\omega_1)^2\sin^2(\omega_1 t)]$$
$$\times [\Theta(T_1 - t) - \Theta(-t)],$$

$$p_2(t) = \left(\frac{|\lambda_1|}{\omega_1}\right)^2\left(\frac{|\lambda_2|}{\omega_2}\right)^2\sin^2[\omega_2(t - T_1)]$$
$$\times [\Theta(T_1 + T_2 - t) - \Theta(T_1 - t)], \quad (7)$$

$$p_3(t) = \left(\frac{|\lambda_1|}{\omega_1}\right)^2\{[\Theta(T_1 - t) - \Theta(-t)]\sin^2(\omega_1 t)$$
$$+ [\Theta(T_1 + T_2 - t) - \Theta(T_1 - t)]\{\cos^2[\omega_2(t - T_1)]$$
$$+ (\delta_2/2\omega_2)^2\sin^2[\omega_2(t - T_1)]\}\};$$

the frequencies of the electron transitions between the dots have the form

$$\omega_i = \sqrt{\left(\frac{\delta_i}{2}\right)^2 + |\lambda_i|^2}.$$

The probability of electron transfer between the two outer dots can be expressed as

$$p_2^{\max} = p_2(T_1 + T_2) \approx 1 - \left(\frac{\delta_1}{2|\lambda_1|}\right)^2 - \left(\frac{\delta_2}{2|\lambda_2|}\right)^2. \quad (8)$$

Assuming that the field is polarized along the x axis (i.e., $\mathbf{E}_{1,2} = E\mathbf{e}_x$), we calculate $|\lambda_1|$:

$$|\lambda_1| = \gamma eEa\left(\frac{a}{c}\right)^{3/2}\frac{\varepsilon_1^2}{\hbar^3\Omega_{31}^2}\sqrt{\frac{\varepsilon_3}{U - \varepsilon_3}}\sinh^{-1}(br_c/c). \quad (9)$$

Here, the numerical factor γ depends on the parameters of the structure. A similar expression can also be obtained for $|\lambda_2|$. Formula (9) clearly illustrates the features of diagonal transitions. For fairly wide barriers, we have

$$|\lambda_1| \approx \lambda_0\sqrt{\frac{\varepsilon_3}{U - \varepsilon_3}}\exp(-br_c/c),$$

where λ_0 corresponds to the transition $|1\rangle \rightleftharpoons |2\rangle$ in an infinitely deep one-dimensional rectangular quantum well. For $b \gg c/r_c$, the transitions are almost suppressed. The smallness of the factor $\sqrt{\varepsilon_3/(U - \varepsilon_3)}$ indicates that there is no resonance between the outer wells for the energy $\varepsilon_3 = \varepsilon_1 + \hbar\Omega_{31} = \varepsilon_2 + \hbar\Omega_{32}$.

Let us estimate the value of $p_2^{\max}$ using the parameters mentioned in Section 2 and setting $\delta_i = 10^9$ s^{-1}. Formula (9) yields $|\lambda_1| \approx 16.2 \times 10^9$ s^{-1} and $|\lambda_2| \approx 6.5 \times 10^9$ s^{-1} for $E = 500$ V/cm and $\gamma \approx 8$. Thus, $T = T_1 + T_2 \approx 0.3$ ns and $p_2^{\max} = 0.993$. The quantities λ_i should satisfy the inequalities

$$|\lambda_i| \ll \frac{(\varepsilon_4 - \varepsilon_3)}{\hbar}, \quad |\lambda_i| \ll \frac{(\varepsilon_2 - \varepsilon_1)}{\hbar},$$

where ε_4 is the energy of the level that is closest to the transport level. The first inequality indicates that no transitions from the transport state to the higher part of the spectrum are induced, and the second inequality is the condition for applicability of the two-level scheme (indeed, if $|\lambda_i| \geq (\varepsilon_2 - \varepsilon_1)/\hbar$, then the transition is a single-stage process). These conditions are satisfied for $|\lambda_i| \leq 10^{11}$ s^{-1}.

4. DISCUSSION

In [2] the probability of electron transfer between the ground states of two QDs with nearly the same sizes is shown to depend on the difference in their geometrical parameters. This probability is close to unity if the widths of the quantum wells in the tunneling direction differ by no more than a few percent. Such a mechanism of electron transfer is complicated, since the number of conditions that should be imposed on the system parameters affecting the transfer probability is large. Therefore, the electron transport mechanism itself should be simplified. The feasibility of such a simplification is related to the above method of dividing a complex single-stage process into two simpler ones, where the diagonal transitions occur independently and are characterized by different sets of parameters. We see that the asymmetry does not adversely affect the transfer probability. At the same time, the presence of asymmetry is necessary for the parameters of electron transitions to differ from each other. Accordingly, the requirements for the fabrication technology may be considerably relaxed. The fact that one of the localized levels is used as a transport level makes this mechanism more stable with respect to electron excitations to the continuous spectrum. Note that precise synchronization of two successive pulses is a necessary condition for the realization of this mechanism.

The lifetime of an electron in an excited state is mostly limited by the time of electron–phonon relaxation. The contribution of other processes to the destruction of the wave-function coherence is much weaker. The main mechanism that is responsible for electron relaxation in QDs is the interaction with longitudinal acoustic (LA) phonons [3]. The probability of transitions involving phonon emission or absorption can be significantly decreased by an appropriate choice of the parameters of the structure. Specifically, the parameters should be taken so that the minimal difference between the energy levels satisfies the inequality $3\hbar^2\pi^2/2m^*L^2 > \varepsilon_{crit}$, where $\varepsilon_{crit} \approx 3\pi\hbar v_s/2a$ is the maximum energy of acoustic phonons and v_s is the velocity of sound (we assume that $a, c < L$). Therefore, the linear size L of the structure should satisfy the inequality $L < L_{crit} \approx \sqrt{\pi\hbar a/m^* v_s}$; then the relaxation probability decreases as L^8 [3]. For conventional materials, setting $a \approx 20$–30 nm, we obtain $\varepsilon_{crit} \approx 0.5$–$1$ meV and $L_{crit} \approx 150$ nm. In this case, the time of electron–phonon relaxation time τ_{ph} ranges from 10^{-6} to 10^{-7} s and, obviously, $T \ll \tau_{ph}$. With a further decrease in a, the relaxation rate increases due to the stronger interaction between electrons and interface (IF) phonons [4].

5. CONCLUSIONS

The coherent evolution of an electron in a structure consisting of three quantum dots in a resonance electric field was studied. It was shown that dot-to-dot electron transfer can be described in terms of a two-level model with diagonal transitions. The probability of transfer is close to unity if the detuning δ_i from the resonance is appreciably smaller than the matrix elements of electron–field interaction λ_i. In addition, by appropriately choosing the parameters of the structure, one can almost entirely prevent the electron from leaving the structure and exclude the hybridization of closely spaced energy levels and electron–phonon relaxation. Such a transfer scheme can be used in the design of quantum computers, in which the information is encoded in electron orbital states, as well as for some versions of solid-state NMR quantum computers [5, 6].

ACKNOWLEDGMENTS

I thank L.A. Openov for discussion of the results and K.A. Valiev and I.A. Semenikhin for their interest in this study.

REFERENCES

1. L. A. Openov, Phys. Rev. B **60**, 8798 (1999).
2. A. V. Tsukanov and L. A. Openov, Fiz. Tekh. Poluprovodn. (St. Petersburg) **38**, 94 (2004) [Semiconductors **38**, 91 (2004)].
3. H. Benisty, Phys. Rev. B **51**, 13281 (1995).
4. P. A. Knipp and T. L. Reinecke, Phys. Rev. B **52**, 5923 (1995).
5. A. A. Larionov, L. E. Fedichkin, and K. A. Valiev, Nanotechnology **12**, 536 (2001).
6. A. V. Tsukanov, A. A. Larionov, and K. A. Valiev, Proc. SPIE **5128**, 131 (2003).

Translated by A. Sidorova

Semiconductors, Vol. 38, No. 11, 2004, pp. 1344–1349. Translated from Fizika i Tekhnika Poluprovodnikov, Vol. 38, No. 11, 2004, pp. 1386–1391.

AMORPHOUS, VITREOUS, AND POROUS SEMICONDUCTORS

Effect of Adsorption of the Donor and Acceptor Molecules at the Surface of Porous Silicon on the Recombination Properties of Silicon Nanocrystals

E. A. Konstantinova, Yu. V. Ryabchikov^, L. A. Osminkina, A. S. Vorontsov, and P. K. Kashkarov

Department of Physics, Moscow State University, Moscow, 119992 Russia

^e-mail: yuri_r@vega.phys.msu.ru

Submitted March 1, 2004; accepted for publication April 6, 2004

Abstract—The effect of adsorption of the donor and acceptor molecules on the spectra of photoluminescence and electron spin resonance (ESR) of microporous silicon is studied. It is found that photoluminescence of microporous silicon is quenched, the photoluminescence peak shifts to shorter wavelengths, and the intensity of the ESR signal increases after adsorption of molecules of nitrogen dioxide and pyridine. The results obtained are interpreted using a model of radiative excitonic recombination in porous silicon that takes into account the formation of both the charged $(NO_2)^-$ and $(C_5H_5N)^+$ complexes and defects (e.g., dangling bonds at the silicon surface) at the surface of silicon nanocrystals. © *2004 MAIK "Nauka/Interperiodica"*.

1. INTRODUCTION

The discovery of intense luminescence of porous silicon (*por*-Si) in the visible region of the spectrum at room temperature [1] provided a powerful stimulus to the studies of optical, electrical, and structural properties of this material [2–4], which includes a variety of nanocrystals with sizes ranging from several nanometers to hundreds of nanometers [4]. However, the presence of an extremely large specific surface that is very sensitive to the effects of a surrounding medium hampers the use of *por*-Si in light-emitting diodes. This evident drawback (from the viewpoint of optoelectronics) is compensated by new prospects for using *por*-Si nanocrystals for the development of the next generation of gas sensors based on this material [5].

In the literature there is now extensive data from research into the effect of dielectric media on the optical and electrical properties of *por*-Si [6–9]. A partially or completely reversible quenching of photoluminescence (PL) and an increase in the electrical conductivity were observed in *por*-Si immersed in spirits or exposed to the vapors of various liquids whose dielectric constants varied within a wide range [6–9]. In order to interpret the results obtained, several models were used. These models implied a modification of defects on the surface of silicon nanocrystals [6], variations in the coverage of the *por*-Si surface with molecules as the gaseous medium in the *por*-Si pores was changed [7], and a decrease in the binding energy of excitons (consequently, a decrease in the exciton concentration at a given temperature) with increasing permittivity of the medium that surrounds the nanocrystals [8, 9].

At the same time, the effect of molecules adsorbed in the form of charge-transfer complexes on optoelectronic characteristics of nanocrystals in *por*-Si layers has been inadequately studied. In addition, the initial *por*-Si samples in a number of cases exhibited different degrees of oxidation [8, 10, 11], which significantly influences the effect of these molecules on the physical properties of *por*-Si and makes it difficult to analyze and compare the available published data.

Therefore, the objective of this study was to gain insight into the effect of adsorption of the donor and acceptor molecules (pyridine C_5H_5N and nitrogen dioxide NO_2, respectively) on PL and paramagnetic centers (defects) in microporous silicon. The surface composition of silicon nanocrystals in the *por*-Si layers was determined using infrared (IR) spectroscopy.

2. EXPERIMENTAL

We used *por*-Si layers formed on the substrates of single-crystal silicon (*c*-Si) with *p*-type conductivity, (100) orientation, and resistivity $\rho = 12\ \Omega$ cm. The *por*-Si layers were obtained by electrochemical etching of *c*-Si in an electrolyte based on hydrofluoric acid and ethanol (proportion of 1 : 1) at a current density of 50 mA/cm^2. The *por*-Si thickness was measured using an optical microscope and was equal to 38 μm. The porosity was evaluated gravimetrically and amounted to ~70%. In order to remove the loosely bonded molecules from the *por*-Si surface before measurements, we kept the samples in vacuum (at a residual pressure of $P = 10^{-6}$ Torr) for 24 h.

We obtained nitrogen dioxide using the following chemical reaction: Cu (copper chips) + $4HNO_3$ =

$2NO_2$ (gas) + $Cu(NO_3)_2$ + $2H_2O$. In order to remove water, the NO_2 gas was passed through a flask filled with a P_2O_5 desiccator. We used commercially produced extrapure pyridine.

The PL spectra of *por*-Si were measured at room temperature using a computer-controlled setup. The PL was excited by a nitrogen laser (wavelength λ = 337 nm, pulse duration τ = 10 ns, and energy density in a pulse W = 0.2 mJ/cm^2). The PL signal was detected using a cooled Hamamatsu RS 632-01 photomultiplier. All molecules were adsorbed from the gaseous phase using a Varian oil-free vacuum system. The measured PL spectra were corrected for the spectral sensitivity of the experimental setup.

The concentration of paramagnetic centers was determined from the measurements of the electron spin resonance (ESR) using a PS 100.X spectrometer with an operating frequency of 9.5 GHz and a sensitivity of 5×10^{10} spin/G. In order to calculate the *g*-factors and defect concentrations, we used the reference samples MgO with Mn^{++} ions and $CuCl_2 \cdot 2H_2O$, respectively.

The *por*-Si surface composition was evaluated using a Perkin Elmer RX I IR spectrometer with the inverse Fourier transform (measurement range 6000–400 cm^{-1}, resolution 2 cm^{-1}).

3. RESULTS

Let us first discuss the modification of the surface bonds of silicon nanocrystals as a result of the adsorption of molecules. In Fig. 1, we show the spectral dependences of the IR absorption coefficient $\alpha(\nu)$ determined from the transmission spectra using the formula $\alpha(\nu) = -d^{-1}\ln[T(\nu)]$, where $T(\nu)$ is the transmission coefficient, d is the layer thickness, and ν is the wave number. As can be seen from Fig. 1 (curve *1*), the surface of freshly prepared *por*-Si layers has a predominantly hydrogen coating (bending vibrations of Si–H_x with the band peaked at 660 cm^{-1}, scissor vibrations of Si–H_2 at 910 cm^{-1}, and stretching modes of Si–H_x (x = 1, 2, 3) at ν = 2070–2170 cm^{-1} [2]).

The oxidation of the surface of silicon nanocrystals as a result of the adsorption of NO_2 molecules is first observed at gas pressure $P_{NO_2} > 0.1$ Torr and increases as the pressure of NO_2 gas increases further. In the spectrum shown in Fig. 1 (curve *2*), the absorption band corresponding to stretching Si–O–Si vibrations in the range from 1050 to 1100 cm^{-1} corresponds to the oxide [2]. In addition to the aforementioned absorption bands, the IR absorption at ν = 1620–1680 cm^{-1} is also observed in the *por*-Si films exposed to NO_2 molecules at high pressures. This observation indicates that Si–O–N=O nitrites are formed at the *por*-Si surface [12]. Thus, the interaction of NO_2 molecules with the surface of silicon nanocrystals can be described by the following reaction: $NO_2 + Si_3{-}Si{-}H \longrightarrow SiO_x + Si{-}O{-}N{=}O + H_2O$, where $1 \le x \le 2$.

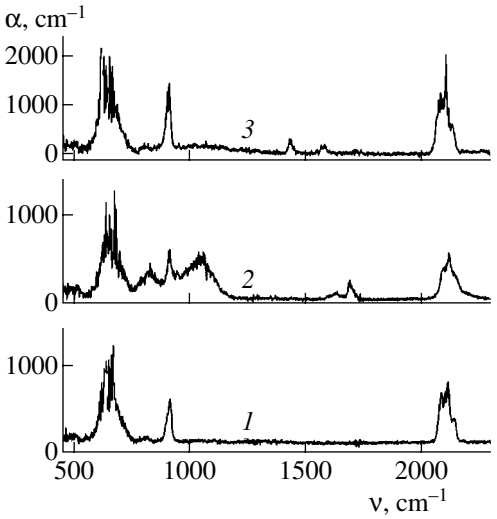

Fig. 1. Spectra of the coefficient of IR-radiation absorption in *por*-Si (*1*) in vacuum at a residual pressure of 10^{-6} Torr (as-prepared samples), (*2*) in an atmosphere of NO_2 molecules at a pressure of 10 Torr, and (*3*) in an atmosphere of C_5H_5N molecules at a pressure of 2 Torr.

In complete agreement with published data [13], the adsorption of pyridine is not accompanied by the formation of covalent chemical bonds with the adsorbent. As can be seen from Fig. 1 (curve *3*), only the bands peaked at wave numbers of 1438 and 1588 cm^{-1} are observed in the IR spectra. These bands correspond to absorption by the C–H stretching vibrations of the C_5H_5N molecules adsorbed in the neutral state [14].

In Fig. 2 we show the PL spectra of both the as-prepared sample and *por*-Si in the NO_2 medium under various pressures. The spectra are represented by broad bands that result from the superposition of contributions of nanocrystals with different sizes [2]. The quenching of PL is observed for all pressures of NO_2 introduced into the vacuum cell with the sample (Fig. 2, inset). The PL intensity I_{PL} of *por*-Si in an NO_2 atmosphere at P_{NO_2} = 10 Torr is at least 20 times lower than that of as-prepared samples.

In addition, the adsorption of NO_2 molecules causes the PL spectral peak to shift to shorter wavelengths. For example, the peak of the spectrum for *por*-Si in an NO_2 atmosphere at P_{NO_2} = 10 Torr is shifted by $\Delta\lambda$ = 50 nm to shorter wavelengths with respect to its position for the as-prepared sample (Fig. 2).

The PL quenching was partially reversible if the cell was evacuated after the inlet of NO_2. For example, curve *4* in Fig. 2 illustrates a partial recovery of the PL intensity after evacuation of the cell with samples exposed previously to NO_2 at P_{NO_2} = 10 Torr.

The effect of the adsorption of pyridine on PL spectra of *por*-Si at various pressures of C_5H_5N vapors is

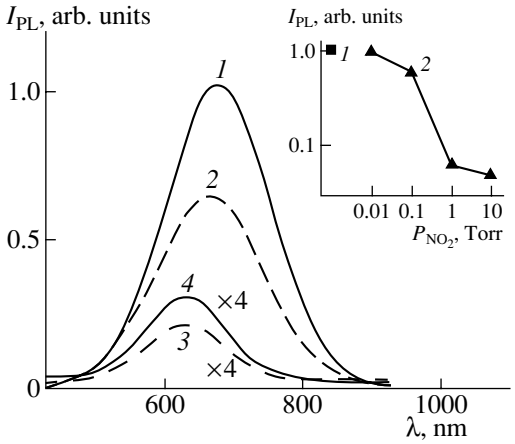

Fig. 2. Photoluminescence spectra of *por*-Si in vacuum and under different pressures of NO_2 (P_{NO_2}): (*1*) in vacuum (10^{-6} Torr, as-prepared samples), (*2*) at P_{NO_2} = 0.1 Torr, (*3*) at P_{NO_2} = 10 Torr, and (*4*) after evacuation of the cell (to 10^{-6} Torr) following the introduction of NO_2 at P_{NO_2} = 10 Torr. Inset: dependence of the photoluminescence intensity measured at the spectral peak on the NO_2 gas pressure: (*1*) as-prepared samples in vacuum (10^{-6} Torr) and (*2*) samples in an atmosphere of NO_2.

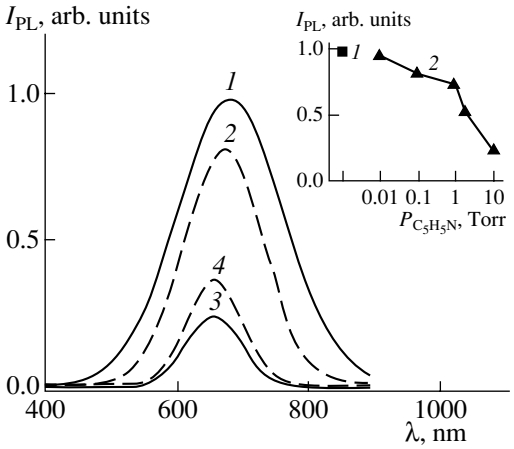

Fig. 3. Photoluminescence spectra of *por*-Si in vacuum and at various C_5H_5N pressures ($P_{C_5H_5N}$): (*1*) in vacuum (10^{-6} Torr, as-prepared samples), (*2*) at $P_{C_5H_5N}$ = 0.1 Torr, (*3*) at $P_{C_5H_5N}$ = 3.8 Torr, and (*4*) in a cell evacuated to 10^{-6} Torr after the introduction of C_5H_5N at $P_{C_5H_5N}$ = 3.8 Torr. Inset: the dependence of the photoluminescence intensity measured at the spectrum peak on the pressure of C_5H_5N gas: (*1*) for as-prepared samples in vacuum (10^{-6} Torr) and (*2*) for samples in an atmosphere of C_5H_5N.

illustrated in Fig. 3. A decrease in the value of I_{PL} is observed as a result of exposure to C_5H_5N molecules. However, the degree of quenching is lower than in the case of NO_2 adsorption (Fig. 3, inset). For example, the value of I_{PL} for *por*-Si in an atmosphere of C_5H_5N at vapor pressure $P_{C_5H_5N}$ = 3.8 Torr is four times smaller than that for the as-prepared sample.

In addition, as in the case of adsorption of NO_2, the interaction of C_5H_5N molecules with the *por*-Si surface gives rise to a shift of the PL spectral peak to shorter wavelengths. However, this shift is smaller than that observed for NO_2 adsorption. In particular, the PL spectral peak of *por*-Si in a pyridine atmosphere at vapor pressure $P_{C_5H_5N}$ = 3.8 Torr is shifted by $\Delta\lambda$ = 20 nm to shorter wavelengths with respect to that of the as-prepared sample (Fig. 3).

The PL quenching was also partially reversible if the inlet of C_5H_5N was followed by evacuation of the cell. Curve *4* in Fig. 3 illustrates the partial recovery of the PL intensity of *por*-Si in a cell evacuated after C_5H_5N molecules were introduced at $P_{C_5H_5N}$ = 3.8 Torr.

Note that the PL bands are narrowed as a result of the interaction of molecules with the surface of silicon nanocrystals (Figs. 2, 3).

It follows from the above data that the adsorption of NO_2 and C_5H_5N molecules leads to considerable variations in the PL parameters of *por*-Si. These variations may be caused by changes in the mechanisms of both radiative and nonradiative recombination of charge carriers. According to the published data [8], nonradiative recombination occurs via defects at the surface of nanocrystals in *por*-Si layers. Therefore, in order to gain independent information about the effect of adsorption on these defects, we performed a series of measurements of ESR spectra for the *por*-Si samples.

In Fig. 4 we show the ESR spectra of *por*-Si before and after adsorption of NO_2 molecules. The values of the most important parameters (calculated from the ESR spectra) $g_{eff} = 2.0064 \pm 0.0005$ and $\Delta H = 12 \pm 0.5$ G indicate that the defects detected in our experiments are the so-called P_{b0} centers (dangling silicon bonds at the Si/SiO_2 interface [15]). The absence of a two-component structure of the spectrum, which is characteristic of this type of paramagnetic center, can be attributed to the fact that the network of nanocrystals is more disordered in microporous silicon than that in mesoporous silicon [16]. As a result, the lines in the ESR spectrum are broadened and only the envelope curve is detected experimentally.

As the pressure of NO_2 gas increases, the ESR signal intensity (I_{ESR}) increases (Fig. 4). The ESR spectrum of *por*-Si in the cell that is evacuated after the introduction of nitrogen dioxide at P_{NO_2} = 1 Torr is also shown in Fig. 4. It can be seen that the ESR spectrum hardly changes as a result of evacuation. The fact that the variation in the ESR signal as a result of the introduction of NO_2 molecules was not affected by the sub-

sequent evacuation was observed for all the used pressures of NO_2.

We also calculated the concentrations of defects N_s in as-prepared *por*-Si and in *por*-Si exposed to NO_2 gas (Fig. 5). It follows from Fig. 5 that the concentration of paramagnetic centers in *por*-Si exposed to NO_2 (at P_{NO_2} = 10 Torr) is 30 times higher than that in as-prepared *por*-Si.

An increase in the concentration of P_{b0} centers as a result of adsorption of C_5H_5N molecules is observed (Fig. 6) as in the case of adsorption of NO_2 molecules. This effect of C_5H_5N adsorption was partially suppressed if the cell was evacuated after the inlet of C_5H_5N.

4. DISCUSSION

According to the model of recombination processes in silicon nanocrystals that we developed previously [8, 17], the PL in *por*-Si is caused by radiative excitonic recombination in Si nanocrystals with various sizes. Calculations [18] show that the existence of excitons at room temperature in these systems is caused by high exciton-binding energies E_{exc} (on the order of hundreds of millielectronvolts). Nonradiative recombination occurs at the surface defects. Thus, the PL spectrum recorded at this temperature includes contributions of nanocrystals with various sizes; the value of each contribution is governed by the relation between the probabilities of radiative and nonradiative recombination in a nanocrystal.

Adsorption can affect both the radiative- and nonradiative-recombination channels. Kashkarov *et al.* [8] suggested three mechanisms for this effect: (i) the formation of surface defects that act as nonradiative-recombination centers; (ii) the formation of charged adsorption-related centers that destroy the excitons with their electric fields; and (iii) the condensation of the vapors of liquids (with high permittivities) in the pores of the sample, which leads to a decrease in the exciton-binding energy and, consequently, to a decrease in the exciton concentration at a given temperature. The above three mechanisms lead to PL quenching in the course of adsorption.

Taking into account the above reasoning, we now discuss the experimental data reported in this paper. We assume that a decrease in the PL intensity as a result of adsorption of the NO_2 and C_5H_5N molecules at low pressures ($P = 10^{-2}$–10^{-1} Torr) is caused by the dissociation of excitons due to local electric fields of the Coulomb $(NO_2)^{-\delta}$, $(NO_2)^-$, $(C_5H_5N)^{+\delta}$, and $(C_5H_5N)^+$ centers adsorbed at the *por*-Si surface. The superscript δ denotes a partial charge transfer between the adsorbate and adsorbent ($0 < \delta < 1$). This type of adsorption is a weak form of chemisorption that is partially reversible at room temperature. The formation of the above com-

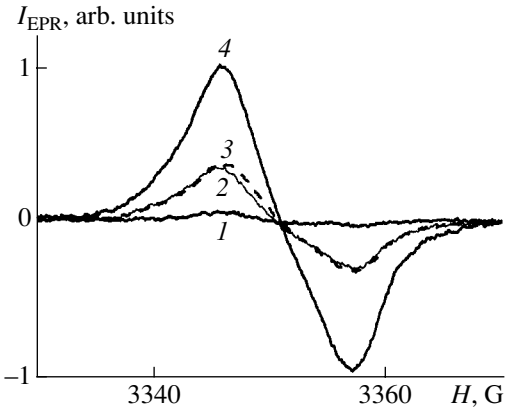

Fig. 4. ESR spectra of *por*-Si samples in vacuum and at various pressures of NO_2 (P_{NO_2}): (*1*) in vacuum (10^{-6} Torr, as-prepared samples), (*2*) at P_{NO_2} = 1 Torr, (*3*) in a cell evacuated after the introduction of NO_2 at P_{NO_2} = 1 Torr, and (*4*) at P_{NO_2} = 10 Torr.

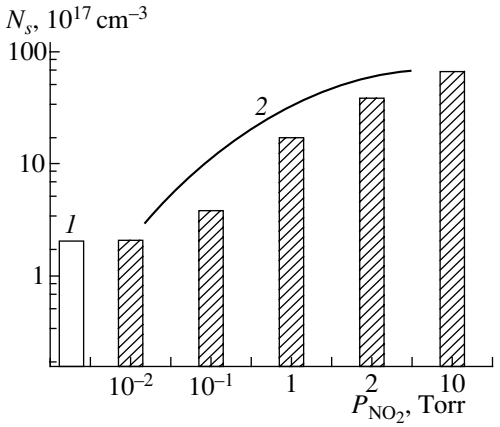

Fig. 5. Dependence of the defect concentrations N_s in *por*-Si on the pressure of NO_2 gas: (*1*) in vacuum (10^{-6} Torr, as-prepared samples) and (*2*) in an atmosphere of NO_2.

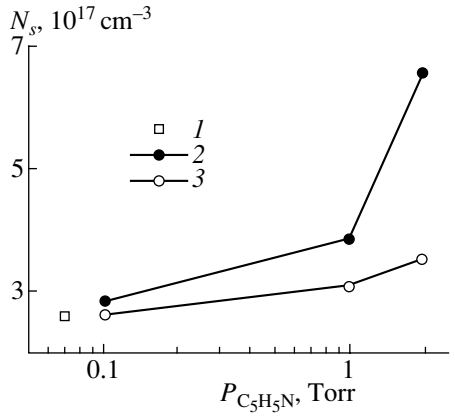

Fig. 6. Dependence of the defect concentrations in *por*-Si on the pressure of C_5H_5N vapors: (*1*) in vacuum (10^{-6} Torr, as-prepared samples), (*2*) in an atmosphere of C_5H_5N, and (*3*) in a cell evacuated after the introduction of C_5H_5N molecules at the corresponding pressure.

plexes is made possible because of the high electron and hole affinity of the corresponding molecules [19].

If the NO_2 and C_5H_5N molecules are adsorbed at higher pressures ($P > 0.1$ Torr), two additional mechanisms of PL quenching are conceivable as complementary to the formation of these complexes. Let us discuss these mechanisms in more detail.

In the case of adsorption of NO_2 molecules, the defects of the P_{b0} type centers are formed as a result of oxidation of the *por*-Si surface. As is well known, these centers play the role of nonradiative-recombination centers in silicon. This process is irreversible in a sequence that includes the introduction of molecules and subsequent evacuation of the cell. It is worth noting that an increase in the concentration of paramagnetic centers as a result of adsorption of the NO_2 molecules cannot be attributed to a change in the charge state of the P_{b0} centers that already exist. Indeed, the defects in *por*-Si formed on a *p*-type substrate can exist in both the neutral form (P_{b0}) and as centers that are positively charged as a result of the capture of the charge carriers, i.e., holes (P_{b0}^+). Among all the possible charge states of the silicon dangling bonds (P_{b0}, P_{b0}^+, and P_{b0}^-), only the neutral defects P_{b0} are paramagnetic (and, therefore, detectable by ESR). Consequently, an additional negative charge at the surface of nanocrystals as a result of the formation of the NO_2^- complexes can only increase the number of free holes in a nanocrystal and, thus, increase the number of P_{b0}^+ centers. This circumstance should lead to a decrease in the ESR signal, which is inconsistent with experimental data (Fig. 4).

The above increase in the concentration of P_{b0} centers in *por*-Si exposed to pyridine vapors (Fig. 6) is apparently not related to the formation of new defects. However, this increase can be completely attributed to the appearance of a positive charge at the surface of nanocrystals. Indeed, the charged $(C_5H_5N)^{+\delta}$ and $(C_5H_5N)^+$ complexes formed as a result of adsorption donate electrons to the *por*-Si layers (electrons are the minority charge carriers before adsorption). Thus, neutral defects are charged negatively (P_{b0}^-) as a result of capturing the electrons, whereas positively charged defects become neutral. An increase in N_s in the pyridine atmosphere (Fig. 6) indicates that the following reaction is prevalent:

$$P_{b0}^+ + e^- \longrightarrow P_{b0}.$$

Another additional mechanism of PL quenching at high pressures of gaseous media is in effect when pores in the samples are filled with dielectric liquid as a result of pyridine condensation. The instant of time corresponding to the onset of condensation of C_5H_5N molecules was determined from an increase in the coefficient of reflection of the beam of a He–Ne laser from the *por*-Si surface. The dielectric constant of C_5H_5N is $\varepsilon = 12.3$, which somewhat exceeds the corresponding value for silicon ($\varepsilon_{Si} = 11.8$). Consequently, according to [18], the value of E_{exc} decreases, which leads to thermal decomposition of some excitons and, as a result, to a decrease in the PL intensity.

The shift of the PL spectrum to shorter wavelengths for *por*-Si in the NO_2 atmosphere (Fig. 2) can be attributed to a decrease in size of the silicon nanocrystals as a result of oxidation. The "blue" shift of the PL spectrum of *por*-Si in the C_5H_5N atmosphere (Fig. 3) is apparently caused by the fact that, as a result of the dielectric effect, the value of E_{exc} decreases to a greater extent for large nanocrystals, whose emission contributes to the long-wavelength PL.

The observed shift of the PL spectral peak to shorter wavelengths may also be caused by the fact that the relaxation time of nonequilibrium charge carriers decreases (accordingly, the nonradiative-recombination rate increases) predominantly for large-sized nanocrystals, which contribute to the PL spectrum in the low-energy region [17]. Indeed, due to the low PL efficiency in the samples under study, the relation between the characteristic times of the radiative- and nonradiative-recombination processes can evidently be written as $\tau_r > \tau_{nr}$. This relation becomes stronger ($\tau_r \gg \tau_{nr}$) if we consider large nanocrystals, for which τ_r is longer [20].

Finally, we believe that the general narrowing of the *por*-Si PL spectra as a result of adsorption of NO_2 and C_5H_5N molecules can be accounted for in the following way. The destructive effect of the fields of the formed Coulomb $(NO_2)^-$ and $(C_5H_5N)^+$ centers is most significant for nanocrystals with the smallest sizes (r); the electric-field strength is largest ($E \propto 1/r^2$) for these nanocrystals. At the same time, the exciton-binding energy decreases as the size of nanocrystals increases [18]. Thus, symmetric quenching of the entire PL band is apparently caused by a decrease in the exciton concentration both in small-sized nanocrystals (due to the greater strength of the Coulomb field) and in larger nanocrystals (due to lower exciton-binding energies).

5. CONCLUSIONS

We studied the effect of adsorption of the acceptor and donor molecules of pyridine and nitrogen dioxide at the *por*-Si surface on the recombination characteristics of silicon nanocrystals in *por*-Si layers and on paramagnetic centers at the surface of these nanocrystals.

We suggest the following major mechanisms of PL quenching in the material under consideration.

(i) The formation of Coulomb $(NO_2)^-$ and $(C_5H_5N)^+$ centers at the *por*-Si surface ($P = 10^{-2}$–10^{-1} Torr); the strong electric fields of these centers destroy the excitons in nanocrystals.

(ii) The formation of P_{b0} centers as a result of adsorption of NO_2 ($P > 0.1$ Torr) with the subsequent

oxidation of the *por*-Si layers. The free charge carriers that are generated as a result of dissociation of excitons can effectively recombine nonradiatively at defects, which causes the value of I_{PL} to decrease.

(iii) The filling of the pores with a dielectric liquid in a C_5H_5N atmosphere (at $P > 1$ Torr) as a consequence of the condensation of pyridine in the pores of the samples. This process causes the value of E_{exc} to decrease and, as a consequence, leads to thermal dissociation of excitons at a given temperature.

ACKNOWLEDGMENTS

We thank V.Yu. Timoshenko for helpful discussions. E.A. Konstantinova acknowledges the support of a grant from the President of the Russian Federation (no. MK-2036.2003.02).

This study was also supported by a program of the Ministry of Industry, Science, and Technology of the Russian Federation (contract no. 40.012.1.1.1153).

REFERENCES

1. L. T. Canham, Appl. Phys. Lett. **57**, 1046 (1990).
2. W. Theib, Surf. Sci. Rep. **29**, 91 (1997).
3. S. P. Zimin, Fiz. Tekh. Poluprovodn. (St. Petersburg) **34**, 359 (2000) [Semiconductors **34**, 353 (2000)].
4. A. G. Gullis, L. T. Canham, and P. D. J. Calcott, J. Appl. Phys. **82**, 909 (1997).
5. L. Boarino, C. Baratto, F. Geobaldo, *et al.*, Mater. Sci. Eng. **69–70**, 210 (2000).
6. K. H. Li, S. Tsai, J. Sarathy, and J. C. Campbell, Appl. Phys. Lett. **62**, 3192 (1993).
7. M. Ben-Chorin, A. Kux, and I. Schechter, Appl. Phys. Lett. **64**, 481 (1994).
8. P. K. Kashkarov, E. A. Konstantinova, and V. Yu. Timoshenko, Fiz. Tekh. Poluprovodn. (St. Petersburg) **30**, 1479 (1996) [Semiconductors **30**, 778 (1996)].
9. S. Fellah, R. B. Wehrspohn, N. Gabouze, *et al.*, J. Lumin. **80**, 109 (1998).
10. V. Yu. Timoshenko, Th. Dittrich, and F. Koch, Phys. Status Solidi B **222**, R1 (2000).
11. L. Boarino, F. Geobaldo, S. Borini, *et al.*, Phys. Rev. B **64**, 205308 (2001).
12. L. J. Bellamy, *Advances in Infrared Group Frequencies* (Methuen, London, 1968; Mir, Moscow, 1971).
13. A. N. Nesmeyanov and N. A. Nesmeyanov, *Principles of Organic Chemistry* (Khimiya, Moscow, 1974), Vol. 2 [in Russian].
14. G. Mattei, V. Valentini, and V. A. Yakovlev, Surf. Sci. **502–503**, 58 (2002).
15. H. J. von Bardeleben, D. Stievenard, A. Grosman, *et al.*, Phys. Rev. B **47**, 10 899 (1993).
16. V. Lehmann, R. Stengl, and A. Luigart, Mater. Sci. Eng. **69–70**, 11 (2000).
17. P. K. Kashkarov, B. V. Kamenev, E. A. Konstantinova, *et al.*, Usp. Fiz. Nauk **168**, 577 (1998) [Phys. Usp. **41**, 511 (1998)].
18. M. G. Lisachenko and V. Yu. Timoshenko, Vestn. Mosk. Univ., Ser. Fiz. **5**, 30 (1999).
19. F. F. Vol'kenshteĭn, *Electron Processes on Semiconductor Surfaces under Chemisorbtion* (Nauka, Moscow, 1987) [in Russian].

Translated by A. Spitsyn

Semiconductors, Vol. 38, No. 11, 2004, pp. 1350–1355. Translated from Fizika i Tekhnika Poluprovodnikov, Vol. 38, No. 11, 2004, pp. 1392–1398.

PHYSICS OF SEMICONDUCTOR DEVICES

Nonlinear Frequency Conversion in a Double Vertical-Cavity Surface-Emitting Laser

Yu. A. Morozov*^, I. S. Nefedov*, and V. Ya. Aleshkin**

**Institute of Radio Engineering and Electronics, Russian Academy of Sciences, Saratov, 410019 Russia*

^e-mail: mor@ire.san.ru

***Institute for Physics of Microstructures, Russian Academy of Sciences, Nizhni Novgorod, 603600 Russia*

Submitted January 27, 2004; accepted for publication March 9, 2004

Abstract—Optical characteristics of a double vertical-cavity surface-emitting laser using the lattice nonlinearity of a GaAs/AlGaAs structure for emission in the mid-IR region are analyzed in detail. The conditions for continuous-wave lasing with a power of ~0.1 mW at 13 μm at a pump current density of 5 kA/cm^2 are determined. *© 2004 MAIK "Nauka/Interperiodica".*

INTRODUCTION

Radiation sources operating at the mid-infrared (IR) region (from 3 to 30 μm) are of great interest for monitoring the environment and for various military and medical applications. To date, significant progress has been made in covering this region using so-called quantum-cascade lasers (QCLs) [1–3]. Considering all their parameters, such lasers have no competitors among semiconductor lasers. However, it is well known that QCLs have active regions that are complex in design; they include hundreds of quantum-confinement layers and requires that the wave functions of carriers be matched in the adjacent layers. Presently, the fabrication of such lasers can be afforded by only a few scientific centers. This circumstance is one of the driving forces behind the search for new principles that could be used in developing devices emitting in the mid- and far-IR regions. In this context, the principle of nonlinear frequency conversion through either the lattice [4] or the electron [5] nonlinearity in quantum wells has been considered. This concept implies that the desired optical emission arises as a result of the nonlinear mixing of two simultaneously generated waves of higher frequencies (for example, in the near-IR region). Furthermore, it is assumed that the nonlinear conversion yielding the difference frequency is performed in an external unit, while the initial modes should be formed in a coupled-cavity laser [6].

We believe that the use of the lattice nonlinearity of a GaAs/AlGaAs structure [4] for the implementation of three-wave nonlinear mixing of two high-frequency oscillations in the laser cavity and emission at the difference frequency [4] is more promising. It is well known that the amplitude value of an electric field in the laser cavity can be as high as 10^4–10^5 V/cm, and the elements of the nonlinear susceptibility tensor in such structures are about 10^{-8} cm/V. Under these conditions, the nonlinear polarization in the bulk of the cavity appears to be sufficiently high to ensure a reasonable lasing power in the mid-IR region. However, in stripe lasers that emit through the end face [4], one of the main obstacles to optimal performance is the difficulty in ensuring the phase-matching conditions for the nonlinear-polarization wave at the difference frequency and the waveguide mode at the same frequency. Recently, we proposed a new laser in which this principle is realized in a vertical-cavity structure [7]. Since the length of the vertical cavity considered in [7] does not exceed the coherence length $l_c = \pi/\Delta k$ (Δk is the difference between the wave numbers of the nonlinear polarization wave and the waveguide mode at the difference frequency), it is not necessary to provide for the phase-matching conditions for these waves. The desired effect can be obtained by an appreciable increase in the amplitudes of high-frequency waves, which serve as the sources of nonlinear polarization due to the high Q factor of a vertical cavity with Bragg mirrors having a reflection coefficient of ~0.995. It should be noted that a vertical-cavity surface-emitting laser was described, in which the lattice nonlinearity of a GaAs/AlGaAs structure is used for the second harmonic generation in the visible range (0.5 μm) [8].

In this study, we performed a detailed numerical analysis of the characteristics of optical radiation resulting from nonlinear conversion in a double vertical-cavity surface-emitting laser, which was proposed by us for the first time in [9]. One of the cavities is tuned to high-frequency oscillations and the other cavity is tuned to the difference harmonic. According to our calculations, such a structure makes it possible to significantly increase both the nonlinear polarization and the stored energy at the difference frequency in the mid-IR region. As a result, the power density of the desired

radiation significantly increases (by approximately a factor of 100 compared with the laser described in [7]).

THE LASER MODEL

A schematic diagram of the structure of a double vertical-cavity surface-emitting laser is shown in Fig. 1. Two quantum-confinement $In_xGa_{1-x}As/GaAs$ active layers responsible for near infrared lasing at $\lambda_{1,2}$ (~1 μm) are separated by an $Al_{0.2}Ga_{0.8}As$ layer. The thickness of the latter is about a quarter of λ_m, which is the mean value of $\lambda_{1,2}$ (taking into account the refractive index). In this case, the longitudinal distribution of field in the active regions is such that the antinodes of one of the high-frequency modes fall close to the nodes of the other mode. As a result, the influence of each active layer on the field amplified in the neighboring active layer decreases. The nonlinear three-wave mixing with the generation of the difference mode with λ_r occurs mainly in the intermediate $Al_{0.2}Ga_{0.8}As$ layers, which are referred to as the nonlinear conversion layers. We propose using two sets of Bragg reflectors composed of alternating quarter-wave GaAs/AlAs layers. One of these sets (the first, for definiteness) limits the vertical cavity, which is tuned to the waves with the wavelengths $\lambda_{1,2}$; i.e., these waves belong to the neighboring longitudinal modes of this cavity. The Bragg mirrors from the second set are tuned to reflect the difference wave and are transparent at the wavelengths $\lambda_{1,2}$. Thus, the laser structure is formed by two vertical cavities one of which is enclosed by the other. The internal cavity ensures the lasing conditions in the near-IR region. The external cavity, when it is precisely tuned to the wavelength λ_r, considerably amplifies the field at the difference frequency in the region of its interaction with the nonlinear polarization at this frequency. In this case, as analysis shows, the conversion efficiency increases significantly and, therefore, the power density of the mid-IR radiation increases as well. The additional (tuning) AlAs layers, adjoining from inside the Bragg reflectors of the second set, ensure accurate tuning of the resonant frequency of the external cavity to the difference frequency.

It is well known that the Drude absorption by free charge carriers is one of the main reasons for high nonresonant losses of optical radiation in the mid-IR region. Therefore, in order to increase the Q factor of the cavity tuned to the wavelength λ_r, we propose to use undoped layers in all Bragg reflectors. Current pumping can be provided by heavily doped contact p- and n-type layers located in the cavities. Along with a decrease in the optical losses, the method proposed is likely to reduce the series resistance and, therefore, the structure heating. The current and the optical fields in the transverse section of the laser are limited by oxide (AlO) apertures (windows). Preliminary analysis shows that a reasonable value of power in the mid-IR region is attained only when the diameter of the oxide windows considerably exceeds the wavelength at the difference frequency. Therefore, the approximation of plane uniform waves propagating in the vertical direction (across the layers) can serve as a first approximation for the analysis of the electrodynamic characteristics of lasing.

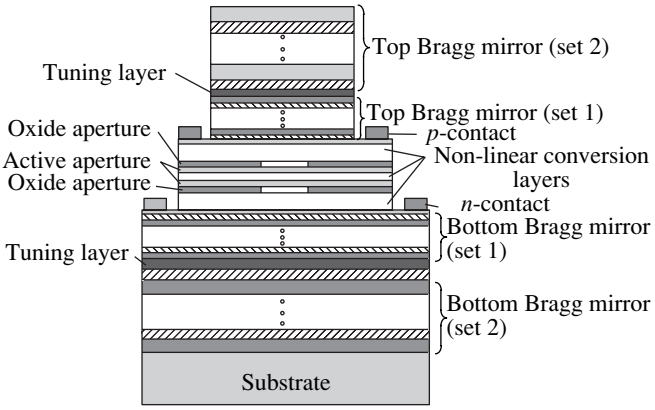

Fig. 1. Schematic of the laser structure.

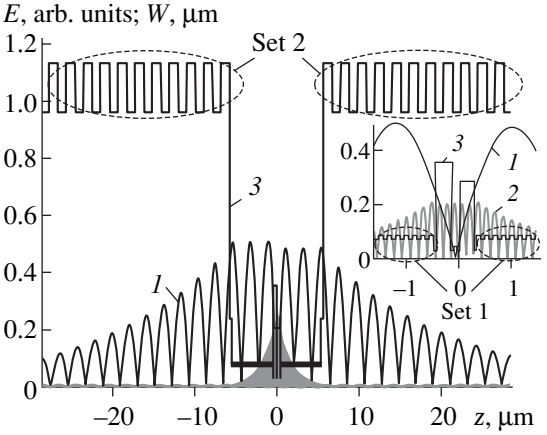

Fig. 2. Absolute values of the cavity eigenfunctions for (*1*) the difference wave and (*2*) one of the near-IR waves along with (*3*) the layer thickness vs. the longitudinal coordinate z. Inset: the same for the central part of the structure on an enlarged scale.

Figure 2 shows the distribution of the electric field amplitudes (E) in the mid-IR region (curve *1*) and one of the high-frequency eigenmodes (curve *2*) along the z direction, which is perpendicular to the structure layers. The corresponding eigenvalues are λ_r and λ_1. Curve *3* characterizes the change in the thickness W of the layers forming the laser structure. The inset shows the same dependences for the central part of the structure on an enlarged scale. The calculation was carried out for $\lambda_1 = 0.96$ μm and $\lambda_2 = 1.037$ μm, which corresponds to the difference wavelength $\lambda_r = 12.86$ μm. The upper and the lower mirrors contain equal numbers of periods and, in the case under study, consist of 32 (set 1) and 11 (set 2) pairs of layers. Either $3\lambda_1/n(\lambda_1)$ or $2.5\lambda_2/n(\lambda_2)$ fit

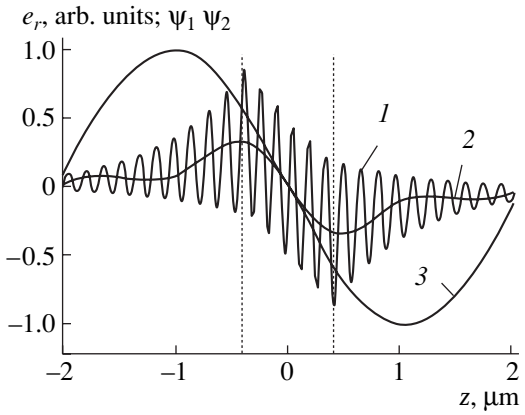

Fig. 3. Distributions of (*1*) nonlinear polarization, (*2*) its envelope, and (*3*) the cavity mode at the difference frequency over the cavity length. Dotted lines mark the internal boundaries of the Bragg mirrors (set 1).

into the length of the internal cavity, i.e., between the Bragg reflectors from set 1. In other words, the waves with wavelengths λ_1 and λ_2 are formed by the neighboring longitudinal modes of this cavity. As is evident, the external cavity has a length of $2.5\lambda_r$ with regard to the refractive index n. It can be seen that the thickness W of the layers forming the external cavity is 1 μm. Since the drive current does not pass through these mirrors, the epitaxial growth used for their production can be replaced by deposition as an alternative method. If the deposition technique is used, the GaAs/AlAs pair can be replaced by another pair of materials that are transparent in the mid-IR range under consideration. All the conclusions of the analysis carried out below remain qualitatively valid.

MATHEMATICAL BACKGROUND

The structure of the nonlinear permittivity tensor for zinc blende–type crystals is such that the nonlinear mixing of waves running in the crystal-growth direction is possible if the substrate orientation differs from the (100) plane. Recently, frequency doubling was successfully realized in a vertical-cavity surface-emitting laser grown on an inclined (311)-oriented substrate [8]. Therefore, for definiteness, we assume that the double vertical-cavity surface-emitting laser under study is also grown on a GaAs(311) substrate.

It can be shown that the module of the second-order nonlinear polarization related to the interaction between waves with amplitudes $E^{(1)}$, $E^{(2)}$ and wavelengths λ_1, λ_2 is equal to $\mathcal{P} = 2\chi\varepsilon_0 d_{14} E^{(1)} E^{(2)}$. Here, d_{14} is the element of the nonlinear susceptibility tensor, $\chi = 27/(11\sqrt{22}) \approx 0.523$, and ε_0 is the permittivity of free space.

Writing the high-frequency electric fields as functions of the longitudinal coordinate in the form $E^{(1,2)} = E_0^{(1,2)}\psi_{1,2}(z)$, where $E_0^{(1,2)}$ are the amplitude values in the corresponding active layers, and using the theory of external excitation of cavities [10], we obtain the following expression for the power density at λ_r:

$$\frac{P_r}{S} = \frac{1}{2\rho_0}\left[\frac{4\pi\chi}{\lambda_r}E_0^{(1)}E_0^{(2)} \times \int_l d_{14}\psi_1\psi_2 e_r dz \Big/ \left(1 + \int_l n_r\alpha_r e_r^2 dz\right)\right]^2. \quad (1)$$

Here, n_r, α_r, and $e_r = E_r/E_{r\text{surf}}$ are the refractive index, the damping constant, and the amplitude of the difference eigenmode normalized to the electric field of this wave at the emitting surface, respectively; $\rho_0 = 120\pi$ is the wave impedance of free space. The integration is carried out over the entire length of the structure l. Note that the expression in the denominator of the fraction in square brackets describes the normalized total power of the eigenmode losses due to the damping of field in the material of the cavity and the radiative losses. The amplitude of the difference eigenmode is normalized to the power of the eigenmode radiative losses.

The power density of the difference wave is controlled to a great extent by the overlap integral of the normalized nonlinear polarization $\psi_1(z)\psi_2(z)$ and the cavity eigenmode $e_r(z)$. Figure 3 shows the behavior of these values for the central part of the laser. The abscissa axis begins from the middle of the lower active layer. It can be seen that the nonlinear polarization (curve *1*) contains a fast oscillating component, which excites waves at the sum frequency, and the envelope, which is responsible for the formation of the difference wave. The envelope of the nonlinear polarization (curve *2*), which is obtained by filtering out the fast oscillating component, is of greatest interest. The analysis of these curves suggests the following. First, the polarization envelope is an odd function and, at given laser parameters, its peak values lie close to the positions of the internal boundaries of the Bragg reflectors from the first set. Therefore, the cavity eigenmodes at the difference frequency must also be odd, i.e., have a node at $z = 0$, which is evidenced by curve *3*. The eigenmodes with λ_r that feature an antinode in the vicinity of $z = 0$ correspond to an external cavity of a size that is a multiple of an even number of half-waves, and they are not excited by the polarization wave specified. Second, the nonlinear polarization at the difference frequency exists only within the region that does not exceed the polarization wavelength. Therefore, it is not necessary to provide for the phase-matching conditions for the polarization wave and the cavity eigenmode at the difference frequency.

The amplitudes of the fields in the active layers are related to the laser parameters via the rate equation for the carrier concentration (see, e.g., [11]):

$$\frac{J}{ed_a} = \frac{N_{\text{th}i}}{\tau_N} + BN_{\text{th}i}^2 + CN_{\text{th}i}^3 + g(N_{\text{th}i})c\frac{n_a\varepsilon_0 E_0^{(i)^2}}{2hf_i}, \quad i = 1, 2. \tag{2}$$

Here, J is the drive current density; e is the elementary charge; h is Planck's constant; $N_{\text{th}i}$ and $g(N_{\text{th}i}) = g_0\ln(N_{\text{th}i}/N_0)$ are the threshold carrier concentration and the gain factor in the ith layer, respectively; $f_i = c/\lambda_i$; c is the speed of light; n_a is the refraction index of the active layer; τ_N is the nonradiative recombination lifetime; B and C are the radiative and Auger recombination coefficients, respectively; and N_0 is the transparency carrier concentration. Remaining within the above one-dimensional approximation, we assume the drive current density in Eq. (2) to be independent of the coordinates in the planes of the active layers and disregard the diffusion of carriers over these planes.

Introducing the normalized values $\nu_{\text{th}} = N_{\text{th}}/N_0$ and $G_{\text{th}} = g(N_{\text{th}})/g_0$ of the squared amplitudes of fields in the active layers, we obtain

$$E_0^{(i)^2} = D(\nu_{\text{th}i} + \gamma\nu_{\text{th}i}^2 + \delta\nu_{\text{th}i}^3) \times \frac{1}{G_{\text{th}i}n_a\lambda_i}\left(\frac{J}{J_{\text{th}i}} - 1\right), \tag{3}$$

where $D = 2hcN_0\rho_0/(g_0\tau_N)$, $\gamma = BN_0\tau_N$, $\delta = CN_0^2\tau_N$, and $J_{\text{th}i}$ is the threshold current in the ith active layer.

The normalized gain factors $G_{\text{th}i}$ at the lasing threshold for $\lambda_{1,2}$ were determined, as usual, from the condition for balance between the gain and the total loss due to both the wave attenuation in the cavity bulk and the escape through the interface with the environment. We also assume that the frequency dependence of the gain factor in the ith active layer can be represented as a Lorentzian:

$$G_i(\lambda) = G_{i0}\left[1 + \left(2\frac{\lambda - \lambda_i}{\Delta\lambda_{gi}}\right)^2\right]^{-1},$$

where G_{i0} is the maximum gain factor and $\Delta\lambda_{gi}$ is the gain bandwidth.

Bearing in mind the relation between the electric field and the power of radiation at the interface with the environment, we obtain the following expression for the power density of the high-frequency lasing modes:

$$\frac{P_i}{S} = D'(\nu_{\text{th}i} + \gamma\nu_{\text{th}i}^2 + \delta\nu_{\text{th}i}^3)\frac{1}{G_{\text{th}i}n_a\lambda_i} \times (e_{\text{surf}}^{(i)})^2\left(\frac{J}{J_{\text{th}i}} - 1\right). \tag{4}$$

Table 1. Parameters of the structure

Parameter	Value
Mean wavelength λ_m, μm	1
Active layer thickness d_a, μm	0.03
The refractive index of the active layers n_a	3.6
Contact layer thickness d_c, μm	0.03
The element of nonlinear susceptibility tensor d_{14}, cm/V	1.7×10^{-8} (GaAs [8]) 0.39×10^{-8} (AlAs [8])
Carrier lifetime τ_N, ns	5 [11]
Gain factor g_0, cm^{-1}	2000 [11]
Transparency concentration N_0, cm^{-3}	1.5×10^{18} [11]
Radiative recombination coefficient B, cm^3/s	10^{-10} [11]
Auger recombination coefficient C, cm^6/s	3.5×10^{-30} [11]
Amplification band width $\Delta\lambda_g$, μm	0.1

In expression (4), $D' = hcN_0/(g_0\tau_N)$ and $e_{\text{surf}}^{(i)} = E_{\text{surf}}^{(i)}/E_0^{(i)}$ is the ratio of the electric field amplitudes at the emitting interface and in the ith active layer.

THE RESULTS OF CALCULATIONS

Table 1 lists the parameters of the laser structure that were used in the calculations. As was mentioned above, the power density at the difference frequency in many respects depends on the radiative losses in the laser structure. The wave damping in the doped layers at near-IR frequencies determines the required value of the gain factor in the active regions and, therefore, the threshold current for lasing at $\lambda_{1,2}$. In turn, the power density of the electric fields that give rise to the nonlinear polarization depends on the excess of the working current over its threshold value (see Eq. (2)). At the same time, it follows from Eq. (1) that losses at the difference frequency directly affect the intensity of the radiation formed as a result of nonlinear conversion. The damping constants for waves in the doped layers of the laser structure are listed in Table 2. As the main mechanism responsible for the attenuation in the n-type layers, we considered the free carrier absorption and used the results reported in the reviews of Blakemore [12] and Adachi [13]. Note the fairly high value of the damping constant at the difference frequency in the n-doped contact layer. This result accounts for the fact that, at a given doping level, the wavelength of the reflectance plasma edge is ~9 μm; i.e., the difference frequency is lower than the plasma frequency.

It is well known that, along with the free-carrier absorption, the intersubband absorption scattering in the valence band of p-doped layers may also play a significant role. However, it is difficult to estimate this contribution theoretically. Hence, the estimations for

Table 2. Absorption factors of the structure in the near-IR region ($\alpha_{1.2}$) and the mid-IR region (α_r)

Layer	Carrier concentration, 10^{18} cm^{-3}	$\alpha_{1.2}$, cm^{-1}	α_r, cm^{-1}
p-GaAs (contact)	10	120	5400
p-$Al_{0.2}Ga_{0.8}As$ (nonlinear conversion layer)	1	15	460
n-GaAs (contact)	10	60	33000
n-$Al_{0.2}Ga_{0.8}As$ (layer of nonlinear conversion)	1	5	500

p-type layers were obtained by processing the experimental data of [14–16].

Figure 4 shows the power density of radiation at the difference frequency in the mid-IR region (curve *1*) and the modes with frequencies in the near-IR region (curves *2*, *3*) versus the drive-current density. The calculations were performed for a laser with an internal cavity limited by the Bragg reflectors consisting of 32 pairs of layers. The external cavity, which is tuned to the difference frequency, contains 11 pairs of layers. As one would expect, the dependence of the intensity of radiation due to the nonlinear conversion appears to be square. At the given laser parameters, the power density at the difference frequency is lower than that of the high-frequency modes by a factor of about 2000; it is equal to ~10^{-3} μW/μm^2 at a drive-current density of 5 kA/cm^2.

It is of interest to analyze the dependence of the power density of radiation in the mid-IR region on the parameters of the laser under study, in particular, on the reflection coefficient of the Bragg mirrors forming the external cavity. This dependence is illustrated by Fig. 5. It can be seen that, with an increase in the number of pairs of the layers M_2 forming the mirrors, the radiation power first increases, then the dependence levels off, and finally decreases. (The optimum number of periods for the GaAs/AlAs pair is $M_2 = 11$.) This behavior can be attributed to the double effect of the increase in the power density of the difference mode with increasing reflection coefficient of mirrors limiting the external cavity. At first, when the losses in the cavity material are low, an increase in the electric field at the difference frequency in the region of interaction with the nonlinear polarization (i.e., in the central part adjacent to the active layers) enhances the interaction and, consequently, increases the output power in the mid-IR region. As the amplitude of the difference wave increases, the role of the damping in the cavity material becomes significant. Recall that these losses are proportional to the squared amplitude or, in other words, to the energy density (see expression (1)). As a result, the output power at the difference frequency decreases. Note that, in the limiting case when the external cavity is absent (i.e., $M_2 = 0$), the laser structure studied here can be described by the model considered in [7], which assumed that the standing wave of nonlinear polarization gives rise to a running wave at the difference frequency.

For the chosen value $M_2 = 11$, we analyzed the power of radiation in the mid-IR region as a function of the reflection coefficient of the mirrors forming the internal cavity (Fig. 6). Since these mirrors are transparent for radiation at the difference frequency and are used in the cavities tuned to this frequency, the number of their periods M_1 can vary discretely with a step for which the external-cavity length varies by λ_r with regard to the refractive index. The reason for the latter fact is as follows. As was mentioned above, the spatial distribution of nonlinear polarization in this laser is such that the difference mode is generated only if an odd number of half waves λ_r fits in the cavity length. The squares in Fig. 6 show the values of M_1 which satisfy this condition. Thus, for 19, 32, and 45 periods in each reflector of the first set, the length of the external cavity amounts to 3, 5, and 7 half-waves, respectively; and this sequence can be continued. The analysis of this

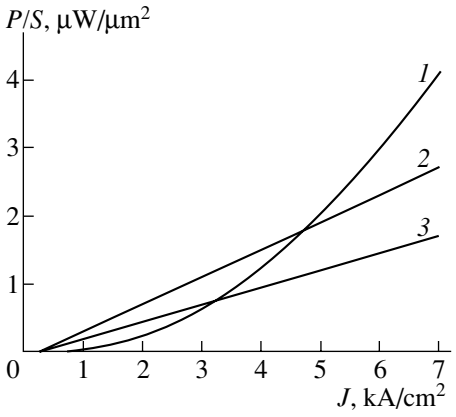

Fig. 4. Intensity of radiation P/S in the (*1*) middle and (*2, 3*) near-IR regions vs. the drive current density. For curve *1*, the data on the ordinate axis are scaled up by 2×10^3 times.

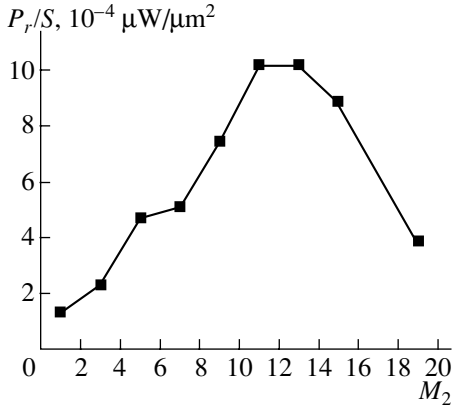

Fig. 5. Power density of radiation at the difference frequency vs. the number of pairs of layers in the mirrors of the external cavity. The internal cavity is limited by reflectors consisting of 32 pairs of layers.

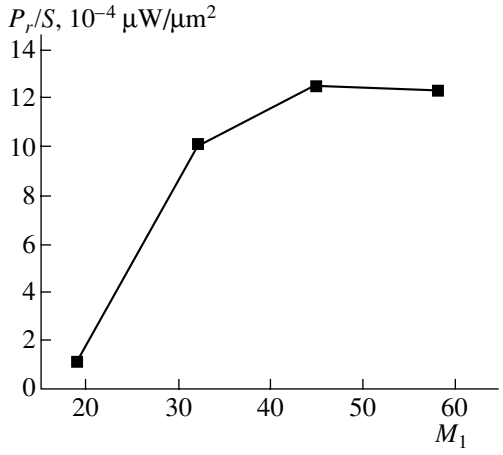

Fig. 6. Intensity of lasing in the mid-IR region vs. the reflectivity of the mirrors of the internal cavity.

dependence suggests that, as M_1 grows, the mid-IR power at the output aperture first sharply increases and then levels off. This behavior is caused by the initial rapid increase in the amplitudes of the optical fields with wavelengths $\lambda_{1,2}$ and their subsequent falloff (due to the fact that the losses related to the emission of these waves from the cavity become much lower than the damping in the cavity itself).

CONCLUSIONS

A model of a vertical-cavity laser operating in the mid-IR region is proposed on the basis of the principle of nonlinear frequency conversion.

The validity of the plane-wave approximation is substantiated, and the electrodynamic problem for eigenvalues in the complex region is solved in this approximation, which enables the geometrical and electrical laser parameters to be determined.

The profile of the second-order nonlinear polarization in the structure is calculated. It is demonstrated that there is no need to match the phase velocities of the polarization wave and the cavity eigenmode at the difference frequency.

The behavior of a double vertical cavity pumped by a nonlinear polarization wave at the difference frequency in the mid-IR region is analyzed. It is shown that the power density in this region is the quadratic function of the pump and attains 10^{-3} μW/μm^2 (which corresponds to the power ~100 μW for the aperture 350 μm) at a drive current density of ~5 kA/cm^2.

The intensity of lasing in the mid–IR region is studied as a function of the structure parameters.

It is established that an increase in the reflectivity of the Bragg mirrors that form the external cavity subsequently leads to the growth, saturation, and drop of the output power. For the damping constant typical of a cavity with built-in current contacts, we estimate the optimal number of periods in the mirrors as 11 if the periods consist of GaAs/AlAs layers.

The effect of the number of the pairs of layers M_1 comprising the internal cavity on the power density of the difference mode is also calculated. The value of M_1 is allowed to vary with a step corresponding to a change in the external cavity length by λ_r, taking into account the refractive index. An increase in the reflection coefficient of the mirrors of the internal cavity is shown to result in the initial rapid growth and the following saturation of the mid-IR radiation intensity. At the given parameters of the laser structure, the optimal number of M_1 is 45.

ACKNOWLEDGMENTS

This work was supported by the Russian Foundation for Basic Research–Belarusian Republican Foundation for Fundamental Research (project no. 02-02-81036-Bel2002_a), the Russian Foundation for Basic Research (project no. 04-02-17432), and the International Science and Technology Center (ISTC) (project no. 2293).

REFERENCES

1. A. Matlis, S. Slivken, A. Tahraoui, *et al.*, Appl. Phys. Lett. **77**, 1741 (2000).
2. R. Kôhler, A. Tredicucci, F. Beltram, *et al.*, Nature **417**, 156 (2002).
3. J. Faist, D. Hofstetter, M. Beck, *et al.*, IEEE J. Quantum Electron. **38**, 533 (2002).
4. V. Ya. Aleshkin, A. A. Afonenko, and N. B. Zvonkov, Fiz. Tekh. Poluprovodn. (St. Petersburg) **35**, 1256 (2001) [Semiconductors **35**, 1203 (2001)].
5. A. Belyanin, F. Capasso, V. Kocharovsky, *et al.*, Phys. Rev. A **63**, 53803 (2001).
6. L. Chusseau, G. Almuneau, L. Coldren, *et al.*, IEE Proc.: Optoelectron. **149** (3), 88 (2002).
7. Yu. Morozov, I. Nefedov, and V. Aleshkin, in *Proceedings of 5th International Conference on Transparent Optical Networks (ICTON2003)* (Warsaw, 2003), p. 243.
8. Y. Kaneko, S. Nakagawa, Y. Ichimura, *et al.*, J. Appl. Phys. **87**, 1597 (2000).
9. Yu. Morozov, I. Nefedov, and V. Aleshkin, Appl. Phys. Lett. (in press).
10. B. Z. Katsenelenbaum, *High-Frequency Electrodynamics* (Nauka, Moscow, 1966) [in Russian].
11. G. Hadley, K. Lear, M. Warren, *et al.*, IEEE J. Quantum Electron. **32**, 607 (1996).
12. J. Blakemore, J. Appl. Phys. **53**, R123 (1982).
13. S. Adachi, J. Appl. Phys. **58**, R1 (1985).
14. J. Piprek, D. Babić, and J. Bowers, J. Appl. Phys. **81**, 3382 (1997).
15. W. Songprakob, R. Zallen, D. Tsu, and W. Liu, J. Appl. Phys. **91**, 171 (2002).
16. W. Songprakob, R. Zallen, W. Liu, and K. Bacher, Phys. Rev. B **62**, 4501 (2000).

Translated by A. Sidorova

Semiconductors, Vol. 38, No. 11, 2004, pp. 1356–1363. Translated from Fizika i Tekhnika Poluprovodnikov, Vol. 38, No. 11, 2004, pp. 1399–1407.

PHYSICS OF SEMICONDUCTOR DEVICES

Properties of GaSb-Based LEDs with Grid Ohmic Contacts

A. N. Imenkov, E. A. Grebenshchikova, B. E. Zhurtanov, T. N. Danilova, M. A. Sipovskaya, N. V. Vlasenko, and Yu. P. Yakovlev^

Ioffe Physicotechnical Institute, Russian Academy of Sciences, St. Petersburg, 194021 Russia

^e-mail: yak@iropt.ioffe.rssi.ru

Submitted April 7, 2004; accepted for publication April 19, 2004

Abstract—We studied light-emitting diodes (LEDs) based on GaSb–GaInAsSb–GaAlAsSb heterostructures with the emission due to electron transitions from the conduction band to levels of intrinsic double-charged acceptors. Parallelepiped-shaped LEDs with a round or gridlike contact on the surface of the epitaxial layer were studied experimentally and theoretically. The relations describing the current spreading from round and grid contacts are presented. It is shown that grid contacts, in contrast to round ones, provide a uniform distribution of current over the emitting layer. The current density under a grid contact is smaller than under a round one by a factor of 20, which is especially important for long-wavelength ($\lambda \gtrsim 2$ μm) LEDs, in which the contribution of the nonradiative Auger recombination is significant. An emission power of 3.5 mW at 300 mA current is obtained from grid-contact LEDs. © *2004 MAIK "Nauka/Interperiodica".*

1. INTRODUCTION

As shown in our earlier study [1], light-emitting diodes (LEDs) in which the emitting layer is close to the external surface carrying the ohmic contact are liable to an undesirable physical effect: the emission is concentrated under the contact, which, when the current increases, leads to a considerable decrease in the differential efficiency and to a high current density under contact. The latter circumstance causes a decrease in the length of the superlinear portion in the light–current characteristic with small currents. The contribution of nonradiative Auger recombination becomes significant even with a small current, because the density of nonequilibrium carriers increases. The emission efficiency decreases. In the subsequent study [2], we examined LEDs with a developed light-emitting outer surface, which ensured that the emission within the crystal was omnidirectional. It was shown that the external quantum yield of emission increases as the ratio between the area of light-emitting chip and its volume increases. This means that it is desirable that the LED chip be thin. The theoretical relations obtained showed the possibility of total extraction of the emitted light from the chip if the chip thickness is reduced. This effect is ensured by multipass propagation of light and its reemission and low nonphotoactive absorption.

The reduction of the thickness of the chip to ~100 μm as a method for the production of high-efficiency LEDs for the near-IR range has long been in use [3, 4]. Recently, the thickness of the chip was further reduced by nearly two orders of magnitude [5, 6], and problems arose related to insufficient current spreading under the ohmic contacts. The concentration of current under the contact is especially undesirable in LEDs for the mid-IR spectral range, because the contribution of nonradiative Auger recombination is large, and the emitted light is strongly absorbed by free carriers. An increase in the carrier density related to the concentration of current compounds these undesirable effects.

The goal of the present study was to reduce the concentration of emitted light under the contact in mid-IR LEDs by fabricating grid ohmic contacts, and to investigate the spreading of current from these contacts over a thin semiconductor layer.

2. EXPERIMENTAL PROCEDURE

The LED structures under study were fabricated by liquid-phase epitaxy on (100) *n*-GaSb substrates that were 400 μm thick. The substrates were doped with Te to an electron density of 8×10^{17} cm^{-3}. At the first stage, an active undoped layer with a composition similar to GaSb was grown from a standard melt with 0.03% In added. The In doping reduced the layer bandgap by only 1 meV. This layer had *p*-type conduction because some Ga atoms occupied Sb. The thickness of the layer was 2 μm. A 3.5-μm-thick *p*-$GaAl_{0.34}SbAs$ confining layer with a wider bandgap was then grown; it was doped with Ge to a hole density of 1×10^{18} cm^{-3}. On top, a 0.5-μm-thick *p*-GaSb contact layer was grown, heavily doped with Ge to a hole density of 8×10^{19} cm^{-3}.

For experimental studies, a wafer with epitaxial layers was cut into several parts, and LED structures with metal contacts of different shape and size were fabricated by contact photolithography (Fig. 1).

The first type of semiconductor LED structures was conventional. After polishing, the thickness of the structure was 300 μm. Contacts of 100 μm in diameter were formed on the side of the epitaxial layer, i.e., on the *p* region, by successive deposition of Cr, Au + Ge

1063-7826/04/3811-1356$26.00 © 2004 MAIK "Nauka/Interperiodica"

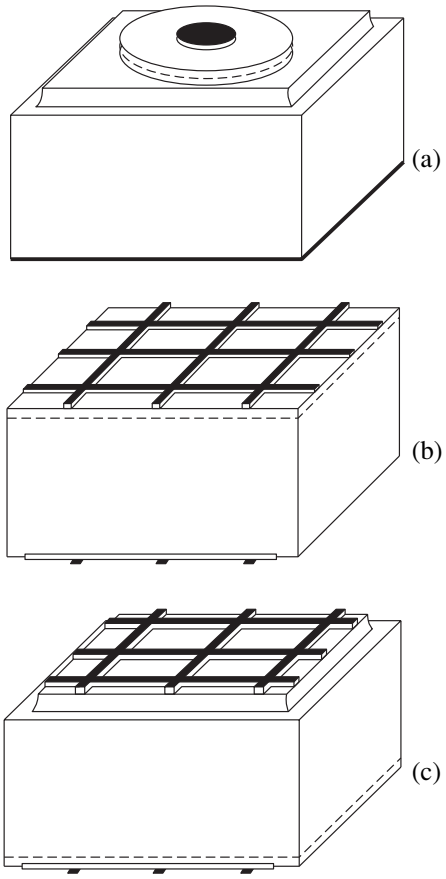

Fig. 1. Three types of LED crystals: (a) with round contacts and the light-emitting region in the front-face mesa structure, (b) with grid contacts and the light-emitting region in the front-face position, and (c) with grid contacts and the light-emitting region near the crystal holder.

alloy, and Au in a VUP-4 vacuum installation. On the substrate side, i.e., on the *n* region, Cr, Au + Te, and Au were deposited. Then the contact layers were fired-in for 1 min at a temperature of 250°C. After that, a pattern in the form of squares with 475 μm sides and a step of 500 μm was formed by photolithography to divide the structure into separate chips. At the next stage, mesas of 300 μm in diameter and 10 μm in height were formed at the square centers, so that the previously fired-in contacts of 100 μm in diameter were in the center of the mesa. After the LED crystal was cleaved into separate chips, each chip was mounted, substrate down, in a TO-18 LED case with a planar table.

In order to compare LEDs of conventional configuration (Fig. 1a), chips with gridlike contacts were fabricated from the same LED structure (Figs. 1b, 1c). The width of stripes was 25 μm; the step, 150 μm. The LED structure was preliminarily thinned to a thickness of 270 μm by chemical etching of the substrate. Grid contact layers were deposited both on the epitaxial layer (*p* region) and on the substrate (*n* region) sides: (Cr, Au + Ge, and Au) and (Cr, Au + Te, and Au), respectively. After the deposition, the grid contacts were fired-in for 1 min at a temperature of 250°C. A pattern in the form of squares with a 500-μm step and 25-μm-wide separating stripes was then formed by photolithography to divide the structure into separate chips. After the structure was cleaved, each chip was mounted in a TO-18 LED case with a planar table. Some of the chips were mounted with the substrate down; others, with the epitaxial side down (Figs. 1b and 1c, respectively).

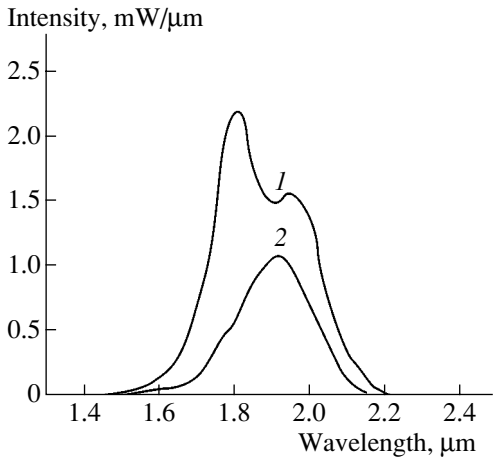

Fig. 2. Emission spectra of a round-contact LED at current 75 mA, measured in two directions: (*1*) normal to the front face and (*2*) normal to the lateral face.

The emission spectra and far-field pattern were studied at room temperature with currents in the range 10–300 mA. To reduce heating, the LEDs were cooled with a domestic fan. The spectra were recorded with an MDR-2 diffraction monochromator, which was calibrated in emission power units per unit wavelength, mW μm^{-1}. To calculate the total emission power, spectra were recorded in two orientations: normal to the *p–n* junction plane and parallel to it, but normal to one of the crystal faces. In the calculation of the total emission power, the power in the parallel direction was doubled, which corresponds exactly to the far-field pattern of parallelepiped-shaped LEDs.

3. EXPERIMENTAL RESULTS

LEDs with round and grid contacts differ in their fundamental parameters: emission spectra, far-field patterns, and light–current characteristics (Figs. 2–6).

3.1. Emission Spectra

First, we will discuss type-I LEDs with a round contact on the epitaxial outer side and a uniform contact on the substrate soldered to the sample holder. The emission spectrum recorded in the direction normal to the *p–n* junction plane exhibits two bands with peak wavelengths of 1.76 μm (photon energy 0.705 eV) and 1.9 μm (0.65 eV) and FWHM of 0.14 and 0.17 μm,

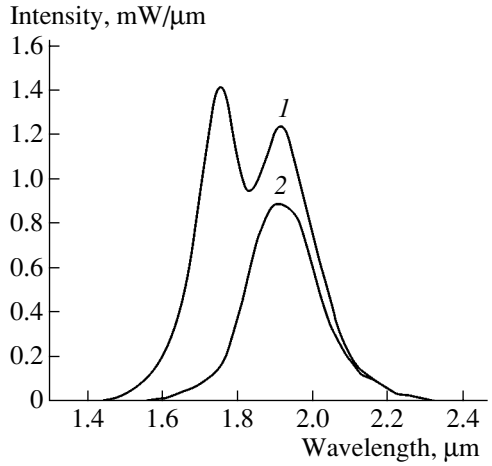

Fig. 3. Emission spectra of a grid-contact LED, with the emitting region in the front-face position, measured in two directions: (*1*) normal to the front face and (*2*) normal to the lateral face.

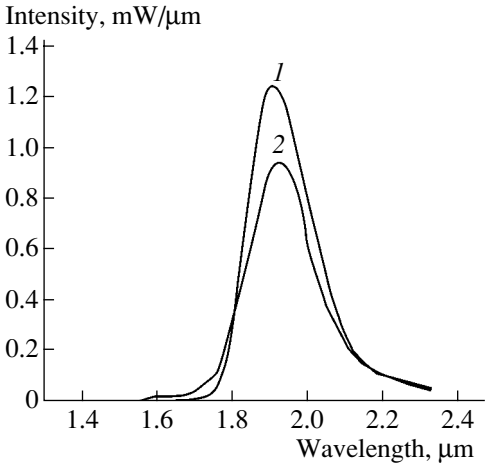

Fig. 4. Emission spectra of a grid-contact LED, with the light-emitting region near the crystal holder, measured in two directions: (*1*) normal to the front face and (*2*) normal to the lateral face.

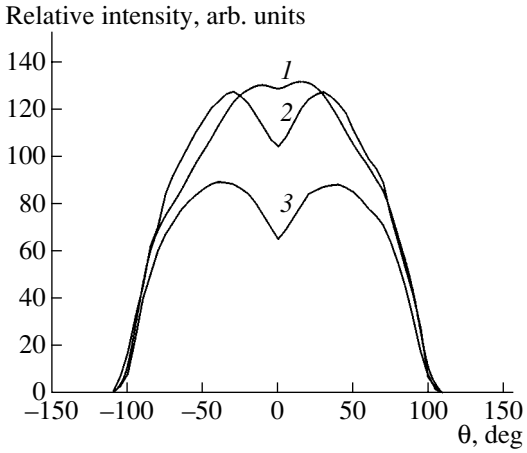

Fig. 5. Far-field pattern for three types of LEDs: (*1*) with round contacts, (*2*) with grid contacts and the light-emitting region in the front-face position, and (*3*) with grid contacts and the light-emitting region near the crystal holder.

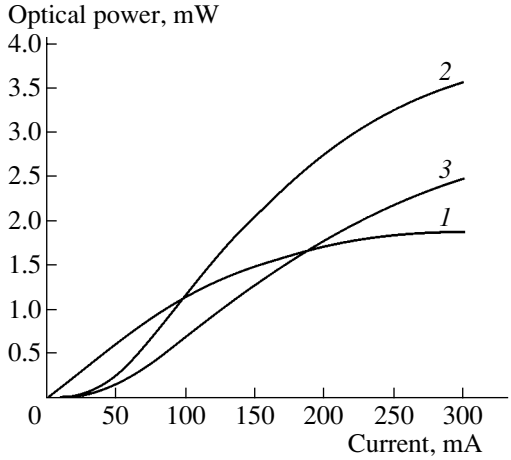

Fig. 6. Light–current characteristics for three types of LEDs: (*1*) with round contacts, (*2*) with grid contacts and the light-emitting region in the front-face position, and (*3*) with grid contacts and the light-emitting region near the crystal holder.

respectively (Fig. 2, curve *1*). The integrated power of the short-wavelength band is 20% higher than that of the long-wavelength one. In the *p–n* junction plane, only the long-wavelength band is observed (Fig. 2, curve *2*). Its integrated power nearly equals the power of the long-wavelength band recorded in the direction normal to the *p–n* junction plane, and the width is 20% larger.

Type-II LEDs, which have grid contacts and the epitaxial side facing outwards, demonstrate very similar emission spectra (Fig. 3). For these LEDs, the power of the short-wavelength and long-wavelength bands is nearly the same for emission normal to the *p–n* junction plane, whereas the power of the long-wavelength band for the in-plane emission is ~15% higher.

Type-III LEDs, with grid contacts, emit only in the long-wavelength band (Fig. 4). The emission power in the normal direction (Fig. 4, curve *1*) is 25% higher than the power of emission in the *p–n* junction plane (Fig. 4, curve *2*). For both directions of emission, FWHM is 0.2 μm.

3.2. Far-Field Pattern

Each type of LED demonstrates its own far-field pattern of emission (Fig. 5). The emission of type-I LEDs, with a round contact on the outer *p* surface, is the

strongest in the direction normal to the *p–n* junction plane (Fig. 5, curve *1*), although, strictly speaking, a slight dip is often observed in this direction, as can be seen in Fig. 5. As the angle θ of deviation from the normal direction increases, the emission intensity first increases by 5%, and at the deviation angles θ > 20° it decreases smoothly; at θ = 80° it is about 30–35% of the zero-angle value. At deviation angles θ > 90°, the emission intensity sharply decreases, which is typical of all LED types, because of shading by the sample holder.

Type-II LEDs demonstrate much a stronger dip in the far-field pattern at a zero angle (Fig. 5, curve *2*). At first, the emission intensity increases by 23% as the angle increases to 30°; then, at θ = 80°, it decreases to 50–60% of its zero-angle value.

Type-III LEDs with grid contacts demonstrate an even stronger zero-angle dip in the far-field pattern (Fig. 5, curve *3*). As the angle increases, the intensity first rises smoothly; at θ = 40° it becomes 35% higher than the zero-angle value, and then it smoothly decreases, so that at θ = 80° it is 80% of the zero-angle value.

3.3. Quantum Efficiency

In the LEDs under study, the dependence of the emission power *P* on current *I* is nonlinear (Fig. 6). It is superlinear at small currents of up to 10 mA in type-I diodes (Fig. 6, curve *1*) and up to 75 mA in type-II and type-III diodes (Fig. 6, curves *2*, *3*); at higher currents, it is sublinear.

The almost total absence of the superlinear portion in LEDs with a small-area round contact on the outer *p* surface has been observed in [1]. It was explained by the weak spreading of current under this contact over the *p* surface and the concentration of current under the contact. The density of nonequilibrium carriers under the contact and near it is sufficient for the saturation of deep recombination centers, which do not produce emission even at small currents (<10 mA). Such a strong concentration of current does not occur in the case of grid contacts.

In terms of emission power, type-II and type-III LEDs are more efficient than type I at currents >90 and >190 mA, respectively (Fig. 6). The emission power of type-I LEDs does not exceed 2 mW at any current (see Fig. 6 and the table), whereas the emission power of type-II and type-III LEDs at a current of 300 mA is as high as 3.5 and 2.5 mW, respectively.

The integral external quantum yield of photons η_e at 75 mA, when heating by current and current concentration under the contact are insignificant, is the highest in type-I LEDs (~2%, see table), because nonemitting deep levels are saturated at this current, whereas in LEDs of other types they are not saturated. However, the maximum differential external quantum yield of photons in type II (η_{ed} = 3.5%) is higher than in type I, where it reaches 2.5%. In this respect, type-III LEDs

LED parameters

LED type	*P*, mW (*I* = 300 mA)	η_e, % (*I* = 75 mA)	η_{ed}, %	η_{em}, %	I_{opt}, mA
I	2.0	1.94	2.5	2.2	40
II	3.5	1.91	3.2	2.4	180
III	2.5	1.34	2.2	1.7	225

are inferior (2.2%) to other types, because the light-emitting region lies at a considerable distance from the outer face. The current at which η_{ed} is the highest is 20 mA in type-I and 100 mA in type-II and type-III LEDs.

In type I, the integral external quantum efficiency of emission reaches its maximum, η_{em} = 2.2%, at current I_{opt} = 40 mA (see table). In type II, η_{em} = 2.4%, i.e., higher than in type-I diodes at higher current (I_{opt} = 180 mA), and in type-III LEDs η_{em} = 1.7% at I_{opt} = 225 mA.

Thus, LEDs with grid contacts can work at higher currents and demonstrate higher external quantum efficiency and emission power than LEDs with round contacts.

However, to obtain the quantitative relationships between the LED parameters and the configuration of contacts, a theoretical examination of the current spreading is necessary. The spreading depends on a variety of parameters, including the conductivity and thickness of the epitaxial layers, the mechanisms of recombination of nonequilibrium carriers, and the shape and size of ohmic contacts. The chosen parameters must provide the desired spectra, a high quantum efficiency of emission, and a fast speed of operation, among other things.

4. THEORETICAL EXAMINATION OF CURRENT SPREADING

The current spreading from ohmic contacts is followed by ohmic voltage drop over the area of the *p–n* structure that is not covered by the contact and a gradual decrease in current because of the electron–hole recombination. The spreading current becomes zero at the boundary of the *p–n* structure that is the farthest from the contact. In the LEDs under study, the voltage drop occurs mainly in the *p* region, because it is considerably thinner than the *n* region, and its conductivity is lower. Therefore, we disregard the resistance of the *n* region. First, we consider the current spreading in a thin *p* region of LEDs with a round contact, and then with the grid contact.

4.1. Round Contact

Let a round ohmic contact of the radius r_c be located on the surface of a round *p* region of the radius r_s. Let σ be the conductivity of the *p* region, and *a*, the *p*-layer thickness. The variation of current *I* and voltage *V*

along the radius r, starting from the central point, are described by the relations

$$\frac{dI}{dr} = -J_0(e^{eV/\beta kT} - 1)2\pi r, \quad (1)$$

$$\frac{dV}{dr} = -\frac{I}{\sigma a 2\pi r}, \quad (2)$$

where J_0 is the density of the saturation current corresponding to the operative recombination mechanism, which is characterized by the coefficient β; kT, the thermal energy of an elementary particle; and e, the elementary charge.

To simplify the solution of the system of equations (1) and (2), we neglect the unity in Eq. (1), assuming that $eV \gg kT$ in LEDs operating under forward bias. To make Eqs. (1) and (2) dimensionless, we make the substitutions

$$y = e\frac{(V - V_c)}{\beta kT}, \quad x = r/r_c$$

and denote

$$I_\sigma = \frac{\beta kT}{e}\sigma a, \quad I_c = \pi r_c^2 J_0 e^{eV_c/\beta kT},$$

where V_c is the voltage across the p–n junction under the contact, and I_c the current concentrated under the contact. Then Eqs. (1) and (2) take the form

$$\frac{dI}{dx} = -2I_c x e^y, \quad (3)$$

$$I = -2\pi I_\sigma x\frac{dy}{dx}. \quad (4)$$

Now we make the substitution $xdy/dx = u$ in Eq. (4) and obtain

$$I = -2\pi I_\sigma u. \quad (5)$$

We then differentiate Eq. (5) and substitute it into (3), which is thereby transformed into the following dimensionless equation

$$\frac{du}{dx} = \frac{I_c}{\pi I_\sigma} x e^y. \quad (6)$$

The differentiation of (6) and the necessary transformations lead us to an equation for u:

$$x\frac{d^2u}{dx^2} - (1 + u)\frac{du}{dx} = 0. \quad (7)$$

The spreading current $I = -2\pi I_\sigma u$, which is dependent on x, is easily calculated from u.

The value of u at $x = 1$ yields the total spreading current I_0. We limit our consideration to calculating the total spreading current I_0. By substituting $u(x) = \eta(\xi)$ and $\xi = \ln x$, Eq. (7) is transformed into an equation with constant coefficients:

$$\eta'' - 2\eta' - \eta\eta' = 0. \quad (8)$$

The solution to a similar equation can be found in the handbook [7, p. 500]. Equation (8) is integrated termwise, and a first-order equation with separable variables is obtained:

$$\eta' = 2\eta + \frac{1}{2}\eta^2 + C, \quad (9)$$

where C is the integration constant.

Equation (9) can be written in the former variables, u and x:

$$x\frac{du}{dx} = \frac{1}{2}u^2 + 2u + C. \quad (10)$$

Using (5) and (6) with $x = 1$, Eq. (10) gives a formula that relates I_c, I_0, and C:

$$I_c = \frac{I_0^2}{8\pi I_\sigma} - I_0 + \pi I_\sigma C. \quad (11)$$

Separating variables in (10) and integrating with respect to u from $-I_0/2\pi I_\sigma$ to 0 and with respect to x from 1 to x_s, we obtain expressions that relate I_0 and C:

$$I_0 = 2\pi I_\sigma \times \begin{cases} (x_s^{\sqrt{4-2C}} - 1)2C \\ \times \dfrac{1}{x_s^{\sqrt{4-2C}}(2 + \sqrt{4-2C}) - (2 - \sqrt{4-2C})} & \text{at } C < 2, \\ 2\ln x_s/(1 + \ln x_s) \text{ at } C = 2, \\ 2 - \sqrt{2C-4} \\ \times \tan\left(\arctan\dfrac{2}{\sqrt{2C-4}} - \dfrac{\sqrt{2C-4}}{2}\ln x_s\right) & \text{at } C > 2. \end{cases} \quad (12)$$

The relations (11) and (12) allow the calculation of currents in the area that is free of the contact and under the contact, I_0 and I_c, corresponding to the same value of C. Setting different C values, we can obtain the dependence of I_0 on I_c. Curve *1* in Fig. 7a shows the thus obtained dependence of I_0 on the total current in the LED, $I_\Sigma = I_0 + I_c$, for the LED under study with I_σ = 2.5 mA and $x_s = 3$. As can be seen, the dependence is sublinear beginning with a zero current. Curves *1* in Figs. 7b and 7c, respectively, show the dependences of the current under the contact J_c and of the ratio $s_0 = I_0/I_c$ on I_Σ. The superlinearity of the dependence $I_c(I_\Sigma)$ is noticeable, as is the sharp decrease in I_0/I_c at currents <100 mA. At $I_\Sigma > 180$ mA, $I_0 < I_c$.

The limiting relations for the spreading current have the form

$$I_0 \approx sI_c \text{ at } I_\Sigma < 8\pi I_\sigma(s + 1)s^{-2}, \quad (13)$$

$$I_0 \approx \sqrt{8\pi I_\sigma I_c} \text{ at } I_\Sigma > 8\pi I_\sigma(s + 1)s^{-2}, \quad (14)$$

where $s = x_s^2 - 1$ is the ratio between the area free of contact to that under the contact. It can be seen from (13) and (14) that the dependence $I_0(I_c)$ is linear at small currents and of square-root type at high currents. In the structures under study, the transition from a linear to a square-root dependence occurs at the total current I_Σ = 9 mA.

4.2. Grid Contacts

The contact grid divides the *p* surface into separate cells. First, we will consider the current spreading within a single cell; then, we will summarize over all the cells. To deal with a one-dimensional problem, we assume that the free-of-contact *p* surface of a cell is not square, but round with the same area. This substitution of shape introduces no significant error but allows us to use the solution obtained for a round contact. We place the point of origin at the center of a cell. The equivalent radius of the free-of-contact *p* surface of a cell is $r_c = (b - \delta)/\sqrt{\pi}$, where *b* is the step of the contact grid and δ, the width of stripes. The dimensionless radius is expressed by the same formula as that used for a round contact, $x = r/r_c$. Since the inverse geometrical situation is considered in the case of a grid contact, the directions of current spreading and the *x* axis are the opposite, and the current *I* in Eqs. (1) and (2) and the spreading current will have the same absolute value, but with opposite signs. Applying the boundary conditions at $x = 0$, where $u = 0$ and $u' = 0$, to Eq. (10), we obtain $C = 0$. For $C = 0$, the spreading current at $x = 1$ is easily calculated from (10). For the case of a grid contact, Eq. (6) can be represented as

$$\frac{du}{dx} = \frac{sI_{c1}}{\pi I_\sigma} x e^y, \tag{15}$$

where $s = (b - \delta)^2 b^{-1}(2b - \delta)^{-1}$ is the ratio between the free-of-contact and under-contact areas of the *p* surface, and I_{c1} is the recombination current under the contact within a cell. It is taken into account that the spreading current in a cell I_{01} is the current *I* in Eq. (5) at x =1, with the opposite sign. Now Eq. (10) gives the dependence of I_{01} on I_{c1}:

$$I_{01} = 4\pi I_\sigma \left(-1 + \sqrt{1 + \frac{sI_{c1}}{2\pi I_\sigma}}\right). \tag{16}$$

The desired dependence of the total spreading current I_0 on the current under contact I_c is related to the number of cells $m = S_k/b^2$ (where S_k is the total area of the *p* surface) by

$$I_0 = 4\pi I_\sigma m \left(-1 + \sqrt{1 + \frac{sI_c}{2\pi I_\sigma m}}\right). \tag{17}$$

The limiting formulas for the spreading current in the case of grid contacts have the form

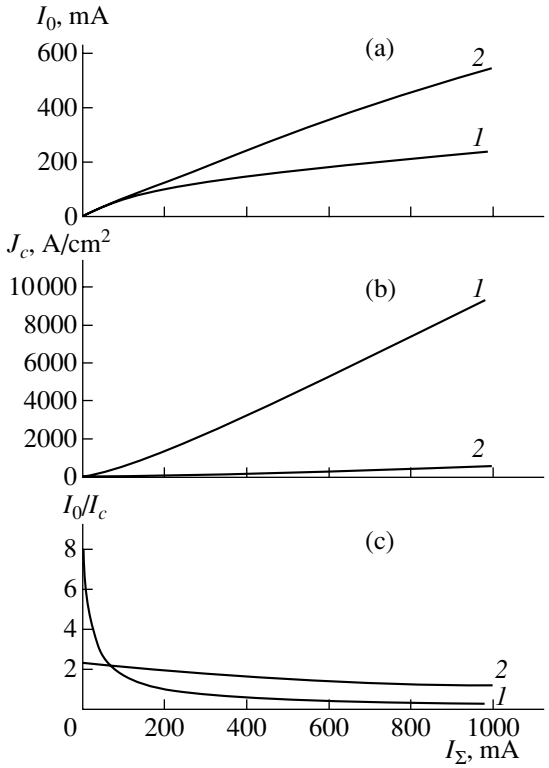

Fig. 7. Theoretical dependences of (a) current in the free-of-contact area I_0, (b) current density under the contact J_c, and (c) the ratio of currents in the free-of-contact area and under the contact I_0/I_c on the total current I_Σ. (*1*) Round-contact and (*2*) grid-contact LED.

$$I_0 \approx sI_c \quad \text{at} \quad I_\Sigma < 8\pi m I_\sigma (1 + 2s^{-1}), \tag{18}$$

$$I_0 \approx \sqrt{8\pi I_c I_\sigma sm} \quad \text{at} \quad I_\Sigma > 8\pi m I_\sigma (1 + 2s^{-1}). \tag{19}$$

It can be seen from (18) and (19) that the general form of the relations describing the spreading of current under the contact in a grid-contact LED is similar to that in a round-contact LED. The difference is that the transition from linear to square-root behavior occurs at much higher currents. In the structure under study with s = 2.27, m =11, and I_σ = 2.5 mA, this transition occurs at a total current of 1300 mA. As can be seen in Fig. 7a, in a grid-contact LED the dependence of I_0 on I_Σ remains nearly linear up to a total current of 1300 mA, whereas in the case of a round contact this becomes a root dependence at currents that are 100 times smaller. The current density under a grid contact is 20 times smaller than under a round one (Fig. 7b). Grid contacts can provide a reasonably uniform distribution of current over the emitting layer, and the internal quantum yield of photons is the highest for a given narrow-gap layer.

Now we will calculate the voltage variation over the layer, which is less than or approximately equal to *kT/e* with a uniform distribution of current and much larger with a nonuniform distribution. In the case of a grid contact, this can be done easily, because $C = 0$. After the

substitution $x = udx/dy$ in the left-hand part of (10), it takes the form

$$dy = \frac{2du}{u+4}. \quad (20)$$

Integrating (20) with respect to y and u in the range of their spatial variation from the origin of coordinates to the contact, we calculate the desired variation of dimensionless voltage over the spreading layer:

$$-\Delta y = 2\ln\left(1+\frac{u_0}{4}\right), \quad (21)$$

where $u_0 = u(x = 1)$.

Since $u_0 = 4$ at the boundary between the square-root and linear portions of the dependence $I_0(I_c)$, at this boundary $\Delta y = -2\ln 2$ in accordance with (21); i.e., the magnitude of voltage variation over the layer is $\sim 1.4\beta kT/e$. In this case, the density of the recombination current changes by a factor of 4, i.e., twice that of the average value, in other words, insignificantly. Since $u_0 < 4$ at the linear portion, the recombination current density in the layer varies less than twice that of its average value. At the square-root portion, the variation is much stronger, so the distribution of current cannot be regarded as uniform.

A similar dependence is obtained for the case of a round contact, but the distribution of the recombination current can be regarded as uniform for a current that is 100 times smaller than that for a grid contact.

Note also that, in the case of grid contacts, $I_0 > I_c$ for currents up to $I_\Sigma = 1300$ mA or higher, whereas for round contacts $I_0 > I_c$ for $I_\Sigma < 200$ mA. Therefore, the emission is shaded by grid contacts less than by round ones.

5. INTERNAL QUANTUM YIELD OF PHOTONS

The emission through the front face contains a component with a spectrum similar to the original spectrum of the active region. To select this component, we use the fact that the second component is similar to the emission through the lateral faces. As we have shown in [2], with isotropic emission in the crystal these components differ in the external quantum yield of photons by a factor equal to the ratio of the free-of-contact areas of the facets. The isotropy of emission in the LEDs under study is maintained by the roughness of the polished surface of the substrate and by the etching grooves from which the emitted light is reflected diffusely. In the case of grid contacts, the ratio between the free areas of the front and the lateral faces is given by

$$s_f = \frac{Ls}{H(s+1)}, \quad (22)$$

where L is the step of the separating grid and H, the crystal thickness.

The external quantum yield of photons through a single lateral face is conveniently determined from the angle θ_{max} in the far-field pattern, which corresponds to the maximum intensity of the photon flux. Also, it must be taken into account that the emission intensity in the p–n junction plane is doubled due to the reflection from the crystal holder. With regard to these factors, we obtain a simple relation which determines the ratio between the internal quantum yields of the short- and long-wavelength emission, η_s and η_l:

$$\frac{\eta_s}{\eta_l} = \frac{k_s}{1-k_s-0.5s_f\tan\theta_{max}}, \quad (23)$$

where k_s is the fraction of the short-wavelength photons emitted from the crystal in the direction normal to the front face. For type-II LEDs at $k_s = 0.5$, $s_f = 1.16$, and $\theta_{max} = 30°$, we obtain $\eta_s = 3\eta_l$; i.e., the internal quantum yield for the short-wavelength photons is threefold larger than for the long-wavelength ones. We believe that the undistorted emission spectrum from the narrow-gap layer contains a single band with a small shoulder at the position of the long-wavelength band. The value of η_s is easily determined from the external yield of the short-wavelength photons η_{es}, because η_{es} is only affected by the coefficient of the emergence of emission from the crystal and by the shading from contacts, and not by the nonphotoactive absorption in the crystal, which can be expressed by the relation

$$\eta_s = \frac{1+\eta_{es}}{1+s_0/(s_0+1)n(n+1)^2\eta_{es}}, \quad (24)$$

where n is the refractive index.

In type-II LEDs at 75 mA current, $\eta_{es} = 0.424\%$, and $s_0 = 2$, we obtain $\eta_s = 37.5\%$; in this case, $\eta_l = 12.5\%$.

Now it is convenient to use Eq. (4) from our study [2] for the external quantum yield of the long-wavelength photons, η_e, which is totally applicable to type-III LEDs, to determine the coefficient of nonphotoactive absorption in the crystal, α_d. Preliminarily, the effective absorption coefficient in the crystal, which characterizes the emergence of emitted light from the crystal, must be calculated using relation (6) from [2]:

$$\alpha_e = \frac{S}{Vn(n+1)^2}, \quad (25)$$

where S is the free-of-contact area of the crystal surface and V is the crystal volume. For type-III LEDs, $\alpha_e = 1.13\ \text{cm}^{-1}$.

Relation (4) for η_e from [2], resolved with respect to the nonphotoactive absorption coefficient α_d, has the form

$$\alpha_d = \alpha_e\left[\frac{\eta_l}{\eta_e(1-\eta_s)}-1\right]. \quad (26)$$

For type-III LEDs at $\eta_e = 1.34\%$ and 75 mA current, we obtain $\alpha_d = 16\ \text{cm}^{-1}$. The fact that α_d is an order of mag-

nitude greater than α_e stresses the importance of nonphotoactive absorption. Furthermore, estimates of the internal quantum yield of photons at optimal current give $\eta = \eta_s + \eta_l = 63\%$, i.e., a value approaching 100%.

6. ANALYSIS OF THE EXPERIMENTAL DATA

LEDs with an active region located near the outer front face, with a round or a grid ohmic contact, emit light with a spectrum that contains both the short-wavelength band and the long-wavelength band related to double-charge acceptors (Figs. 2, 3).

The weak dependence of the emission spectra on current indicates that the emission is generated in the *p* region, where the occupancy of the double-charge centers is virtually independent of current, in contrast to the *n* region. The *n* region in the substrate plays the main role in nonphotoactive absorption due to its large thickness.

A significantly lower current density under a grid contact (Fig. 7), compared to round one, is confirmed by the large length of the superlinear portion of light–current characteristics (Fig. 6), from 0 to 200 mA in type-II and type-III LEDs (curves *2*, *3*), whereas in type-I LEDs this portion extends only as far as 10 mA (curve *1*). In this portion, deep nonradiative recombination centers are saturated, which demands a high current density.

Owing to the low current density in grid-contact LEDs, the internal quantum yield of radiative recombination does not noticeably decrease as current increases from 100 to 300 mA. Therefore, the emission power at a current of 300 mA reaches high values: 2.5–3.5 mW. LEDs with an active region near the outer face have an advantage in the form of the short-wavelength band. The thermal resistance of crystals in type-II and type-III LEDs is nearly the same (~15 K/W), because heat is released mainly in the crystal bulk in nonphotoactive absorption of the emitted light.

Note that the internal parameters of the LED crystal $\eta_s = 37.5\%$, $\eta_l = 12.5\%$, $\eta = 50\%$, and $\alpha_d = 16$ cm^{-1} are calculated for type-II and type-III LEDs at a current of 75 mA, when the external quantum yield of photons is 1.91 and 1.34%, respectively. At optimal current, the external quantum yield of photons reaches 2.4 and 1.7%, respectively. The maximum external quantum yield of photons is achieved at $\eta_s = 47\%$, $\eta_l = 16\%$, and $\eta = 63\%$. So the high emission efficiency is accounted for by the uniformity of the current distribution over the *p–n* junction area in grid-contact LEDs, which makes it possible to operate the whole active area in the optimal emission mode.

If the differential external quantum yield of photons of 3.2 and 2.2%, respectively, is taken into account, we obtain an internal quantum yield of photons of 84%, which is very close to 100%. This quantum yield of photons equals the fraction of recombination via double-charged acceptors in the total interband and quasi-interband recombination, including nonradative recombination. The results obtained open up prospects for the development of high-efficiency high-power LEDs that operate on electron transitions via double-charge acceptors.

7. CONCLUSION

The results obtained suggest the following.

(1) The emission spectra obtained for LEDs with grid and round contacts are similar.

(2) Grid-contact LEDs have a much higher emission power than round-contact ones.

(3) Mathematical relations have been derived that describe the current spreading from round and grid contacts and make it possible to choose the parameters of the semiconductor layers to provide a uniform distribution of current over the *p–n* junction area.

(4) Experiments and calculations show that the current density under grid contacts is 20 times smaller than under round ones, which significantly reduces the contribution of nonradiative Auger recombination and makes it possible to obtain a high emission power—up to 3.5 mW at a current of 300 mA.

(5) The internal quantum yield of emission in the long- and short-wavelength bands of the double-charge acceptor in *p*-GaSb, as determined from the experiment, is 16 and 47%, respectively. The coefficient of nonphotoactive absorption of the recombination emission in an LED is 16 cm^{-1}.

ACKNOWLEDGMENTS

This study was supported in part by the Russian Foundation for Basic Research (project no. 04-02-17655) and by the U.S. Civilian Research and Development Foundation (CRDF) (grant no. Rpo-1407-ST-03).

REFERENCES

1. E. A. Grebenshchikova, A. N. Imenkov, B. E. Zhurtanov, *et al.*, Fiz. Tekh. Poluprovodn. (St. Petersburg) **37**, 1465 (2003) [Semiconductors **37**, 1414 (2003)].
2. E. A. Grebenshchikova, A. N. Imenkov, B. E. Zhurtanov, *et al.*, Fiz. Tekh. Poluprovodn. (St. Petersburg) **38**, 745 (2004) [Semiconductors **38**, 717 (2004)].
3. Zh. I. Alferov, V. M. Andreev, D. Z. Garbuzov, *et al.*, Pis'ma Zh. Tekh. Fiz. **2**, 1066 (1976) [Sov. Tech. Phys. Lett. **2**, 420 (1976)].
4. Zh. I. Alferov, V. M. Andreev, D. Z. Garbuzov, *et al.*, Pis'ma Zh. Tekh. Fiz. **3**, 657 (1977) [Sov. Tech. Phys. Lett. **3**, 268 (1977)].
5. I. Schnitzer, E. Yablonovitch, C. Caneay, *et al.*, Appl. Phys. Lett. **63**, 2174 (1993).
6. R. Windisch, P. Heremans, A. Knobloch, *et al.*, Appl. Phys. Lett. **74**, 2256 (1999).
7. É. Kamke, *Gewöhnliche Differentialgleichungen* (Akademie, Leipzig, 1959; Nauka, Moscow, 1971).

Translated by D. Mashovets